Orbital excitations
of
transition-metal oxides
in
optical spectroscopy

Inaugural Dissertation

zur

zur Erlangung des Doktorgrades
der mathematisch-naturwissenschaftlichen Fakultät
der Universität zu Köln

vorgelegt von

Reinhard Rückamp

aus Bensberg

Köln, im März 2006

*Das Ganze ist mehr
als die Summe der Teile.*

Diese Arbeit widme ich
meiner Familie

Contents

Introduction

At first sight one might think that orbital physics does not contribute to our daily life but is restricted to the labs of some physicists. For the novel collective phenomena proposed for the orbital degree of freedom this is certainly true at this stage. However, looking at a bottle of green glass its green color is given to it by iron(III) and iron(II) ions which are diluted in the silicon dioxide of which a colorless, transparent glass consists. Visible light that passes through the glass of the bottle is absorbed by these so called color centers in a characteristic way. Our visual perception of the resulting spectrum gives us the impression of green. One might ask: Fine, but where is orbital physics involved here? Well, it happens on the color centers. The iron(III) and iron(II) ions are present in their ground state. By the absorption of photons of a certain energy (corresponding to light of a certain color) the electronic state of the iron ions is changed to an excited state. The excited state differs from the ground state by the occupation of the $3d$ orbitals (with excitation energies in the visible spectrum). In a free ion all the states that differ only in the $3d$ orbital occupation have the same energy, i.e. they are degenerate. For an ion within a crystal this degeneracy is lifted at least partially due to the reduction of the rotational symmetry by the crystalline environment. States of different energy will allow transitions between them. For chromium(III) ions in an Al_2O_3 host lattice (well known as ruby) the absorption spectrum is shown in Fig. 1 [1]. Chromium ions in ruby and the iron ions in green glass are isolated and do not interact with each other. However, new fascinating physics will arise in case of interaction between ions with degenerate or nearly degenerate orbital states. The degeneracy then will be lifted by collective phenomena.

Orbital physics requires an orbital degree of freedom in the sense that there is an electronic shell which is partially filled. One class of compounds where this condition is often fulfilled are transition-metal oxides. But these are famous not only for orbital physics. Transition-metal oxides were placed on top of the agenda of solid-state physicists after the discovery of high-temperature superconductivity in the cuprates in 1986 by Bednorz and Müller [2]. From this strong activity followed not only an increase of the superconducting T_c up to 134 K, but also the discovery of many unusual physical properties in other compounds of this class. One of the most prominent is certainly the colossal magneto resistance[1] that has been found in the manganites [3]. In many cases only small changes of parameters like variation of doping concentration induce drastic changes in physical properties which lead to rich phase diagrams. This complex behavior is founded in the electronic structure of the transition-

---

[1]Colossal magneto resistance denotes a high sensitivity of the resistance of a crystal on a weak applied magnetic field (the resistance drops e.g. about nine orders of magnitude in $La_{1-x}Sr_xMnO_3$).
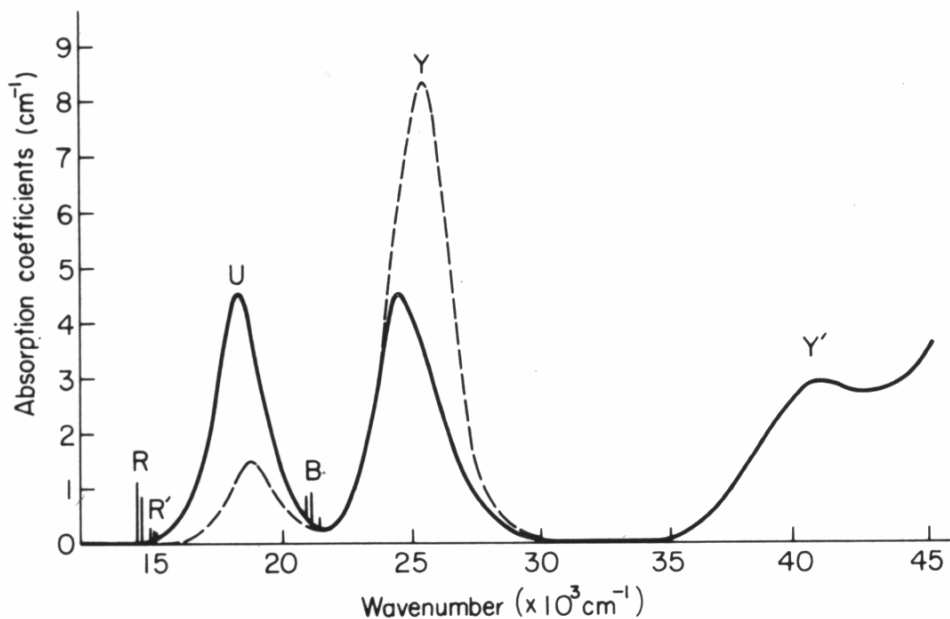
1

Figure 1: The absorption spectrum of ruby [1]. One observes strong and broad absorption peaks above 15000 cm^{-1}. The absorption peaks reflect transitions between different orbitals. In the visible spectrum (12500 cm^{-1} - 25000 cm^{-1}), ruby is opaque except for the range below 15000 cm^{-1}. This is where the deep red color of ruby comes from.

metal ions. The characteristic feature of transition-metal compounds is that the metal ions exhibit a partially filled $3d$ shell with strong correlations between the electrons. The spin degree of freedom opens the way to a rich variety of magnetic states.

For such a partially occupied shell, band-structure theory predicts a metallic state. However, it is possible that the system is in fact insulating due to the *on-site* Coulomb repulsion between electrons. This phenomenon occurs when the bandwidth (kinetic energy gain) is small compared to the strong Coulomb repulsion U. Hence the electrons do not hop to a neighboring site in order to avoid double occupancy. Such an insulator is called Mott insulator. The most important difference from the usual band insulator is that the internal degrees of freedom, spin and orbital, survive in the Mott insulator. The localized electrons occupy a linear combination of atomic states. Interactions of electrons on adjacent sites are mediated on the one hand by the lattice and on the other hand by (virtual) hopping. An increase of virtual hopping lowers the kinetic energy. Thus neither a fully local nor a fully delocalized description applies. A further complication for understanding the physics arises from the strong interaction of several degrees of freedom. In order to solve this problem one has to take all of them into account on an equal footing. At present it is not possible to do so and this intricate problem is far from being understood [4].

In this field of physical research many different new ground states are proposed. The orbital degrees of freedom and the spin degrees of freedom have a similar structure. This

2

leads to predictions for the existence within the orbital sector of nearly every effect that has been found in the spin channel. For instance different types of orbitally ordered states, orbital liquids [34], orbital Peierls [8], and the orbital Kondo effect [12] have been predicted. However, there exists a big difference between the orbital and the spin degree of freedom: spins couple only weakly to the lattice, but $3d$ orbitals do so much more strongly. Interesting physics and also controversial discussions emerge from the competition of the different interactions. Orbital order may reduce the dimensionality due to the anisotropy of the electron distribution as e.g. in TiOCl (see chapter 5). An even more striking example is $KCuF_3$. It is nearly cubic but due to orbital ordering the magnetic structure turns out to be quasi-one-dimensional [86]. The two-dimensionality of the high-T_c cuprates – although largely due to their layered structure – is substantially enhanced by the fact that the charge carriers (holes) occupy mostly the $x^2 - y^2$ orbitals. Spectacular superstructures are observed in some spinels with transition metals on the B-sites [39]. Examples are an "octamer" ordering in $CuIr_2S_4$ [9] or a "chiral" structural distortion in $MgTi_2O_4$ [10]. Other interesting orbital physics arise from frustration of the orbital exchange. A prominent example is $LiNiO_2$ which is suggested to be a realization of an orbital liquid [11]. It is impossible to list here all the interesting phenomena where orbital physics is involved. But certainly the field of orbital physics is very vivid and rapidly expanding.

The central aim of this thesis was the observation of novel orbital excitations. In the literature, reports of orbital waves have been based on Raman measurements [44, 6, 7]. Optical spectroscopy is a well established tool for the investigation of crystal-field excitations and has become a standard method in chemistry [88]. Therefore it provides an excellent means for the study of novel orbital excitations. In particular, the comparison of infrared and Raman data may offer the possibility to decide on the character of the excitations.

This thesis is organized as follows. The first chapter is devoted to introduce the experimental method of Fourier spectroscopy. It includes the physical foundation of optical properties that are presented in this thesis. The second chapter is about orbital physics. It starts with a short review of conventional crystal-field theory, which is the theoretical approach for local crystal-field excitations. The second part reviews the novel ground states that have been predicted for systems investigated in this thesis. As a third subject the orbital excitations of different ground states are discussed.

In the third chapter results on the orbitally ordered compound $LaMnO_3$ (Mn^{3+} $t_{2g}^3\,e_g^1$) are presented. The key question in this system addresses the nature of the orbitally ordered state. A conventional scenario invokes a collective Jahn-Teller effect (electron-phonon coupling) as the driving force of orbital order. On the other hand, superexchange (electron-electron coupling) is also proposed to lead to an orbitally ordered ground state. These two possible origins of orbital order can be seen as limiting cases, since in fact both interactions are present simultaneously. However, on the basis of the orbital-order pattern it is not possible to decide which of them dominates as both scenarios are able to explain the experimentally observed orbital order. The orbital excitations play an important role in this context as they are well distinct for the two cases. For dominating electron-phonon coupling they are local crystal-field excitations. In the scenario of strong electron-electron coupling, new collective elementary excitations are predicted which exhibit a significant band width. In 2001 Saitoh *et al.* [44] reported the observation of peaks in Raman data which have been interpreted as

collective orbital excitations. This has motivated us to determine the optical conductivity in order to check this claim.

In the fourth chapter we compare our results on the compounds $RTiO_3(R = La, Sm, Y;$ with Ti^{3+} t_{2g}^1 e_g^0) which in the sense of orbital degeneracy are a t_{2g} analogue to $LaMnO_3$. The orbital ground state of $LaTiO_3$ has been discussed controversially in the literature [34, 49, 57, 59, 60]. The observation of a small spin-wave gap and a strongly reduced magnetic moment in this compound seem to contradict each other, since the former suggests a small orbital moment whereas the latter indicates a large orbital moment. Khaliullin has explained these observations by the novel orbital-liquid ground state [34]. In this scenario, the orbital occupancy resists long-range order by fluctuations. On the other hand, the reduction of the magnetic moment has been explained by enhanced charge fluctuations due to the small Mott-Hubbard gap within the more conventional picture of an orbitally ordered ground state [57]. The orbital excitations may also here give a hint which ground state is realized.

In the fifth chapter the results on $TiOX$ (X = Cl, Br) (Ti^{3+} t_{2g}^1 e_g^0) are presented. The bilayer systems are structurally two-dimensional [138]. However, the magnetic susceptibility behaves like in the case of a $S = \frac{1}{2}$ Heisenberg chain at high temperatures [50]. At low temperatures it starts to deviate from the spin-chain behavior and drops to zero below a critical temperature. This has been attributed to a spin-Peierls transition. The one-dimensionality is induced by the orbital ground state in which the occupied orbitals have large overlap only in one direction [50, 143]. Unexpected in a spin-Peierls scenario is however a second transition that occurs at higher temperatures. Due to e.g. a broad NMR signal between the two transition temperatures this behavior has been assigned to strong orbital fluctuations [122]. This motivated us to search for orbital excitations below the electronic gap. Moreover, we measured the phonon range in order to see in how far the lattice is involved in the transitions.

Finally in chapter 6 the results obtained within this thesis are summarized.

In the appendix additional information and some useful results are given which are not new but hard to find in the literature. In part A the Wigner-Eckhart theorem is introduced in the most straight and clear way that we can imagine. In particular the mathematical apparatus is reduced to a minimum. We have not found such a distinct view on the main proposition of the theorem elsewhere in the literature, although it will probably already exist somewhere. Part B gives a detailed view on the structure of the octahedral group O and its representations. In part C and D we provide useful information on the transformation of d-waves under rotations and on p-d matrix elements, respectively. These have been obtained within the research project of this thesis and shall be made available to others. In part E the Kramers-Kronig relations are derived with some additional hints for readers not familiar with complex analysis. In part F the cluster-calculation model used within this thesis is described briefly.

Chapter 1

Optics

Optical properties of matter are near to our own sensory perception. For instance we see that the glass of the window is highly transparent and that a metal spoon is well reflecting (if it is polished). Moreover our eyes are sensitive for colors. We find a golden ring shining yellow, a copper wire red, and a silver server shining white. This tells us immediately that copper is reflecting red light very well but other colors (at higher frequencies) much less. For gold the good reflectivity persists for a wider range in the visible spectrum. Silver however is equally reflecting all components we are able to see to a very proportion. So we are familiar with at least a simple form of optical spectroscopy from our daily live. For more detailed information about a certain material we obviously want to know how its optical properties depend on the frequency (or energy, or wavelength) of the electromagnetic wave, and of course we want to investigate not only the visible part of the spectrum but also below and above it, i.e. the infrared and the ultraviolet spectral range. For this purpose sophisticated experimental setups have been developed which measured the desired properties with very high accuracy. We discuss this subject later in this chapter. Now we turn to the question:

What can we learn from the optical spectra obtained by such measurements? The first answer to this question is: excitation energies! From the transmittance and the reflectance one can calculate the amount of light that has been absorbed by the crystal. But light (photons) of a certain energy is absorbed only if there are states of the crystal that are at the same amount of energy above the ground state, so that a resonance between the photon and the excitation mode may occur. Therefore peaks in the absorption spectrum provide information on the energy of excitations that do exist in the compound under investigation. However not all excitations existing in a crystal can actually be excited by light but only the ones that are dipole active, i.e. that carry a dipole moment. Another restriction of optical spectroscopy is that a dispersive mode is only probed at $k \approx 0$. This is due to the steep dispersion ($\omega = \frac{c}{n} \cdot k$ with c the speed of light in vacuum) and hence a small momentum k of the photons at the considered optical frequencies. However this is true only for processes involving the photon and only one quasiparticle. If more than one particle is involved in the absorption processes this can lead to zero total momentum whereas the single contributions are located throughout the entire Brioullin zone. For example in a two phonon process the phonons do not have to have $k \approx 0$ but can carry an arbitrary momentum $|k|$ if only the total momentum is zero

($k_1 = -k_2$). In such a case an absorption continuum is observed in which the information of k-space is inherent in the line shape. This can lead sometimes to an astonishing amount of information on the dispersion if the line shape can be compared with theoretical predictions [55]. Another important source of information on the crystalline properties is provided by the temperature dependence of the spectrum. Across phase transition not only the structural and thermodynamical properties change but in general also the optical spectrum. Moreover the polarization dependence gives additional information on the orientation of the dipole moments in the crystal. Structural information is obtained from the phonon energies and their polarization dependence.

In conclusion optical spectroscopy provides a powerful tool for investigating the properties of crystals. This holds equally for insulators and metals, as opaqueness is not a general problem but can be overcome by a Kramers-Kronig analysis of the reflectance spectrum, which is discussed in Appendix E.

1.1 Interaction of light with matter

In this section we will discuss the description of the interaction of light and matter. First we will consider the description on a macroscopic level, and turn than to the microscopic view as a second point. There we will consider the Drude-Lorentz model in detail. This model explains the shape of the quantities observed in experiment. However, preluding the discussion of the optical properties we will introduce the more general concept of response functions to which for instance the optical conductivity and the electrical susceptibility belong.

1.1.1 Response function

Every experimental result we may obtain of a certain crystal has the form of an answer of the crystal to an applied perturbation. For instance we apply a voltage and measure the responding current or we apply a magnetic field and measure the magnetization and so on. A compact form to describe the interaction of a system with an external perturbation p is provided by a response function G. This function gives the connection between the perturbation $p(\mathbf{r}, t)$ as function of spatial position r and time t and the response $a(\mathbf{r}, t)$ of the crystal, which is also a function of r and t. Since the response may be delayed and at a different place, one has to account for all perturbations in time (only before the response) and space. This is a rather complex connection between the stimulus and the response. It can be simplified by the assumption of a linear relation of the response to the amplitude of the stimulus.[1] Assuming linearity we are able to write down the following:

$$a(\mathbf{r}, t) = \int G(\mathbf{r}, \mathbf{r}', t, t') \, p(r', t') d(r', t')$$

This general connection of the perturbation p and the response a (answer) can be simplified for our case of the interaction of light and matter in several ways (we will also assume a weak field for which we are in the linear regime).

---

[1]The assumption of linearity is reasonable if the perturbation added to the Hamiltonian is small. The amplitude is not that large that higher orders contribute.

- The spatial dependence of the response function G is suppressed, i.e. we do not account for a perturbation elsewhere in the crystal. This is justifiable since the transport of the perturbation through the crystal by quasiparticles like for instance phonons is rather weak compared to the original perturbation. This definitely changes in the regime of non-linear optics.

- The time dependence takes into account only the time difference between the perturbation and the response. So G is a function of $(t' - t)$ only.

Altogether the above equation is reduced to:

$$a(t) = \int G(t - t')\, p(t')dt'$$

where $G(t - t') = 0$ for times $t < t'$ to obey the principle of causality (no response before the perturbation). The response $a(t)$ is therefore just the convolution of $G(t - t')$ and $p(t')$. Such an integral appears as a simple product in Fourier space[2]:

$$a(\omega) = G(\omega) \cdot p(\omega)$$

An example for a response function in Fourier space is the dielectric function $\varepsilon(\mathbf{q}, \omega)$

$$D(\mathbf{q}, \omega) = \varepsilon(\mathbf{q}, \omega)E(\mathbf{q}, \omega)\quad.$$

Here $\mathbf{q}$ denotes the wave vector. In real space this equation reads

$$D(\mathbf{r}, t) = \int_{-\infty}^{\infty} \int_{-\infty}^{t} \varepsilon(\mathbf{r}, \mathbf{r}', t)E(\mathbf{r}', t')\, dt'd\mathbf{r}'\quad.$$

This shows that it is convenient to consider the response function in Fourier space.

Finally we discuss the derivative with respect to the time coordinate becomes merely a factor $-i\omega$ in Fourier space which we will use below:

$$
\begin{aligned}
\frac{\partial}{\partial t}f(t) &= \frac{\partial}{\partial t}\int_{-\infty}^{\infty} e^{-i\omega t}f(\omega)d\omega \\
&= \int_{-\infty}^{\infty} \frac{\partial}{\partial t}e^{-i\omega t}f(\omega)d\omega \\
&= \int_{-\infty}^{\infty} e^{-i\omega t}(-i\omega f(\omega))d\omega \\
\Rightarrow \frac{\partial}{\partial t}f(t) &\xrightarrow{FT} -i\omega f(\omega)
\end{aligned}
$$

Analogously one obtains for one spatial dimension:

$$\frac{\partial}{\partial x}f(x) = iq_x f(q_x)$$

---

[2]Expanding the two "real-space" functions in series of cosine functions, i.e. Fourier-transforming them, one finds that - due to the orthogonality of the cosine functions ($\int_{-\infty}^{\infty} \cos(\omega_i t)\cos(\omega_j t)dt = \delta_{i,j}$) - only terms with equal frequency contribute. The product in the integral is hence merely the simple product of the expansion coefficients for equal ω.

1.1.2 Macroscopic properties

We start with the Maxwell equations in SI units and use this system of units throughout this thesis. We will present here a derivation of quantities describing the optical properties of solids, namely the dielectric function $\varepsilon(\omega)$ and the optical conductivity $\sigma(\omega)$ as well as an equation connecting both. To take into account that these two functions are generally defined as complex functions, we denote them with a hat wherever there can be confusion: $\hat{\varepsilon} = \varepsilon_1 + i\varepsilon_2$ and $\hat{\sigma} = \sigma_1 + i\sigma_2$. Our starting point will be the Maxwell equations[3]:

$$
\begin{aligned}
dD &= \rho & D &= \varepsilon_0 \star E & dE &= -\dot{B} \\
dB &= 0 & H &= \tfrac{1}{\mu_0} \star B & dH &= j + \dot{D}
\end{aligned}
$$

The charge density ρ and the current density j amount for all charges and all currents. Even for a crystal in vacuum we will not get rid of these two properties, since any interaction with electromagnetic waves will eventually dissociate the formerly neutralized charges and hence give $\rho \neq 0$ and $j \neq 0$. It is therefore convenient to divide the total quantities ρ_{total}, j_{total} into two parts. One will apply to the external charges ρ_{ext} and currents j_{ext} which we are able to control and which will be zero in case of a perturbation of the crystal by an electromagnetic wave. The other part accounts for the charge density ρ_{mat} and current density j_{mat} which arise within the crystal by the interaction with an electromagnetic wave. This part usually defies control. Because we do not know its microscopic appearance, it will enter the Maxwell equations in a kind of black box. Introducing two auxiliary properties $\mathcal{D}$ and $\mathcal{H}$ (which do not have a physical meaning) the electrical flux D and the magnetic field H are replaced by

$$\mathcal{D} = D + P \qquad \mathcal{H} = H - M \quad .$$

Here P is defined by

$$\rho_{mat} = -dP$$

and M by

$$j_{mat} - \dot{P} = dM \quad ,$$

accounting for the contribution raised within matter. The polarization P and the magnetization M are contributions to D and H, respectively, depending on the electric and the magnetic field applied to the crystal. Like the above Maxwell equations that are containing all charges and currents, the resulting modified Maxwell equations - where we have separated the contribution arising from matter - are exact.

$$
\begin{aligned}
d\mathcal{D} &= \rho_{ext}, & \mathcal{D} &= \varepsilon_0 \star E + P(E), & dE &= -\dot{B} \\
dB &= 0, & \mathcal{H} &= \tfrac{1}{\mu_0} \star B - M(B), & d\mathcal{H} &= j_{ext} + \dot{\mathcal{D}}
\end{aligned}
$$

---

[3]We make use of the more concise calculus of differential form [5] instead of the conventional vector analysis. The major theoretical benefit of this formalism is that it does not require the underlying space to be euclidian but only needs an analytic manifold (something that only locally looks like an euclidian space).

The problem of the unknown contribution of charges and currents has been shifted to the problem of knowing the functions $P(E)$ and $M(B)$[4]. So the discrimination between external and matter-inherent charges and currents does not help in order to get an exact solution for a microscopic description. But it opens the opportunity to include approximations for the contributions of charges and currents within matter.

We will make use of this opportunity and refer to the linear approximation in the following considerations. The response of the system (crystal) ought to be linear in the perturbation. This means that the polarization P is a linear function[5] in E, and the magnetization M is linear in B. In space and time coordinates this yields the still cumbersome equations

$$P(\mathbf{r}, t) = \varepsilon_0 \int \int \hat{\chi}_{el}(\mathbf{r}, t, \mathbf{r}', t') \star E(\mathbf{r}', t') d\mathbf{r}' dt'$$

$$M(\mathbf{r}, t) = \mu_0^{-1} \int \int \hat{\chi}_{mag}(\mathbf{r}, t, \mathbf{r}', t') \star B(\mathbf{r}', t') d\mathbf{r}' dt' .$$

The Fourier transformed equations however look much more simple:

$$P(\mathbf{q}, \omega) = \varepsilon_0 \hat{\chi}_{el}(\mathbf{q}, \omega) \star E(\mathbf{q}, \omega)$$

$$M(\mathbf{q}, \omega) = \mu_0^{-1} \hat{\chi}_{mag}(\mathbf{q}, \omega) \star B(\mathbf{q}, \omega)$$

so we will consider Fourier space from now on. The response functions $\hat{\chi}_{el}$ and $\hat{\chi}_{mag}$ depend in general not only on the frequency ω but also on the wave vector $\mathbf{q}$. Due to the tiny momentum of photons $q \approx 0$ we will consider only $q = 0$ in the following. Then the so called material equations look like

$$\mathcal{D}(\omega) = (1 + \hat{\chi}_{el}(\omega)) \ \varepsilon_0 \star E(\omega)$$

$$\mathcal{H}(\omega) = (1 - \hat{\chi}_{mag}(\omega)) \ \mu_0^{-1} \star B(\omega) .$$

The dielectric function $\hat{\varepsilon}$ is therefore defined as $\hat{\varepsilon} = 1 + \hat{\chi}_{el}$. It depends on many parameters, for instance temperature or the polarization of the electrical field relative to the crystallographic axes (which makes $\hat{\varepsilon}$ in general a tensor of rank 2), but for our purpose only the dependence on the frequency of the electromagnetic wave is of relevance: $\hat{\varepsilon} = \hat{\varepsilon}(\omega)$. Analog one may define the relative magnetic permeability $\hat{\mu}(\omega)$ as $\hat{\mu}^{-1} = 1 - \hat{\chi}_{mag}$. With this the material equations are of the form

$$\mathcal{D}(\omega) = \varepsilon_0 \varepsilon(\omega) \star E(\omega)$$

$$\mathcal{H}(\omega) = \mu_0^{-1} \mu^{-1}(\omega) \star B(\omega) .$$

---

[4]Talking here about functions $P(E)$ and $M(B)$ is making an implicit requirement on the system we consider. Namely the system may be considered to be homogenous on a relevant scale set by the wave length of the light. This condition is certainly fulfilled in the case of optical wavelengths of some hundred nm in contrast to the inhomogeneity of crystals which usually is less than 1 nm.

[5]For anisotropic systems the function turns out to be a tensor of rank 2. Note that in this case $1 + \chi$ is interpreted as $\begin{pmatrix} 1 & 0 & 0 \\ 0 & 1 & 0 \\ 0 & 0 & 1 \end{pmatrix} + \begin{pmatrix} \chi_{11} & \chi_{12} & \chi_{13} \\ \chi_{21} & \chi_{22} & \chi_{23} \\ \chi_{31} & \chi_{32} & \chi_{33} \end{pmatrix}$

In the following we will derive an equation which relates $\hat{\varepsilon}(\omega)$ and $\hat{\sigma}(\omega)$. Since the electrical interaction is usually dominating the magnetic interaction by orders of magnitude and so it is justifiable to neglect the magnetic contribution completely in the following and assume a non-magnetic crystal ($\chi_{mag} = 0$, $\mu(\omega) = 1$).

An additional consequence of the linear approximation is that Ohms law can be applied. It states that

$$j_{mat}(\omega) = \hat{\sigma}(\omega)D(\omega) = \hat{\sigma}(\omega)\varepsilon_0 \star E(\omega) \ .$$

Here j_{mat} denotes the conducting current. The conductivity σ depends also on many parameters but anyway we regard it here as a function of ω, $\sigma = \sigma(\omega)$. Now we return to $j_{mat} - \dot{P} = dM$ which is in fact the Ampere-Maxwell law ($j - \dot{D} = dH$) restricted to the matter inherent charges.

We refer to the assumption of a nonmagnetic crystal $M = 0$ ($\Rightarrow dM = 0$) which yields

$$j_{mat} - \dot{P} = 0 \quad .$$

The Fourier transform of $\dot{P}(t)$ is $-i\omega P(\omega)$ (see section 1.1.1). Thus we can rewrite the above equation as follows

$$\sigma(\omega)\varepsilon_0 \star E(\omega) + i\omega P(\omega) = 0$$

Inserting $P(\omega) = \chi_{el}(\omega) \star E(\omega)$ we obtain

$$\sigma(\omega)\varepsilon_0 \star E(\omega) + i\omega \ \chi_{el}(\omega) \star E(\omega) = 0$$

$$(\sigma(\omega)\varepsilon_0 + i\omega \ \chi_{el}(\omega)) \star E(\omega) = 0 \quad .$$

This must hold independent of the electrical field $E(\omega)$ and hence we get

$$\sigma(\omega)\varepsilon_0 + i\omega \ \chi_{el}(\omega) = 0$$

which is equivalent by the use of $\chi_{el}(\omega) = \varepsilon(\omega) - 1$ to the common form[6]:

$$\frac{i \ \sigma(\omega)}{\omega} = \frac{\varepsilon(\omega) - 1}{\varepsilon_0}$$

Split up into real and complex part this yields

$$\sigma_1 = \frac{\omega}{\varepsilon_0}\varepsilon_2 \qquad \text{and} \qquad \sigma_2 = \frac{\omega}{\varepsilon_0}(1 - \varepsilon_1)$$

---

[6]This equation is often presented in cgs units where it reads:

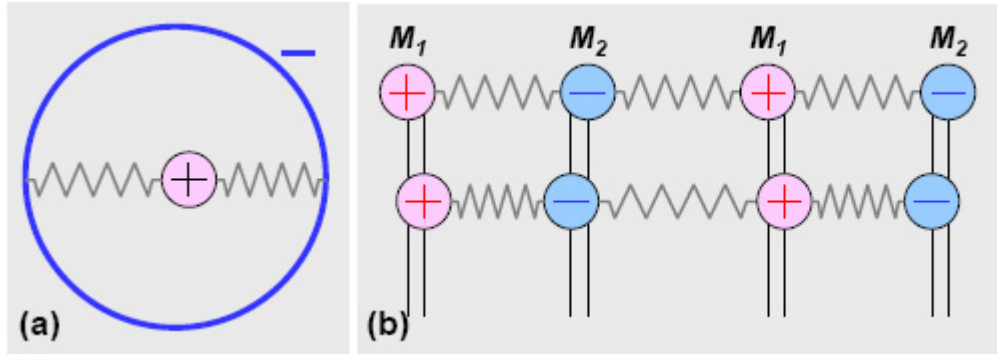$$\frac{4\pi i \ \sigma(\omega)}{\omega} = \varepsilon(\omega) - 1$$

Figure 1.1: Two different mechanisms leading to a dipole moment of an insulating ionic crystal. (a) Shift of the negative electron cloud against the positive nucleus. (b) Shift of negatively charged ions M_2 against the positively charged ions M_1.

1.1.3 Microscopic description

We will describe now the microscopic model for the interaction between an electromagnetic wave and matter, i.e. we will open the black box of the macroscopic view. We start with the classical picture assuming classical oscillators present in the crystal. This model is known as Drude-Lorentz model. Clearly the oscillating electromagnetic field will displace charges from their equilibrium position of the ground state and create thereby an oscillating dipole moment. In the following we will neglect again the presence of the magnetic field simply because the magnetic interaction is rather weak compared to the Coulomb interaction. For an insulating, ionic crystal (the kind of crystals considered in this thesis[7]) the displacement of charges can be separated into different contributions shown in Fig. 1.1.

One way to create a dipole moment is to shift the negatively charged electron cloud against the positively charged nucleus. However, the resonance of this so called electronic polarization is at high frequencies, far above the visible. The second possibility is to displace the negatively charged ions against the positive ones (ionic polarization). Its resonance frequencies lie in the far-infrared region. In other terms this is nothing else than the coupling of the photon to phonons (lattice vibrations). In metals the free charge carriers provide another way to create a dipole moment which is resonant down to zero frequency due to the absence of a force opposed to the displacement. For paraelectric crystals the orientation of already existing electrical dipole moments provides a further mechanism. In a quantum mechanical view in principal a transition to any state higher in energy will contribute if it is dipole allowed. However, we will treat the more instructive classical case here.

Consider now an electromagnetic wave interacting with an ionic crystal. Here, we will restrict the discussion to the process of ionic polarization. The strength of the interaction depends on the frequency ω of the electromagnetic wave with respect to the eigenfrequency ω_0 of the lattice vibration. This is actually the phenomenon of forced oscillation well known from

---

[7]An ionic crystal consists of different charged ions as for example NaCl ($Na^{+1}Cl^{-1}$), whereas for example pure silicon is not ionic since the ions are all equal and therefore by symmetry they can not be charged differently.
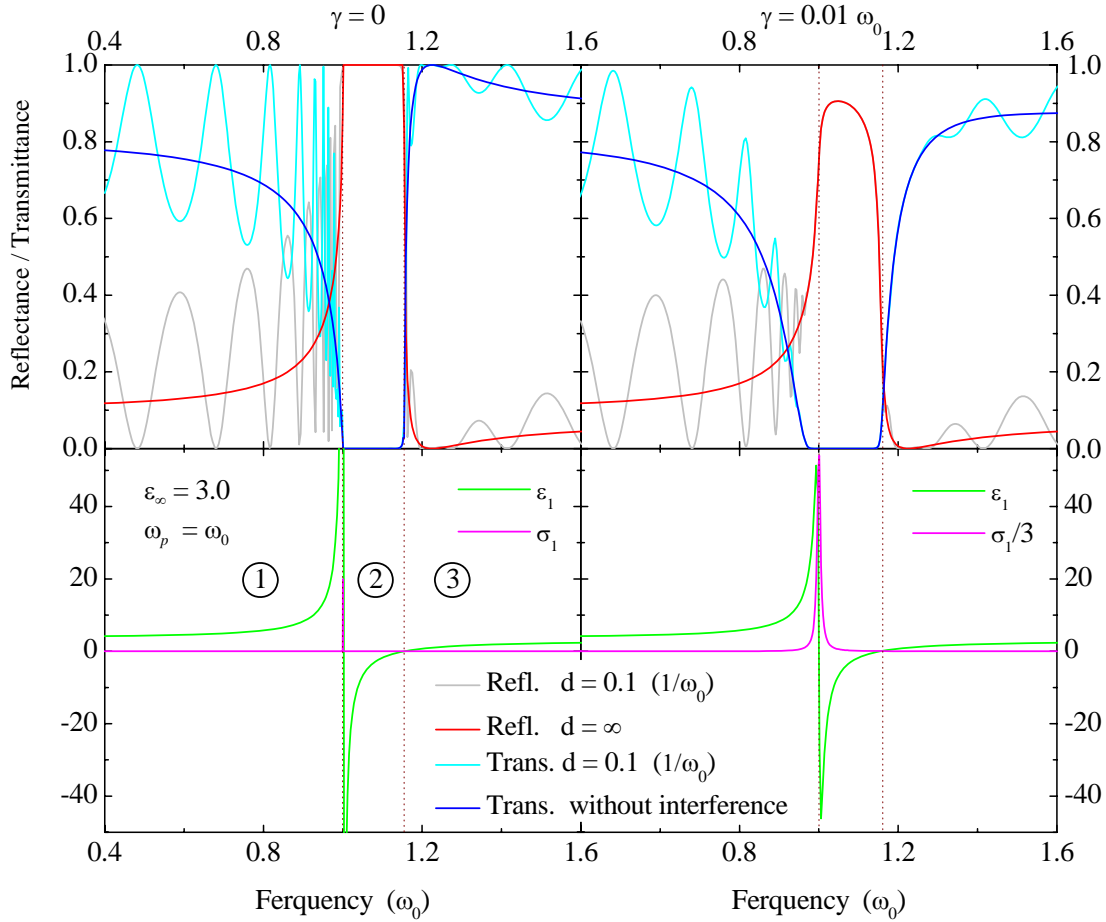
Figure 1.2: Top panels: typical shape of the transmittance T and the reflectance R for a phonon mode is shown. The data have been generated in two ways: 1) accounting for finite thickness effects (the data exhibits strong interference fringes) 2) neglecting multiple reflections. Bottom panels: Optical properties corresponding to R and T are depicted. The case of zero damping is shown on the left hand. The panels on the right hand display the same data but for a finite (weak) damping.

classical mechanics. Let us discuss the frequency dependence of optical properties like the dielectric function $\varepsilon(\omega)$ and the optical conductivity $\sigma(\omega)$ as well as of measured properties like the reflectance R and the transmittance T. In the left panels of Fig. 1.2, these properties are shown for the case of vanishing damping of the oscillators. For clarity we consider here only one mode of the system at the eigenfrequency ω_0, in real systems there are usually more than one mode. In the bottom left panel the frequency range is divided by dashed lines (at ω_0 and ω_L) into three parts.

- At frequencies much lower than ω_0 the system is following the oscillating field more or less, so the dielectric function (or the amplitude of the displacement) has values similar

to the static case ($\omega = 0$). Increasing the frequency of the electromagnetic wave towards ω_0, the amplitude of the oscillating dipole moments in the crystal are rising more and more and diverge at $\omega = \omega_0$. This unphysical behavior follows from the assumption of vanishing damping γ. The increasing amplitude of the oscillations for $\omega \to \omega_0$ leads to an increase of reflectance, i.e. the reflectance approaches 1 for $\omega \to \omega_0$ and therefore the transmittance decreases. The energy inherent in the electromagnetic wave is not transferred to the oscillators for $\gamma = 0$ except at $\omega = \omega_0$.

- Above ω_0 one might expect a situation approximately symmetric to that below ω_0. However, this is by no means the case. This asymmetry emerges from the fact that the phase shift θ between the electromagnetic wave and the oscillations of the dipoles within the crystal jumps from 0 for $\omega < \omega_0$ to $\pi/2$ at ω_0 and finally to π for $\omega > \omega_0$. This discontinuity at ω_0 results again from the non-physical assumption of vanishing damping γ. However, for weak damping things do not look much different from the case of completely vanishing damping. A phase shift of π means that the dipole moments are oriented just opposite to the applied electrical field, i.e. $\varepsilon(\omega)$ becomes negative for $\omega > \omega_0$. The electromagnetic wave and the outgoing wave of the oscillators are compensating each other in the crystal. The electromagnetic wave is therefore completely reflected and the transmittance is zero. If ω is moving further away from ω_0, the dielectric function stays below zero as long as the dipole oscillation can compensate the electromagnetic wave. For increasing difference $\omega - \omega_0$ this mechanism is getting less efficient. The amplitude of the oscillators is decreasing which means that the penetration depth of the light is increasing.

- The dielectric function $\varepsilon_1(\omega)$ will reach zero at a frequency ω_L called plasma frequency. The dielectric function approaches $\varepsilon_1 = 1$ for $\omega \to \infty$. For a single oscillator, there thus has to be a zero of ε_1 between ω_0 and ∞. Additional oscillators are assumed to be far away and can be included by a constant offset of ε_1 which is denoted ε_∞. The frequency ω_L is the eigenfrequency of a longitudinal oscillation. The difference between the transversal and the longitudinal mode is shown in Fig. 1.3. To avoid any misunderstanding, the longitudinal mode is never excited by a transversal wave. The longitudinal mode has nothing to do with the absorption process, it is just giving the frequency of vanishing ε_1 its name. For frequencies above ω_L the transmittance is rising and the reflectance is decreasing.

From the formal functional form of $\varepsilon(\omega_L)$ depending on $\varepsilon(0)$, ε_∞ and ω_T

$$\varepsilon(\omega_L) = \varepsilon_\infty + [\varepsilon(0) - \varepsilon_\infty] \frac{\omega_0^2}{\omega_0^2 - \omega^2}$$

one can deduce the Lyddane-Sachs-Teller relation from $\varepsilon(\omega_L) = 0$. This equation relates the oscillator strength with the ratio of ω_L/ω_0.

In the above consideration we have excluded dispersion, i.e. the momentum of the excitations. This is justifiable by the steep dispersion of light which stays in the vicinity of $k = 0$ for optical frequencies. In a quantum-mechanical picture (the most appropriate) we would
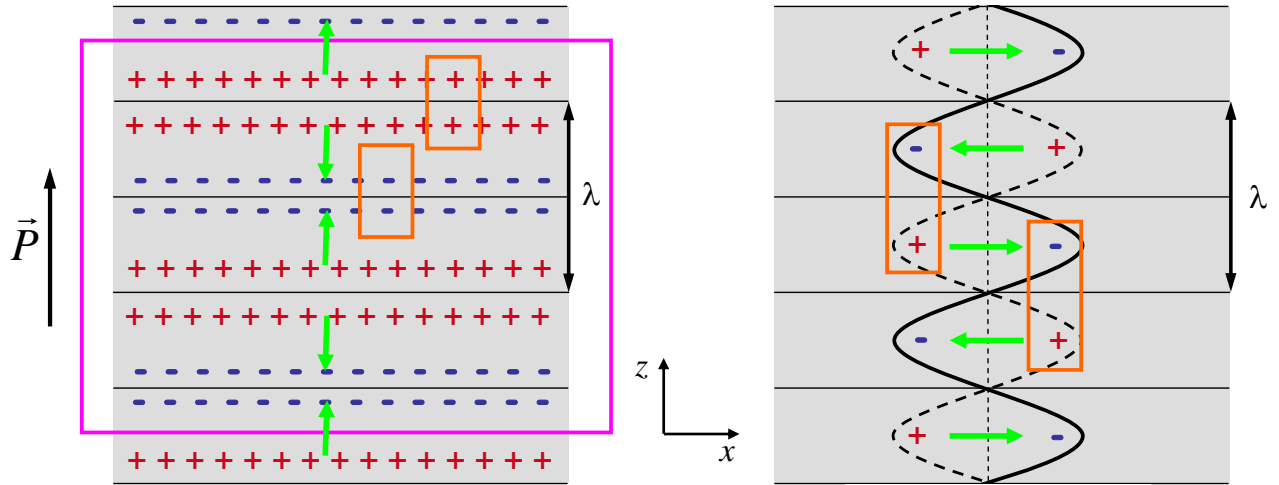
Figure 1.3: The charge distribution of a longitudinal wave on the left is compared with a transversal wave on the right. Both waves propagate in z direction with the same wavelength λ. The black lines indicate planes (perpendicular to z) of vanishing displacement of charges, separating layers of the thickness $\lambda/2$. The wavelength is assumed to be much larger than the unit cell of the crystal so that one may think of a homogeneous medium. This assumption is certainly fulfilled for optical wave lengths. The direction of the local dipole moment is shown by the green arrows. The difference between both waveforms is seen from the charge distribution of adjacent layers indicated by the orange frames. In the case of a transversal wave, the charge distribution in the adjacent layers support the formation of the dipole moment of the layer in between whereas for the longitudinal wave the formation is hindered by the electrical field of neighboring layers. This leads to a strong restriction for the eigenfrequency of the longitudinal mode. Since the net charge is zero no charges can be accumulated within the crystal it follows that macroscopical by $dD = 0$ (no external charges). From $D = \varepsilon_0 \star E + P = \varepsilon(\omega) \star E$ it follows immediately that $\varepsilon(\omega_L)$ has to be zero as the gradient of electrical field is clearly $dE \neq 0$. In short this tells us that the electrical field induced by the local displacement of charges has to be compensated by the field raised by the displacements of the rest of the crystal. This leads to a macroscopic dipole moment for the longitudinal wave since charges at the surface are not compensated.

not talk of forced oscillation describing the interaction of light with matter but of interaction of photons and phonons.[8] These two particles will interact in general and will therefore loose their own identity in favor of a new mixed mode. This new mode is called polariton. The polariton dispersion as well as the dispersion of the corresponding unperturbed particles (photon and phonon) is shown in Fig. 1.4.

For photonic energies far below the phononic eigenmode the interaction does not matter a lot for photon and phonon since nearly no resonance occurs. This changes drastically

---

[8]We will think of phonons in the following but any dipole-active eigenmode of the system would do as well.
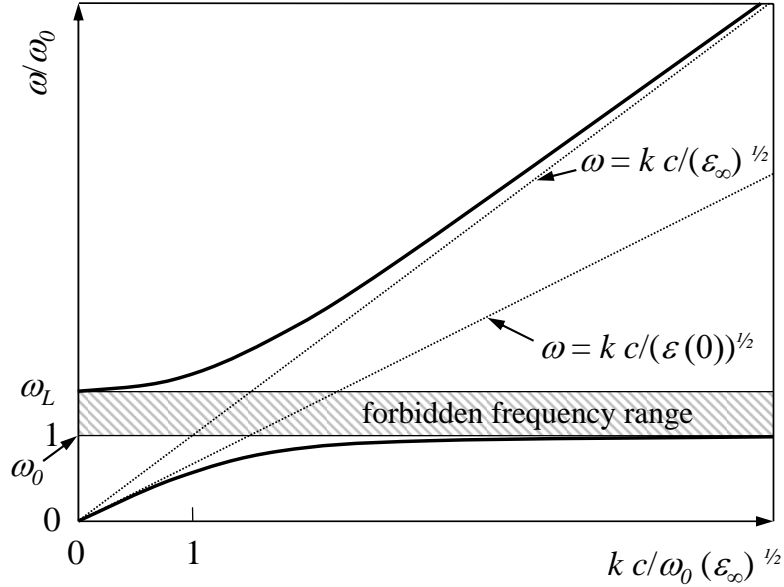
Figure 1.4: The photon-phonon or polariton dispersion is shown by the solid black curve (two branches). The dotted lines give the linear photonic dispersion for $\omega \ll \omega_0$ and for $\omega \gg \omega_0$. The slope is determined by the value of the dielectric function far away from the resonance ($\omega = 0$ and $\omega \to \infty$). The frequency range between ω_0 and ω_L indicated by the hatching is forbidden since in this range no eigenmode exists within the crystal.

around the resonance where the two modes are not distinguishable anymore. The branch of the former photon dispersion becomes the phonon branch and vice versa. So the resonance between the photon and the phonon can be seen as a kind of level repulsion avoiding the crossing of the two branches and hence the corresponding degeneracy.

The above statements were made only for the case of an ionic crystal. However, for metals the above considerations can be applied to the free charge carriers by assigning an eigenfrequency of $\omega_0 = 0$ to their oscillations. The electron gas (plasma) is playing the role of the negative ions. The corresponding longitudinal eigenfrequency ω_L of such an excitation is called plasma frequency. For this longitudinal oscillation of the electron gas within the crystal the corresponding quasiparticle is termed plasmon. Plasmons are not excited by transversal electromagnetic waves (in analogy to the polaritons) but can be observed by for instance inelastic electron energy loss spectroscopy (EELS).

1.2 Fourier spectroscopy

The importance of optical properties for understanding the physics of the solid state has motivated the experimentalists to measure them accurately. The dielectric function or the optical conductivity are hard to measure directly, the quantities one is able to observe in

Absorption

Transmittance

Reflectance
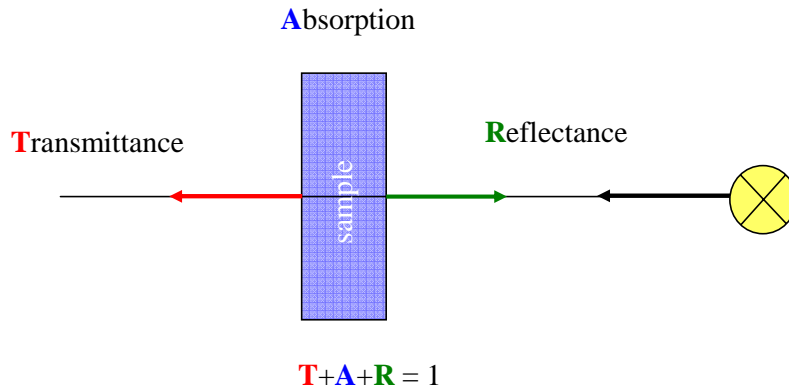
sample

$\mathbf{T} + \mathbf{A} + \mathbf{R} = 1$

Figure 1.5: Light can be reflected, transmitted or absorbed by a sample. The corresponding three quantities reflectance, transmittance, and absorption together equal unity.

experiment are the transmittance T and the reflectance R.[9]

As $T + R + A = 1$ with the absorption A, we will get the latter immediately when measuring T and R. From these two properties we will be able to calculate other optical property. In order to obtain the transmittance (reflectance) of the sample, it is necessary to compare the transmitted (reflected) amount of light with the amount that has hit the sample from the light source. So one always depends on a reference measurement to determine the proportion of transmittance (reflectance) as the quotient of the transmitted (reflected) light to the incoming intensity.[10] The actual setup of switching between the reference and the sample is shown in Fig. 1.6

A straightforward experimental setup for measuring T and R is shown in Fig. 1.7. Light coming from a source with a continuous spectrum is split up into its frequency components by a grid. A narrow frequency range is picked up by a slit, passes the sample and is measured by a detector. Repeating the measurement without the sample, one gets the amount of light of the particular frequency region in the spectrum of the source. The quotient of the intensity that got through the sample and the incident intensity is the transmittance at that frequency. This method has been used for decades. However, due to some disadvantages compared to a Fourier spectrometer it is more or less replaced by Fourier spectroscopy, especially in the infrared range.

The principle experimental setup of a Fourier spectrometer is shown in Figs. 1.8 and 1.9. The light passes through a Michelson interferometer before hitting the sample. The striking difference to the conventional setup is the absence of a monochromator. So there is no discrimination of the frequency before hitting the sample. Also the detector is not

---

[9]In sophisticated experiments also other quantities are observed, e.g. by ellipsometry the ratio R_p/R_s (R_p reflectance of light polarized parallel to the plane of incidence, R_s reflectance of light polarized perpendicular to the plane of incidence) and the phase shift θ of the reflected light are measured. From these two quantities other optical properties are obtained.

[10]This is not the case for ellipsometry where no additional reference measurement is needed. Only for calibrating the system a reference sample with known optical properties has to be measured.
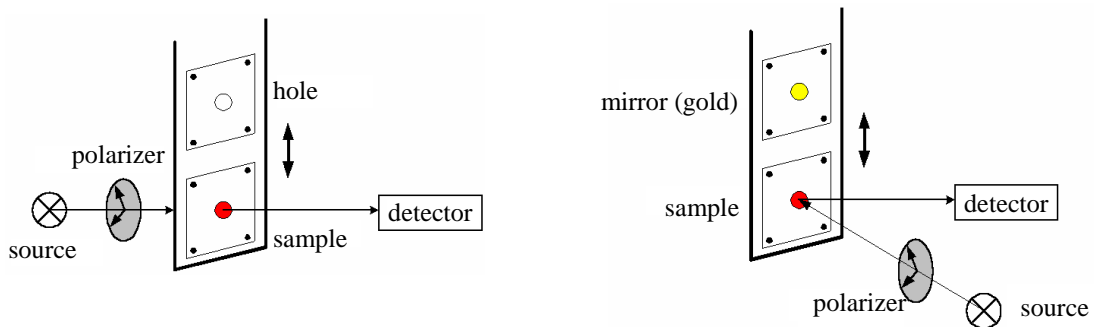
Figure 1.6: The position of the sample and of the reference can be switched rapidly at any temperature. Both are mounted on the same copper plate. The picture is taken from [56].

sensitive to the wavelength of the incident light (in contrast to the human eye). It measures only intensities, i.e. the absorbed energy regardless of the single photon energies. Actually the discrimination between the different frequencies is done after the measurement. The trick is that during a measurement one of the mirrors of the interferometer is moving. Hence the length of the path for the bundle of light reflected at the moving mirror is varying in comparison to the one coming from the fixed mirror. By this the intensity of light of one wavelength is oscillating between constructive and destructive interference with a period that is determined by the mirror velocity and the wavelength. As the velocity of the mirror is the same for all wavelengths, the period of the oscillations is characteristic for the wavelength of the light. The intensity oscillations can be detected by a detector. For a constant mirror velocity the resulting intensity for light of one single wavelength will be a cosine measured as function of the mirror position.

In one scan of the mirror all wavelengths from the source are measured simultaneously,
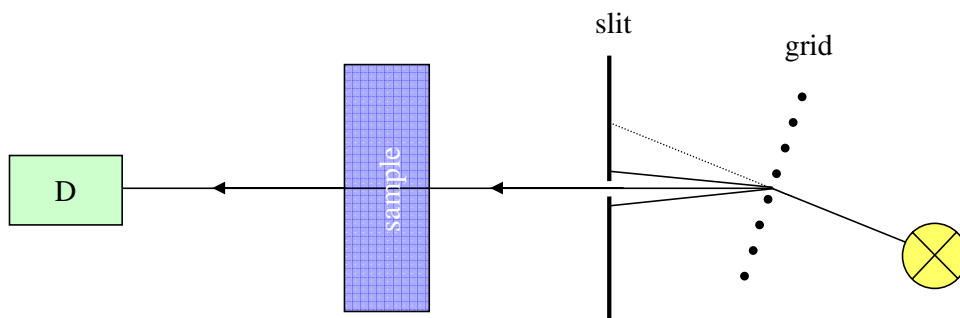

Figure 1.7: The principle setup of a spectrometer using a monochromator. The light from the source is passing a grid first. Under a certain diffraction angle, a narrow frequency band with its maximum at that angle is selected by a slit. The beam is passing the sample and is detected by a detector D.
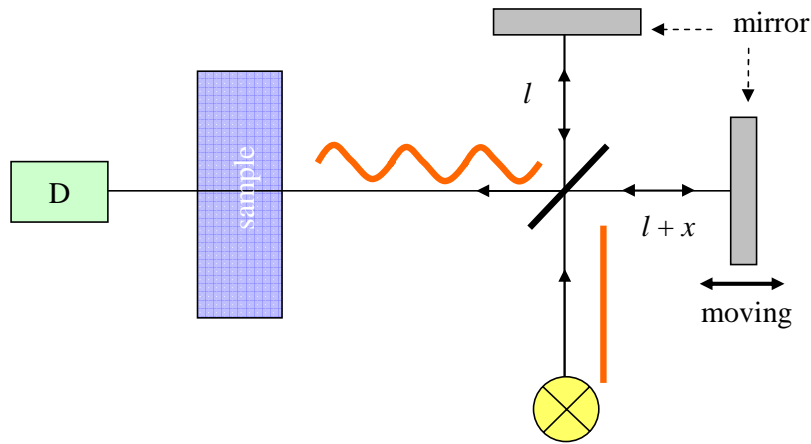
Figure 1.8: The principle components of a Fourier spectrometer. On the time scale relevant for the detector, the light from the source has constant amplitude, indicated by the orange line. After passing the interferometer, the amplitude depends on the difference x (relative to the wavelength) of the paths the two beams have traveled before interfering. Upon moving one of the mirrors, the amplitude oscillates in time between constructive and destructive interference as indicated by the oscillating orange line. After passing the sample the intensity is measured by a detector D.

giving a superposition of all cosine terms from all frequencies contained in the spectrum of the source. The intensity as a function of the position of the mirror is called interferogram. An example of an interferogram is given in Fig. 1.10. The original spectrum is obtained by decomposing the interferogram into cosine terms. The coefficient obtained for one frequency indicates the amount of light with the corresponding frequency contributing to the spectrum. This decomposition is actually a Fourier transformation, from which the name of the method is derived from.

So far we have discussed the basic mode of operation of a Fourier spectrometer. However, there are more components which are essential for receiving the spectrum of the sample. First it is important to determine the way the mirror moves in order to find the correspondence between the frequency of the cosine terms and the actual wavelength of the light. This is done by measuring additionally the interferogram of a laser which is detected by a diode after passing the interferometer. The laser gives a well-defined cosine signal. Since the laser intensity is orders of magnitude stronger than the intensity of the light coming from the source, the signal obtained by the diode is not influenced by the light of the source. The signal detected by the diode is used to trigger the detector, so that a data point is collected whenever the mirror has moved by one laser wavelength.[11] The laser wavelength is known with high accuracy of 1 to 10^6. Compared to the use of a momochromator, the advantages

---

[11]In between two minima of the diode signal the detector is triggered electronically, giving a higher density of data points. This is needed to measure a broader range of frequencies. With the density of data points acquired for a laser frequency ω_L, only a frequency interval of width $\omega_L/2$ can be measured.
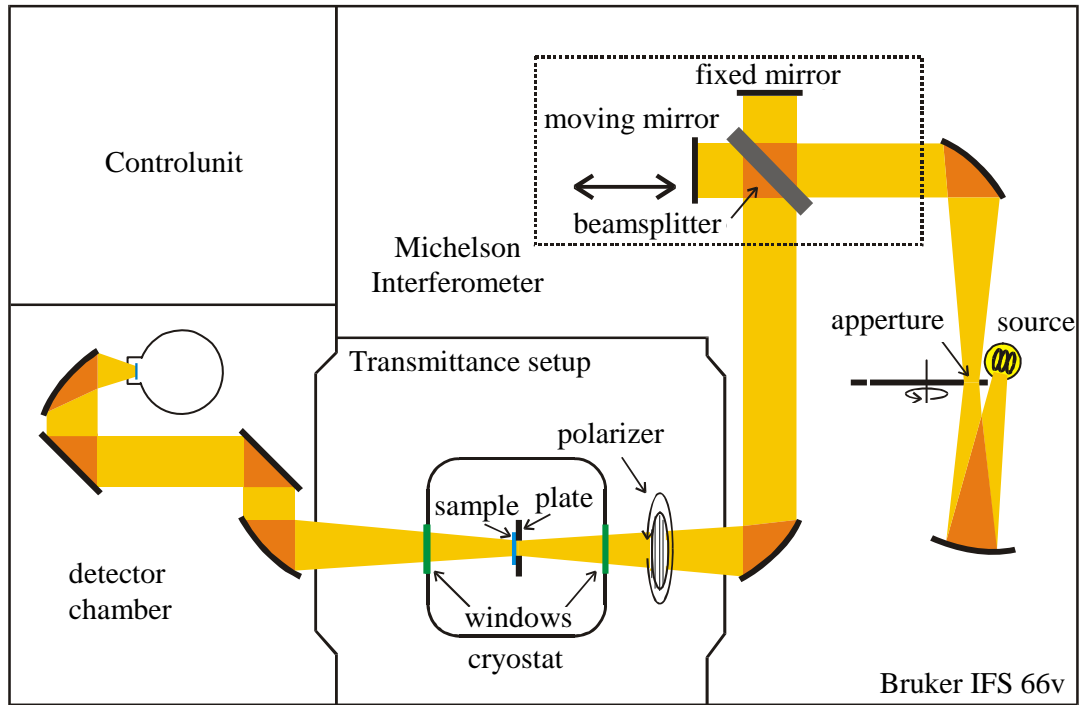
Figure 1.9: Sketch of the Bruker IFS 66 v/S. All results within this work were obtained with this spectrometer.

of Fourier spectroscopy in the infrared range are

- short measuring times due to the measurement of all frequencies simultaneously.

- the resolution depends only on the length of the interferogram. It can be increased by increasing the distance the mirror moves. Therefore no intensity of the signal is lost, i.e. the signal-to-noise ratio is independent of the resolution.

- due to the precise knowledge of the laser wavelength, Fourier spectroscopy has a very high accuracy in frequency.

- for the short measuring times all other parameters like for instance the temperature stay constant between measuring the sample and the reference.

Triggered by the laser interferogram, the spectrum consists of discrete data points. Therefore a discrete form of the Fourier transformation has to be used.

$$S(k \cdot \triangle \nu) = \sum_{m=0}^{N-1} I(m \cdot \triangle x) \exp(i\, 2\pi k m/N)$$

In comparison with the continuous transformation

$$S(\nu) = \int I(x) \cdot \exp(i\, 2\pi\nu) dx$$

one finds a one-to-one correspondence by $k \cdot \Delta\nu \equiv \nu$, $m \cdot \Delta x \equiv x$, and regarding that the sum runs only over a finite range due to the finiteness of the interferogram.[12] Performing the Fourier transformation one has to be careful since only the measured interferogram has unambiguous physical relevance. The resulting spectrum depends on some choices one has to make when applying the Fourier transformation. This ambiguity is due to the finite length of the interferogram, whereas the cosine function extends from $-\infty$ to ∞. The finite interferogram may therefore be regarded as an infinite interferogram times a function (apodisation function) that is identical 0 beyond the range of the measured interferogram. The Fourier transformation is also sensitive to this function, i.e. the result of the Fourier transformation is a convolution of the infinite interferogram (which would give the unaltered spectrum) and the apodisation function. However, this effect gets important only for rapid variation of the intensity within the spectrum, i.e. for very sharp lines (compared to the frequency resolution). Such features occur in spectra of for instance molecules. About the results presented in this work we do not have to worry.

Another point one has to keep in mind when applying the Fourier transformation is that the frequency range under investigation is at least as wide as the physical spectrum of the light source. Otherwise frequencies higher than the cut-off frequency are folded back, falsifying the resulting spectrum. It is also worth to note that the resolution of the *spectrum* corresponds to the length of the interferogram, and that the resolution of the *interferogram* determines the width of the spectral range obtained. This correspondence opens the opportunity to increase the density of points in the spectrum by adding zeros to the interferogram. However, this is not increasing the information but corresponds to a spline through the discrete spectrum. The final remark is about the occurrence of a phase $\neq 0$ of the cosine terms due to a deviation of the mirror symmetry of the measured interferogram at the white-light position. The asymmetry results form the discrete structure that is in general not centered exactly at the white-light position. This phase shift is corrected by taking the absolute value of the amplitude.

In conclusion, Fourier spectroscopy is an excellent tool for the investigation of optical properties of matter. It is fast and provides a very high accuracy. The commercially available spectrometer comes along with a software which makes the measuring procedure rather convenient and the results very satisfying.

1.3 Sample preparation

The method of optical spectroscopy needs planar surfaces of the crystals under investigation in order to give exact values for the measured (and the related) properties. Scattering at surface defects for instance will lead to an overestimation of the absorption. In the transmittance,

---

[12]Also common is the form where $\omega = 2\pi\nu$ is used instead of ν. This gives an extra factor of $1/2\pi$ from the substitution $d\omega = 2\pi d\nu$. This factor is split up by the convention in order to restore the symmetry between the two directions of the transformation: $S(\omega) = 1/\sqrt{2\pi} \int I(x) \cdot \exp(i\,\omega x) dx$ and $I(x) = 1/\sqrt{2\pi} \int S(\omega) \cdot \exp(-i\,\omega x) d\omega$.
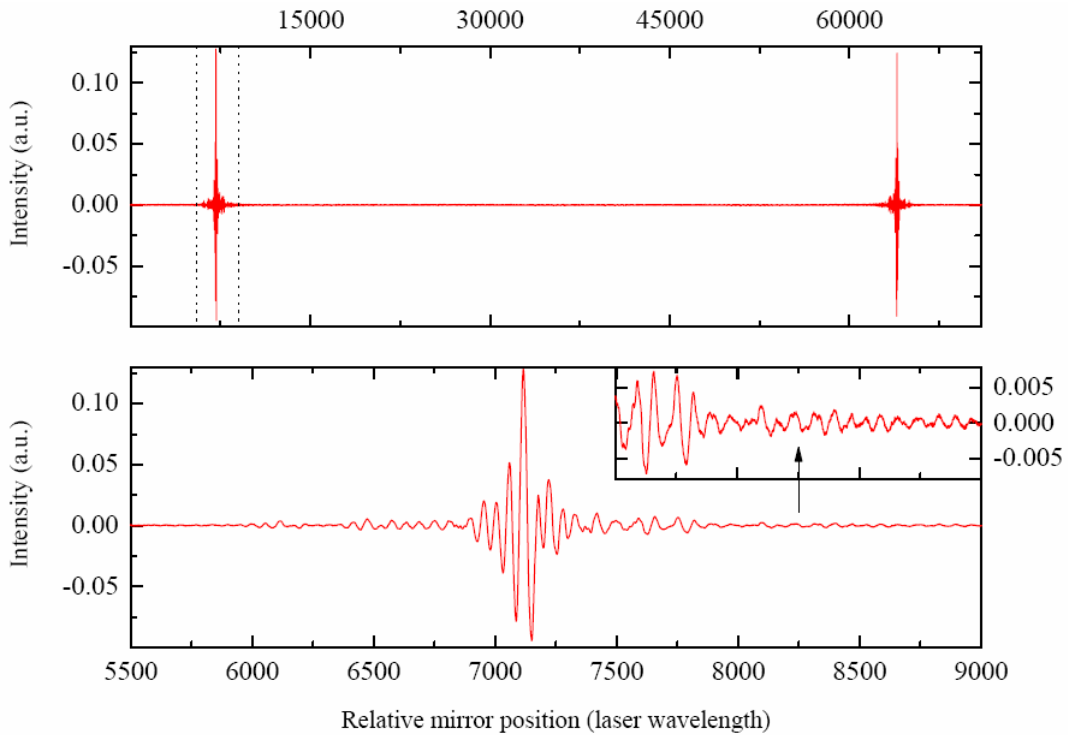
Figure 1.10: In the upper panel an interferogram is shown. The peaks (white-light position) correspond to the position for which both mirrors have equal distance to the beamsplitter. Two peaks occur because the mirror has been moved forward and backward, crossing the white-light position twice in one scan. In the lower panel the part between the dashed lines (in the upper panel) is plotted on an enlarged scale in order to show the detailed structure of the interferogram. The inset displays the fine structure of the interferogram away from the white-light peak. It has the same x axis as the whole panel but is enlarged in y direction.

this effect is increasing with decreasing thickness, i.e. decreasing total absorption within the sample. It is therefore important to prepare samples with a high planarity of the surface. For transmittance measurements it is also important to have two parallel surfaces in order to have a well defined thickness. The standard procedure for preparation of such a sample is grinding and polishing afterwards [55]. This has been done mechanically, using a commercial polishing machine. The results have been checked under a microscope. For a well polished surface there were no defects or surface roughness observed by a magnification of 64 times. An estimation of the surface roughness is provided by ellipsometry measurements where in modeling the data of $LaMnO_3$ the parameter for the surface roughness could be determined to be < 3 nm [33]. This procedure has been applied to all samples investigated within this work except TiOX which will be discussed later (see chapter 5).

Chapter 2

Orbital physics

In this chapter the state of the art of orbital physics is presented. It is divided into three parts. In the first part a summary of the basic ideas of the crystal-field theory is given. This is well established since the 1960's. The second part treats more recent approaches for novel scenarios of collective orbital physics. In the third part we will discuss how orbital excitations ought to appear in the optical conductivity.

2.1   Local orbital physics

For electrons in a crystal there exist two limiting cases. Weakly bound electrons delocalize completely and can not any longer be assigned to a single site. These electrons are forming bands and they are best described by band-structure calculations. On the other side there are electronic states of core shells which are strongly bound deep in the potential of the nucleus. These electrons feel the crystalline environment only as a small perturbation which adds to the Hamiltonian of the free ion. Here we will consider the partially filled $3d$ shell. Band structure theory supposes that a partially filled $3d$ shell forms a conducting band. However, many transition-metal compounds turn out to be pretty good insulators. The insulating property originates in a comparably small bandwidth and a strong Coulomb repulsion. A double occupancy on one site is several eV higher than the ground state. This prevents the $3d$ electrons to leave their sites although there were unoccupied states available. This class of insulators is called Mott-Hubbard insulators. It is therefore justifiable to consider the transition-metal ions in a local limit and add the influence of crystalline environment only as an electrostatic potential at the metal site. Effects due to the interaction of adjacent metal sites are apparently neglected within this limit.

The electronic state within the $3d$ shell of a transition-metal ion in a crystal is characterized by its spin and orbital state. In a partially filled $3d$ shell the fivefold orbital degeneracy of a free ion is lifted by interaction with the crystal, yielding orbital multiplets of different energy. The most important interaction of the ion with the crystal that accounts for this splitting is the Coulomb potential present at the ion site. It originates from all other ions in the crystal. The other interaction we will take into account is the hybridization with the ligands. The splitting of orbital states gives rise to the possibility of transitions between

different states. These so-called orbital excitations have been observed in optical spectra for many decades and so far were successfully described by the local approach of crystal-field theory that we will consider in the following in detail. The method of crystal-field theory is also the approach behind the cluster calculation performed within this thesis.

2.1.1 Crystal-field theory

We will restrict ourselves to the case of an open $3d$-shell of a transition-metal ion in a crystal. Let us initially assume a crystal field of octahedral (or cubic) symmetry O because it provides the predominant part of the crystalline field not only in the compounds investigated in this thesis but also in many other transition-metal oxides. The most simple case that may occur is that of one electron in the $3d$ shell. In the free ion (no crystal around) the electronic state is fivefold orbitally and twofold spin degenerate due to the full rotational symmetry $SO(3)$. So there are $5 \times 2 = 10$ degenerate states. These states are characterized by the eigenvalues of S and L since these are good quantum numbers (in a first approximation we neglect the spin-orbit coupling). Reducing now the symmetry from $SO(3)$ to O, L is no longer a constant of motion and one expects to lift the tenfold degeneracy at least partially. The degeneracy according to the spin will not be lifted except a magnetic field is applied which breaks the time-inversion symmetry.[1] The radial wave function is suppressed in the following since only the angular dependence is affected by the reduction of symmetry. Our task is to find the new eigenstates and the corresponding eigenvalues. The Hamiltonian of the free ion

$$H_0 = \frac{\nabla^2}{2m} + V(r)$$

(V(r) accounts for the potential of the nucleus and electrons of the inner shells) is solved by the hydrogen wave functions. The potential aroused by all other ions of the crystal (the crystal field) V_{CF} has to be added to H_0,

$$H = H_0 + H_{CF} .$$

The crystal field represents only a small perturbation compared to the field of the nucleus and hence perturbation theory can be applied. The eigenfunctions of the unperturbed system are denoted by $|\psi\rangle$. They form a basis of the 10-dimensional Hilbert space of the free ion. Diagonalization of the matrix $(H_{ij}) = \langle\psi_i|V_{CF}|\psi_j\rangle$ yields the eigenvalues and eigenstates of the perturbed system. The new eigenstates are linear combinations of the 10 spin-orbital states. These states have to transform under operations of the octahedral group according to a representation of O. It turns out that the representation of $SO(3)$ for $L = 2$ splits into the representations $E + T_2$. We neglect the spin-orbit coupling here and discuss it later in this section. The degeneracy of the spin state is not affected and will be suppressed in the following. Since the rotational symmetry is nearly lost for a strong crystal-field splitting, the corresponding eigenfunctions are combinations of the angular momentum eigenfunctions to

---

[1]For systems with an odd number of electrons there exists always a twofold spin degeneracy which is called Kramers doublet. The origin of this degeneracy lies in the time-inversion symmetry. Putting it in other words, the odd number of spins can not be coupled to $S = 0$ and hence the spin states of $(S_z = \pm\frac{1}{2})$ have the same energy if no magnetic field is present that breaks time-inversion symmetry.
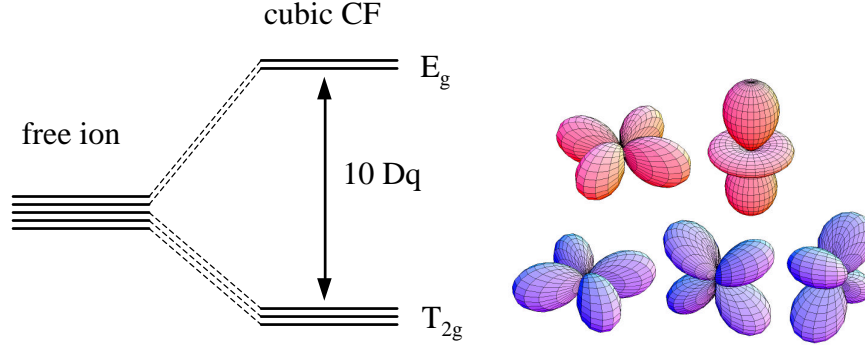
Figure 2.1: On the left the lifting of degeneracy by reduction of the symmetry from full rotational to cubic is shown for a $3d^1$ configuration. On the right the angular dependence of the basis functions $3z^2 - r^2$, $x^2 - y^2$ (red, e_g symmetry) and yz, zx, xy (blue, t_{2g} symmetry) is displayed.

$m_L = 0$, i.e. standing waves without a complex phase. The angular dependence of the angular momentum eigenfunctions for $L = 2$ – the spherical harmonics – are denoted by $|l\, m_l\rangle$.

$$
\begin{aligned}
u &= |2\,0\rangle & &= \frac{1}{4r^2}\sqrt{\frac{5}{\pi}} & &3z^2 - r^2 \\
v &= \frac{1}{\sqrt{2}}(|2\,2\rangle + |2\,-2\rangle) & &= \frac{1}{4r^2}\sqrt{\frac{15}{\pi}} & &x^2 - y^2 \\
a &= \frac{i}{\sqrt{2}}(|2\,1\rangle + |2\,-1\rangle) & &= \frac{1}{2r^2}\sqrt{\frac{15}{\pi}} & &yz \\
b &= \frac{1}{\sqrt{2}}(-|2\,1\rangle + |2\,-1\rangle) & &= \frac{1}{2r^2}\sqrt{\frac{15}{\pi}} & &zx \\
c &= \frac{i}{\sqrt{2}}(-|2\,2\rangle + |2\,-2\rangle) & &= \frac{1}{2r^2}\sqrt{\frac{15}{\pi}} & &xy
\end{aligned}
$$

These functions are refered to as $\{u, v, a, b, c\}$ or $\{3z^2 - r^2, x^2 - y^2, yz, zx, xy\}$, respectively. The first two belong to the E_g and the other three to the T_{2g} representation (the subscript g *gerade* – german for even – indicates the behavior under inversion). The energy of the E_g states are raised by an energy of $10Dq$ with respect to the T_{2g} states, where the energy Dq is given by $Dq = \langle 2\,2|V_{CF}|2\,2\rangle$. Hence the parameter $10Dq$ represents the strength of the cubic crystal field. If the symmetry of the crystal field is lower than cubic, this leads to a further reduction of degeneracy. The results above are visualized in Fig. 2.1.

Two-electron wave functions

So far we were considering only one electron. This has the advantage that we are dealing with single-particle wave functions and we do not have to consider the Coulomb interaction between different electrons within the $3d$-shell. Moreover, we were able to give the wave function in terms of spherical harmonics times a radial part which can be visualized easily. But for two or more electrons the wave functions are more complicated. There is an additional term in the Hamilton operator due to the repulsion of the electrons, and we are dealing with many-body wave functions for which it is not possible to draw a picture. The full Hamiltonian is then

$$H \;\; = \;\; H_1 + H_2 + H'$$

$$H' \;\; = \;\; \frac{1}{r_{12}}$$

where $H_{1,2}$ are one-electron Hamilton operators as given above for the two electrons (1,2), H' is a two-electron operator that accounts for the Coulomb repulsion of the two electrons, and r_{12} is the distance between them. We will consider here only the minimal case where the Coulomb interaction has to be considered in order to keep things simple. I.e. two electrons are assumed to be accommodated in the $3d$-shell.

First we have to find basis functions as starting point for the perturbation theory. It is convenient to choose the products of one-electron wave functions of the crystalline field derived above. We could also choose the terms for the free ion which are already diagonal in the Coulomb interaction and then treat the crystal field as a perturbation. This approach is valid if the crystal field is small (weak-field scheme). The way we will treat things here assumes a strong crystal field and is therefore called strong-field scheme. Nevertheless including the full interaction over all configurations, both ways will give the same results since the eigenbasis is independent of the basis we choose to start with. However, if one considers only a part of the Hamiltonian, i.e. a subspace, then both approaches will give different results since different subspaces are excluded. Back to the product of two of the one-electron functions. The simple products like for instance $|a\rangle|b\rangle = |ab\rangle$ lack antisymmetry under particle exchange which is required by the Pauli principle. To restore antisymmetry one builds the so called Slater determinant of the product.

$$\Psi_{kl} = \frac{1}{\sqrt{2}} \begin{vmatrix} \phi_k(r_1, s_1) & \phi_l(r_1, s_1) \\ \phi_k(r_2, s_2) & \phi_l(r_2, s_2) \end{vmatrix} = \phi_k(r_1, s_1)\phi_l(r_2, s_2) - \phi_k(r_2, s_2)\phi_l(r_1, s_1) \equiv |\phi_k \phi_l|$$

Where r_1, r_2 are the spatial coordinates of the two electrons and s_1, s_2 denote the spin state, respectively. Because of the antisymmetry of the determinant under exchange of two columns we obtain the desired antisymmetric property

$$|\phi_k \phi_l| = -|\phi_l \phi_k| \;.$$

For sufficiently large octahedral crystal field (large $10Dq$) the two electrons can be assumed to accommodate the t_{2g} and to avoid the e_g orbitals. So we can restrict ourselves in this case

to the subspace spanned by the products of the one-electron functions of t_{2g} states[2]. It has $15 = \binom{6}{2} = \binom{\text{number of spin orbitals}}{\text{number of electrons}}$ basis functions instead of $45 = \binom{10}{2}$ for all configurations. These 15 product wave functions transform according to the product $T_2 \times T_2$, which is not an irreducible representation of O. Reducing this representation one finds that it decomposes in:

$$T_2 \times T_2 = A_1 + E + T_1 + T_2$$

The sum of the dimensions of the representations accounts only for $1 + 2 + 3 + 3 = 9$ states but not for 15 states. The spin degeneracy $S = 0, 1$ is fourfold (singlet and triplet) and has to be considered, too. But this creates a lot more than 15, namely $9 \times 4 = 36$ states, since in principle all combinations of spin and orbital degeneracy are allowed to occur. So how do we get 15 states out of these? Actually it turns out that the Slater determinants differ substantially from the simple product of one-electron wave functions. The important difference is that due to the antisymmetry of the Slater determinants they are vanishing completely for certain combinations of spin and orbital multiplets. For example the product of $S = 0$ and T_1 is completely vanishing. By this property we find only 15 spin-orbitals that are non vanishing. In order to find a basis for which the decomposition is realized we have to transform the old basis by a matrix built from generalized Clebsch-Gordon coefficients. This is exactly the matrix which provides the reduction of the representation of $T_2 \times T_2$ into its irreducible components.

Now that we have found the basis functions for the problem, we may turn towards the task of including the Coulomb interaction between the two electrons. Like for including the crystal field we will treat the Coulomb interaction as a perturbation of the system. Therefore we have to calculate matrix elements of the form

$$\langle \Psi_i | \frac{1}{r_{12}} | \Psi_j \rangle$$

where Ψ_i is one of the basis functions, and $\frac{1}{r_{12}}$ corresponds to the perturbation term H' of the Hamiltonian. These matrix elements give many parameters especially if one wishes to include e_g states, too [1]. Symmetry properties are helpful to reduce the number of parameters but finally there are as many as 10 different two-electron integrals left. This number is reduced further by assuming that the wave function is of similar shape as the d-orbitals. The radial part of the wave function might be different, actually the radius is reduced in the crystalline environment. Assuming these changes to be small we are able to reduce the number of parameters further. By using the so called Slater integrals $F_k(dd)$ the ten parameters can be reduced to three. These are the so called Racah parameters A, B, C which are connected to the Slater integrals by:

$$
\begin{aligned}
A &= F_0 - 49F_4 \\
B &= F_2 - 5F_4 \\
C &= 35F_4
\end{aligned}
$$

---

[2]The restriction to the $T_2 \times T_2$ is not exact in two ways. First spin-orbit coupling does not care about the octahedral symmetry at all and will therefore mix e_g states into the ground state. Second the e_g states are separated by $10Dq$ which is assumed to be large but certainly not infinite, so a small admixture of e_g states into the ground state is expected.
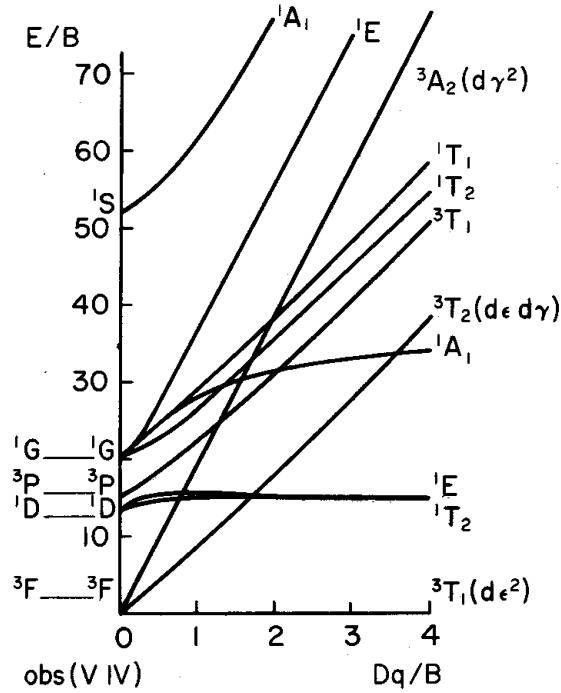
Figure 2.2: Tanabe-Sugano diagram for $3d^2$ configuration. On the left for $Dq = 0$ the splitting due to Coulomb interaction in a free ion is given (labeled by terms). With rising cubic crystal field the terms split up into levels transforming according to an irreducible representation of the octahedral group labeled on the right. The ground state always refers to the x-axis.

The parameter A just accounts for a constant shift of all energies and is hence unimportant for the relative energy positions observed in spectroscopy. The ratio of the parameters B and C is nearly constant for transition-metal ions. So in conclusion we are able to give a good (not exact) estimation of the energetic sequence of states as a function of only one parameter: the ratio of the crystal-field strength and the Coulomb interaction (Dq/B). The diagrams that are obtained if the energy of the eigenstates is plotted versus Dq/B are called Tanabe-Sugano diagrams [1]. The one for a $3d^2$ system in octahedral symmetry is given in Fig. 2.2.

For three and more electrons the wave functions are obtained by successively adding one electron. The product of the already constructed many-electron $(n-1)$ wave function and the one-electron wave function still has to be made antisymmetric with respect to the exchange of the added electron with the others. This is again done by building the Slater determinant of all single-electron wave functions. For instance for three electrons it looks like:

$$\Psi_{klm} = \frac{1}{\sqrt{2}} \begin{vmatrix} \phi_k(r_1, s_1) & \phi_l(r_1, s_1) & \phi_m(r_1, s_1) \\ \phi_k(r_2, s_2) & \phi_l(r_2, s_2) & \phi_m(r_2, s_2) \\ \phi_k(r_3, s_3) & \phi_l(r_3, s_3) & \phi_m(r_3, s_3) \end{vmatrix} \equiv |\phi_k \phi_l \phi_m| \qquad .$$

In order to find the correct multiplets one has to reduce the product of already obtained many-electron wave functions with the single-electron wavefunction (as it was done in the case of two electrons). For example the wavefunctions of three electrons within the t_{2g}-orbitals transform according to the product $T_2 \times T_2 \times T_2$. This decomposes to

$$T_2 \times (T_2 \times T_2) = T_2 \times (A_1 + E + T_1 + T_2) = T_2 \times A_1 + T_2 \times E + T_2 \times T_1 + T_2 \times T_2$$

$$= T_2 \ + \ T_1 + T_2 \ + \ A_2 + E + T_1 + T_2 \ + \ A_1 + E + T_1 + T_2$$

As it is seen from this reduction, one representation may occur several times. This gives rise to several eigenspaces that transform according to the same representation but have different eigenvalues.

Symmetry lower than cubic

In many transition-metal compounds the cubic crystal field is only a rough approximation and the actual symmetry turns out to be lower than cubic. This is especially the case for Jahn-Teller active ions (see below). However, slightly shifting the ligand ions from the positions in cubic symmetry will not turn the energy levels upside down but will introduce a further splitting of degenerate states as seen for instance from Fig. 2.1. The new levels have to transform according to one of the irreducible representations of this point group, hence they will have usually lower degeneracy.

Covalency and molecular-orbital theory

Up to here we have developed a theory that considers the crystal as the origin of an electrostatic potential added to the free-ion Hamiltonian. This purely ionic approach in general does not give satisfying results. The reason for the discrepancy of theoretical and experimental results is that the bonds in the crystal are not purely ionic but exhibit also covalent character. In other words the electrons occupy molecular orbitals, not atomic ones. The molecular orbitals are one-electron wave functions spread over a molecular complex that includes the transition-metal ion and the surrounding ligands. Since the overlap of the wave functions of different ions is comparably small for $3d$ orbitals, the molecular wave functions are expected to be approximately the atomic wave functions near the ion site. Thus the predominant contribution to the potential near one ion is arising from its nucleus, and it is reasonable to assume the molecular wave functions to be linear combinations of atomic orbitals of the respective ions within the complex. This approach is called molecular-orbital theory. In the following the basic idea behind the molecular-orbital theory is pointed out.

Assume a transition-metal ion in octahedral symmetry that is surrounded by six oxygen ligand ions at the corners of an octahedron. If the oxygen ions are sufficiently far away we can assume a purely ionic model. As the metal-oxygen distance decreases, the wave functions will overlap. This means that the electrons of different ions start to interact. But whenever there is an interaction between two systems, the combined system will reorganize to a state lower in energy. This happens schematically in the following way. Consider for example only
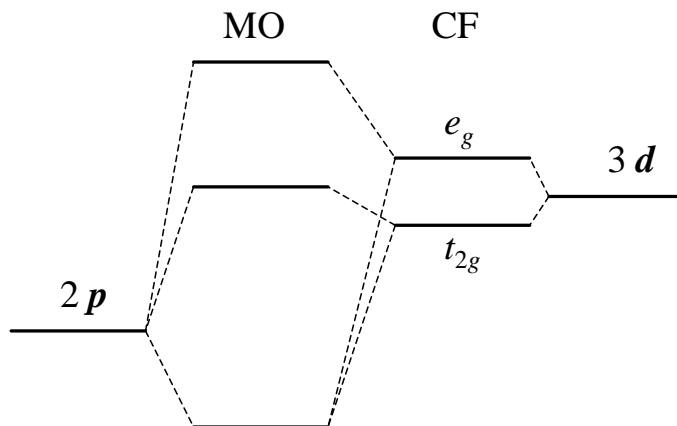
Figure 2.3: The action of covalency on the energy levels of the highest occupied states within a metal-oxygen complex is shown. The partially filled $3d$ states of the metal ion on the right are higher in energy than the fully occupied oxygen $2p$ shell on the left. The cubic crystal field (CF) splits the fivefold degenerate $3d$ states. This splitting is enhanced by hybridization of the $3d$ orbitals with the $2p$ orbitals treated in molecular-orbital theory (MO). Since the e_g orbitals hybridize stronger in an octahedral complex, they rise more than the t_{2g} orbitals. This increases the splitting between e_g and t_{2g} states.

two states with the energies ε_1 and ε_2. Without interaction the Hamiltonian H is simply given by

$$H = \begin{pmatrix} \varepsilon_1 & 0 \\ 0 & \varepsilon_2 \end{pmatrix}, \qquad H' = \begin{pmatrix} \varepsilon_1 & \delta \\ \delta & \varepsilon_2 \end{pmatrix} \qquad .$$

Including an interaction the off-diagonal elements will become different from zero. Diagonalizing the Hamiltonian H' that includes the interaction one gets new eigenstates as a linear combination of the old ones. The eigenvalues will be shifted: the one raised in energy is called antibonding, the other one lowered in energy is called bonding. This actually will happen also to free-ion states within the complex. Since the d-orbitals are higher in energy than the oxygen p-states, the metal d-states will be raised and the oxygen p-states will be lowered. This will affect the t_{2g}-states less because they have less overlap with the oxygen p orbitals. The e_g states will be raised further due to there larger overlap. This enhances the pure crystal-field splitting $10Dq$ (see Fig. 2.3).

Spin-orbit coupling

The crystal field and the covalency provide the gross structure of the energy levels. But there is another term that has to be considered in the Hamiltonian, namely the spin-orbit coupling. It accounts in particular for lifting the spin degeneracy which is preserved under the action of the crystal field. (The Kramers degeneracy for systems with an odd number of electrons is not concerned, it persists until an internal or external magnetic field is applied.)

The spin-orbit coupling has its origin in the relativistic theory, and in the case of a single electron in an atom it is derived as

$$H_{SO} = \xi\, \mathbf{l} \cdot \mathbf{s}$$

where the coupling constant ξ is obtained as

$$\xi(r) = -\frac{e\hbar^2}{2m_e^2 c^2} \frac{1}{r} \frac{dU(r)}{dr}$$

with the spherical potential $U(r)$ for the electron. Classically it may be viewed as the interaction of the magnetic moment of the electron spin with the magnetic field induced by the motion of the nucleus around the electron: the nucleus is seen from the coordinate system fixed on the electron.

2.1.2 Jahn-Teller interaction

As already mentioned, the five $3d$ orbitals ($L = 2$) of a free transition-metal ion are degenerate due to the full rotational symmetry, i.e. the angular momentum L is a constant of motion and it therefore commutes with the Hamiltonian. In a crystalline environment this fivefold degeneracy will be removed at least partially since the symmetry is drastically lowered from full $SO(3)$ to the point group of the crystal. The point group with the highest symmetry that may occur in three-dimensional space permitting also translational symmetry is the octahedral group O. The fivefold degeneracy is reduced to a twofold and a threefold one of the e_g and t_{2g} states, respectively. Depending on the number of electrons and their spin, the e_g doublet or the t_{2g} triplet can be occupied partially and the system remains orbitally degenerate. The Jahn-Teller theorem [108] states that such an orbital degeneracy will always be removed by interaction with the lattice. Its statement is a rather general one and not restricted to $3d$ states but accounts for all degenerate electron ground states of ions in crystals or molecules. The only exceptions are linear molecules or chains and the so called Kramers degeneracy. An ion in a crystal with a degeneracy of the electronic state different from these exceptions is called Jahn-Teller active. For instance in octahedral symmetry a groundstate of a $3d$ shell with 1, 2, 4 or 5 electrons in the t_{2g} orbitals or with 1 or 3 electrons in the e_g orbitals is orbitally degenerate and therefore Jahn-Teller active.

For the purpose of clarity let us first consider the Jahn-Teller effect for an isolated Jahn-Teller active impurity in a host lattice. It is assumed to be surrounded by ligand ions (for example O^{2-} or Cl^{1-}) on the corners of an octahedron placed in a host lattice of cubic symmetry. Like for example ruby where chromium ions are substituted into a cubic Al_2O_3 host lattice giving it its deep red color. The Jahn-Teller theorem states that the orbital degeneracy is unstable with respect to a distortion which lowers the symmetry. In the following we will consider an ion that exhibits a twofold degeneracy within the e_g orbitals if there were no distortion present (e.g. a Mn^{3+} ion with $3d^4$ configuration in the $S = 2$ high-spin state). Lowering the symmetry by a local deformation of the lattice will cause a splitting of the degenerate energy levels. The lowered e_g level will be occupied whereas the raised one will remain vacant (see Fig. 2.4). Since the deformation costs elastic energy, there will be only a small deviation Q of the ligand ions from their position in the undistorted case. Certainly
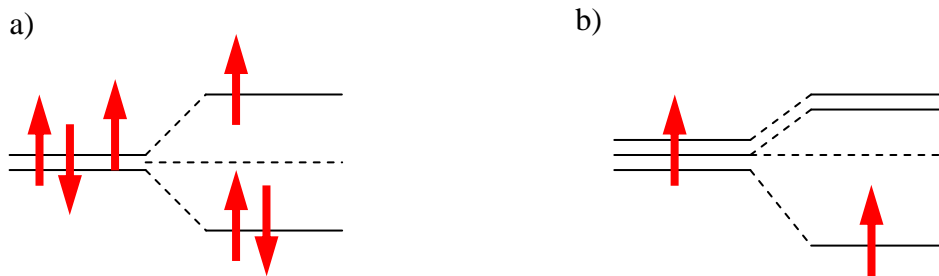
Figure 2.4: Examples of a Jahn-Teller splitting: a) three electrons in the two e_g orbitals, b) one electron in the three t_{2g} orbitals

not any arbitrary kind of distortion will be effective to lift the degeneracy. From the theory of lattice vibrations it is know that any distortion can be written as a linear combination of phonon modes. These phonon modes provide a basis set for all possible deformations of the lattice. It is convenient to choose a basis of eigenvectors of the dynamical matrix, i.e. one of eigenmodes (eigenstates) of the system. For the whole crystal the determination of the eigenmodes is by no means simple. But since we are examining only the local environment of the transition-metal ion, we will consider also only local distortions, the deformation of the surrounding octahedron built up from the six ligand ions. For this cluster of 7 ions there exist $3 \times 7 - 3 - 3 = 15$ linearly independent distortion modes (3 translational and 3 rotational degrees are substracted). Of these 15 modes there are two modes that account for a Jahn-Teller distortion, i.e. an energy splitting within the two e_g orbitals. These modes called q_2 and q_3 are shown in Fig. 2.5. Every relevant distortion Q has to be a linear combination of the two phonons q_2 and q_3. The space of the distortion is a plane spanned by the orthogonal vectors q_2 and q_3. Any point in this space corresponds to an appropriate distortion and it is
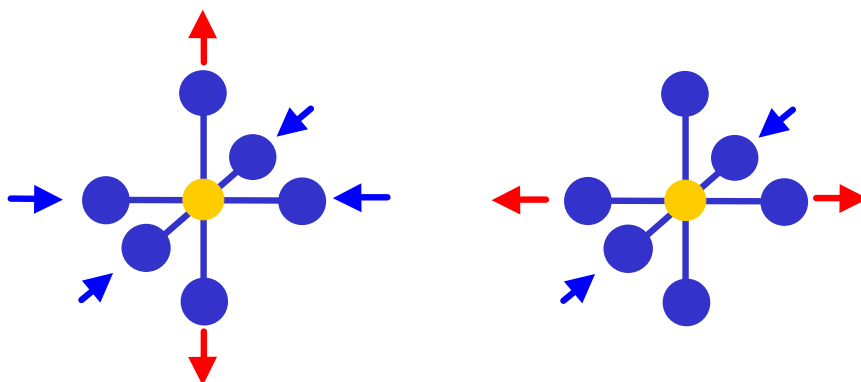

Figure 2.5: Jahn-Teller active distortion modes of a MO_6 cluster. On the left the q_3 mode is shown and on the right the q_2 mode. The arrows give the direction in which the ligand ions move (blue: inwards, red: out).
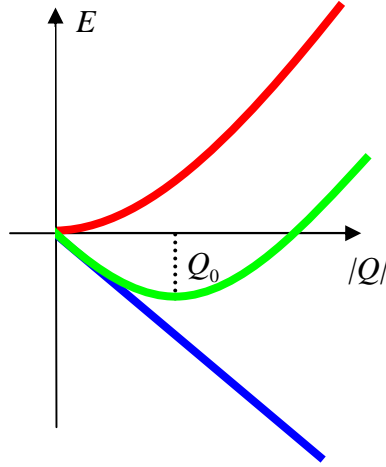
32

Figure 2.6: For a small lattice distortion Q the elastic energy (red) is increasing quadratically in Q (harmonic approximation). The electronic energy gain due to a lower Coulomb repulsion is linear in Q (blue). The total energy (in green) exhibits therefore a minimum at a certain distortion Q_0.

expressed in polar coordinates as

$$Q = \rho(\cos(\phi)q_3 + \sin(\phi)q_2)$$

Now we look at the energy balance which is illustrated in Fig. 2.6. The energy shift of the two orbitals induced by a distortion of amplitude ρ is given by

$$E(\rho) = \frac{C}{2}\rho^2 - g\,\rho$$

The first term accounts for the elastic energy due to the lattice deformation which is quadratic for small ρ (harmonic approximation). The constant C is the elastic modulus. The second term accounts for the energy in the electronic system. In contrast to the lattice the electronic state on its own is not in an equilibrium, thus the linear term is not vanishing here. The constant g accounts for the interaction of the electronic system with the lattice (electron-phonon coupling). Minimizing $E(\rho)$ leads to a value for the distortion $\rho = g/C$ with the corresponding energy

$$E_{JT} = -\frac{g^2}{2C}\ .$$

This gives the total energy gain in the distorted state. However, it does not determine the actual form of the distortion, i.e. it does not provide any information about the linear combination of the two phonon modes q_2 and q_3 that will actually occur (the angle ϕ is not determined). For the following consideration it is convenient to rewrite the orbital state by introduction of a pseudo spin T. The ground state of the undistorted system is given by any normalized linear combination of the two e_g orbitals

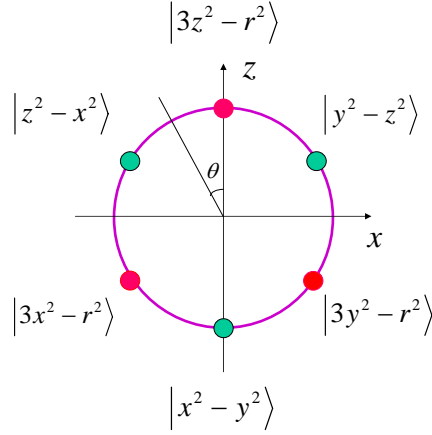$$|\psi\rangle = \cos(\theta/2)|3z^2 - r^2\rangle + \sin(\theta/2)|x^2 - y^2\rangle\ .$$

33

Figure 2.7: Different orbitals are shown as linear combinations in the pseudo-spin T_x T_z plane. The e_g orbitals show a threefold rotational symmetry axis ($S(3)$ symmetry, see Appendix B).

The orbitals resulting for different values of θ are shown in Fig. 2.7. Completely analogue to the spin case ($S = \frac{1}{2}$) one is able to define an operator T

$$T = (T_x, T_y, T_z) \ .$$

Its components are hence given by the Pauli matrices:

$$\frac{1}{2}T_x = \begin{pmatrix} 0 & 1 \\ 1 & 0 \end{pmatrix} \qquad \frac{1}{2}T_y = \begin{pmatrix} 0 & i \\ -i & 0 \end{pmatrix} \qquad \frac{1}{2}T_z = \begin{pmatrix} 1 & 0 \\ 0 & -1 \end{pmatrix}$$

These matrices operate on the two-dimensional space spanned by $\{|3z^2 - r^2\rangle, |x^2 - y^2\rangle\}$. Since T_y gives complex wave functions which is in principle allowed but usually not considered [4], we will take only T_x and T_z into account. Actually there is a more descriptive way to view these operators than the analogy to the spin. The operator T_z is measuring the difference between the occupancy of the orbitals, i.e. it gives extremal value if only one orbital is occupied ($\theta = 0$ or $\theta = \pi$). On the other hand T_x is measuring the mixing of the two orbitals, i.e. it is extremal when both orbitals contribute equally to the ground state ($\theta = \pi/2$ or $= 3\pi/2$). Depending on the electronic state it is easy to predict the distortion. If the $|3z^2 - r^2\rangle$ orbital is occupied the q_3 mode will be lowest in energy, and if $|x^2 - y^2\rangle$ is occupied then $-q_3$ is favorable. Equivalently, the q_2 mode is lowest in energy if not T_z but T_x is extremal. Rewriting the local energy in terms of the operators T_x and T_z we find [86]

$$E = \frac{C}{2}(q_3^2 + q_2^2) - g(q_2 T_x + q_3 T_z) \ .$$

It is clear that the contribution of the elastic energy is completely independent of the linear combination of q_2 and q_3, i.e. of ϕ. The second term is responsible for the energy gain. The maximum energy gain for constant values of $q_2^2 + q_3^2$ and $T_x^2 + T_z^2$ is achieved if the vectors
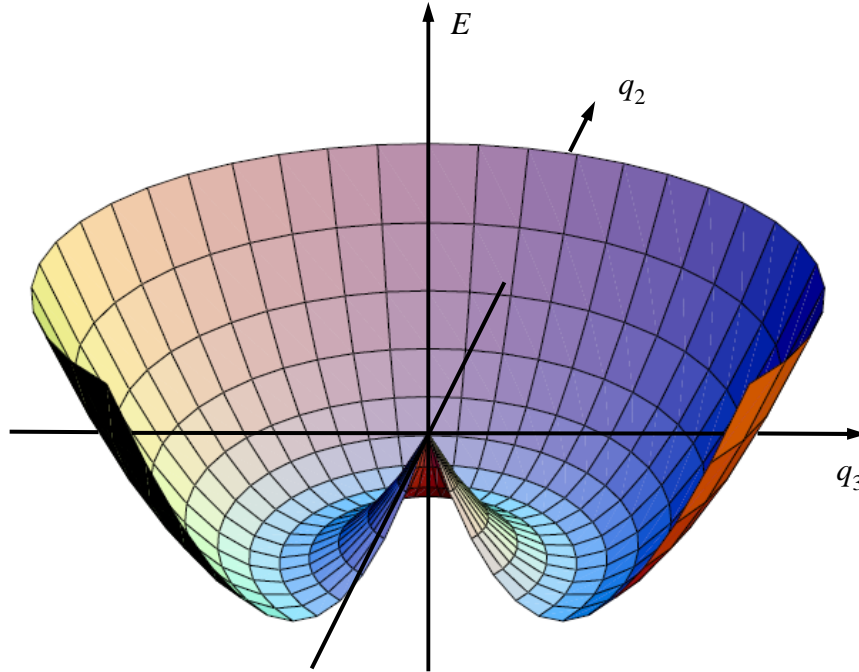
34

Figure 2.8: The "mexican hat": The xy plane is spanned by the two phonon modes q_2 and q_3. Using polar coordinates the energy E is only a function of the radius $E(\rho)$.

$\mathbf{Q} = (q_2, q_3)$ and $\mathbf{T} = (T_x, T_z)$ are parallel, i.e. the angles ϕ and θ are equal.[3] These two degrees of freedom in ϕ and θ are therefore reduced to one by the electron-phonon coupling. This means that for every distortion ϕ there is exactly one orbital state θ lowest in energy and vice versa. But all of these states of a certain orbital occupancy θ accompanied by the corresponding distortion ϕ are still degenerate ($E_{JT} = -\frac{g^2}{2C}$) within the approximations we made above. This can be visualized by the energy dependence of the distortions, the so called "mexican hat" shown in Fig. 2.8. This degeneracy is lifted only by taking terms of higher order into account, i.e. anharmonicity. Doing so it turns out that there are three minima that correspond to a distortion of q_3 type along the x, y and z axis, respectively. This threefold degeneracy remains for an isolated octahedron since the three minima correspond to an elongation (or compression, depending on parameters) along the x, y, or z axis, respectively, which obviously are equivalent.

For an isolated impurity the existence of three degenerate ground states opens the opportunity for the system to tunnel between them. If the probability for tunneling is high, i.e. the potential threshold between the degenerate ground states is small, the fluctuation will be fast. This case is called dynamical Jahn-Teller effect. In contrast, the case of only small tunneling probability is called static Jahn-Teller effect [86]. Anyway it depends on the time scale of the experimental method whether one will see fluctuations or static distortions.

---

[3]The constancy of $|T|$ follows from the normalization of the wave function, whereas $|Q| = Q_0$ is fixed as seen from Fig. 2.6.

So far we have regarded a single octahedron which is a situation that is realized only for a small number of impurities in a host lattice. However, by increasing the concentration of impurities the distortions will start to interact. At least if there are impurities on adjacent sites there will be an interaction, since elongation of the metal-ligand bond length on one site corresponds to a compression on the other site and vice versa. In particular for a lattice where each metal site is occupied by a Jahn-Teller active ion this will lead to cooperative phenomena which will be discussed in the next section.

2.2 Collective orbital physics

The interaction between ions in a crystal with orbital degeneracy will lead to collective phenomena which lift this degeneracy. There are different mechanisms that are capable to do so. One is the Jahn-Teller (or electron-phonon coupling) interaction that has already been discussed for a single impurity. The other interaction of importance is the coupling of the electronic states via the so called superexchange. It provides another way for lifting the degeneracy and is addressed below.[4] The superexchange involves also the spin degree of freedom. It turns out that the theoretical treatment is difficult since the spin, orbital, and lattice degrees of freedom have to be considered for a complete description of orbitally degenerate systems. Solving the resulting Hamiltonian has not been achieved [4]. However, parts of the Hamiltonian can be solved separately, i.e. one is able to make predictions only for limited cases. For dominating superexchange, novel kinds of ground states with novel elementary excitations have been predicted [38, 39]. Among these are an orbitally ordered state that exhibits new dispersive elementary excitations (e.g. $LaMnO_3$ [45, 106]), an orbital liquid state (e.g. $LaTiO_3$ [34]), and an orbital Peierls state (YVO_3 [43, 6]). This variety of fascinating novel scenarios makes orbital physics one of the hot topics in solid state physics that is rapidly developing.

In the following we will first focus on the theoretical description of both the collective Jahn-Teller effect and the superexchange for a system with e_g degeneracy. The more complicated case of a degeneracy within the t_{2g} orbitals will be treated in a separate section.

2.2.1 Orbital order: the collective Jahn-Teller effect

We start from a cubic perovskite structure ABO_3. For a given distortion of an octahedron of negatively charged ligands, the electron density will increase towards ligands that moved further away and decrease towards ligands that came closer (as stated above). Actually this minimizes the energy of the system. A distortion of q_3 (q_2) type corresponds to an eigenstate of T_z (T_x). Since the interaction is along the bonds we are interested in the orbitals pointing along the crystallographic (bond) direction. Therefore we form from the two orbital operators (T_x, T_z) a set of three operators (which are not any longer linearly independent) for which the electron density is extended along the bond directions. These three operators correspond

---

[4]In principle the quadrupole-quadrupole interaction which originates in the quadrupole charge distribution of the different orbitals is another one. The electron on one site will feel via direct Coulomb interaction which d-orbital is occupied on the neighboring site. However, the quadrupole-quadrupole interaction is rather weak and therefore this interaction is negligible.

obviously to a projection onto the orbitals $(|3x^2 - r^2\rangle;\ |y^2 - z^2\rangle)$, $(|3y^2 - r^2\rangle;\ |z^2 - x^2\rangle)$ and $(|3z^2 - r^2\rangle;\ |x^2 - y^2\rangle)$. From Fig. 2.7 one can easily see the linear combinations of T_z and T_x that give the new operators which are denoted by τ^a, τ^b and τ^c:

$$
\begin{aligned}
\tau^a &= -\tfrac{1}{2}T_z - \tfrac{\sqrt{3}}{2}T_x \\
\tau^b &= -\tfrac{1}{2}T_z + \tfrac{\sqrt{3}}{2}T_x \\
\tau^c &= T_z
\end{aligned}
$$

In the same way we may introduce distortions which are orientated along the bonds denoted by q^a, q^b and q^c. The corresponding phonon modes are obtained from q_2 and q_3 by the same linear combinations as in the orbital case:

$$
\begin{aligned}
q^a &= -\tfrac{1}{2}q_3 - \tfrac{\sqrt{3}}{2}q_2 \\
q^b &= -\tfrac{1}{2}q_3 + \tfrac{\sqrt{3}}{2}q_2 \\
q^c &= q_3
\end{aligned}
$$

With these new definitions we turn back to the collective Jahn-Teller effect. If in a crystal of corner-sharing octahedra one octahedron is elongated along for instance the c-direction, the total energy is lowered if the neighboring octahedron in c-direction is compressed along c and vice versa. The distortions on neighboring sites lower the energy if they have opposite sign. At each site r the distortion is given as a vector Q that is a linear combination of q_2 and q_3 and therefore also a linear combination of q^a, q^b, and q^c. The modulus $|Q|$ is constant as seen from Fig. 2.6 and Fig. 2.8, and therefore Q is assumed to be of unit length. So the Hamiltonian for e_g orbitals on a cubic lattice with corner-sharing octahedra that accounts for the interaction of phonons is given by

$$
H = \omega_1 \sum_r q_r^a q_{r+\hat{e}_a}^a + q_r^b q_{r+\hat{e}_b}^b + q_r^c q_{r+\hat{e}_c}^c
$$

where $\hat{e}_{a,b,c}$ are unit vectors along the crystallographic axes, and ω_1 is the constant for the nearest-neighbor coupling of the phonons. The operators q_r^i are phonon annihilation operators, the term $q_r^i q_{r+\hat{e}_j}^i$ thus counts whether the same local mode is excited on adjacent sites. For clarity the situation is shown in Fig. 2.9.

This term will obviously lead to orbitally ordered states on its own. Due to the additional interaction of orbitals based on the superexchange, there is another term that also may account for the occurrence of orbital order. Before deriving this term let us first discuss briefly the superexchange interaction itself.

2.2.2 Superexchange interaction between orbitals

Superexchange provides a rather effective indirect exchange interaction in Mott-Hubbard insulators where the direct overlap is negligible due to the relative large distance (> 4Å) between neighboring metal ions. In contrast to the Jahn-Teller coupling for which direct Coulomb interaction is responsible, the superexchange is due to a gain in virtual kinetic energy[5] of the electrons. This increase is achieved by hopping of electrons between neighboring

---

[5]A more or less localized electron will not be in a momentum eigenstate but in a superposition of a broad band of momentum eigenstates. As stated by the uncertainty principle, $\triangle x \triangle p \geq \hbar$. A large momentum
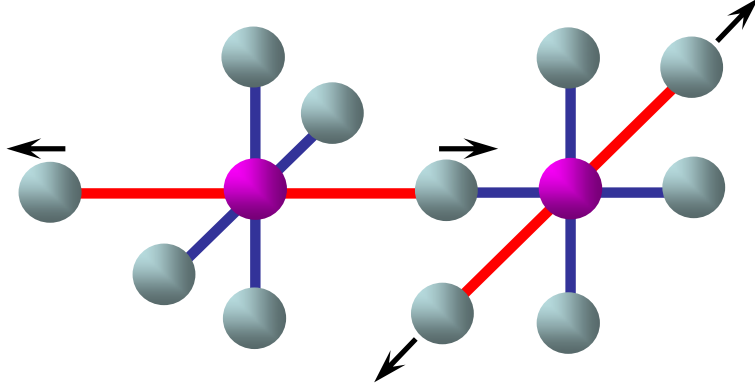
Figure 2.9: Two neighboring O^{2-} octahedra that are both centered by a Jahn-Teller active metal ion (M). The M-O bonds within one octahedron differ due to a Jahn-Teller distortion (tetragonal elongation depicted here). Longer bonds are shown in red, shorter bonds in blue. It is clear that a long bond on the left side has to point towards a short bond of the octahedron on the right in order to minimize the strain within the crystal.

metal sites. Since the probability of the hopping depends strongly on both the spin and the orbital occupancy on the engaged sites, the superexchange couples the spin state and the orbital state. The hopping involves the p orbitals of the ligand anions between the metal sites. However, in a Mott-Hubbard insulator the electrons feel the strong Coulomb repulsion U in case of double occupancy, and hence the electrons will hop only virtually. A large value of U will decrease the superexchange and hence also the energy gain. In contrast a large overlap with the ligand p orbitals will increases the hopping probability and therefore also the energy gain. The effective transition integral to the ligand p orbital is denoted by t. The mechanism is shown in Fig. 2.10 for the case of two holes distributed on two adjacent metal sites, for which only the $3z^2 - r^2$ orbitals are taken into account (no orbital degeneracy on the metal sites).

For parallel spins the Pauli principle forbids the hopping and hence the total energy will not be decreased. For antiparallel spins the energy gain is determined in leading order to be $\frac{4t^2}{U}$. In this situation antiferromagnetism is strongly preferred. If on the other hand the electrons on the two sites occupy orthogonal orbitals, the Pauli principle allows the hopping to the empty orbital for both spin directions. The resulting energy for the different configurations is shown in Fig. 2.11. For parallel spins the Coulomb repulsion energy U is reduced by Hund's rule coupling J_H to $(U - 3J_H)$ [86]. This favors ferromagnetism. But since J_H is about one order of magnitude smaller than U, the difference between the

---

corresponds to a large kinetic energy. A more narrow band of momentum eigenfunctions (i.e. smaller Δp) can be achieved by increasing the uncertainty Δx of the spatial wavefunction. In total this reduces the virtual kinetic energy ("virtual" in the sense that it does not correspond to an actual movement in space).
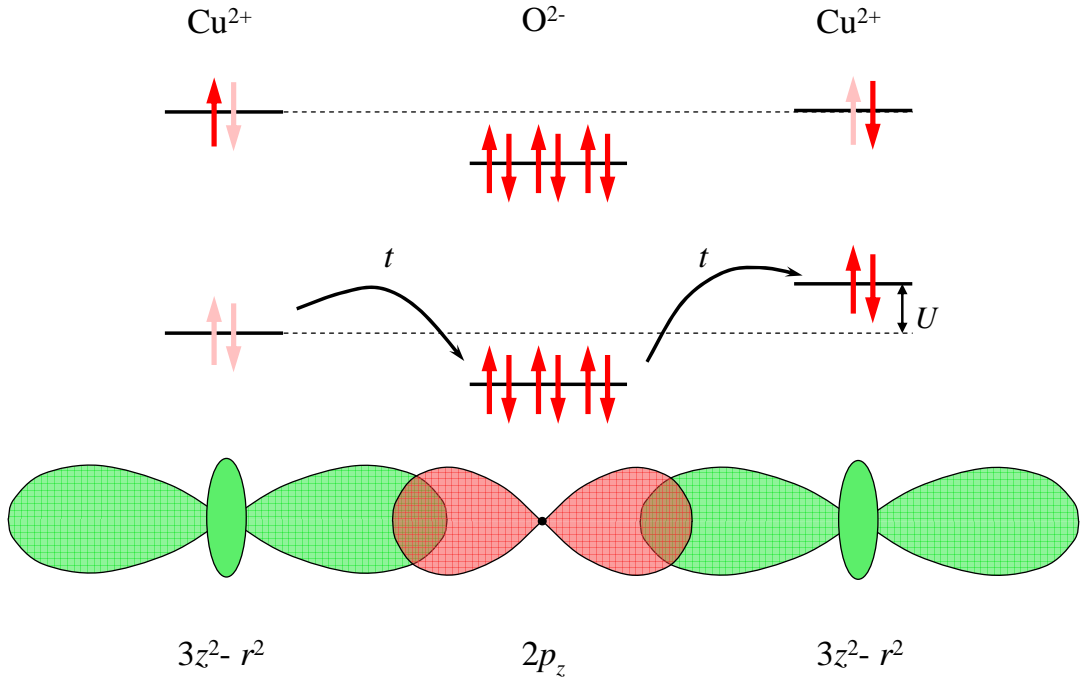
Figure 2.10: Example for the superexchange between two Cu^{2+} ions (t_{2g}^6, e_g^3) linked by an O^{2-} ion (Cu-O-Cu bond). The two $3z^2 - r^2$ orbitals (green) are each occupied by one electron represented by its spin (red arrow). Holes are indicated by light red arrows. The hopping of electrons is symbolized by curved arrows. Each hopping process (Cu$\frown$O and O$\frown$Cu) has the hopping amplitude t. In the upper part the electronic state with one electron on each copper site is depicted. Double occupancy occurs if one electron hops from the oxygen to e.g. the copper ion on the right and in the same process the hole on the oxygen is refilled by the electron from the left copper site. On the copper ion on the right, the state with double occupancy is higher in energy by the Coulomb repulsion U.

hopping processes for different spin states is small compared to the situation of hopping to the same orbital described above. Hence the ferromagnetic coupling is weak. These arguments basically explain the Goodenough-Kanamori-Anderson rules [87, 86]. The general features of these rules may be summarized as follows:

- If half-filled orbitals overlap at adjacent sites, the exchange is antiferromagnetic and comparatively strong.

- If a vacant orbital and a filled orbital overlap, the exchange is ferromagnetic and weaker.

These rules are significantly more detailed in their complete formulation [87]. In particular the angle of the bond along which the exchange occurs turns out to be important. In our case of a cubic lattice a bond angle of 180 degree is realized.
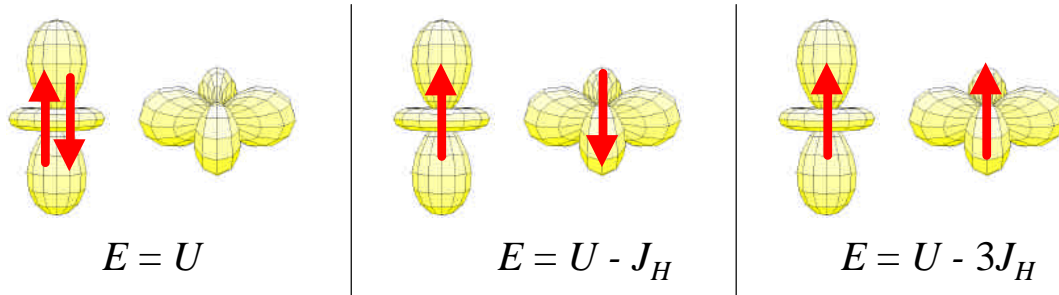
$$E = U \qquad\qquad E = U\text{ - }J_H \qquad\qquad E = U\text{ - }3J_H$$

Figure 2.11: The energy of double occupation within the e_g orbitals on the same site derived for a free atom [86]. Three states of different energy exist. On the left: the two electrons occupy the same orbital ($S = 0$ is required by the Pauli principle). In the middle: different orbitals are occupied with $S = 0$. On the right: different orbitals are occupied with $S = 1$. Of course this is only a sketch, the total wave function has to be antisymmetric. According to Hunds rule the high-spin state is lowest in energy. However, a strong crystal-field splitting may give an additional energy that changes this order of states for an ion in a crystal.

2.2.3   Orbital order in e_g systems

So far we have considered the superexchange for a non-degenerate ground state, i.e. we know which orbitals are occupied and which are empty and we can apply the Goodenough-Kanamori-Anderson rules. However, for an orbitally degenerate ground state this is not the case anymore. The superexchange coupling constant J depends on the orbitals that are occupied on adjacent sites. In the case of e_g orbitals this is illustrated in Fig. 2.12. One can state that the exchange interaction is similar to the Jahn-Teller interaction in the sense that it couples the orbital occupation of neighboring sites. It is often not possible to decide form the orbital order pattern which of the two mechanisms is dominating if both prefer the same ordering of orbitals. For instance in LaMnO$_3$ both the Jahn-Teller interaction and the exchange interaction prefer an orbital order pattern where an occupied orbital points towards a vacant orbital on the adjacent site [86, 4]. It is therefore clear that the exchange interaction may also lead to orbitally ordered ground states, just as the interaction of the orbitals via lattice distortions does. Note that also a superexchange-driven orbital order will be accompanied by lattice distortions, i.e. the lattice will relax for a given orbital occupation.

For systems where the orbital order sets in at temperatures far above the spin ordering, it is justifiable to consider only orbital and lattice degrees of freedom. The full Hamiltonian H for the twofold degenerate e_g orbitals on a cubic lattice that considers the orbital state and phonons may be divided into three parts [106, 4].

$$H = H_{orb} + H_{ph} + H_{e-p}$$

One part accounts for the superexchange interaction of orbitals H_{orb}, phonons are not involved here. Another term, the electron-phonon coupling H_{e-p}, describes the coupling of the orbital state to phonons like discussed for the local Jahn-Teller interaction. The third part H_{ph} gives
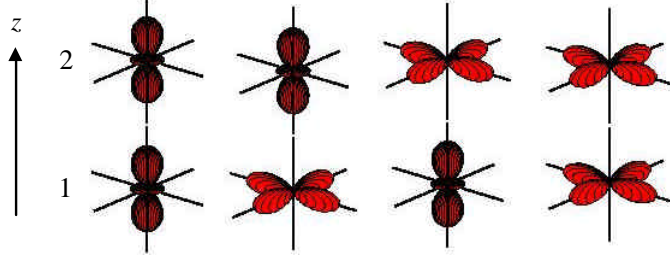
Figure 2.12: Four possible configurations for the exchange of e_g electrons along a bond in z direction on a cubic lattice. Hopping is possible only from the $3z^2 - r^2$ orbital. On the left the $3z^2 - r^2$ is occupied on each site (1,2). In this case the exchange is antiferromagnetic. The two configurations in the middle (the $3z^2 - r^2$ occupied on one site and the $x^2 - y^2$ on the other site) are equivalent. Here the exchange is ferromagnetic because the energy for double occupancy is lower in the ferromagnetic case (see Fig. 2.11). In the case on the right hopping is not possible. Therefore the exchange-coupling constant vanishes and the energy gain due to exchange is zero. In e.g. the manganites, one has to take into account also the coupling to the spins that occupy the t_{2g} orbitals (Hund's rule).

the energy of the phonons and the interaction between them. Let us collect now what has been derived above. The phonon part is of the form [106, 4]

$$H_{ph} = \omega_0 \sum_r (q_{2r}^\dagger q_{2r} + q_{3r}^\dagger q_{3r}) + \omega_1 \sum_r (q_r^a q_{r+\hat{e}_a}^a + q_r^b q_{r+\hat{e}_b}^b + q_r^c q_{r+\hat{e}_c}^c) \quad .$$

Here ω_0 is the local phonon energy and ω_1 is the coupling constant between phonons excited on adjacent sites. The sum runs over all sites r, and $q^\dagger$ (q) is a phonon creation (annihilation) operator. The orbital part is given analogous to the interaction of phonons but with a different coupling constant J. The value of J depends on the strength of the superexchange interaction. The orbital operators T_x and T_z correspond to the phonons q_2 and q_3 on each site, i.e. the vectors $\mathbf{T}$ and $\mathbf{Q}$ are parallel (see section 2.1.2). So one has the freedom of choice to use either T_x and T_z or q_2 and q_3. For clarity we will choose the pair of orbital operators T_x and T_z (or the linearly dependent set of operators along the bonds τ_a, τ_b, τ_c). The orbital Hamiltonian has the simple form [4]

$$H_{orb} = J \sum_r \tau_r^a \tau_{r+\hat{e}_a}^a + \tau_r^b \tau_{r+\hat{e}_b}^b + \tau_r^c \tau_{r+\hat{e}_c}^c$$

The term which corresponds to the ω_0 term in H_{ph} vanishes since we start from degenerate orbitals, i.e. in cubic symmetry a local orbital flip is assumed to cost no energy. The on-site electron-phonon interaction has already been mentioned in the discussion of the local Jahn-Teller effect [106],

$$H_{e-p} = g \sum_r T_{xr} q_{2r} + T_{zr} q_{3r} \quad .$$

The magnitude of the coupling constant g will turn out to be crucial for the character of orbital excitations (see below).
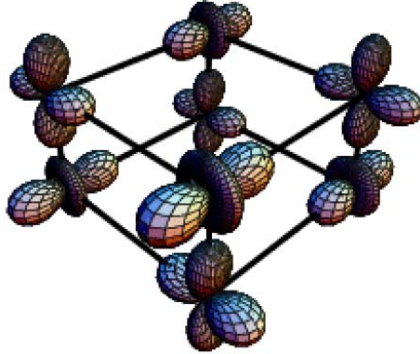
Figure 2.13: Orbital order that is predicted for e_g states in an orbital only model on a cubic lattice (only the orbital degree of freedom is considered)[4].

At this point we want to discuss the orbital order pattern that is produced by the Hamilton operator given above. It is clear from our considerations that occupied orbitals will avoid pointing towards each other since this costs lattice energy ($\omega_1 > 0$) and at the same time it costs superexchange energy ($J > 0$). The resulting orbital order is shown in Fig. 2.13 [4].

However, the orbital order observed by experiment in LaMnO$_3$ differs from the calculated one [166]. It seems that in the real crystal the occupation of the $x^2 - y^2$ type of orbital is not favorable. This discrepancy is proposed to be due to anharmonic lattice effects [36]. The occupation of the $x^2 - y^2$ orbital always comes along with a compression of the octahedron whereas the $3z^2 - r^2$ orbital corresponds to an elongation of the octahedron. The two distortions belong to different signs of the q_3 mode. They are degenerate in the harmonic approximation. Going beyond the harmonic approximation by taking into account the next (third) order of the lattice energy one finds

$$E_{lattice} = \frac{C}{2}u^2 - \frac{\xi}{2}u^3$$

where $C, \xi > 0$. It is obvious that the harmonic term does not care about the sign of the distortion u whereas the anharmonic term does. It favors the elongation of the octahedron according to $u > 0$. Possible ordering patterns are shown in Fig. 2.14. Both have been observed experimentally [165]. For instance in KCuF$_3$ where two distinct crystal structures exist, the so-called a-type and d-type. The two phases support different orbital ordering patterns and are stable to very high temperature [166]. In a classical system (no quantum fluctuations) these two patterns of orbital order are degenerate [4]. In Fig. 2.15 a) the distortion pattern of a single xy layer is shown. This pattern can be identically repeated in the adjacent layer or it can be shifted. Two possible cases are shown in Fig. 2.15 b) belonging to an ordering type η (either $\eta = 0$ for identical pattern or $\eta = \pi$ for altering distortions). Classically both cases have the same energy. So for more than two layers all possible combinations of η for successive layers can occur. The degeneracy rises exponentially with the number of layers. However, one ground state is selected in a real system. This is due to a mechanism called "order by disorder". It simply means that for a system with a
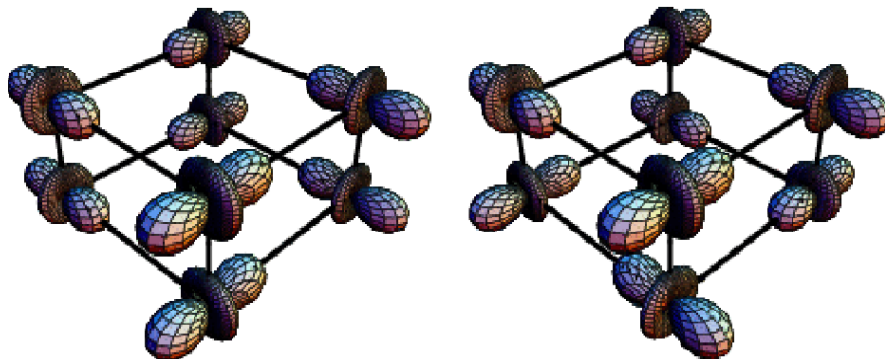
Figure 2.14: Schematic picture of the orbital ordering pattern that is observed in Jahn-Teller distorted LaMnO$_3$ and d-type KCuF$_3$ (left) and a-type KCuF$_3$ (right) [86]. The occupied orbitals are shown. This figure is taken from [4].

classically degenerate ground state this degeneracy is lifted by quantum fluctuations. Thus fluctuations that usually account for disorder here lead to a single, ordered ground state. This is where the contradictory term "order by disorder" comes from. The free energy of lattice fluctuations depends on η. Lattice fluctuations can achieve order since the oscillations have different stiffness for different stacking, and soft modes are preferred to hard ones.

2.2.4 Ground states of t_{2g} systems

So far we have only considered the case of degenerate e_g orbitals. But degeneracy can as well occur within the t_{2g} orbitals. However, things turn out to be different from the e_g case [4]. The most obvious difference is the increased number of orbitals. Since there are three degrees of freedom (xy, zx, yz) the operator T is now a vector with three (not complex) components. Hence two angles are necessary to describe T in spherical coordinates, i.e. T lies on the unit sphere, not on a circle. Other differences originate from the different geometry of the t_{2g} orbitals. First, their lobs of high electron density do not point towards the ligand ions in octahedral coordination but in between. Therefore the coupling to the lattice is weaker than for e_g orbitals. Second, along each bond direction there are two equivalent orbitals. Moreover, within the t_{2g} subshell there is a pseudo angular momentum $\tilde{L} = 1$ which gives rise to spin-orbit coupling, whereas in the e_g orbitals the angular momentum is quenched completely.

The Hamiltonian that describes the interaction of the t_{2g} orbitals with a Jahn-Teller distortion turns out to be more complex [4]. The two phonon modes with e_g symmetry (q_2 and q_3) give rise to an effective Jahn-Teller splitting of the t_{2g} orbitals. The q_3 mode (elongation of the ions in z direction and compression in the xy plane, see Fig. 2.5) will lower the zx and the yz orbital and raise the xy orbital in energy. The q_2 mode (elongation along x and compression along y) will raise the yz and lower the zx orbital, whereas the xy orbital is not affected. Moreover, there are three modes of t_{2g} symmetry that may contribute as well to the electron-phonon interaction. They are shown in Fig. 2.16. In contrast to the
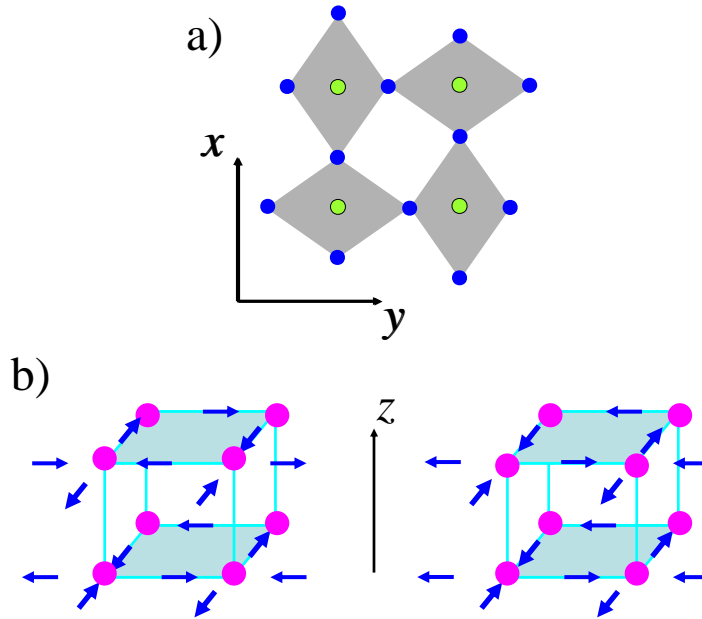
Figure 2.15: Top: distortion pattern in an orbitally ordered ground state within the xy plane of an e_g system. Bottom: stacking of two xy layers can occur in two ways (for the orbital order see Fig. 2.14). Classically this leads to a highly degenerate ground state for the infinite 3D compound. This degeneracy is removed by a mechanism called "order by disorder" based on quantum fluctuations.

bond-stretching modes q_2 and q_3, these are bond-bending vibrations. For e_g orbitals the lattice interaction and the superexchange give a similar orbital Hamiltonian [106]. This is quite different for t_{2g} orbitals. A full treatment for the t_{2g} case including the phonon part of the Hamiltonian (like it has been discussed for the e_g's in [106]) is still lacking. However, a model which considers only the electron-electron interaction is investigated by Khaliullin and Okamoto in [34].

Orbital liquids

The case of degenerate t_{2g} orbitals turns out to be drastically different from a degeneracy within the e_g orbitals. The fact that there are three t_{2g} orbitals instead of two e_g orbitals changes the situation substantially. In the perovskite structure, the probability of an electron to hop to a neighboring site is reduced compared to the e_g case. The different orientation of the orbitals yields a reduction of the energy gained by fluctuations based on superexchange. In the e_g system LaMnO$_3$ the spin ordering temperature is far below the temperature of the orbital ordering transition. This makes it reasonable to neglect the spin degree of freedom there (see table 4.2). For some t_{2g} systems like LaVO$_3$ both ordering temperatures are similar (see table 4.2) which indicates that orbitals and spins have to be treated on equal footing here.
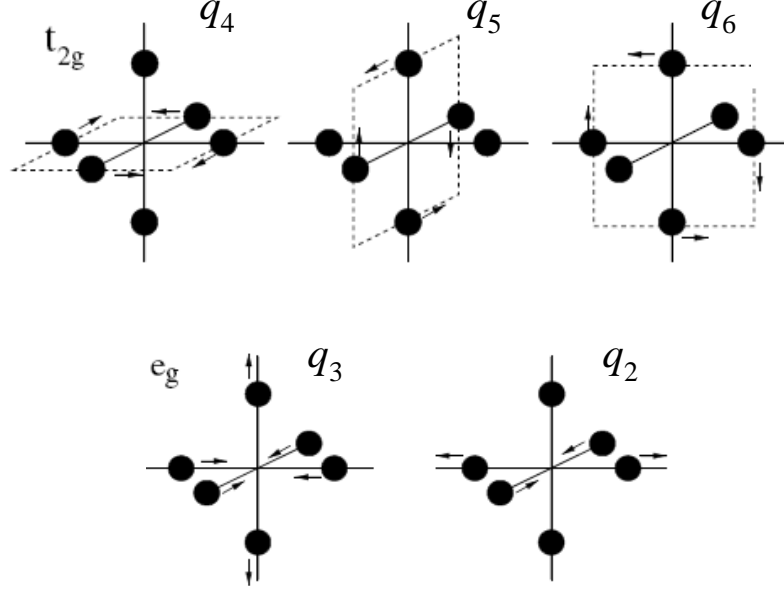
Figure 2.16: Top: The shift of the ligand ions corresponds to the three t_{2g} bond-bending phonon modes (q_4, q_5, q_6) that lift the degeneracy of the t_{2g} orbitals. Bottom: For comparison the two e_g bond-stretching phonon modes are shown which account also for a splitting of the t_{2g} orbitals [4].

A spin-orbital Hamiltonian for partially filled t_{2g} orbitals is presented in [38]. It has to be specified to the system under investigation, which has been done in [38] for various cases. For a $3d^1$ system like LaTiO$_3$ the superexchange Hamiltonian in the limit of negligible Hund coupling ($J_H \ll U$) reads as [34, 38]

$$H_{SE} = -\frac{4t^2}{U} + \frac{4t^2}{U} \sum_{\langle i,j \rangle} (\mathbf{S}_i \cdot \mathbf{S}_j + \frac{1}{4}) \hat{J}_{ij}^{(\gamma)}$$

Where $4t^2/U$ represents the overall superexchange energy scale. The orbital operator $\hat{J}_{ij}^{(\gamma)}$ depends on the bond direction $\gamma (= a, b, c)$. For a bond along the c-axis it has the form:

$$\hat{J}_{ij}^{(c)} = 2 \left(\tau_{ab}^i \tau_{ab}^j + \frac{1}{4} n_{ab}^i n_{ab}^j \right)$$

with $n_{ab}^i = n_a^i + n_b^i$. Here, n_α^i is the number operator of the orbital occupation on the i-th site, and $\alpha = a, b, c$ corresponds to the yz, zx, and xy orbital, respectively. τ_{ab}^i is the pseudo-spin operator (see 2.1.2) of the subspace of the two orbitals (a, b corresponding to yz, zx) that are relevant on a bond along the c-axis. The pseudo-spin operators $\tau_{bc,ca}^i$ and the orbital operators $\hat{J}_{ij}^{(a,b)}$ for bonds along the a and b-axis are obtained by cyclic permutation of a, b, c.
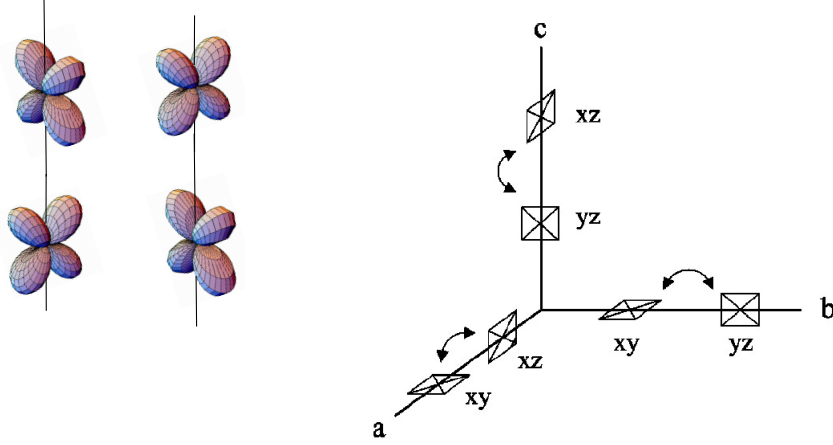
Figure 2.17: On every bond of a cubic crystal, two out of three t_{2g} orbitals are equally involved in the superexchange and may resonate. The same two orbitals select also a particular component of the angular momentum. The figure on the right is taken from [42]. It shows the geometry of the t_{2g} orbitals on a 3D cubic lattice. Resonance for all three bond directions will be only possible for fluctuating orbitals.

The spin part $(\mathbf{S}_i \cdot \mathbf{S}_j + \frac{1}{4})$ and the orbital part $\tau_{ab}^i \tau_{ab}^j + \frac{1}{4} n_{ab}^i n_{ab}^j$ of the Hamiltonian show a remarkable difference. The spin on one site i is either up or down and hence $n_{i,\uparrow} + n_{i,\downarrow} = 1$. This effectively corresponds to half filling, in which case one expects long-range order in 3D. For e_g systems where only two orbitals are available at each site the orbital sector is also half filled which leads to long-range order of orbitals. There a $SU(2)$ (spins) $\times$ $SU(2)$ (orbitals) symmetry is present there. In comparison to this the orbital part of the t_{2g} Hamiltonian considered above is not half filled. Along one bond the orbital part is $(\tau_{ab}^i \tau_{ab}^j + \frac{1}{4} n_{ab}^i n_{ab}^j)$ which has only to obey the requirement $n_a^i + n_b^i + n_c^i = 1$. Thus n_{ab}^i is not conserved but fluctuates around the average value 2/3. This difference between the e_g and the t_{2g} case has far reaching consequences for the resulting ground state. For a $SU(2) \times SU(2)$ symmetry, exchange energy is gained by the resonance of the degenerate states ("orbital triplet $\times$ spin singlet") and ("orbital singlet $\times$ spin triplet")(see Fig. 2.17 and below). The excitations here are mixed modes of $SU(4)$ symmetry. For the above Hamiltonian an exact $SU(2) \times SU(2)$ symmetry is not present, but exchange energy is gained by virtual $SU(4)$ resonance [34]. However, orbitals will not exhibit long-range order due to the fact that the energy gained from spin fluctuations for a static orbital ordering is small compared to the e_g case because of the different geometry of the t_{2g} orbitals. On a cubic lattice, the gain of exchange energy is much larger for an orbitally disordered state (see Fig. 2.17). Therefore static orbital order is not favorable within this model [34]. This ground state with strong quantum fluctuations in the orbital sector is termed "orbital liquid" [34, 35, 38] expressing that no long-range order of orbitals is established even for $T = 0$ K. Such a state can be regarded as a realization of Anderson's resonating-valence-bond idea [204] in a three-dimensional insulator with orbital degrees of freedom.

In order to gain more insight into the resonating ground state we will consider the situation on a single bond (see Fig. 2.17). At each site only two orbitals are involved. If we assume that only one orbital at each site is occupied (as it is the case in the $3d^1$ titanates), several spin-orbital states different in energy may occur at one bond. They are formed by the spin states (singlet and triplet) times the orbital states (orbital singlet and orbital triplet). The states ("orbital triplet × spin singlet") and ("orbital singlet × spin triplet") are lowest in energy. The energy of the ground state may further be lowered by resonance between these states[6]. In a three-dimensional crystal with octahedral environment, resonance may occur along the six bonds (see Fig. 2.17). Since the hopping integrals of all orbitals are strongly anisotropic, such a 3D resonance is only possible for fluctuating orbitals.

In the case of $LaTiO_3$ the experimentally observed reduction of the ordered magnetic moment has been assigned to quantum spin fluctuations induced by orbital fluctuations of the ground state [34]. On the other hand the nearly isotropic spin wave spectrum arises naturally from the cubic symmetry of the fluctuating orbitals. However, the reduction of the ordered magnetic moment can also be explained in a conventional crystal-field scenario [57] (see chapter 4).

However, the model Hamiltonian considered above does not include the interaction of the orbital degree of freedom with the lattice. In the case of t_{2g} orbitals this interaction is assumed to be weaker than for e_g orbitals. The role played by the coupling to the lattice is discussed controversially in the literature [59, 57, 38]. This role is crucial to decide whether an orbital liquid state is realized in the titanates (see chapter 4).

2.2.5 Superexchange vs. Jahn-Teller interactions

The crucial point for the concepts of orbital liquids or of propagating orbital waves is that the superexchange interaction has to be the leading term of orbital interactions, i.e. it has to be dominating over the Jahn-Teller interaction. However, the Jahn-Teller interaction has been shown to give the major contribution to the orbital interactions for an overwhelming number of insulators. For doped, metallic Mott-Hubbard insulators the situation may be different. The mobile charge carriers scramble the lattice distortion and suppress the Jahn-Teller effect. At the same time, the scattering of the mobile charge carriers on orbital degrees of freedom may be very important. This situation is comparable to the case of mobile carriers interacting with localized spins, as encountered e.g. in the high-T_c cuprates. The physics may then be described by a t-J model. A recent example may be the doped CoO_2 layers of Na_xCoO_2 [38]. However, the example of the cuprates shows how complex the physics may become upon doping. It thus may be very helpful to study the undoped case first. In the spin sector this has been pursued very actively in the past years. The important question is whether there is hope to find an insulating system with localized electronic states wherein the superexchange dominates over the Jahn-Teller interaction. Figure 2.18 shows how the parameters of such a system would have to be.

Let's imagine for a moment that we could control parameters of the crystal continuously. For a small value of the Hubbard energy U the system is metallic. With increasing U the

---

[6]Such a resonance may be regarded as an analog to the splitting of a two-spin system into a singlet and a triplet by mixing the simple product states ($\uparrow\uparrow$), ($\uparrow\downarrow$), ($\downarrow\uparrow$), ($\downarrow\downarrow$).
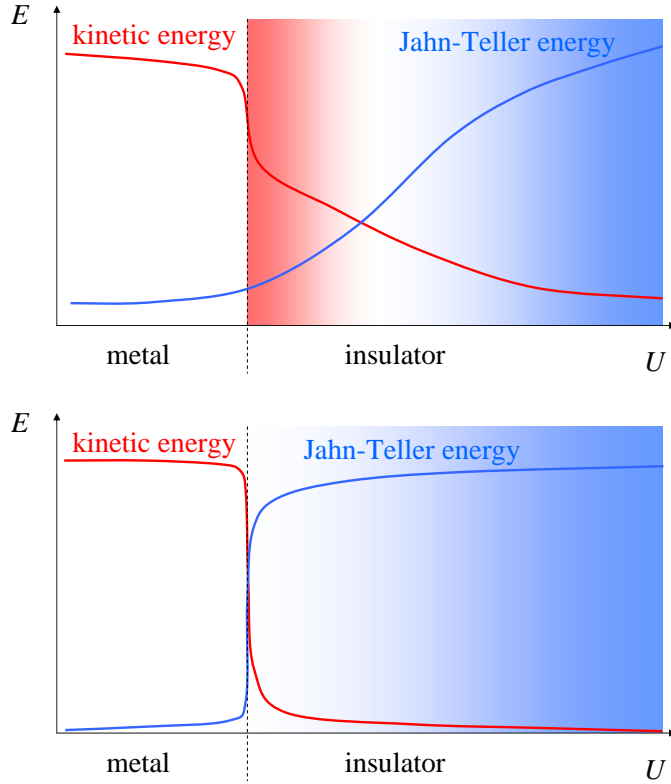
Figure 2.18: Two possible scenarios for the relative values of the kinetic energy and the Jahn-Teller coupling as a function of U/W. Top: For large values of U/W the Jahn-Teller effect provides the dominating energy scale (blue region). However, in the proximity of the metal-insulator transition the increase of the band width W and hence kinetic energy becomes dominating over the Jahn-Teller energy (red region). In this region collective orbital physics based on the superexchange will arise. Bottom: Immediately after the metal-insulator transition the kinetic energy drops strongly and the Jahn-Teller effect becomes the leading energy scale [98].

system will reach a critical value for which the conducting band splits into a lower and an upper Hubbard band. Beyond this critical value it becomes insulating. With increasing U, the kinetic energy of the electrons will strongly decrease, in particular across the metal-insulator transition. If U is not too large compared to the band width W, the Hubbard gap may be small and hence the superexchange may still be strong enough to dominate over the Jahn-Teller interaction (indicated by the red region in Fig. 2.18). Anyway this scenario of variation of the exchange interactions with the parameter U is not derived from experimental results and therefore also an alternative scenario could be a suitable description for real systems. It is shown in the bottom panel of Fig. 2.18. Here, the Jahn-Teller effect is rising so strongly upon localization of the electrons that it will immediately take over the control when the Hubbard gap opens and the system becomes insulating. In such a scenario, orbital
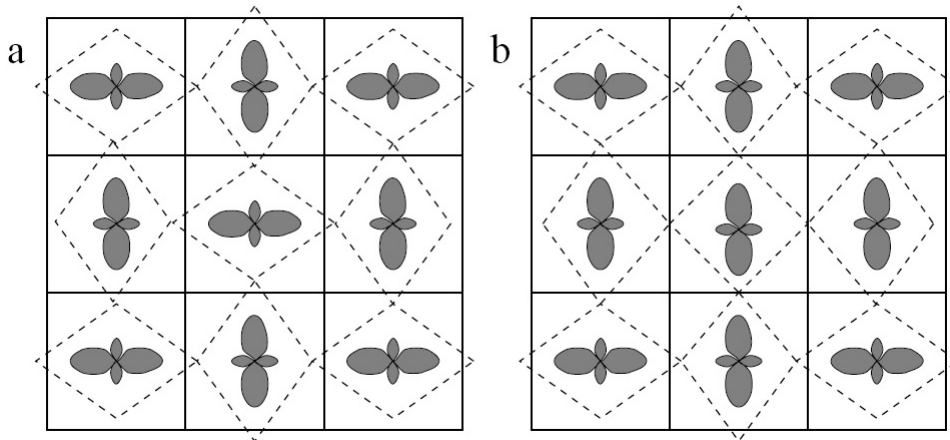
Figure 2.19: (a) Schematic view of the Jahn-Teller distorted xy plane of $LaMnO_3$ with ordered orbitals. (b) The lowest electronic excitation with an orbital rotated at the center and the lattice relaxed. This figure has been taken from [178].

physics will in any case be restricted to electron-phonon interactions.

2.3 Orbital excitations

2.3.1 Orbitons vs. crystal-field excitations

In general any kind of order from a spontaneously broken symmetry is giving rise to new elementary excitations. These can be viewed as a disturbance of this order. Excitations with a well-defined, quantized energy and with a long lifetime are quasi-particles. Examples for order and for the corresponding excitations or quasi-particles are the lattice (spontaneously broken translational invariance) and lattice vibrations (phonons) or magnetic order (spontaneously broken rotational invariance of the spins) and spin waves (magnons). In the case of orbital order one expects also novel elementary excitations. The quasi-particles of orbital waves are termed orbitons. However, the properties and the character of these excitations depend strongly on the mechanism that is responsible for the emergence of the orbital order. As already mentioned, the two possible mechanisms are the collective Jahn-Teller effect and the superexchange (electron-electron) interaction. For an orbitally ordered ground state it is therefore *a priori* not possible to determine which one is dominating. In order to pronounce the difference we will first discuss the limiting cases, although we have to be aware that both mechanisms are present simultaneously in a real crystal, only with different proportion.

Let's assume first that the Jahn-Teller effect, i.e. the lattice distortion, is the origin of orbital order. How do the orbital excitations look like? Assume we change the orbital occupancy on one site, i.e. we promote an electron from one orbital to a higher-lying one at the same site (see Fig. 2.19). This single site is not in its ground state any more but in an excited state. Since the change of the electronic state happens quickly compared to

phonon energies, there is no time for the lattice to relax, i.e. the lattice is not in its ground state. If the new orbital state is assumed to be fixed, then the lattice can gain energy by accommodating to the new charge distribution. The unrelaxed state can be viewed as a state in which some phonons are excited statically (see Fig. 2.28 below). The lattice relaxes then without emitting radiation by coupling to phonons (see Fig. 2.19). The orbital excitation may be treated as rather local. In order to hop, the electron has to drag along the lattice relaxation. Due to the strong dressing by phonons the orbiton acquires a large effective mass. Therefore the probability to hop to a neighboring site is very small. A hopping process would require that two electrons interchange their sites. One hops from the ground-state orbital of the adjacent site to the ground-state orbital on the first excited site and simultaneously the excited electron hops in the other direction into the excited orbital.

In [178] the energy of such a "local" excitation in $LaMnO_3$ has been calculated in the strong-coupling approximation $U \to \infty$ by considering only states with no double occupancy of e_g orbitals. The hopping of electrons is completely suppressed in this model. The Hamiltonian accounts for vibrational energy and electron-phonon coupling of the occupied e_g orbital at each site. By solving this Hamiltonian Allen and Perebeinos [178] predict that the electronic excitations in $LaMnO_3$ are self-trapped[7] by local rearrangements of the lattice. The energy of this excitation is estimated to be about 2 eV. The optical spectrum is expected to show a Franck-Condon series, that is, a Gaussian envelope of vibrational sidebands (see Fig. 3.13).[8] The Raman spectrum is predicted to have strong multi-phonon features [171].

Consider the other limit of an orbital order that emerges due to the superexchange interaction only, i.e. assume an undistorted cubic lattice. The propagation of an orbital excitation requires the exchange of two electrons on adjacent sites. This exchange is the very basis of the superexchange interaction, thus a delocalization is natural, in contrast to the Jahn-Teller case. The orbital propagation is analogous to magnetic excitations in a magnetically ordered state (see Fig. 2.20). Like the spin waves, the orbital waves will propagate through the crystal with a significant dispersion. The dispersion of the orbiton has been calculated for instance in [159] for the case of $LaMnO_3$ (see Fig. 2.21), i.e. for a C-type orbitally ordered state with the A-type antiferromagnetic structure. On the basis of this dispersion, Saitoh and collaborators claimed the first observation of orbitons in Raman data of $LaMnO_3$ [44]. The relevant peaks are observed around 150 meV (see chapter 3).

A Hamiltonian that treats the electron-electron superexchange interaction and the lattice dynamics in $LaMnO_3$ on an equal footing has been considered by van den Brink [106]. It has been shown that the orbiton dispersion is strongly reduced by the electron-phonon coupling. The exchange coupling also mixes the orbiton and phonon modes and causes satellite structures in the orbiton and phonon spectral functions. The elementary excitations of the system, in other words, are mixed modes with both orbital and phonon character as seen from Figs.

---

[7]In principle, an excitation in a translationally invariant system has to be viewed as delocalized. In particular, it does not become local or trap itself. However, excitations with a very large mass hardly show any dispersion and thus may be treated as "local". Moreover, such heavy excitations may be trapped easily by an impurity.

[8]Due to the finite dispersion of the phonons and the existence of several relevant phonon modes, usually only very broad features are observed in solids. The observation of Franck-Condon series is usually restricted to molecules or molecular solids.
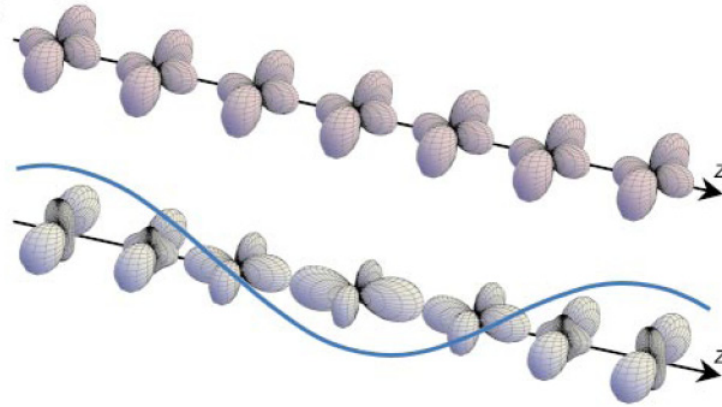
Figure 2.20: Schematic illustration of an orbital wave. Top: the electron cloud in the ground state. Bottom: a snapshot of the electron cloud when an orbital wave is excited. The wavevector of the orbital wave is chosen to be $(0, 0, 6\pi/a)$, with a being the bond length between nearest-neighbor Mn ions. The figure is taken from [44].

2.22, 2.23 and 2.24. In Fig. 2.22, both orbitons and phonons are assumed to be local. This corresponds to the Franck-Condon limit as discussed by Allen and Perebeinos [178]. In Fig. 2.23, the dispersion of both kinds of excitations is taken into account, but dynamical effects of the electron-phonon coupling are neglected. Only Fig. 2.24 refers to the full Hamiltonian. On the basis of his results van den Brink interprets the features observed around 150 meV in the Raman data of $LaMnO_3$ [44] as orbiton-derived satellites in the phonon spectral function. These satellites are predicted to be observable also in other experiments that probe phonon
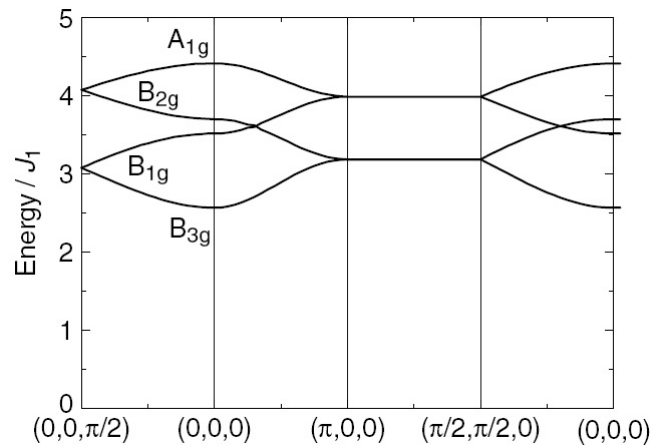
Figure 2.21: The dispersion relation of orbital waves calculated for $LaMnO_3$. The energy is given in units of the coupling constant J_1, which is estimated to be about 50 meV [44]. The figure is taken from [159].

51
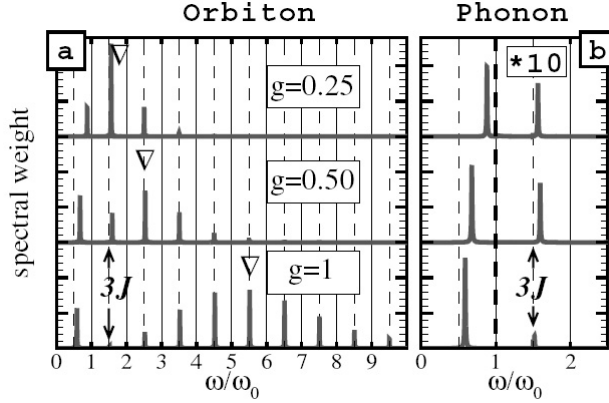
Figure 2.22: (a) Orbiton and (b) phonon spectral function in the localized limit (dispersion is neglected). The first pole due to the orbital exchange is indicated at $3J$ ($J = \omega_0/2$ and $\omega_0 = 80$ meV). In the orbital spectrum the static crystal-field energy $\bar{J}$ is indicated by ∇. The spectral weight in (b) is multiplied by 10 for $\omega > \omega_0$ [106].
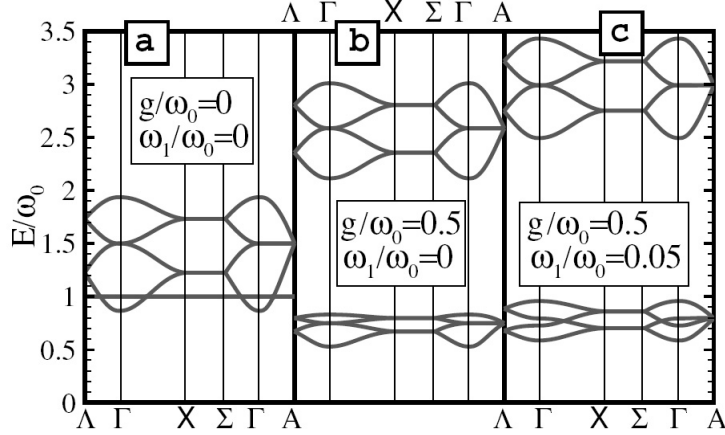
Figure 2.23: Orbiton and phonon dispersion, neglecting dynamical effects due to the electron-phonon coupling. (a) without electron-phonon coupling $g = 0$ and without bare phonon dispersion, (b) no bare phonon dispersion, and (c) $g/\omega_0 = 0.5$, finite bare phonon dispersion (ω_1 is the nearest-neighbor coupling between the phonons). The points of high symmetry in the Brillouin zone correspond to those of Ref. [44]. The figure is taken from [106].

dynamics, for instance neutron scattering. The resulting value of $g/\omega_0 = 0.35$ corresponds to rather weak electron-phonon coupling, in contrast to the result of Ref. [178]. For larger values of g, the orbiton dispersion becomes too small to explain the experimentally observed peaks in the Raman data at 150 meV in the sense of orbiton satellites of the phonon peaks around 80 meV [106, 4].

In [48] a theory of the collective orbital excitations in perovskite titanates and vanadates with triply degenerate t_{2g} orbitals is given. The dispersion relations of orbital waves for orbitally ordered LaVO$_3$, YVO$_3$ and YTiO$_3$ are examined in the effective spin-orbital coupled
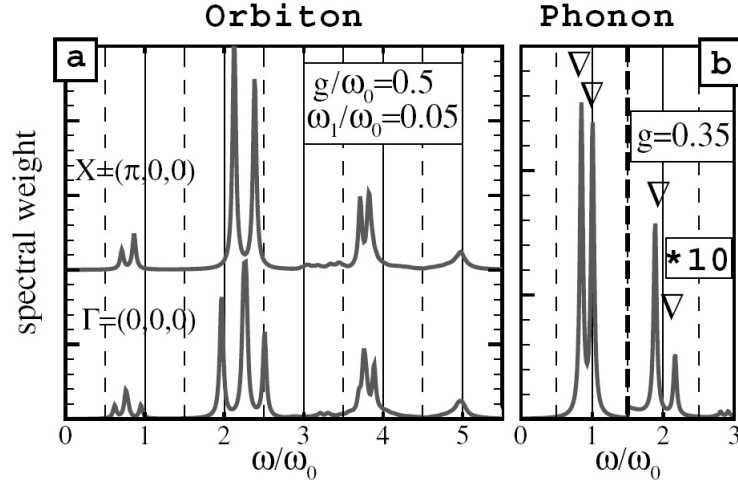
Figure 2.24: (a) Orbiton spectral function at the Γ and X point, $g = \omega_0/2$. (b) Spectrum of the Raman-active A_g and B_{1g} phonon modes for $\omega_1/\omega_0 = 0.05$ and $g/\omega_0 = 0.35$. The experimental peak positions [44] are indicated by ∇. For $\omega > \omega_0$ the spectral weight is multiplied by 10. The figure is taken from [106].

Hamiltonians. Ishihara [48] proposes possible scattering processes for Raman and inelastic neutron scattering from orbital waves and calculates the scattering spectra for titanates and vanadates. It is found that both the excitation spectra and the observation methods of orbital waves are qualitatively distinct from those for the orbitally ordered e_g systems.

Another approach was proposed by Khaliullin and Okamoto [46] for YTiO$_3$ in order to explain the isotropy of the spin-wave dispersion [155]. They found that frustration of
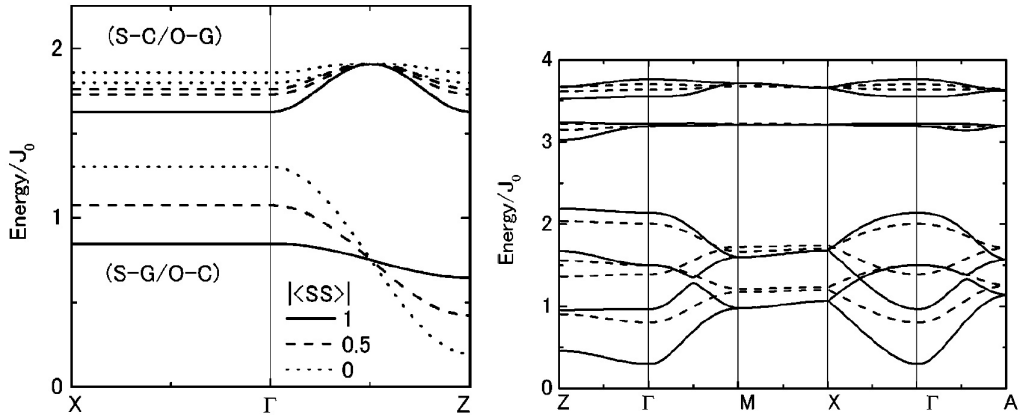
Figure 2.25: Dispersion of orbital excitations as calculated in [48]. Left: the dispersion in a $3d^2$ system for different ordering patterns and different spin-correlation functions. Right: the dispersion for a $3d^1$ system with the orbital ordering pattern of YTiO$_3$. The figure is taken from [48].
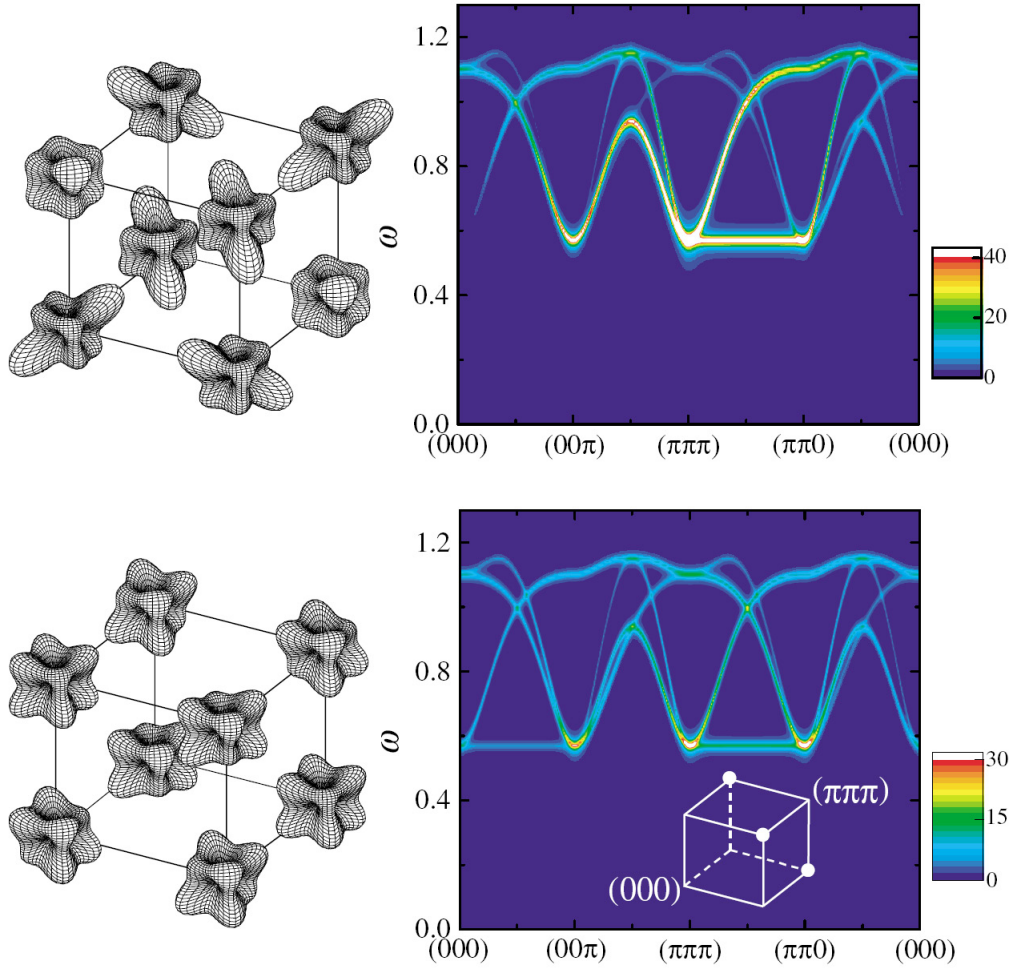
Figure 2.26: On the left the t_{2g} electron density is shown for two orbital order patterns. On the right the intensity of the corresponding orbital contribution to the structure factor $S(\vec{q}, \omega)$ is shown. The upper panels belong to a quadrupole ordered state, the lower panels belong to a magnetic state. The figure is taken from [46].

the interactions leads to an infinite degeneracy of classical states. By quantum effects four distinct orbital orderings are lowest in energy (see Fig. 2.26). They make specific predictions for neutron scattering experiments. From this it should be possible to detect the elementary orbital excitations in YTiO$_3$.

All the theoretical approaches for t_{2g} systems do not consider the coupling to the lattice. We think that although the coupling to the lattice, i.e. the Jahn-Teller effect, is weaker than in the e_g case it can not be neglegted. In summary we find

- In the case of dominant Jahn-Teller interactions the orbital excitations are local crystal-field excitations.

- For dominant superexchange interactions the orbital excitations are propagating waves with a significant dispersion.

2.3.2 Orbital excitations in optical spectroscopy

In the following paragraph we first consider the physics of a single ion embedded into a host lattice. The effects of interactions between the transition-metal ions will be addressed in the next section.

The case of a single ion

The dominant contribution to the optical conductivity $\sigma(\omega)$ arises from electric dipole transitions. The matrix element for a d-d transition induced by a photon is proportional to

$$\langle \psi_{final} | \mathbf{p} | \psi_{initial} \rangle \,.$$

The dipole operator $\mathbf{p}$ has odd parity. Considering a transition-metal site with inversion symmetry, the above matrix element vanishes due to the even parity of the $3d$ wave functions (see Appendix A) ψ_{final} and $\psi_{initial}$,

$$\langle \text{even} | \text{odd} | \text{even} \rangle = 0 \,.$$

Hence a mere d-d transition is forbidden within the dipole approximation in compounds with inversion symmetry on the transition-metal site, i.e. the d-d transitions do not contribute to $\sigma(\omega)$. However, there are several processes which allow the observation of d-d transitions, but one has to keep in mind that the corresponding features are only weak. In this thesis we will show examples for orbital excitations observed in $\sigma(\omega)$ which are due to (i) the absence of inversion symmetry on the transition-metal site (TiOX, see chapter 5) and (ii) a phonon-activated mechanism (RTiO$_3$, see chapter 4).

A very attractive way for the observation of orbital excitations opens up if the crystal structure does not show inversion symmetry on the transition-metal site, as e.g. in TiOCl (see chapter 5). In this case, parity is not a good quantum number, so that even and odd states mix. The amount of mixing can be estimated within the point-charge model. It depends on the difference in energy between the even ($3d$) and odd (e.g. $3p$ or $4p$) states and on how strong the deviations from inversion symmetry are. The small spectral weight of the orbital excitations is taken away from the dipole-allowed absorption band, e.g., from the $3d$-$4p$ transition. The major advantage of this structurally induced mechanism is that it allows to make clear predictions on the polarization dependence of the orbital absorption features because the (local) *symmetry* of the mixed states can be determined unambiguously within the point-charge model. We use the room-temperature structure of TiOCl as an example (see chapter 5). For this $3d^1$ compound we find that the lowest valence orbital predominantly shows $d_{y^2-z^2}$ character[9] with a small admixture of p_z character. The first excited state shows pure d_{xy} character, while the second excited state is mixed from d_{yz} and p_y states. Therefore,

---

[9]The ligands are located approximately along the diagonals of the yz plane, hence $d_{y^2-z^2}$ denotes a state from the t_{2g} subshell (see section 5.2).
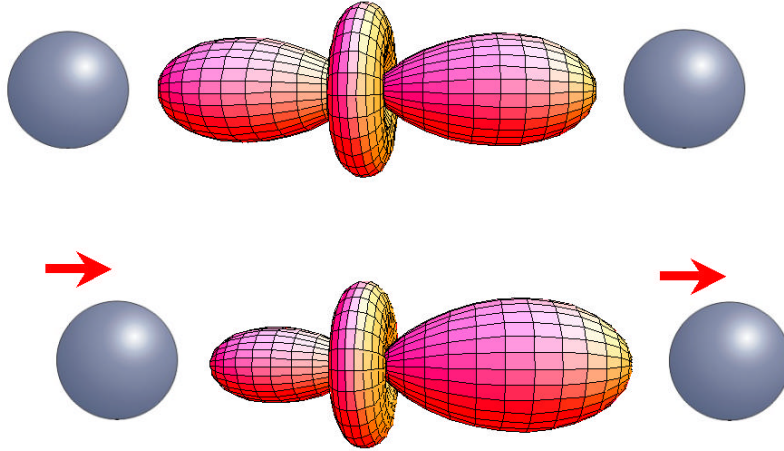
Figure 2.27: Top: Sketch of a $3z^2$-r^2 orbital on a transition-metal site in between two negatively charged ligands. Bottom: Exciting a bond-stretching phonon breaks the inversion symmetry on the transition-metal site, thus parity is not a good quantum number anymore. This gives rise to a mixing of even and odd states, e.g., of the $3d_{3z^2-r^2}$ state with the $4p_z$ state. The sketch indicates an increased electron density on the right side, where the distance to the negatively charged ligand has increased.

a dipole transition from the ground state to the second excited state is weakly allowed for light polarization parallel to the y axis, but not for x or z polarization:

$$\langle \alpha' d_{yz} + \beta' p_y | y | \alpha d_{y^2-z^2} + \beta p_z \rangle \neq 0 \,, \tag{2.1}$$

$$\langle \alpha' d_{yz} + \beta' p_y | x | \alpha d_{y^2-z^2} + \beta p_z \rangle = 0 \,. \tag{2.2}$$

Such polarization selection rules offer the possibility for a straightforward experimental test.

If the crystal structure shows inversion symmetry on the transition-metal site, this symmetry can be broken by an odd-symmetry phonon which is excited simultaneously with the orbital excitation [78, 88]. This again gives rise to the admixture of a small amount of odd character to the $3d$ wave function (see Fig. 2.27). The dependence on the polarization of the incident light is less pronounced for this phonon-activated mechanism than for the structurally-induced mechanism described above, because in general phonons of arbitrary polarization may contribute, i.e. x, y and z character can all be mixed into the $3d$ states. In order to determine the orbital excitation energy, the phonon energy has to be subtracted from the experimentally observed peak position. One has to keep in mind that different phonons may break the symmetry. Typically, stretching and bending modes of the metal-oxygen bonds are most effective in doing so [78]. These modes have typical energies of the order of 50-80 meV. The fact that phonons with different energies may contribute and that these phonons additionally have some dispersion increases the width of the absorption band

(the most important source for the line width is described by the Franck-Condon effect, see below).

Another way to break the symmetry is to add impurities to the system. However, it has been shown experimentally that this in general is by far less effective than the phonon-activated mechanism described above [78]. One way of testing whether a phonon is involved in the infrared absorption process is to compare the energies of the orbital excitations observed in $\sigma(\omega)$ and in Raman scattering (see e.g. the data on $RTiO_3$ in chapter 4). In compounds with inversion symmetry, the exclusion principle states that selection rules for Raman scattering and infrared absorption are mutually exclusive. Orbital excitations can be observed directly in Raman scattering because *two* photons are involved in the scattering process, thus the odd dipole operator has to be applied twice. The incoming photon excites an electron from a $3d$ orbital to, e.g., a $4p$ state, from which it falls back to an excited $3d$ state under emission of a photon. Using again the example of a $3d^1$ system, the transition from, e.g., d_{xy} to d_{xz} is Raman active in crossed polarization, for instance for y (z) polarization of the incoming (outgoing) photon:

$$\langle d_{xz}|z|p_x\rangle\langle p_x|y|d_{xy}\rangle \neq 0\,.$$

Other optical experiments which allow the observation of orbital excitations are, e.g., electroreflectance measurements [90] or third-harmonic spectroscopy [91]. Furthermore, *d-d* excitations have been studied by means of electron energy loss spectroscopy (EELS) [92].

Thus far we have neglected the spin selection rule. One has to keep in mind that optical spectroscopy with linearly polarized light is only sensitive to spin-conserving excitations, $\Delta S=0$. This selection rule can be relaxed by taking into account spin-orbit coupling. Another possibility is to excite two spin-carrying modes simultaneously in such a way that the total spin amounts to zero. An orbital excitation from e.g. a triplet state to a singlet may gain a finite spectral weight by the simultaneous excitation of a magnon, giving rise to a so-called magnon-exciton sideband [82, 93, 94]. The spectral weight of these processes is even smaller than in the cases discussed above where the spin was not involved. Nevertheless these processes are dominant in systems with d^5 ions such as Mn^{2+} [82, 94], in which none of the excited states carries the same spin value as the ^6S ground state. In MnF_2, both magnetic-dipole and electric-dipole transitions have been observed [82]. The magnetic-dipole character can be proven experimentally by the observation of a splitting in an applied magnetic field or by a detailed study of the polarization dependence, i.e. by showing that the absorption features depend on the direction of the magnetic field component and not on the electric field component.

For the discussion of the line shape, one has to take the coupling to the lattice into account. The absorption band will be broadened by phonon sidebands according to the Franck-Condon principle, and the line shape depends on the difference of the relaxed bond lengths of the orbital states involved (for details see the caption of figure 2.28). We emphasize that this reflects the mixed, "vibronic" character of the eigenmodes (phonon + orbiton, or vibrational + electronic → "vibronic" [78]) and thus holds irrespective of the mechanism responsible for the finite spectral weight of an orbital excitation. In particular, these phonon sidebands may not be confused with the phonon-activated mechanism described above and appear also in the case of, e.g., the structurally induced mechanism relevant for TiOCl or in Raman data.
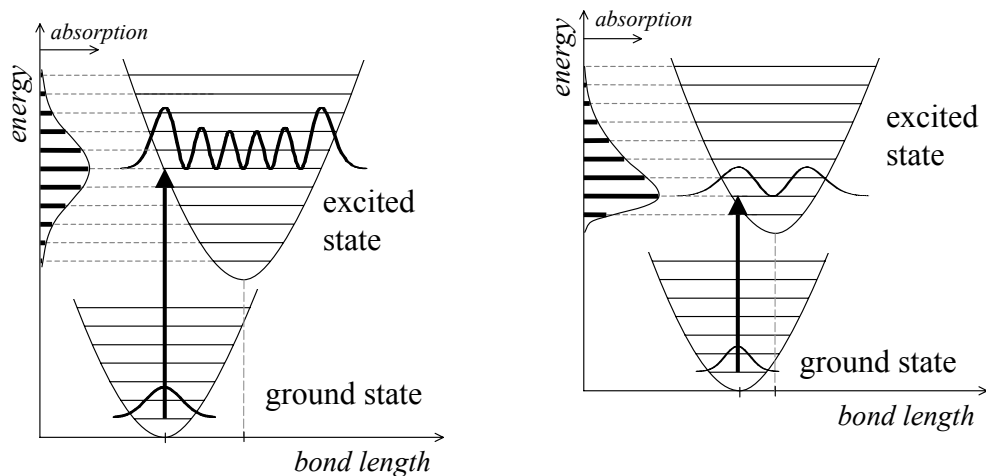
Figure 2.28: Sketch of the Franck-Condon principle. In both panels, each parabola corresponds to a different orbital state and represents the harmonic potential of the lattice. The lines within a parabola denote phonon excitations. The horizontal position of a parabola indicates the distance to the ligands after the lattice has been allowed to relax in the particular orbital state. Promoting e.g. an electron in an octahedral oxygen cage from x^2-y^2 to $3z^2$ tends to push away the two negatively charged oxygen ligands on the z axis. In general, electronic time scales are much faster than the relaxation time of the lattice. A fast electronic excitation, i.e. without relaxation of the lattice, corresponds to a vertical transition (arrow). The transition probability is proportional to the overlap between the wave functions of the ground state and of the excited state. The thick lines denote the amplitudes of the ground-state wave function and of an excited harmonic oscillator. The strongest overlap is obtained for the level which is closest to where the vertical arrow cuts through a parabola. In the final state, both the lattice and the electronic/orbital subsystem are in an excited state, i.e. the excited states are of mixed character (vibrational + electronic → "vibronic"). Summing up the contributions from the different excited states results in the broad absorption peak shown on the left in each panel. Due to the dispersion of the phonons and due to the contribution of phonons with different energies, the sharp subbands of individual excited states are usually not resolved in a solid, yielding a single broad band. The width and the line shape of an absorption band in $\sigma(\omega)$ depend on the difference in bond length of the different orbital states. Large differences in the bond length give rise to symmetric absorption bands (left panel), whereas small differences cause a characteristic asymmetric line shape (right panel).

Interaction effects

We have to address the question how to distinguish experimentally between a collective orbital excitation and a predominantly "local" crystal-field excitation. A direct observation of the dispersion of the orbital-momentum fluctuations by means of inelastic neutron scattering would manifest a watertight proof. While neutron scattering has been used for the study of

crystal-field excitations of f-electron compounds [95], we are not aware of such data for the case of $3d$ electrons. Here, one has to keep in mind that the coupling to the lattice will smear out the orbital excitations significantly. Inelastic x-ray scattering offers another k-dependent tool, but no collective orbital excitations were found in the study of LaMnO$_3$, KCuF$_3$ and YTiO$_3$ presented in [96].

Under the assumption that the dominant energy scale is set by the exchange interactions, the dispersion relations of orbitons have been calculated for the orbitally ordered states of LaMnO$_3$, LaVO$_3$, YVO$_3$, and YTiO$_3$ [44, 45, 48], and within a model focusing on the orbital fluctuations [46, 47] (see section 2.3.1). Predictions have been derived for inelastic neutron scattering and Raman scattering. In the case of a single ion we have discussed a Raman process in which the virtual excitation into a p state was assumed to take place on a single site. In case of dominant exchange interactions, a two-site process involving the upper Hubbard band is considered [48], in analogy to the well-known two-magnon Raman scattering. For simplicity, we consider per site one electron and two orbitals. In the first step, the incident photon promotes an electron from site 1 to site 2, which becomes doubly occupied. In the second step, an electron hops back from site 2 to 1 under emission of a photon. In the final state, one or *both* electrons may be in an excited orbital, i.e. the exchange process may give rise to one-orbiton and/or two-orbiton excitations [48] as seen from Fig. 2.29. Depending on the hopping amplitudes between the different orbitals on adjacent sites, distinct polarization selection rules have been predicted [44, 48]. The excitation of *two* orbitons with momenta $k_1 = -k_2$ in principle allows to probe the orbiton dispersion throughout the entire Brillouin zone, since only the total momentum $k_1 + k_2$ needs to be equal to zero in Raman scattering. Information about the dispersion is contained in the line shape of the two-orbiton Raman band, but a detailed analysis of the line shape encounters several problems: (i) in general, the Raman line shape depends on the frequency of the incident photons (resonance behaviour), (ii) the orbiton-orbiton interactions are essential for the line shape, but have not been taken into account thus far, (iii) the coupling to the lattice reduces the orbiton dispersion.

The optical conductivity thus far has not been considered as a tool for the investigation of orbitons. Starting again from the crystal-field limit, we note that the optical data of a crystal-field Frenkel exciton with a dispersion much smaller than its energy is in principle very similar to the data of a single impurity ion embedded in a host lattice. In particular, optical spectroscopy is restricted to the observation of excitations with momentum $k=0$, and the selection rules are the same as for the case of a single impurity ion. Nevertheless the dispersion may play a role if two modes are excited simultaneously, as e.g. in a magnon-exciton sideband [82] or in the phonon-activated case. Only the total momentum needs to be equal to zero, and one has to sum up contributions from excitons from the entire Brillouin zone.

As far as the intersite exchange processes discussed above for the Raman case are concerned, Khaliullin [98] has pointed out the possibility of two-orbiton-plus-phonon absorption, similar to the two-magnon-plus-phonon absorption proposed by Lorenzana and Sawatzky [99, 100] for spin systems. In systems with inversion symmetry *in between* adjacent sites, the exchange of two electrons does not give rise to a dipole moment. Similar to the phonon-activated mechanism for the observation of crystal-field transitions described above, this selection rule can be relaxed by the simultaneous excitation of a phonon [99, 100]. The two-
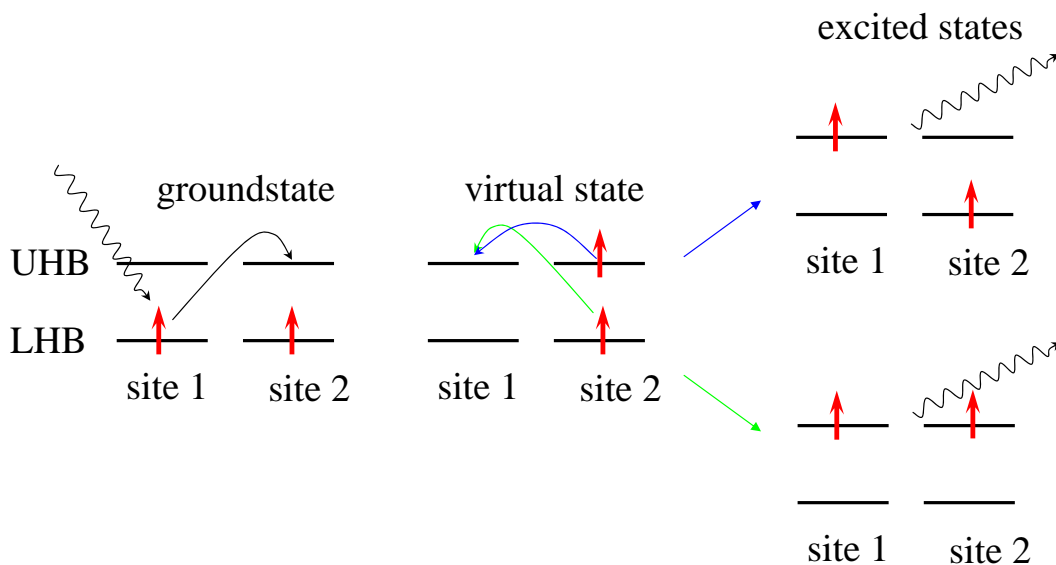
Figure 2.29: A Raman process involving two sites is illustrated. On the left the ground state is shown. By the interaction with a photon one electron is excited into a virtual state in the upper Hubbard band. This state is about the energy for a double occupancy U above the ground state. This virtual state is illustrated shown in the middle by hopping of the electron in a vacant orbital on the neighboring site. This virtual intermediate state may decay into an orbitally excited state on one site (blue arrow) or on two sites (green arrow) under re-emission of a photon. The energy of the photon is shifted by one or two times the orbital excitation energy.

"magnon"-plus-phonon absorption[10] has been established as an interesting tool for studies of antiferromagnetic spin chains, spin ladders, and layered antiferromagnets [27, 101, 102, 89, 103, 104, 105]. Since the phonon contributes to momentum conservation, the optical conductivity probes the two-magnon or two-orbiton spectral function throughout the entire Brillouin zone, in contrast to two-orbiton Raman scattering, which reflects only the $k=0$ part of the two-orbiton spectrum. Thus, both the line shape and the peak position are expected to be different in $\sigma(\omega)$ as compared to Raman data. Here it is also worth to mention that a two-orbiton process may contribute directly to $\sigma(\omega)$ in the absence of inversion symmetry between adjacent sites. This possibility is presently investigated in YVO_3 [97].

In spin systems, the excitation of a single magnon does not contribute to $\sigma(\omega)$ due to the spin selection rule. In the case of orbitons, however, the phonon-activated single-site mechanism used for the study of crystal-field excitations will also be at work if the exchange interactions are dominant. Thus one has to expect a superposition of orbiton-plus-phonon and two-orbiton-plus-phonon or direct two-orbiton contributions.

---

[10]Here, we have used the term "magnon" to denote spinons in spin chains, triplons in spin ladders and magnons in a long-range ordered antiferromagnet.

Thus far we have discussed the two limiting cases, crystal-field excitations for dominant coupling to the lattice and collective orbital waves for dominant exchange interactions. Detailed theoretical predictions for the contribution of orbital waves to the optical conductivity would certainly be very helpful in order to distinguish experimentally between a predominantly local excitation and a collective mode. However, a quantitative description of experimental data will require to treat both the exchange interactions and the coupling to the lattice on an equal footing [106].

Chapter 3

The quest for orbital excitations in LaMnO$_3$

For about one decade manganites attract great interest due to the discovery of the colossal magneto-resistance (CMR) effect [3].[1] The CMR effect has been discovered in La$_{1-x}$Sr$_x$MnO$_3$. This system is metallic due to hole doping by the substitution of La^{3+} by Sr^{2+} ions. In contrast to this the undoped compound LaMnO$_3$ is a good correlated insulator with a band gap of approximately 1.5 eV. It belongs to the class of pseudo-cubic perovskites with the orthorhombic crystal structure *Pbnm*. This compound has been brought to the focus of interest when Saitoh *et al.* [44] claimed that they had observed an orbital wave for the first time in Raman data of LaMnO$_3$.

---

[1]Colossal magneto-resistance effect means that the resistance changes by several orders of magnitude upon applying a small magnetic field to the sample.
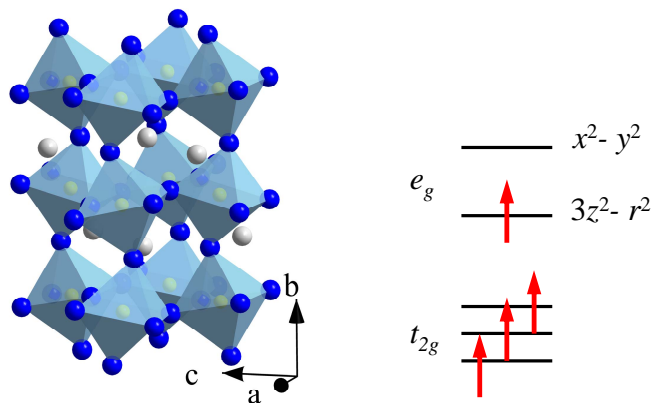

Figure 3.1: On the left the crystal structure of LaMnO$_3$ is depicted. It consists of corner sharing MnO$_6$ octahedra. On the right side the electronic configuration of the Mn^{3+} ions is shown. The orbital degree of freedom in a cubic crystal rises from the electron in the degenerate e_g orbitals. This degeneracy is lifted by deviations from cubic symmetry.
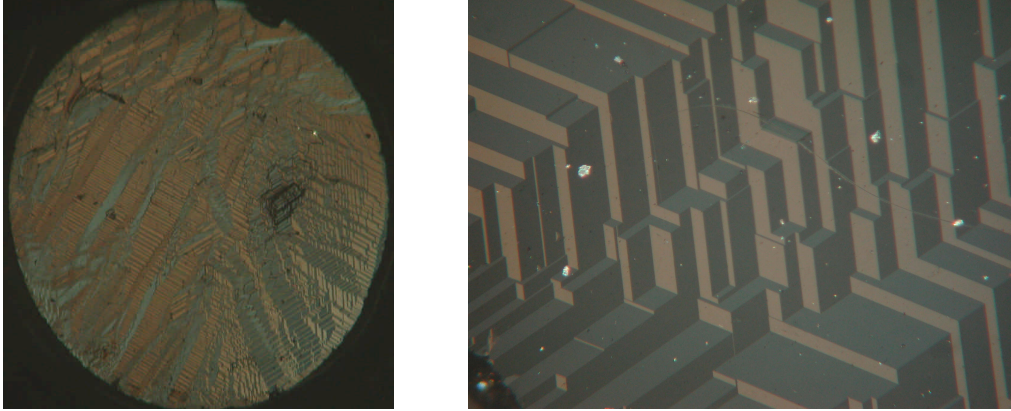
Figure 3.2: Left: typical domain structure on the surface of LaMnO$_3$. The sample diameter is about 4 mm. Right: zoomed-in picture of the same surface. Three orientations can be distinguished by color.

The crystal structure is shown in Fig. 3.1. The Mn^{3+} ions are at the center of O^{2-} octahedra. The orthorhombic distortion of *Pbnm* is derived from the cubic lattice by tilting the octahedra around the crystallographic b axis and afterwards rotating them around the c axis. The octahedra themselves exhibit a Jahn-Teller type distortion which is expressed by a Mn-O bond length variation of 12% within one octahedron [163]. The lattice constants along the crystallographic axes $a \sim b \sim c/\sqrt{2}$ (the factor of $1/\sqrt{2}$ comes from the orthorhombic unit cell) are rather similar. This similarity is responsible for a strong twinning of the single crystals investigated here which makes it impossible to measure any polarization dependence.[2] A slice of a single crystal which we investigated is shown in Fig. 3.2 a. The crystals were grown by P. Reutler[3]. The photo of this sample of about 4 mm in diameter was taken on a polished surface under a polarization microscope.[4] The domains are of the order of 10 μm which is much smaller than the extension of the sample and as well smaller than the illuminated zone. A zoomed-in picture of a domain structure is given in Fig. 3.2b. It shows the typical pattern of the arrangement of the domains.

The electronic configuration of Mn^{3+} ions is $3d^4$ (see Fig. 3.1). In the ground state the four electrons form a spin quintet $S = 2$ (high spin). For a perfectly cubic environment the $t_{2g}^3 e_g^1$ configuration of Mn^{3+} ions is doubly degenerate within the e_g orbitals (see Fig. 3.1). However, the local distortion gives rise to an additional non-cubic crystal field at the Mn sites that lifts the degeneracy. Long-range orbital order occurs at 780 K [161, 162, 164].

---

[2]Note, however, that untwinned single crystals can be obtained by applying uniaxial pressure. The polarization dependence of $\sigma(\omega)$ has been studied on untwinned samples by Tobe *et al.* [175]. The untwinned crystals exhibit a polarization dependence. From this it is not clear whether these crystals are completely untwinned or if one orientation contributes only stronger than the others.

[3]P. Reutler, L. Pinsard-Gaudart, B. Büchner, and A. Revcolevschi [168]

[4]In a polarization microscope the polarized light from a bright source is reflected by the sample and then passes a second polarizer which is perpendicular to the first. So all of the observed light has changed the polarization upon reflection. The angle about which the polarization plane of the light has been rotated depends on the orientation of the domain. This gives the difference in brightness of different domains.
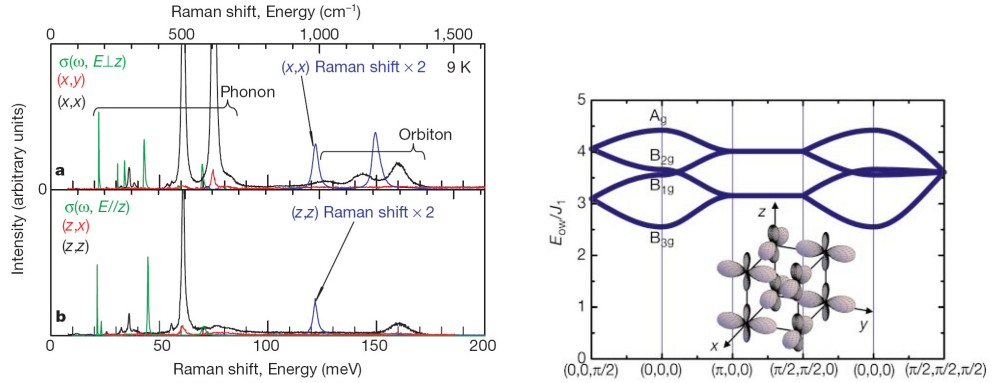
Figure 3.3: Left: Raman data of LaMnO$_3$ for different polarizations [44]. Right: Theoretical results for the dispersion relation of orbital waves in LaMnO$_3$ (C-type orbital order with A-type antiferromagnetic structure). A schematic picture of the orbitally ordered state in LaMnO$_3$ is shown in the inset.

The spins order antiferromagnetically at 140 K, far below the occurrence of orbital order. In order to explain the existence of orbital order at temperatures far above the spin ordering temperature, it is necessary to invoke the Jahn-Teller effect [38]. The orbital ordering pattern is an alternating occupation of the $|3x^2 - r^2\rangle$ and $|3y^2 - r^2\rangle$ orbital in the ab plane, whereas adjacent planes are ferro-orbitally ordered, as shown in Fig. 2.14. As discussed there, this experimentally observed orbital ordering pattern can not be explained within a harmonic approximation. But it has been proposed that it can be explained by taking into account anharmonicity [4]. However, it is discussed controversially whether the orbital order is induced predominantly by the Jahn-Teller effect or by the superexchange interaction of the orbitals [31, 44, 178, 179, 171, 106]. The interaction leading to orbital order is crucial for the kind and character of orbital excitations. Dominating electron-phonon coupling would lead to a local crystal-field splitting and the excitations would be on-site excitations between crystal-field levels. These excitations have negligible dispersion. On the other hand the dominance of the superexchange would lead to orbital excitations with a significant dispersion.

3.1 Orbitons versus multi phonons

Raman scattering data reported for orbitally ordered LaMnO$_3$ have been interpreted as the first experimental evidence for the existence of orbitons [44]. This claim is based on the observation of three Raman lines at 126, 144 and 160 meV (see Fig. 3.3), on their temperature dependence and on the analysis of the polarization dependence, all in comparison with the results of a model calculation. Since Raman spectroscopy is restricted to $k=0$ excitations, it is not possible to follow the dispersion of the elementary excitations. However, in the case of LaMnO$_3$ one expects from the model different excitation branches with different symmetries at the Γ point, and these were identified with the three Raman lines [44] (see Fig. 3.3). In Fig. 3.4 the temperature dependence of the Raman data are compared to Raman
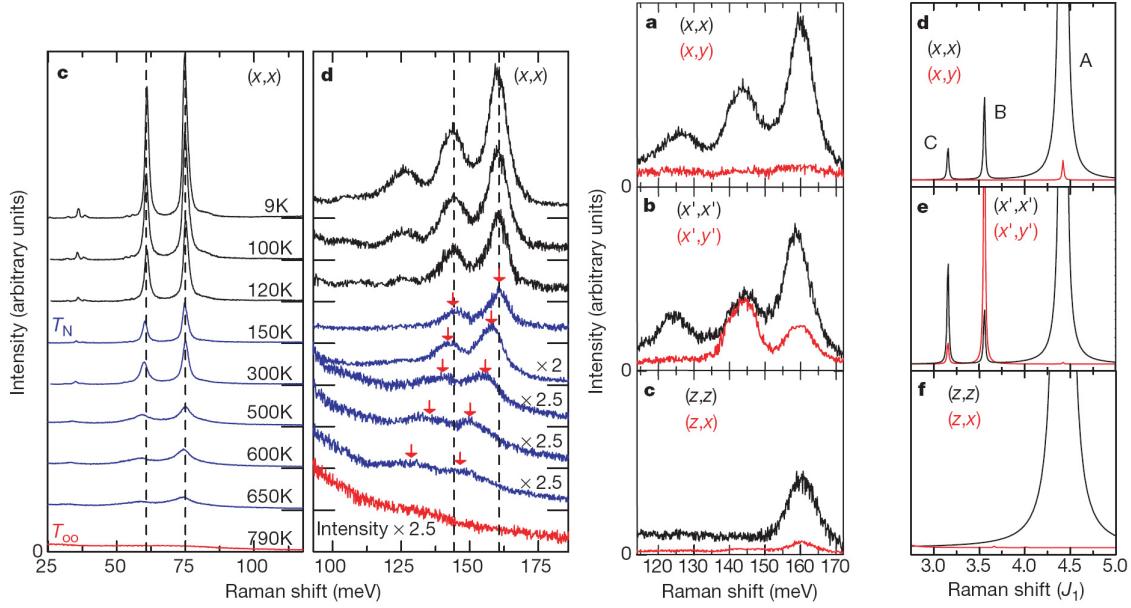
Figure 3.4: Left panels: temperature variation of Raman scattering spectra in the (x,x) configuration for LaMnO$_3$ [44]. (c) prediction by theory and (d) Raman results. Right panels: comparison of Raman data for different polarizations at low temperature (left) with the theory (right). The energy scale J_1 has been estimated to be about 50 meV [44].

intensities calculated for the orbiton excitations at different temperatures. Moreover, the polarization dependence observed experimentally is analyzed in comparison with the results of a model calculation for the corresponding Raman intensities (see Fig. 3.4). The overall agreement between theory and experiment is pretty good. The main discrepancy is that the predicted peak energies are too high ($4.5J_1 \approx 225$ meV), even though a very small Jahn-Teller contribution of only 28 meV has been assumed. In the following we will challenge the orbiton interpretation on the basis of a comparison with the optical conductivity spectrum [75] (see also [169]).

In LaMnO$_3$, the direct observation of orbital excitations is allowed in Raman spectroscopy, but a contribution to $\sigma(\omega)$ requires to break the parity selection rule, e.g., via the simultaneous excitation of a phonon. Therefore, the orbital excitations are expected to be shifted in $\sigma(\omega)$ with respect to the Raman lines by the phonon energy of roughly 50-80 meV (see chapter 2 and reference [167]), in agreement with the results for RTiO$_3$ discussed in the chapter 4.2.

We have determined $\sigma(\omega)$ very accurately in the relevant frequency range (see Fig. 3.7) by measuring both the transmittance of thin twinned single crystalline platelets and the reflectance of a sample with $d \approx 1$ mm (see Figs. 3.6 and 3.5). The small spectral weight of the various features observed in Fig. 3.7 at energies above about 80 meV, i.e., above the range of fundamental phonon absorption, is typical for multi-phonon spectra in insulating transition-metal oxides. For comparison, see, e.g., the spectra of $\sigma(\omega)$ of RTiO$_3$ in the present work or of Y$_2$BaNiO$_5$ and CaCu$_2$O$_3$ in [40] and LaCoO$_3$ in [75]. The uncertainty in $\sigma(\omega)$ is
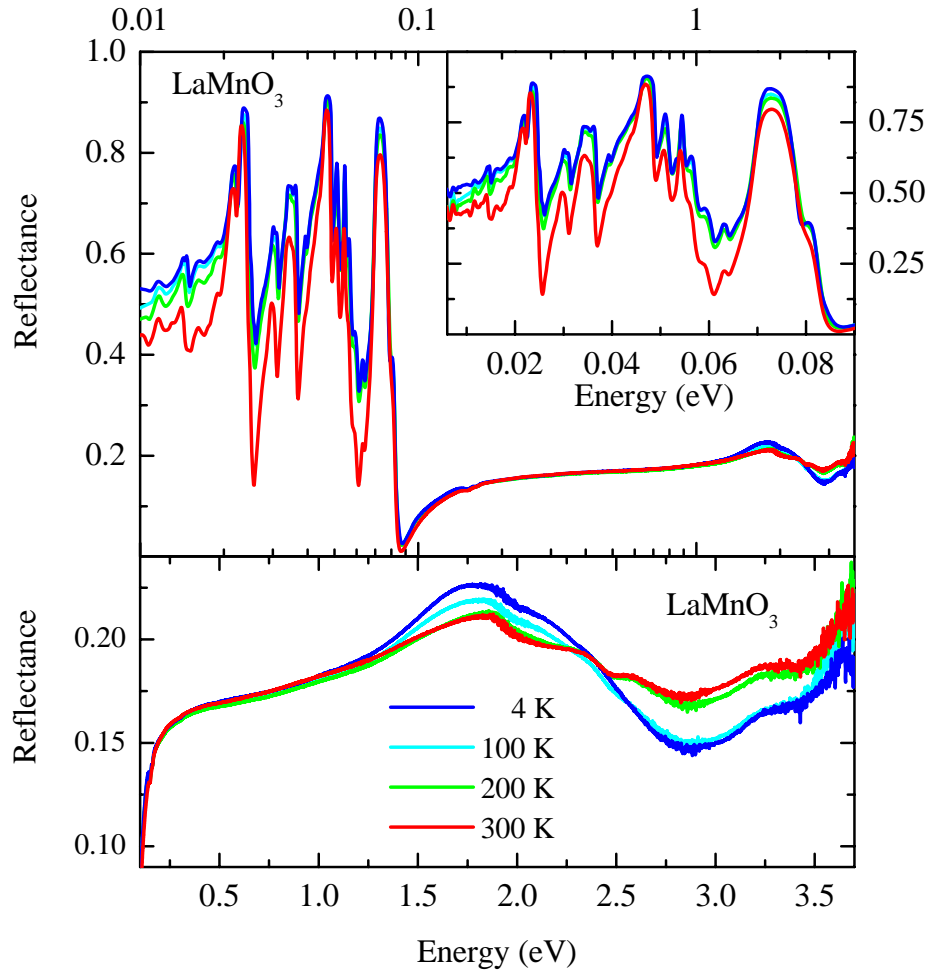
Figure 3.5: The reflectance of LaMnO$_3$ is depicted for different temperatures is depicted. The upper panel shows the measured range from the far-infrared to ultraviolet on a logarithmic scale. In the inset the phonon spectrum is shown on a linear scale. In the bottom panel the range above phonon absorptions is displayed on a linear scale.

depicted in Fig. 3.8.

In $\sigma(\omega)$ we find absorption features at about 118, 130, 146 and 160 meV which are very similar to the three Raman lines mentioned above. Moreover, we identify some weak features at about 240 and 320 meV. At the latter two energies, very similar features have been observed in Raman scattering [5] on the same samples by Choi and collaborators [168] (see Fig. 3.7), using a surface that had been polished for the transmittance measurement. The highest infrared-active fundamental phonon mode is observed in the reflectance data at about 80 meV

[5]The Raman measurements have been performed by K.-Y. Choi, P. Lemmens and G. Güntherodt at the RWTH Aachen, Germany [168]. The Raman data have been obtained in a quasi-backscattering geometry using a laser energy of 2.34 eV (Ar$^+$ laser).
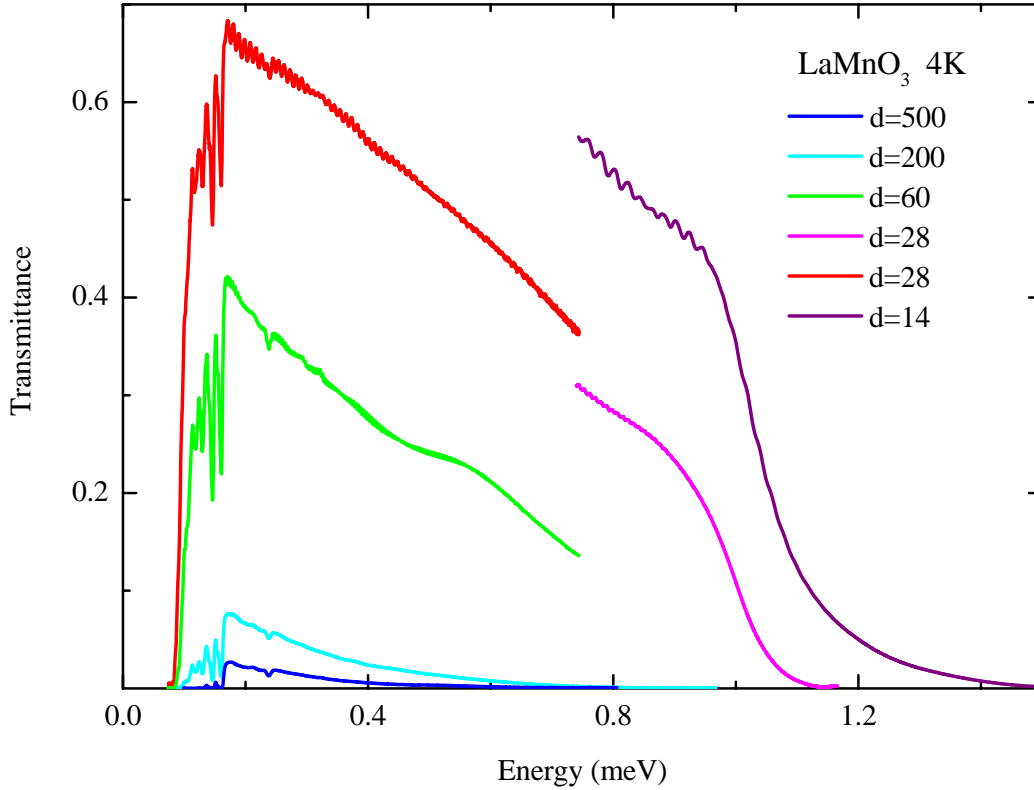
Figure 3.6: The transmittance of several samples of varying thickness is compared. All data sets were obtained at 4 K.

(see Fig. 3.5 and references [169, 170]). It has been interpreted as a zone-boundary Mn-O bond-stretching mode which is folded back to $k=0$ in the orbitally ordered state [169]. A weak Raman line has been found at the same frequency [77, 168]. Given the existence of a fundamental mode at 80 meV, the features at 160, 240 and 320 meV are naturally explained as two-, three- and four-phonon modes, respectively. In particular, the Raman line at 160 meV is certainly not too high in energy for a two-phonon mode. At 160 meV, similar two-phonon features are observed also in other pseudocubic perovskites such as $LaCoO_3$ [75] or $YTiO_3$ (see Figs. 4.6 and 4.9). Three-phonon Raman scattering in $LaMnO_3$ at room temperature and above has been reported recently in the range from 210-250 meV [77] (see Fig. 3.9). Multi-phonon Raman scattering is predicted to be strong in orbitally ordered $LaMnO_3$ due to the Franck-Condon effect [171] (see Fig. 3.10). Raman data of the two-phonon range observed for varying laser energies are reported in [76] (see Fig. 3.9). It has been found that the dependence of the peak intensity around 150 meV on the laser energy is very similar to that observed for the fundamental Mn-O phonon mode. This corroborates the interpretation of the peaks at 150 meV as two-phonon absorptions.

Let us briefly address the issue of selection rules and the problems for a theoretical description of multi-phonon features. The symmetry of a multi-phonon mode has to be derived
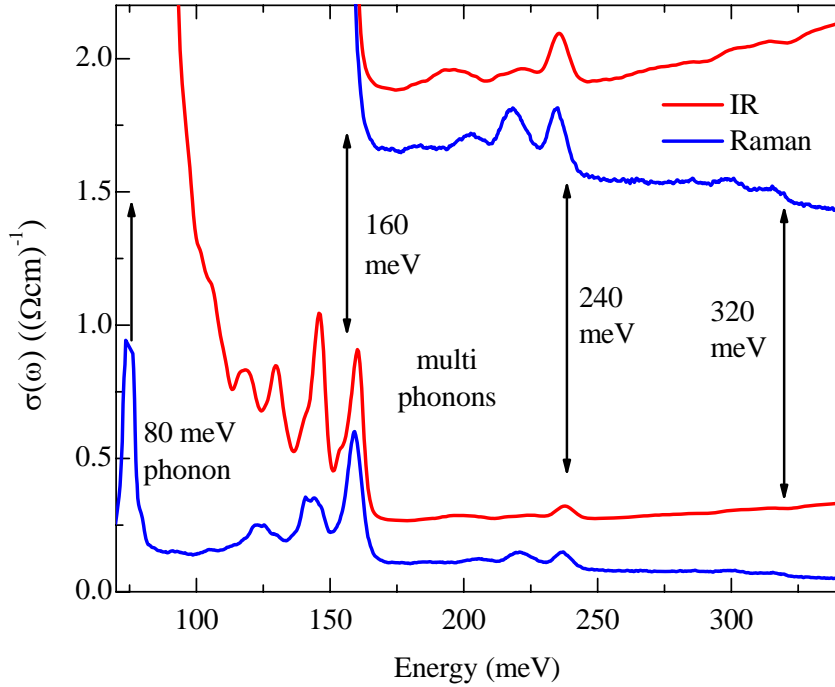
Figure 3.7: Optical conductivity $\sigma(\omega)$ (T=4 K) of LaMnO$_3$ [40, 75] showing multi-phonon features at, e.g., two, three and four times 80 meV. For comparison, we plot the Raman-scattering data (T=15 K) by Choi *et al.* from [168]. The two top curves focusing on the high-energy features show the same data multiplied by a factor of 6 and 10, respectively.

using the multiplication rules of the irreducible representations of the contributing fundamental modes. Thus an overtone of a forbidden fundamental mode may very well be allowed. Peaks within the two- or multi-phonon continua reflect a high density of states and do not necessarily correspond to simple multiples of k=0 phonon modes. A precise theoretical treatment of the two- and multi-phonon continua requires a detailed knowledge of the dispersion of the fundamental modes throughout the entire Brillouin zone. Unfortunately, such a detailed analysis of neutron scattering data has failed so far due to the twinning of the samples [172]. Moreover, multi-phonon features may depend strongly on the sample quality and on details of the sample growth [173], which strongly complicates a meaningful comparison with theory. The bottom panel of Fig. 3.11 shows the k=0 part of the two-phonon density of states calculated for LaMnO$_3$ in *Pbnm* symmetry.[6] The calculation is based on a shell model [174], the parameters have been deduced from similar perovskite compounds where the lattice dynamics was studied in detail. The highest two-phonon peak is predicted slightly below 160 meV, the overall structure is in reasonable agreement with the optical data.

Within the orbiton interpretation, an explanation of features at the same energy (e.g., 160

---

[6]The calculations of the two-phonon density of states have been performed by W. Reichardt (FZ Karlsruhe, Germany).
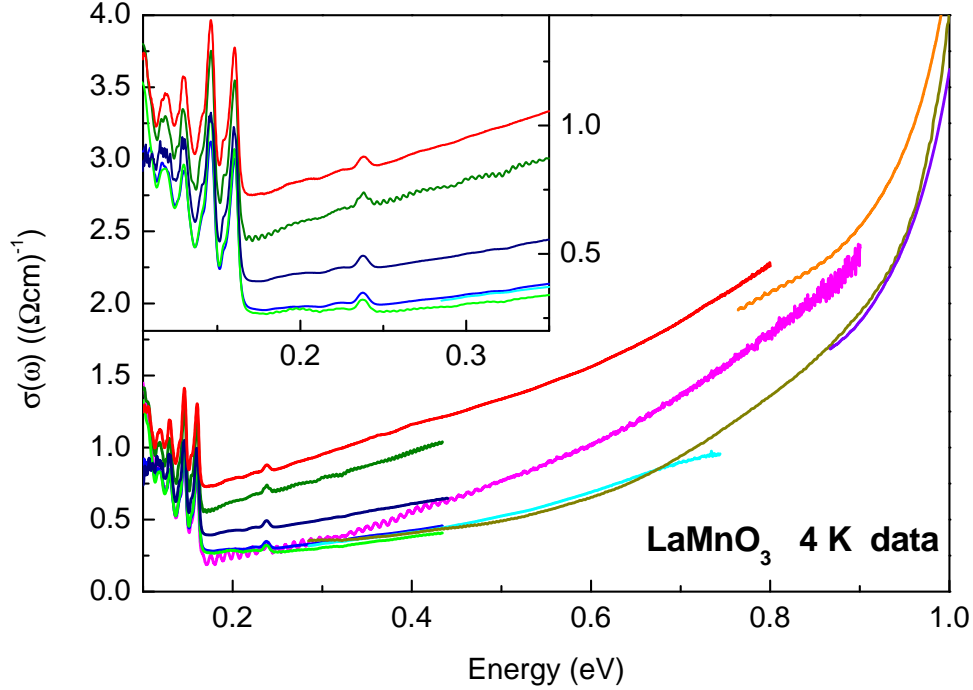
Figure 3.8: The optical conductivity of several samples at 4 K is compared. This indicates the error of the obtained data for the optical conductivity (note the rather small values of the optical conductivity). Features like the peaks at 0.16 and 0.24 eV are present in all data sets as seen from the inset. Thus they have to be attributed to intrinsic properties of $LaMnO_3$. The difference in the absolute value can be attributed to slight changes of the impurity concentration (oxygen non-stoichiometry) or to errors due to scattering on the sample surface.

meV) in Raman and infrared spectroscopy requires to break the parity-selection rule without the simultaneous excitation of a phonon. This can in principle be achieved by impurities, but the phonon mechanism lined out above turns out to be much more effective [78]. Roughly speaking, a small impurity concentration of, e.g., 1% breaks the selection rule only at a small percentage of sites, whereas the phonon is effective throughout the entire sample. This is corroborated by the shift between the Raman and the infrared data observed in $RTiO_3$ (see chapter 4 and in particular Fig. 4.9). Moreover, the remaining differences between the Raman and the infrared spectra – e.g., the peak energies of 126 and 144 meV as compared to 118, 130 and 146 meV – can easily be attributed in the multi-phonon case to the different selection rules, giving different weight to the two-phonon density of states. However, the orbiton scenario including impurities to account for the parity selection rule predicts *identical* peak energies in both spectroscopies.
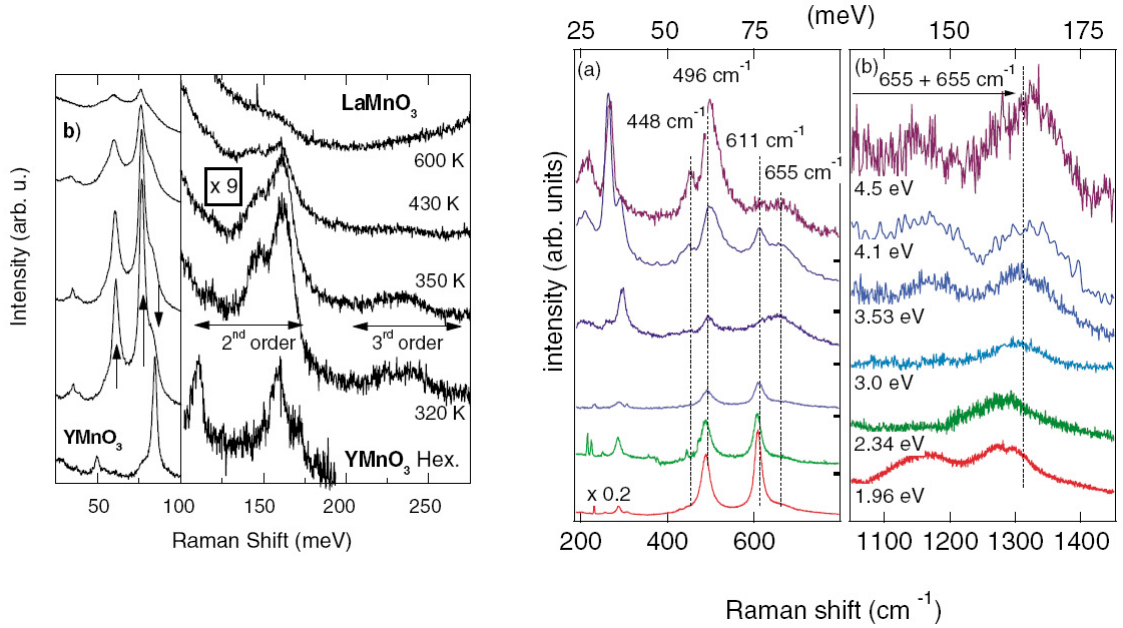
Figure 3.9: Raman spectra of $LaMnO_3$ vs. temperature and of the hexagonal compound $YMnO_3$ at room temperature [77]. Above 100 meV the intensities are enlarged by a factor 9. Two- and three-phonon excitations are observed up to 160 meV and 240 meV, respectively.

One argument favoring the orbiton interpretation was the disappearance of the relevant Raman lines upon heating above the orbital ordering temperature T_{OO}=780 K [44] (see Fig. 3.4). We have measured the transmittance of $LaMnO_3$ at temperatures up to 775 K (see figure 3.11), the highest temperature available in our experimental setup. The room-temperature spectra before and after heating to 775 K are identical, showing that the oxygen content of the sample did not change significantly upon heating. The absorption bands in the range of 120-160 meV broaden strongly with increasing temperature, but they clearly persist also at 775 K, i.e., close to T_{OO}. The sensitivity of the Raman lines [44, 168] indicates that these multi-phonon lines are Raman forbidden in the high-temperature structure and become Raman allowed due to the symmetry change across the phase transition.

The eigenmodes show a mixed character (phonon-orbiton) if the coupling to the lattice (Jahn-Teller effect) and the orbital exchange interactions are taken into account on an equal footing [106] (see chapter 2.3.1). In reference [168], the coupling between phonons and orbitons is discussed on the basis of the changes observed in the (multi-)phonon Raman spectra upon variation of temperature, symmetry or doping level. An interpretation of the Raman features at about 160 meV in terms of phonon-orbiton mixed modes with predominantly orbiton character requires a rather small value for the electron-lattice coupling [106]. However, if the Jahn-Teller splitting is large ($\gtrsim 1$ eV), the spectrum recovers the shape predicted by the Franck-Condon effect (see figure 2.28) [106]. Note that increasing the coupling to the lattice results not only in a blue shift of the average excitation energy but also in a suppression of
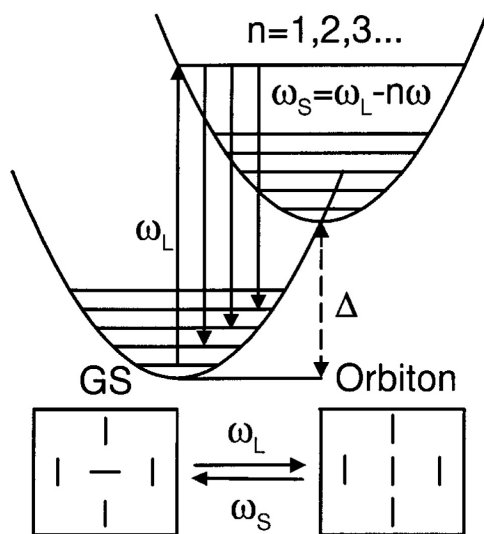
Figure 3.10: Schematic Franck-Condon mechanism for the multiphonon Raman process via the "orbiton" intermediate state (see Fig. 2.28). Left: phonon energy levels of the ground state (GS) (antiferro-orbital order indicated by the box at the bottom left). Right: phonon energy levels of the state with one orbiton excited (Orbiton) (the neighbors become ferro-orbital aligned by the flip of the orbital on the center site). The lowest energy configuration of the orbiton has energy Δ and large oxygen distortions from the Jahn-Teller ground state. The laser energy is denoted by ω_L. A large probability of transitions to multiphonon states ($\omega_S = \omega_L - n\omega$, where ω is the phonon energy) is predicted. This figure has been taken from [171].

the orbital band width.

We have tried very carefully to find the orbital excitations at higher energies by investigating the transmittance of several different samples of $LaMnO_3$, varying the thickness between 2 and 500 μm. Transmittance measurements on a thick sample are sensitive to very weak absorption features, whereas thin samples are better suited for the determination of larger values of $\sigma(\omega)$. Our data do not show any absorption band between the multi-phonon range and the onset of excitations across the Mott gap at about 1 eV [175, 176] (see Fig. 3.12).

3.2   Observation of orbital excitation

The fact that no orbital excitation has been observed so far is frustrating since only via the observation of its energy it will be possible to determine the electron-phonon coupling in this system. There has been a prediction by Allen and Perebeinos [178] of a strong orbital absorption band in $\sigma(\omega)$ centered around 2 eV with a Gaussian envelope of vibrational sidebands starting at about 1 eV. They identify the strong absorption band observed in $\sigma(\omega)$ (see Fig. 3.12) with this orbital absorption feature. However, the spectral weight of the observed
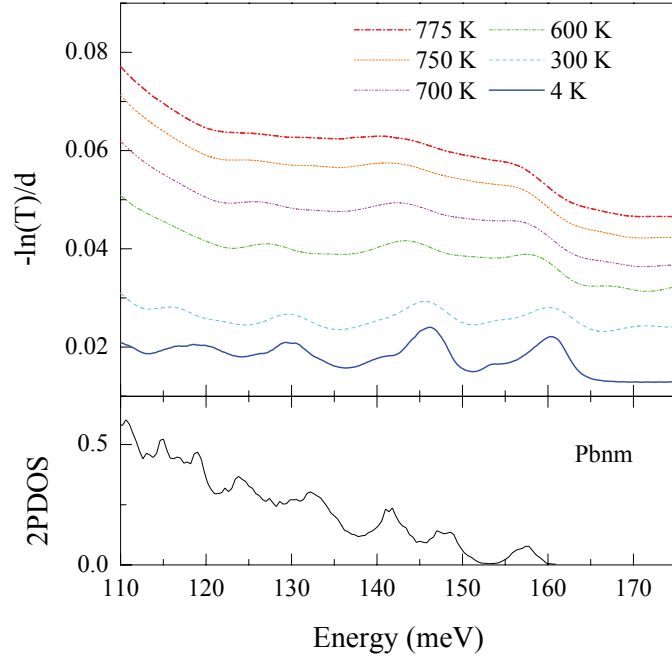
Figure 3.11: Top: Temperature dependence of the multi-phonon features in LaMnO$_3$. Plotting $-\ln(T)/d$, where T is the transmittance and d the sample thickness, yields an estimate of the absorption coefficient [120]. The curves have been shifted vertically for clarity. Bottom: The k=0 part of the two-phonon density of states calculated for LaMnO$_3$ in *Pbnm* symmetry [172].

band is several orders of magnitude larger than what is typically observed for d-d transitions. We thus regard this interpretation as rather unlikely. Note that vibrational sidebands are usually not resolved in solids, with the exception of molecular crystals. Additionally, Allen and Perebeinos predicted a strong temperature dependence close to the onset of the orbital absorption, which in principle is in agreement with our data. However, the shift with temperature of the onset of the strong absorption is much stronger than predicted (see Fig. 3.13). An interpretation in terms of an Urbach tail (of thermally excited phonons) of excitations across the gap is thus much more likely.

In order to investigate the onset of the excitations across the gap up to higher values of σ, we measured samples with thickness d varying from 2 to 28 μm. For comparison all data sets of sufficiently thin samples are shown in Fig. 3.14. In principle, the data for $d = 2$ μm allows to determine $\sigma(\omega)$ up to a value of about 150 $(\Omega\,\mathrm{cm})^{-1}$ at $\omega \approx 1.6$ eV. However, it is difficult to prepare such thin single crystals. In particular, the variation Δd of the thickness is of the same order as the thickness, since the two surfaces are not absolutely parallel after polishing. Since $\sigma(\omega)$ depends exponentially on d, it is not possible to determine $\sigma(\omega)$ quantitatively without a detailed knowledge of the thickness profile. In the case of thicker samples, e.g. $d > 20$ μm, a
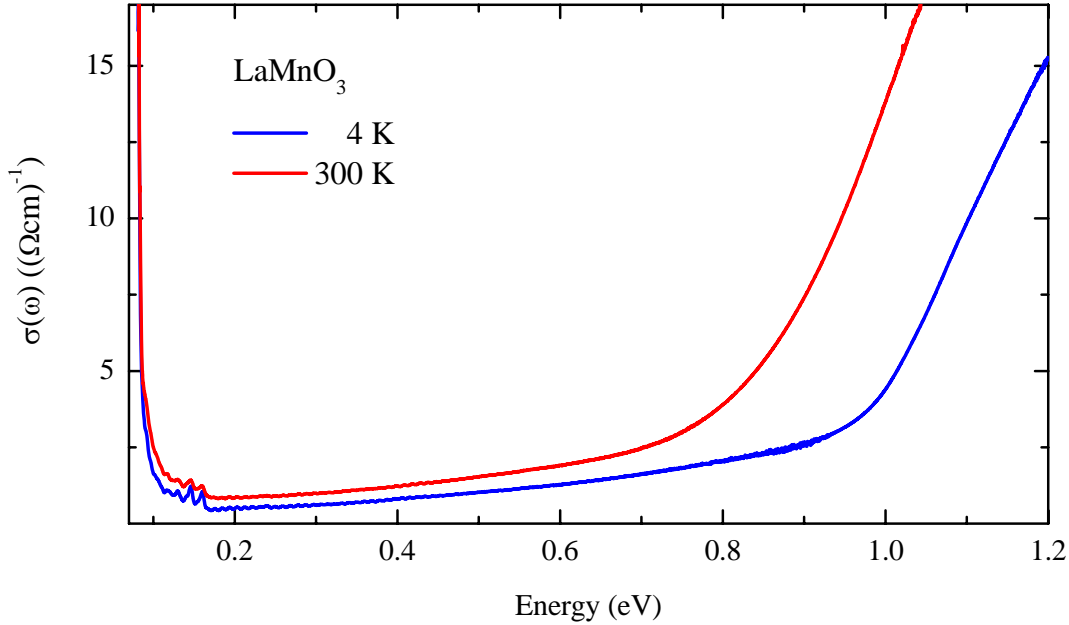
Figure 3.12: Optical conductivity $\sigma(\omega)$ of LaMnO$_3$ in the energy range from phonon absorption to the onset of excitations across the Mott gap.

variation of Δd of a few microns is acceptable. Moreover, the thickness variation Δd leads to a modulation of the interference fringes. For a decrease of d these fringes broaden drastically (the distance between two fringes is proportional to $1/d$). Additionally the total absorption within the sample decreases rapidly for thin samples. Therefore surface defects become more important with respect to the intrinsic absorption, giving rise to an increased background. It is very difficult to discriminate a possible weak, broad intrinsic absorption feature from this background and from the modulated interference fringes. From the data of the 2 μm thick sample we thus cannot clarify whether there is a structure at the onset of the gap or not.

The data of the sample with $d = 14$ μm reach only to values of σ up to 35 $(\Omega\,\mathrm{cm})^{-1}$. Unfortunately this sample seems to have a very thin film on the surface, that leads to very broad interference features on top of the usual fringes. The data for $d = 6$ μm show very regular interference fringes, which indicates that the thickness variation is only small. This data set thus allows a reliable, quantitative determination of $\sigma(\omega)$ in the region of the onset of the gap.

At low temperatures a shoulder appears at ≈ 1.2 eV right at the onset of the gap. The intrinsic character of this feature is supported by comparing the data of samples with different thickness in Fig. 3.14. With increasing temperature the gap is smeared out and the broad peak gets lost in the rising background (see Fig. 3.15). Assuming an exponential increase of $\sigma(\omega)$ above the gap, we can identify the shoulder at 1.2 eV up to room temperature in a logarithmic plot.

In total this gives strong evidence that the feature is not merely an artefact but an intrinsic absorption band of LaMnO$_3$. We are confident that additional measurements in the future

74
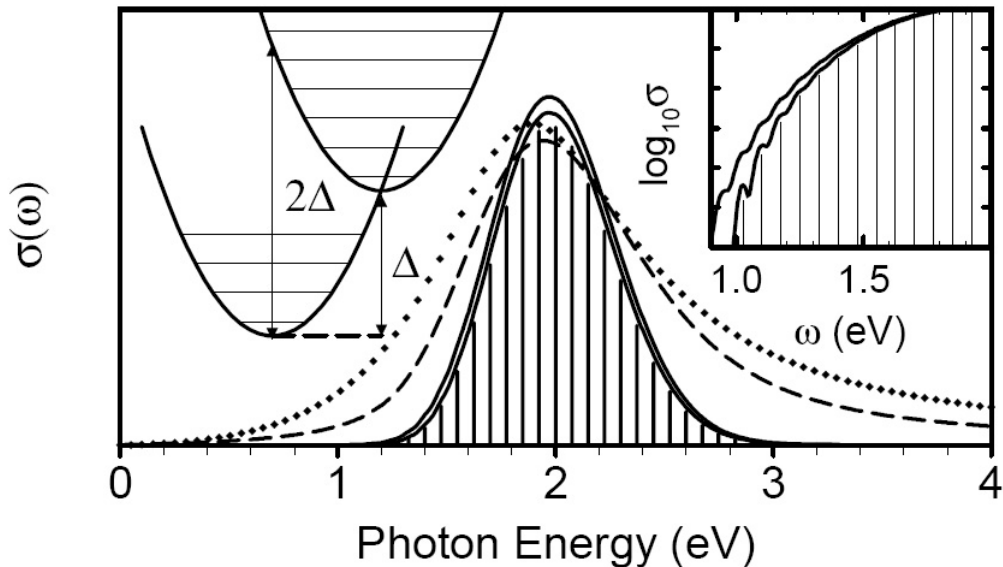
Figure 3.13: Calculated optical conductivity of LaMnO$_3$ [178]. The dotted curve is the lowest Lorentzian oscillator fitted by Jung *et al.* to the optical conductivity obtained by a Kramers-Kronig analysis of reflectance data [177]. The dashed curve is a $T = 0$ sum of convolved Lorentzians centered at the vibrational replicas shown as vertical bars. The solid curves are $T = 0$ (lower) and $T = 300$ K (upper) sums of convolved Gaussians, also shown in the inset on a logarithmic scale.

will confirm this point of view.

This interpretation is corroborated by the results of a cluster calculation (see Appendix F) that we have performed for a MnO$_6$ octahedron. The result for $\Delta = 4.0$ eV and $U = 6.0$ eV is given in Table 3.1 for the five states lowest in energy (in counting levels we neglect the spin degeneracy which is only slightly lifted by spin-orbit coupling).

We find that the first excited state lies 1.16 eV above the ground state, whereas the

	E (eV)	S	$3z^2 - r^2$	$x^2 - y^2$	yz	zx	xy
gs	0.0	2	0.88	0.67	0.75	1.09	1.03
1.	1.16	1	1.19	0.98	0.82	0.53	1.05
2.	1.70	1	0.94	0.70	0.65	0.76	1.49
3.	1.80	1	0.80	0.79	0.64	1.00	1.28
4.	1.93	1	0.72	1.04	0.59	0.99	1.03

Table 3.1: Results of a cluster calculation for LaMnO$_3$ for $\Delta = 4$ eV and $U = 6$ eV.
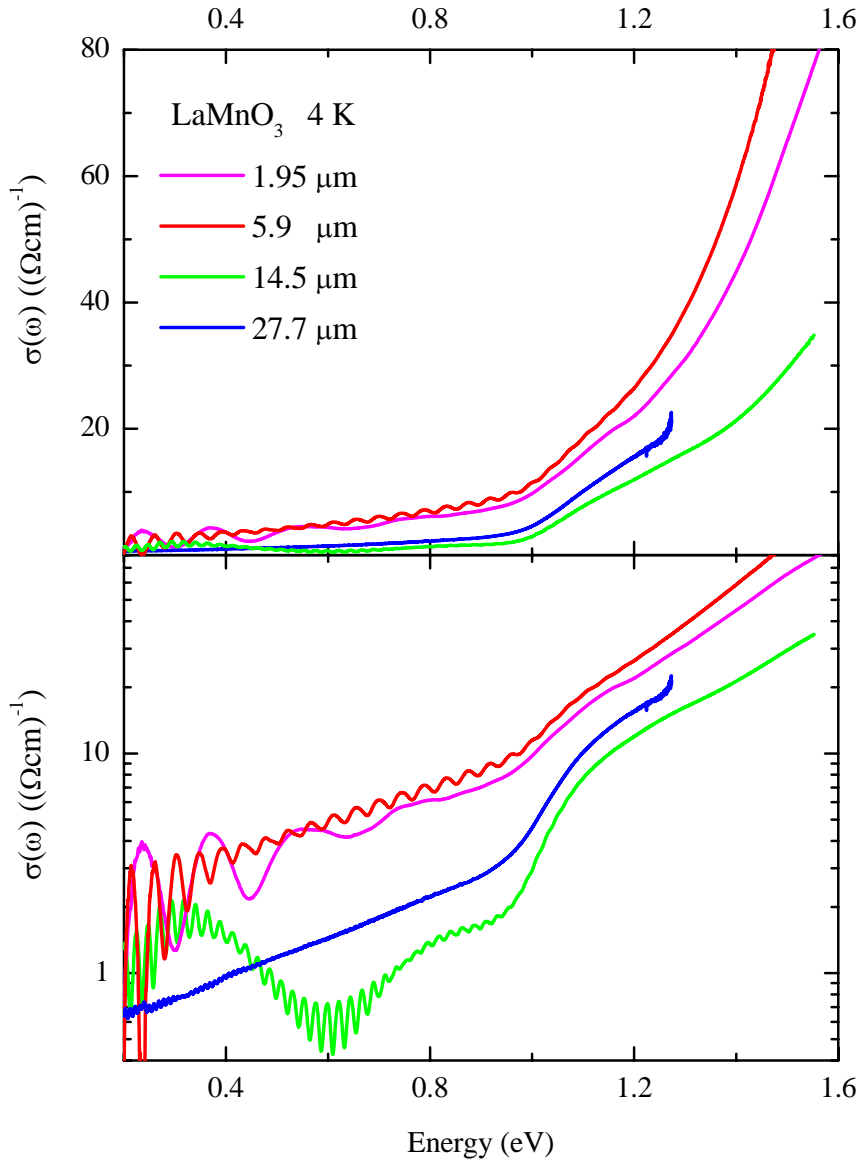
Figure 3.14: The optical conductivity of samples of different thickness d is compared. All data are obtained at 4 K. The top and bottom panels show the same data on a linear and on a logarithmic scale, respectively. The sinusoidal patterns correspond to interference fringes. Their period is proportional to $1/d$. These periodic features do not represent a true absorption within the sample.

following states are at least 0.5 eV higher in energy and are therefore beyond the gap. They will not be observable in $\sigma(\omega)$ since they are expected to be weak features (due to the parity selection rule as discussed in chapter 2) on top of absorption bands that are more than 3 orders of magnitude stronger. Note that the lowest excited state shows $S = 1$, in contrast to the
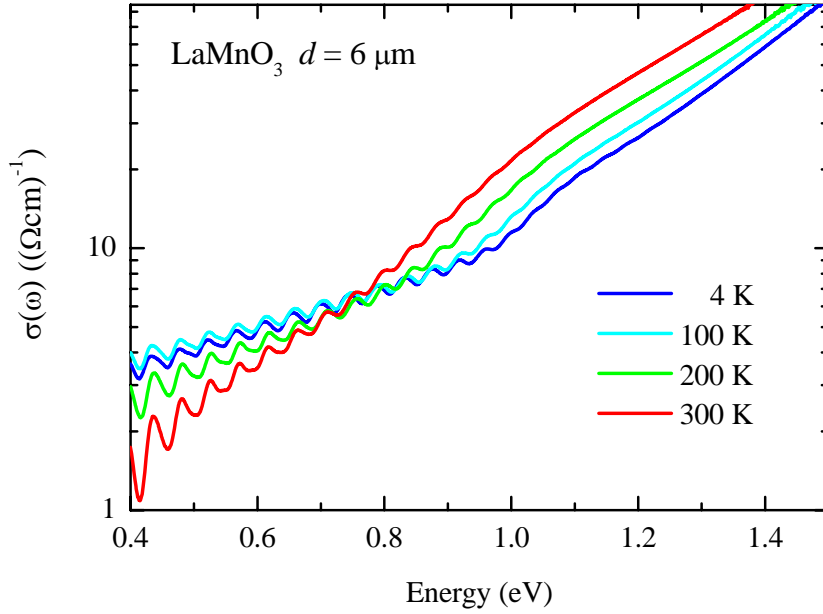
Figure 3.15: Temperature dependence of $\sigma(\omega)$ of LaMnO$_3$ ($d = 6$ μm) on a logarithmic scale.

$S = 2$ ground state. The absorption observed at 1.2 eV possibly can be attributed to a crystal-field excitation from the ground state to the first excited state. However, the amplitude of ≈ 2 $(\Omega$cm$)^{-1}$ is relatively high for a transition between different spin states. There are two effective mechanisms which bypass the strict spin selection rule and allow such a transition. One is the spin-orbit coupling that mixes spin eigenstates, and second there are two-particle
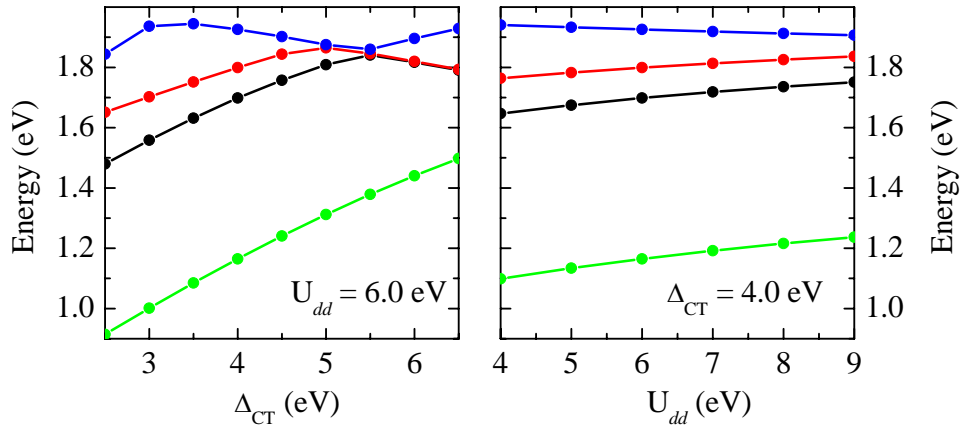
Figure 3.16: Dependence of the results of the cluster calculation for the MnO$_6$ octahedron on the parameters Δ and U_{dd}. The four excited states lowest in energy are shown as function of Δ (left) and U_{dd} (right). The spin degeneracy is neglected.

processes that involve the excitation of a magnon on an adjacent site. Although it is not possible to give a precise quantitative value for the strength of the absorption, it is expected to be about one order of magnitude weaker than for spin-allowed transitions. However, the intensity may increase by mixing with excitations across the gap, i.e. by "stealing" intensity from the strong interband excitations. An alternative explanation for the shoulder at 1.2 eV may be found in the details of the band structure. The precise shape of $\sigma(\omega)$ at the onset of the Mott-Hubbard gap thus far has only been investigated theoretically for 1D systems [200, 201, 202].

In order to show that the choice of the parameters Δ and U is robust in reproducing the value of ≈ 1.2 eV for the first excited state (above the ground state), we varied Δ and U. The dependence of the results on the parameters is shown in Fig. 3.16. That our choice of parameters is very reasonable can also be seen from [203] where $U = 7.5$ eV and $\Delta = 4.5$ eV are determined by x-ray absorption measurements.

In summary, our main intention was to observe collective orbital modes below the band gap, as it has been claimed in [44]. What we found is an absorption at ≈ 1.2 eV. This high energy justifies to ignore collective phenomena and to consider the orbital excitation as a purely local, self-trapped exciton, i.e. a local crystal-field excitation. Due to the failure of finding orbital excitations at low energies we are convinced that undoped LaMnO$_3$ is not a good model system for the study of orbital waves. The coupling of the bond-directional e_g orbitals to the lattice is large and hence the Jahn-Teller coupling is very effective in lifting the degeneracy that exists in cubic symmetry.

3.3 Interband excitations in LaMnO$_3$

In the energy range of interband transitions the optical conductivity usually exceeds values of several hundred $(\Omega\text{cm})^{-1}$. At such high values of $\sigma(\omega)$ even rather thin samples ($d < 10\mu\text{m}$) become opaque. Possible ways to determine the optical conductivity in this region would be to measure thin films grown on a transparent substrate or to do ellipsometry. A third possibility is to measure the reflectance in a large frequency range and obtain $\sigma(\omega)$ by a Kramers-Kronig analysis of the reflectance.

The shoulder we have observed at 1.2 eV (see 3.14) is at the edge of the region accessible by transmittance measurements. In order to confirm that this feature is actually an intrinsic property of LaMnO$_3$, we may also look at $\sigma(\omega)$ obtained from a Kramers-Kronig analysis of the reflectivity data. The reflectance data are shown in Fig. 3.5. In the region of interest considered here (i.e. below 2.5 eV), the Kramers-Kronig result for $\sigma(\omega)$ turned out to be independent from the way the reflectance has been extrapolated above 3.5 eV. The resulting optical conductivity spectrum at 4 K is shown in the bottom panel of Fig. 3.17. The comparison with the data of $\sigma(\omega)$ obtained from the combination of transmittance and reflectance shows a sizable discrepancy in the range of high transparency. Note that the optical conductivity is plotted in Fig. 3.17 on a logarithmic scale, hence differences at small values of $\sigma(\omega)$ are pronounced. The transmittance is highly sensitive to weak absorption features, thus the optical conductivity obtained form it is very reliable. In particular, the transmittance data obtained on the sample with d=200 μm allows to determine $\sigma(\omega)$ very accurately in the range
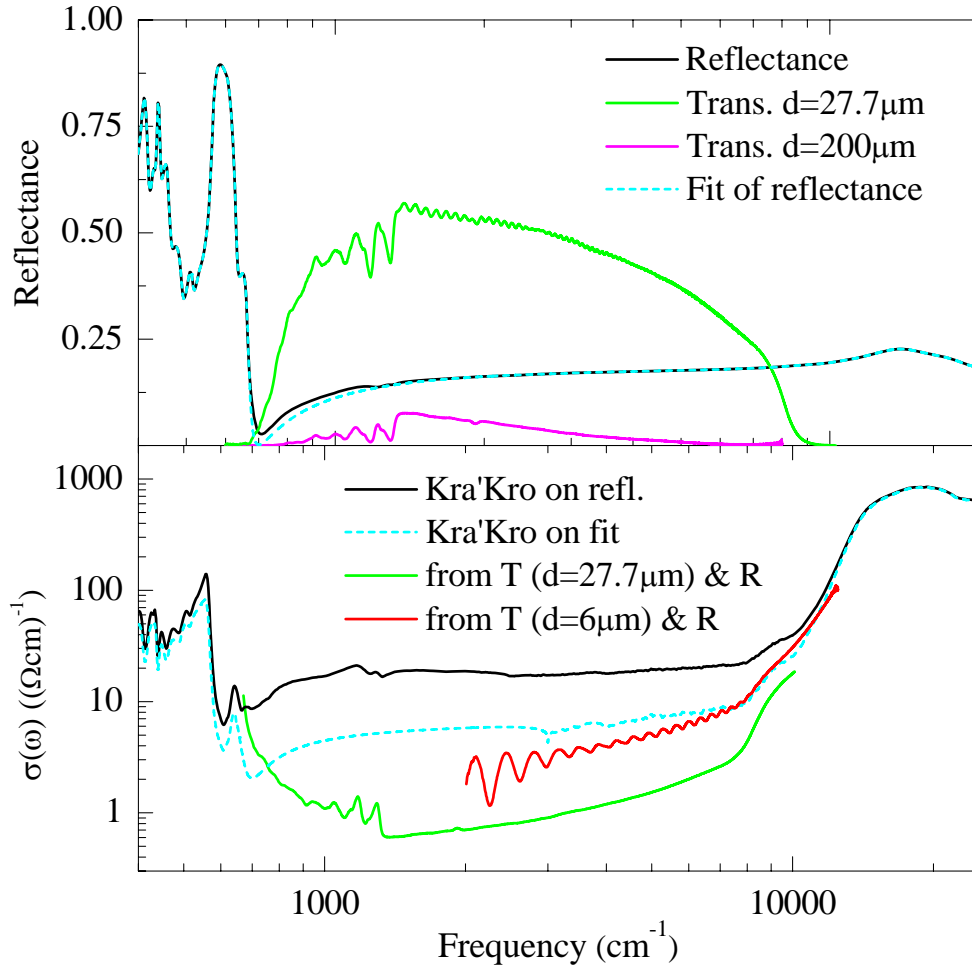
Figure 3.17: Top panel: the reflectance of LaMnO$_3$ at 4 K is compared to at fit. Additionally the transmittance of two samples of different thickness is shown. Bottom panel: the optical conductivity obtained from the Kramers-Kronig analysis is compared to the data of $\sigma(\omega)$ which results from transmittance and reflectance.

where $\sigma(\omega) < 1$ Ωcm^{-1}. The discrepancy with the result obtained from the transmittance of the sample with $d=6$ μm can be attributed to e.g. scattering from the surface. The relative importance of such surface effects increases with decreasing sample thickness. The advantage of the thin sample is that it allows to follow the optical conductivity to higher values. In any case we can state that the Kramers-Kronig analysis of the reflectivity strongly overestimates the absolute value of $\sigma(\omega)$ in the frequency range between the phonons and the interband excitations.

In the top panel of Fig. 3.17 the reflectance of LaMnO$_3$ at 4 K is compared with a fit. It is found that the reflectance can not be fitted well in the range of high transmission, in
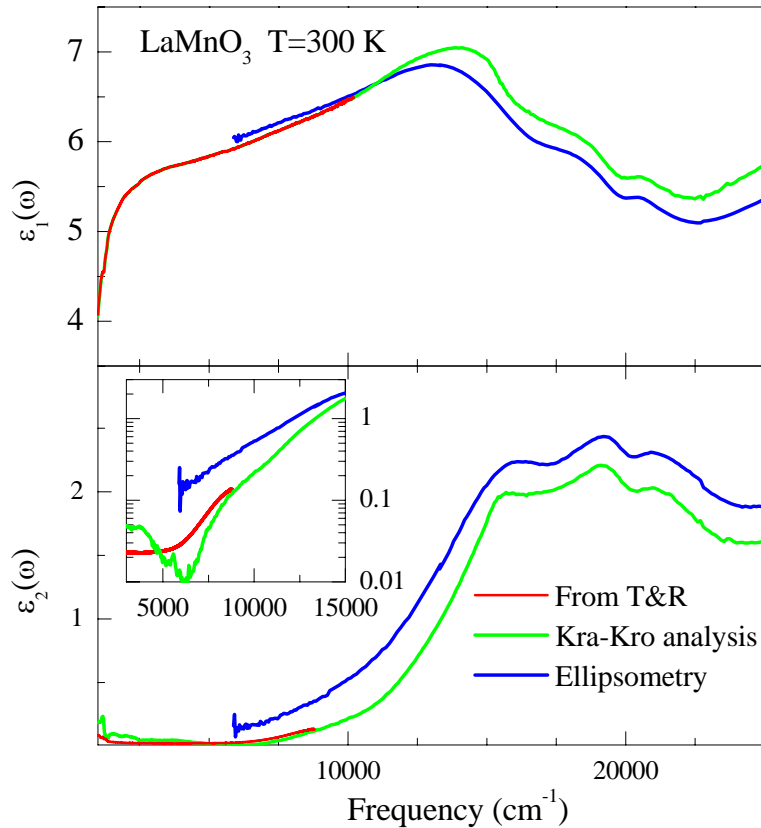
Figure 3.18: The complex dielectric function obtained from the Kramers-Kronig analysis is compared to $\varepsilon(\omega)$ acquired by ellipsometry. In the bottom panel the dielectric function obtained from transmittance and reflectance is shown additionally. In the inset the region of low values of ε_2 is magnified by the logarithmic scale.

fact the reflectance is slightly higher than the fit.[7] The analysis of the reflectance assumes a semi-infinite sample. The finite sample thickness of about 1 mm becomes relevant in the highly transparent range, where an additional contribution arises in the measured reflectivity due to reflections from the backside of the sample. Thus the measured data is higher than the fit. This is corroborated by the weak dips in the reflectance at the position of the multi-phonon peaks (compare the transmittance in the top panel of Fig. 3.17). The multi-phonon absorption within the sample reduces the transmittance and thus also the contribution of backside reflections. The small contribution from the backside provides a strong effect in $\sigma(\omega)$ relative to the very low value. The Kramers-Kronig analysis of the fit of R is much closer to $\sigma(\omega)$ obtained from the transmittance. We emphasize that the Kramers.Kronig analysis is not capable to determine very low values of $\sigma(\omega)$ accurately. Even if a much

---

[7]This effect is largest in the vicinity of the phonon absorption since there the fit is strongly determined by the shape of the phonon.
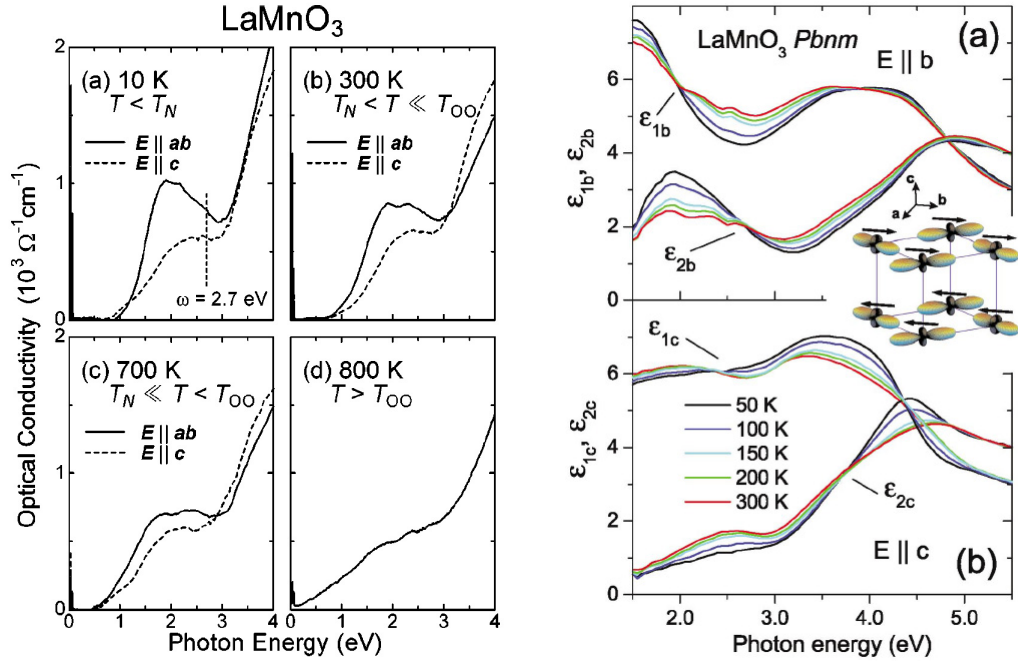
Figure 3.19: Left: the optical conductivity determined form reflectance data by a Kramers-Kronig analysis [175]. Right: the dielectric function obtained by ellipsometry [176]. Both investigations were performed on untwinned crystals.

thicker sample was used, the reflectivity change caused by e.g. the multi-phonon features (without backside refections) is smaller than the typical noise level.

At higher values of $\sigma(\omega)$ the agreement between the two techniques is satisfactory, as seen from the comparison with the data obtained from the transmittance of a 6 μm thin sample (see bottom panel of Fig. 3.17). Despite the failure of the Kramers-Kronig analysis concerning the absolute value of $\sigma(\omega)$, the shoulder at 1.2 eV is also clearly observed here.

A comparison of the dielectric function ($\varepsilon(\omega)$) derived from the Kramers-Kronig analysis with data obtained by ellipsometry is given in Fig. 3.18. We find a very good agreement between the ellipsometry and the Kramers-Kronig results as far as the shape of $\varepsilon(\omega)$ is concerned. For the absolute value the ellipsometry data turn out to be lower than the Kramers-Kronig result in ε_1 and higher in ε_2. The additional comparison with the data obtained from the combination of transmittance and reflectance clearly shows that the absolute value of the Kramers-Kronig result is more reliable. The systematic difference to the ellipsometry data may result from the way the dielectric function is acquired in ellipsometry. The ellipsometry measurement yields the ratio R_p/R_s and the relative phase shift θ upon reflection. Optical properties are then obtained from the measured data by fitting them under the assumption of a model. Such a model may have to include not only bulk properties but also parameters like e.g. the surface roughness. These fits were performed independently from the Kramers-Kronig results. A systematic error can therefore be attributed to the choice of the model. For comparison results reported in [175] and [176] are shown in Fig. 3.19. Note that these results

were obtained on untwinned crystals. However, one finds good agreement of the absolute values. In particular, the data for $E \parallel ab$ – which are expected to contribute stronger than $E \parallel c$ to the results on a twinned crystal – are in good agreement as far as the line shape is concerned.

In summary, we have observed the feature at 1.2 eV also in $\sigma(\omega)$ obtained from a Kramers-Kronig analysis. These data are found to be in good agreement with results reported in the literature.

Chapter 4

Orbital liquid vs. Jahn-Teller effect in RTiO$_3$ (R=La, Sm, Y)

Besides a degeneracy within the e_g orbitals as present in the manganites, orbital physics has been discussed also for a degeneracy within the t_{2g} orbitals. In the perovskites the t_{2g} orbitals on the transition-metal site point in between the ligand ions of the surrounding otcahedra. Compounds with nearly degenerate t_{2g} orbitals are the RTiO$_3$ (R = rare-earth ion or Y) titanates which crystallize in a distorted perovskite structure (space group *Pbnm*) [57, 154, 156]. The Ti^{3+} ions with the electronic configuration $3d^1$ exhibit a threefold degeneracy in a perfectly cubic symmetry. However, the distortion of the real crystal structure lifts this degeneracy. The magnitude of the distortion varies for different rare-earth ions and also other properties of these compounds differ strongly. The nature of the ground state in these crystals is under discussion since the scenario of an orbital liquid has been proposed for LaTiO$_3$ [49, 34]. We have investigated three compounds within this class which exhibit very different properties.

4.1   LaTiO$_3$ and other titanates

The discussion about novel orbital physics in LaTiO$_3$ has been triggered by the unusual observation of a small spin-wave gap in combination with a strongly reduced magnetic moment by neutron scattering [49]. These two properties of LaTiO$_3$ seem to contradict each other. A small spin-wave gap indicates a small anisotropy in spin space. Without any gap in the spin-wave dispersion, all spins could be rotated together without energy to be paid. This applies to magnons with infinite wavelength, i.e. $k \to 0$. In other words the continuous rotational symmetry in spin space produces a Goldstone mode. However, breaking this symmetry a gap opens in the dispersion of the corresponding excitation. In our case the gap in the magnon dispersion indicates the coupling of the spin and the orbital momentum (which has a fixed direction in space). This coupling breaks the rotational symmetry of the spins. A small spin gap indicates the coupling to a *small* orbital momentum. On the other hand the total magnetic moment on the Ti site has been claimed to be only 0.45 μ_B [49]. The contribution to the magnetic moment from the spin is $g\,S \approx 1\mu_B$ which in 3D is reduced
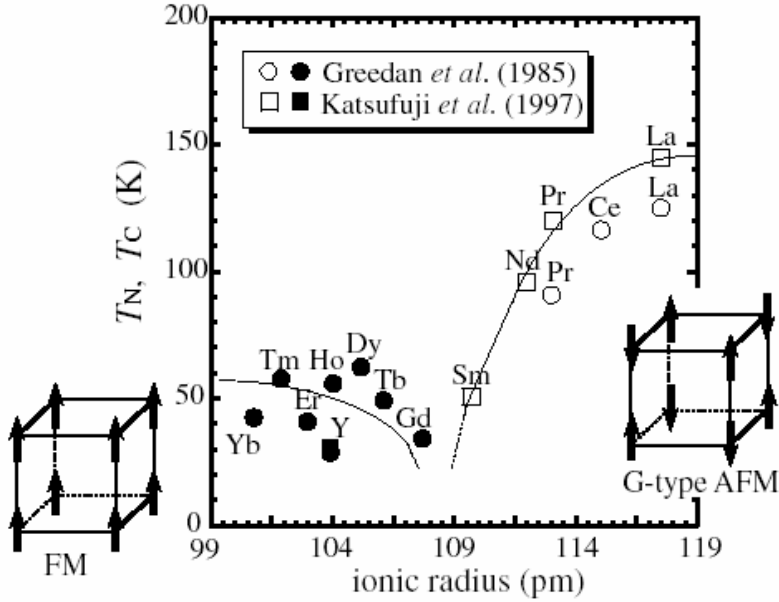
Figure 4.1: The magnetic ordering temperature over the ionic radius of the ion on the rare-earth site in RTiO$_3$. Between Gd and Sm the magnetic order changes from ferromagnetic to antiferromagnetic. This plot has been taken from [63].

by quantum fluctuations to 0.85 μ_B. The fact that the actually observed value is much smaller indicates a strong reduction of the magnetic moment by the (negative) contribution of a *large* orbital momentum.[1] However the orbital momentum cannot be large (reduction of the magnetic moment) and small (small spin-wave gap) at once. In order to reconcile the contradicting results it has been proposed by Khaliullin and collaborators that an orbital liquid is realized in LaTiO$_3$ [34]. Within an orbital-liquid scenario, the small spin-wave gap is explained by the non-degenerate quantum-disordered ground state that strongly suppresses the orbital momentum (and hence spin-orbit coupling is small). The reduced moment arises from the coupling of spin and orbital degrees of freedom: the fluctuating orbitals enhance the fluctuations in the spin channel which leads to a reduced magnetic moment.

If one substitutes La by other rare-earth ions, which are all of smaller ionic radius, the structure deviates stronger from the ideal cubic perovskite structure [154]. Also the magnetic

---

[1]In the first approximation one assumes the orbital momentum to be quenched in a crystal with a non-degenerate ground state. However, in a cubic environment the degenerate t_{2g} orbitals transform according to the T_2 representation so that matrix elements of the form $\langle\psi|\text{operator}|\psi\rangle$ are non-vanishing only if the irreducible representation according to which the operator transforms is contained in the irreducible representation of the reduction of $T_2 \times T_2$. For the magnetic moment M that is transforming according to T_1 this is actually the case (for the e_g orbitals this is vanishing since $E \times E$ does not contain T_1). The constant λ between the eigenfunctions of M and the eigenfunctions of the corresponding eigenspace is found to be -1. Hence one may think of a magnetic moment which corresponds to a pseudo (rotational symmetry is not present) angular momentum $\tilde{L}$ with a g-factor of -1.
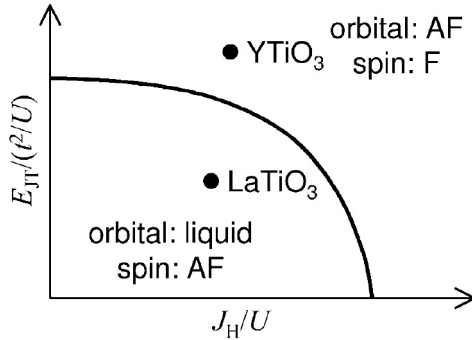
Figure 4.2: Phase diagram proposed in [34] for the t_{2g}^1 Mott insulator on a cubic lattice. At small Hund's rule and Jahn-Teller couplings a quantum Néel state with dynamically quenched orbital moments is stabilized. A quantum phase transition line separates this state from the ferromagnetic phase with static orbital order.

properties change from antiferromagnetic (LaTiO$_3$) to ferromagnetic at low temperatures. The magnetic ordering temperatures for the compounds RTiO$_3$ are plotted in Fig. 4.1 over the ionic radius of the ion on the rare-earth site. One finds that small ionic radii up to Gd correspond to ferromagnetism whereas for larger radii from Sm on antiferromagnetic order is observed. A decrease of the ordering temperature towards a critical ionic radius is interpreted as the approach to a quantum critical point which lies in between [34]. In Fig. 4.2 a qualitative phase diagram proposed by Khaliullin [34] is presented.

We focused our investigation on the observation of the orbital excitations in order to obtain information about the ground state present in LaTiO$_3$. We have measured for comparison the systems YTiO$_3$ and SmTiO$_3$. It has been proposed [98] that although orbital order has been observed in this compound,[2] YTiO$_3$ should exhibit at least partially orbital fluctuations in the ground state.

SmTiO$_3$ is still antiferromagnetic, but lies close to the critical value of the ionic radius [63]. This change is driven by the Ti-O bond angle which is increasing with larger ionic radius on the rare-earth site. A comparison of the crystal structure of the three systems is shown in Fig. 4.3.

Tilting and rotation of the octahedra are not the only deviations from the cubic crystal structure. Additionally, the octahedra deviate from the regular shape. This local distortion is normally measured in the difference of the metal-oxygen bond lengths. In the case of LaTiO$_3$ the relative difference of the Ti-O bonds within the *ab* plane is < 1 % [154] which is rather small. Therefore LaTiO$_3$ has been considered to be nearly cubic [49]. However, a detailed analysis of the crystal structure revealed that the oxygen-oxygen distances in one octahedron vary by about 4 % [57] (see Table 4.1).

The distortion pattern of the TiO$_6$ octahedra turns out to be different for La on the one

---

[2]The orbitally ordered state associated with the Jahn-Teller type lattice distortion has been confirmed by resonant x-ray scattering, NMR and polarized neutron scattering experiments. [149, 150, 151].
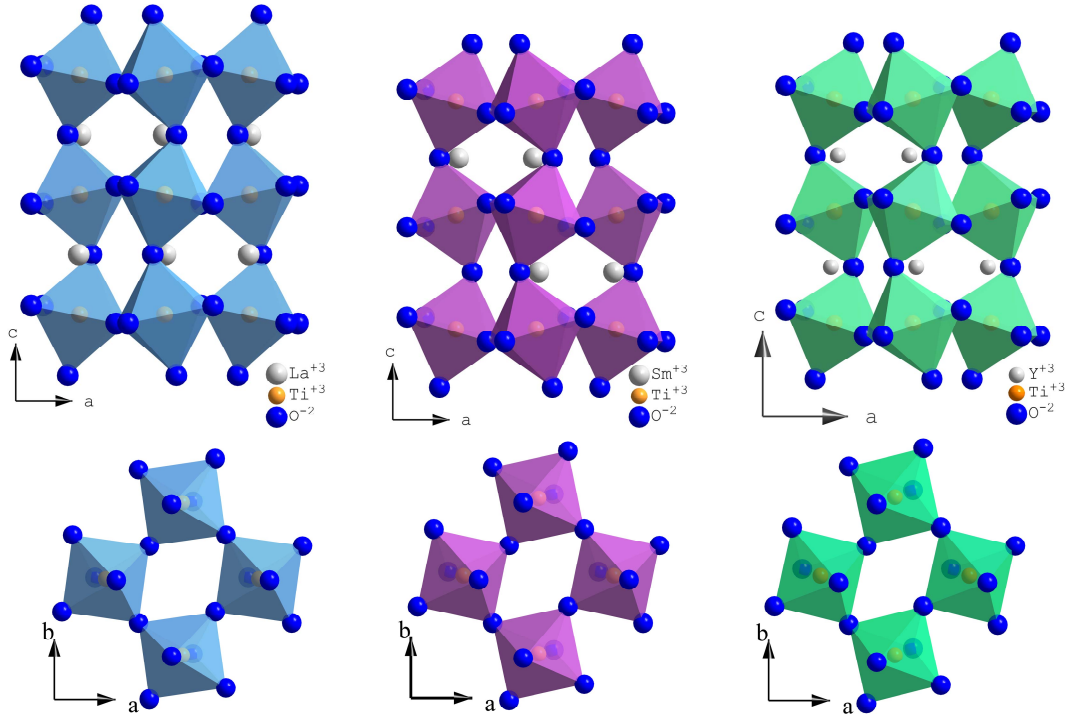
Figure 4.3: Comparison of the crystal structure of the three rare-earth titanates investigated here. LaTiO$_3$ (left) exhibits the smallest tilting due to the large ionic radius of the La ions. With decreasing ionic radius the deviation from the cubic structure gets stronger and the Ti-O bond angle decreases. Middle: SmTiO$_3$. Right: YTiO$_3$.

hand and Sm, Y on the other hand. In LaTiO$_3$ the four oxygen ions within the ab plane surround the metal ion in a rectangular shape, i.e. the diagonals are equal and the edges are different. In Sm and Y the situation is the other way around, the diagonals differ and the edges are equal, corresponding to a rhombus. In general such a deviation from a high symmetry can result from different origins:

- Collective Jahn-Teller distortions which are due to the coupling of the orbitals to the lattice. In this case usually a phase transition is observed.

- Ionic-size mismatch effects generate cooperative rotations and tiltings of the octahedra as well as distortions of the octahedra themselves. These distortions occur to establish a closed-packing condition and have nothing to do with the orbital degeneracy at all. The degenerate orbitals may split under the influence of the distortion, but they are not the driving force. This is obvious as even systems with a non-degenerate orbital state such as for instance LaAlO$_3$ (3d^0) or LaFeO$_3$ (3d^5) exhibit a non-cubic crystal structure. In this case, orbital order is not a cooperative phenomenon.

In general these two contributions both are present and it is not obvious which one is dominant. However, the temperature dependence of the distortion may give some hint. For

	LaTiO$_3$ (1)	LaTiO$_3$ (2)	SmTiO$_3$	YTiO$_3$
a	5.601	5.6336	5.454	5.3350
b	5.590	5.6156	5.660	5.6840
c/$\sqrt{2}$	5.590	5.5964	5.501	5.3846
Ti-O2	2.023	2.057	2.057	2.073
Ti-O2	2.016	2.031	2.043	2.026
Ti-O1	2.015	2.030	2.028	2.027
O2-O2	2.889	2.935	2.907	2.911
O2-O2	2.822	2.845	2.891	2.886
O2-O1			2.892	2.852

Table 4.1: The lattice constants and the bond lengths are listed for comparison. The data of LaTiO$_3$ in the first column are given in [57]. The second data set of LaTiO$_3$ and the data of SmTiO$_3$ are from [154]. The data of YTiO$_3$ is taken from [156]. All data sets were obtained at room temperature.

instance in LaMnO$_3$ a long-range ordering of a distortion of about 15 % sets in at 780 K. A large Jahn-Teller binding energy [179] indicates that dynamical distortions of the octahedra are well present above 780 K, thus the structural transition is of order-disorder type for these distortions. The occurrence of long-range orbital order already at high temperature reflects the strong coupling of the e_g orbitals to the lattice. A low orbital ordering temperature which lies in the range of the magnetic ordering temperature suggests that the exchange interaction is more relevant. The lack of an orbital ordering transition in the titanates is discussed controversially in the literature. The temperatures of orbital order and spin order are shown for several compounds in Table 4.2.

4.2 Results on twinned crystals of RTiO$_3$

We have measured the transmittance and the reflectance of twinned single crystals of YTiO$_3$ and LaTiO$_3$ as a function of temperature. The results for the reflectance are shown in Fig. 4.4. One finds a strong similarity of the two compounds. Below $\approx$ 0.1 eV the spectra are dominated by phonons, followed by a range of nearly constant values. The weak and broad features that occur above 1 eV belong to interband transitions. These spectra are typical for insulators. Transmittance measurements were performed on twinned single crystals of YTiO$_3$, SmTiO$_3$, and LaTiO$_3$ and on untwinned single crystals in the case of YTiO$_3$ and LaTiO$_3$ (see Fig. 4.5 and section 4.3). For the transmittance measurement, the samples were polished to a thickness of $d < 100\mu$m. From the two properties, reflectance and transmittance, we are able to calculate the optical conductivity $\sigma(\omega)$. A comparison of the results at 4 K is shown in Fig. 4.6. In $\sigma(\omega)$ the steep rise at the high-energy edge of the spectra marks the onset of excitations across the gap. On the low-energy side the spectra are limited by

phase transition temperatures			
	system	spin	orbital
t_{2g} $(S = \frac{1}{2})$	LaTiO$_3$	T$_N \approx 140$ K	-
t_{2g} $(S = \frac{1}{2})$	SmTiO$_3$	T$_N \approx 50$ K	-
t_{2g} $(S = \frac{1}{2})$	YTiO$_3$	T$_{\text{Curie}} \approx 30$ K	-
t_{2g} $(S = 1)$	LaVO$_3$	T$_N \approx 140$ K	138 K
t_{2g} $(S = 1)$	YVO$_3$	T$_N \approx 110$ K	200 K
e_g $(S = 2)$	LaMnO$_3$	T$_N \approx 140$ K	780 K

Table 4.2: Magnectic and orbital ordering temperatures [63, 38].

the highest single phonon excitation at around 0.08 eV. Below the samples are opaque. In between these strong features we observe in all three compounds a broad peak at about 0.3 eV that has to be attributed to a phonon-activated orbital excitation. In the following we show that other origins can be excluded. In particular a phonon as well as a multi-phonon origin can be excluded since the energy of single phonons is restricted to 0.08 eV. Hence the two-phonon continuum reaches up to ≈ 0.16 eV. The small peak observed at this energy in YTiO$_3$ marks the upper limit for the two-phonon absorption in transition-metal oxides with perovskite structure (see also Fig. 3.7 for LaMnO$_3$). Absorption of three and more phonons is much weaker since the amplitude decreases at least about an order of magnitude by each additional phonon that is involved. According to the magnon energies observed by inelastic neutron scattering [49, 155], the energy of 0.3 eV is much too high also for phonon-assisted magnetic absorption (i.e., two magnons plus a phonon [99, 100]). In YTiO$_3$, interband excitations set in only above 0.6 eV. Finally an interpretation in terms of doped carriers or impurities is excluded by the comparison of different samples of LaTiO$_3$ in which T_N varies between 143 K and 150 K due to oxygen non-stoichiometry (see Fig. 4.7). Here, the background in $\sigma(\omega)$ increases with increasing impurity concentration (i.e. reduced T$_N$). In contrast, the spectral weight of the feature at 0.3 eV is hardly affected, indicating that it is not related to impurities (see Figs. 4.7 and 4.8). The electronic background is discussed in section 4.4.

The very sharp additional absorption lines observed in SmTiO$_3$ at about 0.15, 0.3 and 0.45 eV are attributed to crystal-field transitions within the Sm $4f$ shell [152]. These lines are much narrower than the d-d bands because in case of the $4f$ levels both the coupling to the lattice and the coupling between nearest-neighbor sites are much smaller.

Our interpretation of the features at about 0.3 eV in terms of orbital excitations is strongly corroborated by Raman scattering data of LaTiO$_3$ and YTiO$_3$ shown in Fig. 4.9. A detailed analysis of the Raman data can be found in reference [153, 53]. The Raman spectra show similar features as the optical conductivity but shifted to lower energies by 50-70 meV. As
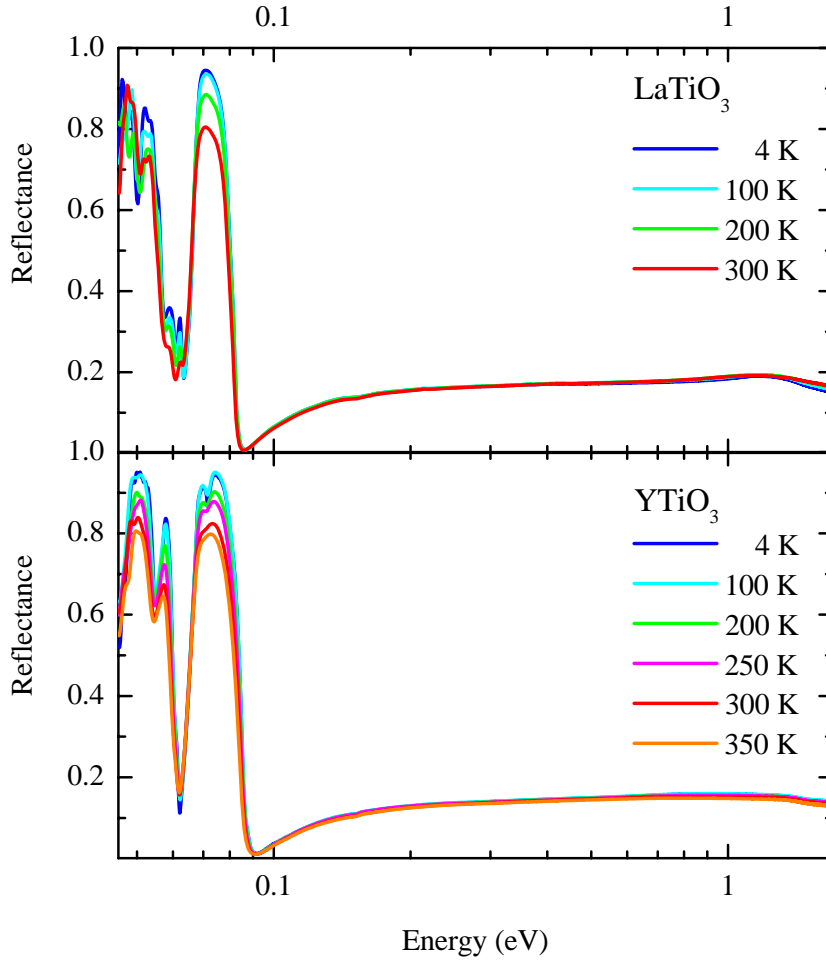
Figure 4.4: The temperature dependence of the reflectance of twinned single crystals of LaTiO₃ (top panel) and YTiO₃ (bottom panel). In the phonon range (below 0.1 eV) a typical broadening is observed with increasing temperature, whereas the spectra are nearly temperature independent above 0.1 eV. The values in this range are almost constant for both compounds (LaTiO$_3$ $\approx$ 17% , YTiO$_3$ $\approx$ 14%).

discussed above, *d-d* transitions have even parity and are thus Raman active, whereas a contribution to $\sigma(\omega)$ arises only due to the simultaneous excitation of a phonon breaking the inversion symmetry on the transition-metal site. The observed shift of 50-70 meV is in good agreement with the energies of the Ti-O bond-bending and bond-stretching phonon modes, which are expected to yield the dominant contributions. Moreover, the transition probability for such a multi-particle excitation (orbital excitation plus phonon) is small, in agreement with the small absolute value of $\sigma(\omega)$. We thus conclude that the orbital nature of these excitations is unambiguous. The orbital excitation energy amounts to about 0.2-0.25 eV
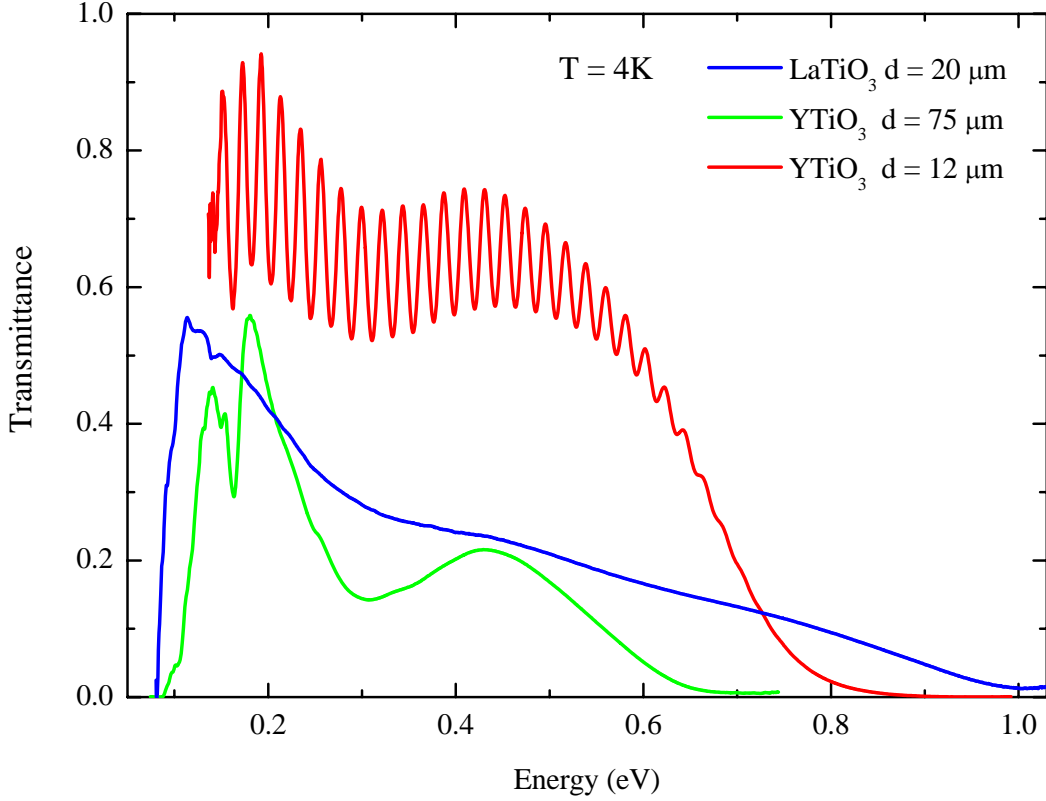
Figure 4.5: The transmittance of a LaTiO₃ sample ($d = 20\,\mu$m ; $T_N = 149$ K) and of two samples of YTiO₃ of different thickness. The orbital excitations are clearly observed at ≈ 0.3 eV as broad dips in the transmittance. The suppression of the transmittance at low energies is due to strong phonon absorption and at high energies it corresponds to electronic transitions across the gap. Strong fringes are observed in the range of high transmittance for the thin sample of YTiO₃. The calculated $\sigma(\omega)$ for the two data sets of YTiO₃ are found to be in almost perfect agreement. A merged data set of $\sigma(\omega)$ is shown in Fig. 4.6.

(without the symmetry-breaking phonon).

The crucial question is whether these features reflect the collective nature of orbital fluctuations [98] or whether they have to be interpreted as local crystal-field excitations. Since predictions including both the coupling to the lattice and superexchange on an equal footing are not available at present, we have to compare our results either with a pure superexchange model or with a cluster calculation for local crystal-field levels. Of the former we know from [38] that there is an excitation of two orbitons predicted for LaTiO₃ at 0.24 eV [38](without symmetry-breaking phonon). On the other hand we have performed a cluster calculation for all three compounds (see Appendix F). We compare these results also with a point-charge model which takes into account only the Coulomb potential of the ionic charges.
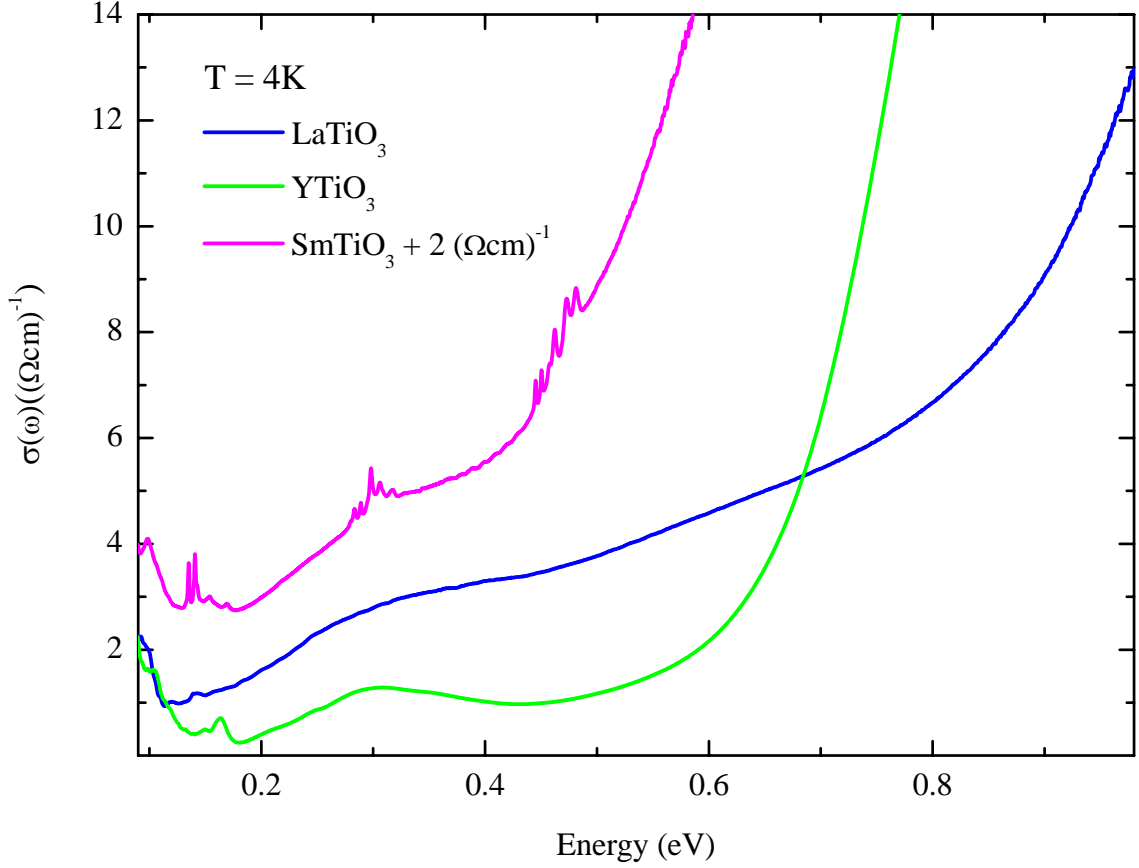
Figure 4.6: Optical conductivity of twinned single crystals of LaTiO$_3$ (T$_N$ = 149 K), SmTiO$_3$ and YTiO$_3$ at T = 4 K. An offset of 2 $(\Omega\text{cm})^{-1}$ has been added to the data of SmTiO$_3$ for clarity. Phonon-activated orbital excitations are observed at about 0.3 eV in all three compounds. The additional sharp features in SmTiO$_3$ at 0.15, 0.3 and 0.45 eV are due to crystal-field transitions within the Sm 4f shell [152]. For the calculation of the optical conductivity of SmTiO$_3$ we used the reflectance of YTiO$_3$. The error caused by this is negligible since the reflectance of insulating SmTiO$_3$ is only small in the considered energy range, and it will certainly look rather similar to that of YTiO$_3$ or LaTiO$_3$. Moreover the reflectance is nearly constant in a wide frequency range and therefore additional features that are not inherent in the transmittance data are not produced by the reflectance.

The results of the cluster calculation for $\triangle$ = 4.0 eV and U_{dd} = 4.0 eV [3] are compared with the point-charge model in Table 4.3. We have used the structural data of reference [57] for LaTiO$_3$, of reference [154] for SmTiO$_3$, and of reference [156] for YTiO$_3$. The structural data are all obtained at room temperature.

---

[3]These parameter values are reasonable (compare for instance [111]).
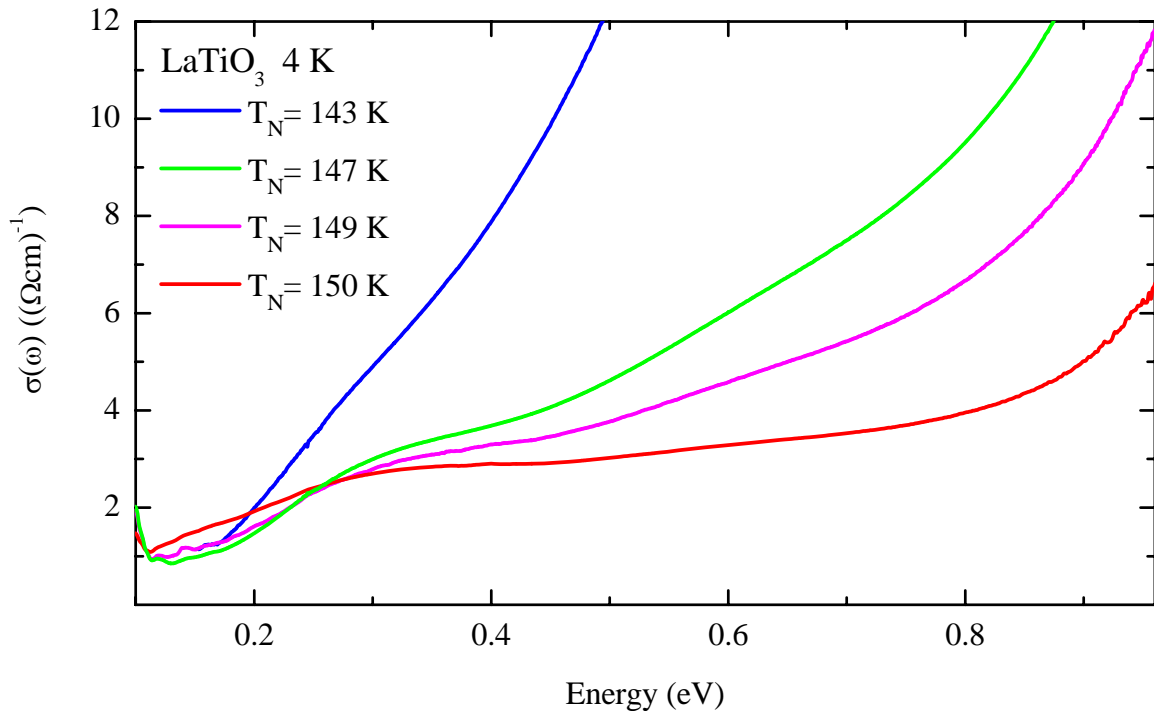
Figure 4.7: The optical conductivity of several samples of LaTiO$_3$ that differ in the oxygen stoichiometry which is seen from their Néel temperature [58] and from the background contribution in the gap. The broad peak at 0.3 eV is a common feature in all samples.

We find that the point-charge model underestimates the splitting between the t_{2g} and e_g subshells by more than 1 eV. This can be attributed to the neglect of hybridization effects, see chapter 2.1.1 (molecular-orbital theory). At the same time, the predictions of the point-charge model and of the cluster calculation for the splitting of the t_{2g} subshell are rather similar, with a maximum difference of 0.06 eV. We find good agreement between theory and experiment concerning the peak energy of 0.2-0.25 eV in all three compounds (see Table 4.3). Similar values for the t_{2g} splitting in LaTiO$_3$ result from a recent LDA+DMFT study, in which the covalency between R and O ions has been identified as the driving force for the distortions [71]. Significantly smaller values (27 and 181 meV for YTiO$_3$; 54 and 93 meV for LaTiO$_3$) have been derived from tight-binding fits of the t_{2g} band structure [73]. On the basis of x-ray absorption and spin-resolved photo-emission data of LaTiO$_3$, it has been concluded that the splitting between the ground state and the lowest excited state is about 0.1-0.3 eV [60].

The above mentioned change of the magnetic ordering pattern as a function of the ionic radius of the rare-earth ions is accompanied by a change of the character of the distortions [154]. The radius of the Sm^{3+} ions is close to the critical value [154]. One thus may have hoped to find a smaller crystal-field splitting in SmTiO$_3$. However, this is not corroborated
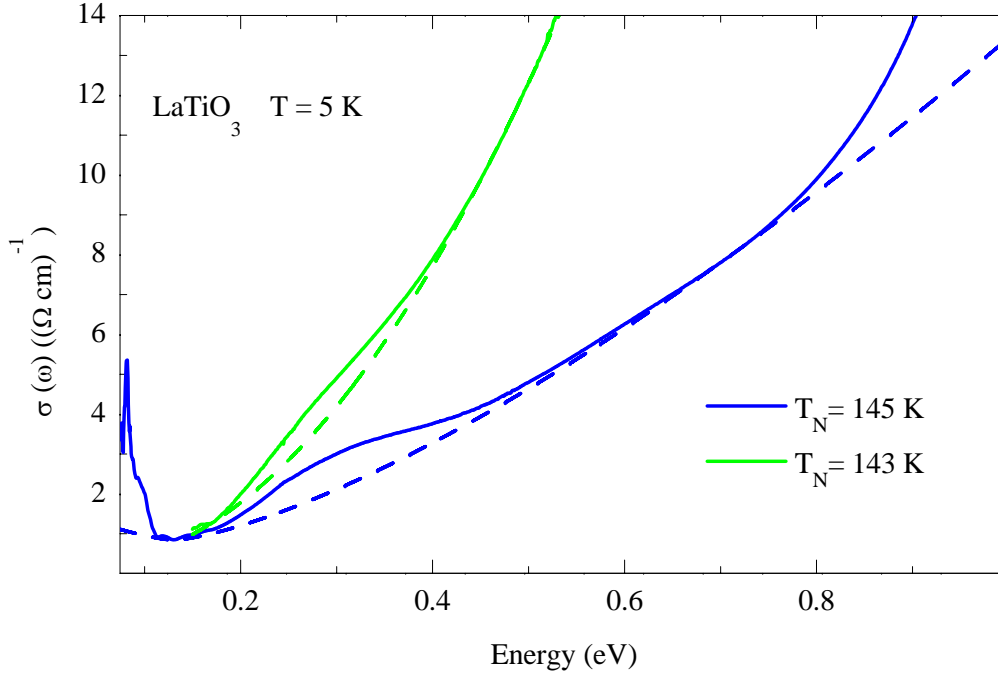
Figure 4.8: A background (dashed curves) has been subtracted from the optical conductivity in order to obtain the orbital excitations. The background has been obtained by fitting the data at higher energies with a power-law fit. The resulting estimate of the orbital excitations is plotted in Fig. 4.9.

by the cluster calculation, which predicts rather similar values for all three compounds. Also the orbital fluctuation model predicts that the orbital excitations for not too low energies are very similar across the quantum critical point [98], in agreement with the experimental result.

La	point charge	0	0.21	0.23	0.9	1.0
	cluster	0	0.24	0.26	2.2	2.4
Sm	point charge	0	0.15	0.26	0.9	1.0
	cluster	0	0.21	0.31	2.2	2.5
Y	point charge	0	0.14	0.28	0.9	1.0
	cluster	0	0.19	0.33	2.2	2.4

Table 4.3: Crystal-field splitting of $3d^1$ Ti^{3+} in $LaTiO_3$, $SmTiO_3$ and $YTiO_3$ as calculated in the point-charge model and in a cluster calculation. All values are given in eV. For comparison with the optical conductivity data in Figs. 4.6 and 4.9, the energy of the symmetry-breaking phonon has to be added.
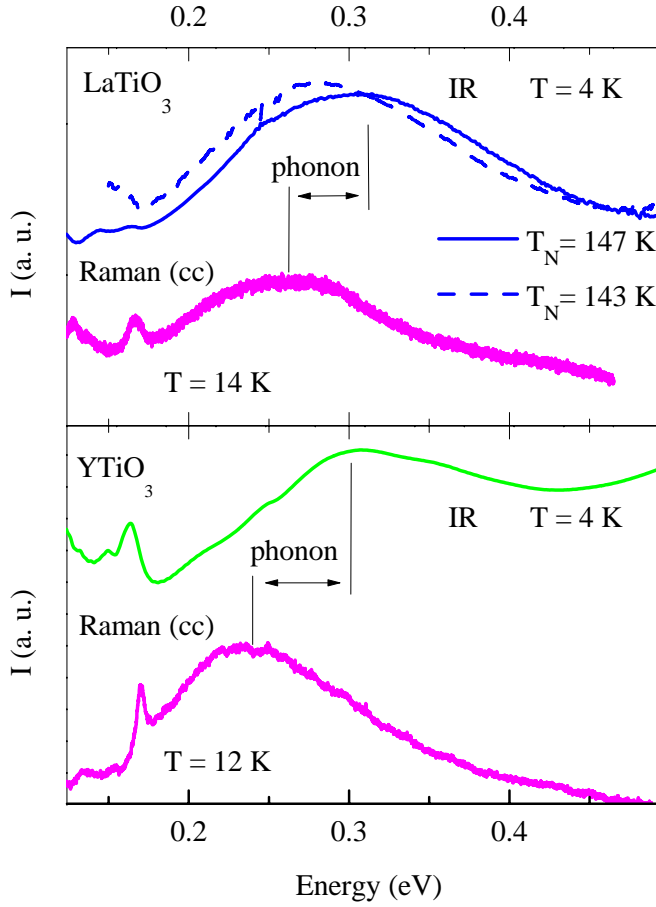
Figure 4.9: Comparison of the orbital excitations in the optical conductivity and in Raman data from [53, 153]. The peak in the optical conductivity is shifted to higher energy by an additionally excited phonon which breaks the inversion symmetry on the Ti site. In the case of $LaTiO_3$ a background has been subtracted in $\sigma(\omega)$ (see Fig. 4.8).

Our calculations predict that the splitting between the first and the second excited state increases from La via Sm to Y. However, the energies are not as sensitive to the radius of the R ions as one may have expected, and we consider these small differences as smaller than the absolute uncertainty of the calculation. Moreover, the experimental features are too broad and too close in energy to the excitations across the gap in order to test this prediction.

Nevertheless, the uncertainty of the theoretical predictions for the crystal-field splitting is too large to rule out a finite contribution from orbital fluctuations. The energy of 0.2-0.25 eV is certainly too high for a one-orbiton excitation in a collective mode scenario. However, it possibly can be reconciled with two-orbiton excitations [98], or with the sum of crystal-field and fluctuation contributions. Additional information can be derived from the Raman data. The resonance behavior and the polarization dependence yield evidence for a collective

nature of the orbital excitations in RTiO$_3$ [153].

The Raman intensities of YTiO$_3$ for polarization along the three crystallographic axes have been compared in [153]. It has been observed that the intensity is equal for all three directions. This is in contradiction to a crystal-field scenario where the matrix elements for the Raman process should differ by about a factor of two. However, this is only valid for an ideal Raman experiment in which the intermediate state is only virtual. In real experiments the laser energy is chosen to be near a resonance of the system in order to increase the signal. Hence the intermediate state becomes real instead of virtual. The intensity is then determined not only by the matrix element, but it also reflects the matrix element for the intermediate state. This transition probability can vary for the different directions. An experiment that will reveal the matrix elements for the different polarizations is ellipsometry. If the optical conductivity shows significant difference for the different polarizations, this may explain the observed intensity values. Recent results show that this is actually the case [53].

4.3 Results on untwinned crystals of RTiO$_3$

The superexchange model assumes cubic symmetry for the orbital state and thus predicts no polarization dependence of the orbital excitations. This prediction does not hold only for the case of LaTiO$_3$ but was at least partially extended to YTiO$_3$ [153, 155]. In the case of LaTiO$_3$ it took a large effort to prepare untwinned samples [54] since the proximity of the cubic lattice increases the tendency to twinned samples. The degree of twinning of the crystals has been checked with a polarization microscope and x-ray diffraction. Transmittance measurements on untwinned samples and nearly untwinned[4] samples have been performed in the case of LaTiO$_3$. The optical conductivity for a nearly untwinned sample is shown in Fig. 4.13. The observed polarization dependence is very weak and cannot be discriminated from experimental effects that do not belong to an intrinsic polarization dependence. Other measurements of untwinned samples do not show any polarization dependence, as seen e.g. from the transmittance data in Fig. 4.10. The lack of a polarization dependence in the untwinned sample might be due to the orientation of the measured surface which contained the (111) direction. This result is in agreement with the orbital-liquid scenario. On the other hand within the local crystal-field approach one would also not expect a drastic polarization dependence. There are in principle two distinct mechanisms that may give rise to a polarization dependence. As we consider a two-particle process, both constituents may exhibit a polarization dependence.

- The two different excitations within the t_{2g} subshell may have different matrix elements for measurement with different polarization.

- The phonon may also show different energies in different crystallographic directions. By adding different phonon energies one should obtain a certain polarization dependence. Note that such a polarization dependence should also be observed for orbital excitations from an orbital-liquid ground state. However, the energy difference and thus the polarization dependence is certainly small.

---

[4]One orientation contributes by more than 90% of the sample.
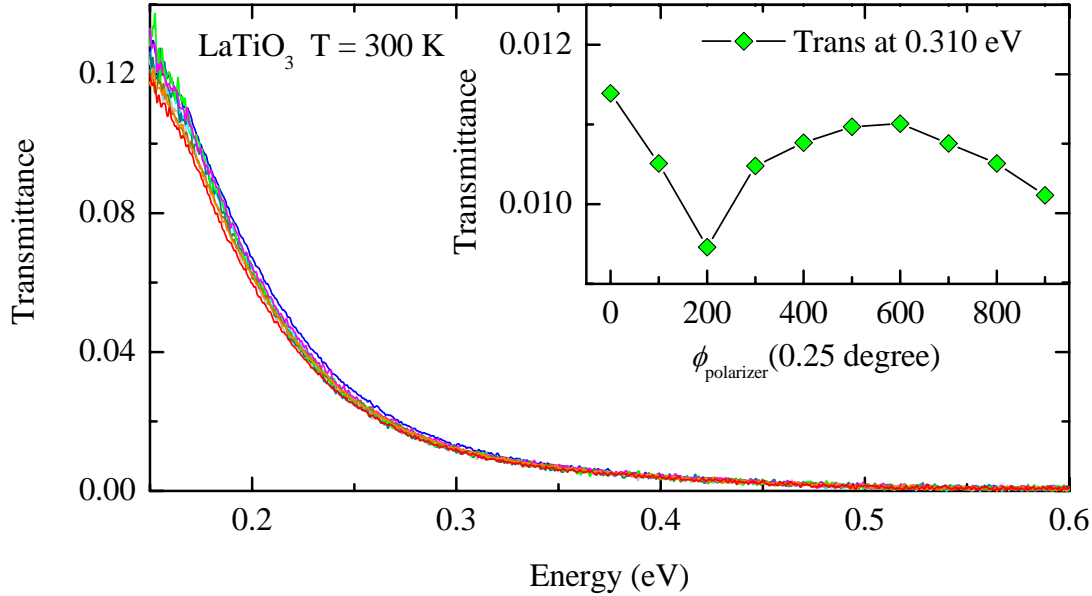
Figure 4.10: Transmittance for different polarizations of an untwinned sample of LaTiO$_3$. The measured surface includes a (111) direction. In the inset the value of the transmittance at 0.31 eV is plotted over the rotation angle of the polarizer.

- Third, a certain polarization dependence of the phonons may cause a difference in the coupling to the orbital excitations and thus a different spectral weight.

For LaTiO$_3$ the phonon contribution to the anisotropy should be rather small since the structure is close to the cubic case. The small energy difference between the first and second excited state obtained from the cluster calculation would lead to a shift of the maximum of the peak by at most that energy difference (assuming that each excitation is seen exclusively in one direction). By the width of the absorption of at least $\gtrsim 0.1 eV$ it becomes clear that a shift of less than 0.02 eV will be hard to observe. Moreover, the matrix elements for coupling the orbital excitation to phonons should be rather similar since the ground-state orbital (of approximately $3z^2 - r^2$ shape) points along the (111) direction, as shown in Fig. 4.11. Hence similar phonons along the a, b, and c direction will give rise to similar matrix elements since the orbital is nearly isotropic.[5] Thus from the polarization dependence of the spectra it is not possible to draw any conclusion about the orbital ground state in LaTiO$_3$.

In YTiO$_3$ the growth of untwinned single crystals is comparably easy. However, to determine the orientation of the single crystal turned out to be difficult and we were only able to identify the c axis unambiguously. The perpendicular axis lies in the ab plane, but it is not

---

[5]Note that the main axes of $\sigma(\omega)$ have to be along the crystallographic axes in orthorhombic symmetry. This is due to the fact that gliding mirror planes of non-symomorphic space groups can be regarded as simple mirror planes for the symmetry properties of the conductivity tensor. Therefore all off-diagonal elements vanish for a basis along the crystallographic axes.
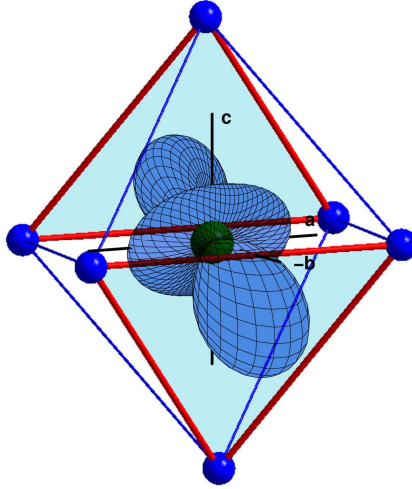
Figure 4.11: The angular dependence of the ground-state orbital of $LaTiO_3$ as obtained in the cluster calculation. The orbital is shown in relation to the surrounding oxygen octahedron [57].

further specified since a and b axis are very similar. We measured the transmittance of a 37 μm thick sample with polished surfaces. The result for the optical conductivity is shown in Fig. 4.12. It has been obtained using the reflectance data of the unpolarized measurement. This is justifiable since the reflectance in the considered frequency range is small (about 15%) and featureless, as shown in Fig 4.4.

We observe a remarkable polarization dependence of the orbital excitations. The conductivity in the ab plane looks similar to the one obtained from the unpolarized measurement of a different sample (see Fig. 4.6). This suggests that the surface of the sample used in the unpolarized measurement was close to the ab plane. However, for the light polarized along the c direction the orbital excitation is shifted by about 10 meV towards lower energies. This shift can be explained by different phonon energies along the two axes. The peak for $E \parallel c$ also appears to be slightly sharper which might be due to a different coupling to phonons (Franck-Condon effect) along the different crystallographic directions. This may also cause a certain difference in the peak energy. This kind of differences between the two polarizations are not surprising and can be well explained in both scenarios (orbital liquid and crystal field).

However, for light polarized along the c direction there is a sizable shoulder at about 0.21 eV. Let us first discuss the origin of this shoulder. Magnetic excitations can be excluded, as discussed above. In this energy range, three-phonon processes are expected. However the observed shoulder is rather unusual for three-phonon excitations due to the following arguments:

- The strength of multi-phonon absorption is decreasing by at least one order of magnitude with each additional phonon involved. Consider for instance $LaMnO_3$ with a
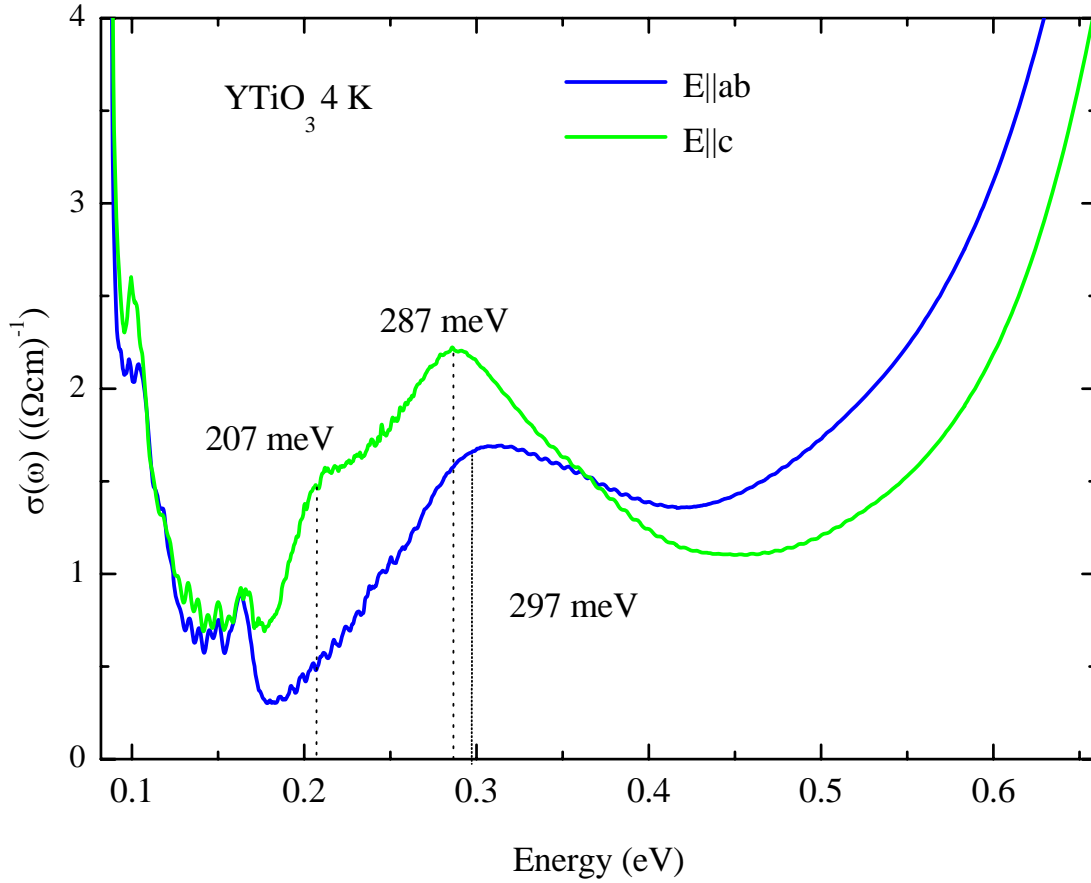
Figure 4.12: The optical conductivity of YTiO$_3$ for light polarized parallel to the c axis (green) and perpendicular (blue) is shown. The direction within the ab plane could not be specified further. The peak energies are marked by dash lines.

similar crystal structure. The results on LaMnO$_3$ are shown in Fig. 3.7. The amplitude of the shoulder in YTiO$_3$ can be estimated to be $\gtrsim 0.3$ $(\Omega \text{cm})^{-1}$ which is of the same strength as the two-phonon continuum.

- The strong polarization dependence. Three-phonon modes should also be observed within the ab plane.

- The disappearance of the shoulder above 100 K (see Fig. 4.14) is not expected for multi-phonon features. Normally they simply broaden with increasing temperature, as seen for example from the two-phonon spectra of LaMnO$_3$ in Fig. 3.11.

So from this we consider it to be rather unlikely that this feature is due to three-phonon processes. Hence it is most likely that the origin is an orbital excitation. This interpretation is corroborated by the broad line shape which is explained by phonon sidebands (see Fig. 2.28).
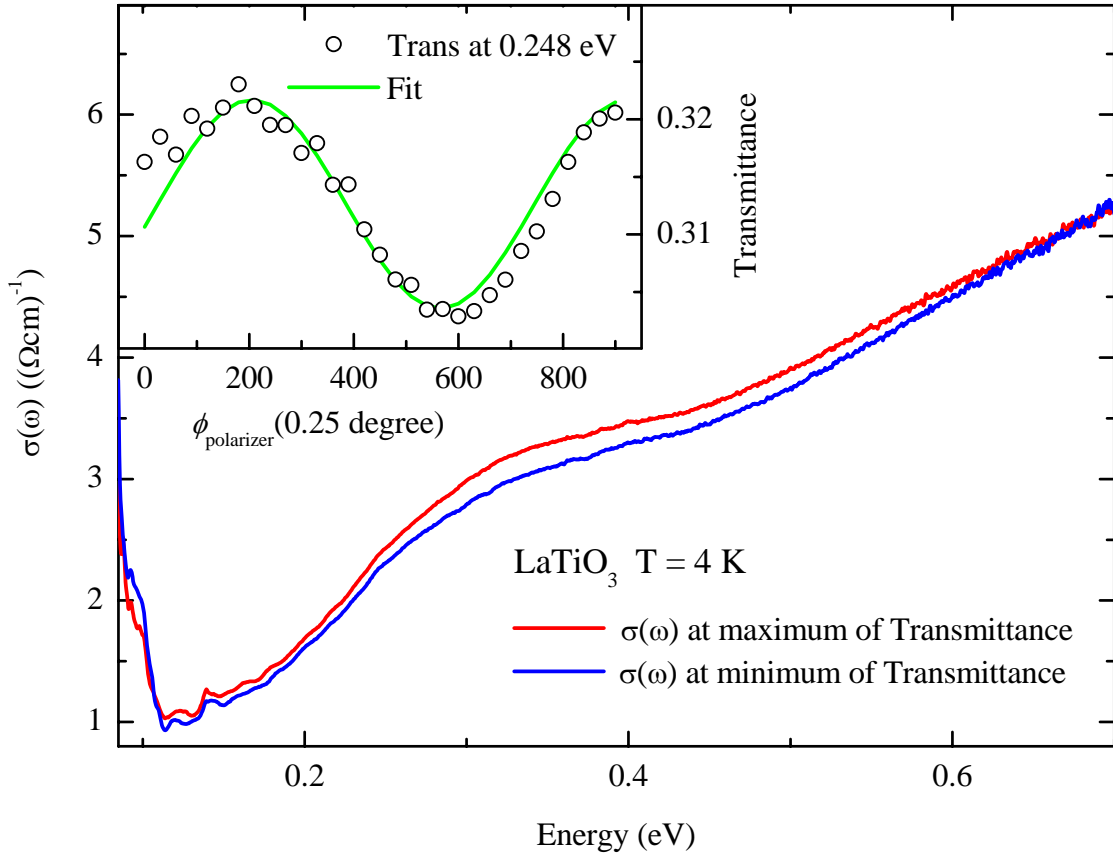
Figure 4.13: The optical conductivity of untwinned $LaTiO_3$ for light polarized along two perpendicular directions. The orientation of the crystal is unknown. The inset shows the dependence of the transmittance at 0.248 eV over the rotation angle of the polarizer. A clearly observable but weak polarization dependence is found.

Let us assume that we are dealing with an orbital excitation at 0.2 eV. What can be concluded for the question which kind of ground state is present in $YTiO_3$? The result is in good agreement with the crystal-field scenario, as the calculation predicts two well-separated orbital excitations in this energy range (see Table 4.3). The energies of 0.19 and 0.33 eV given by the cluster calculation are too high, as the phonon energy has to be added. But within the uncertainty of the model the agreement is satisfactory. The polarization dependence is not easily explained in the crystal-field scenario. Actually it is expected to be not that drastic. Since the phonon may have arbitrary polarization, we expect only a small polarization dependence of phonon-assisted crystal-field excitations. Nevertheless we have observed pronounced polarization effects of the crystal-field excitations in Y_2BaNiO_5 which has a highly anisotropic structure [40]. The strong temperature dependence of the shoulder is unusual, too. Let us assume now an orbital-liquid ground state. The orbitons are predicted at about 120 meV at $k = 0$ [38]. An energy of about 240 meV accounts for two orbitons to
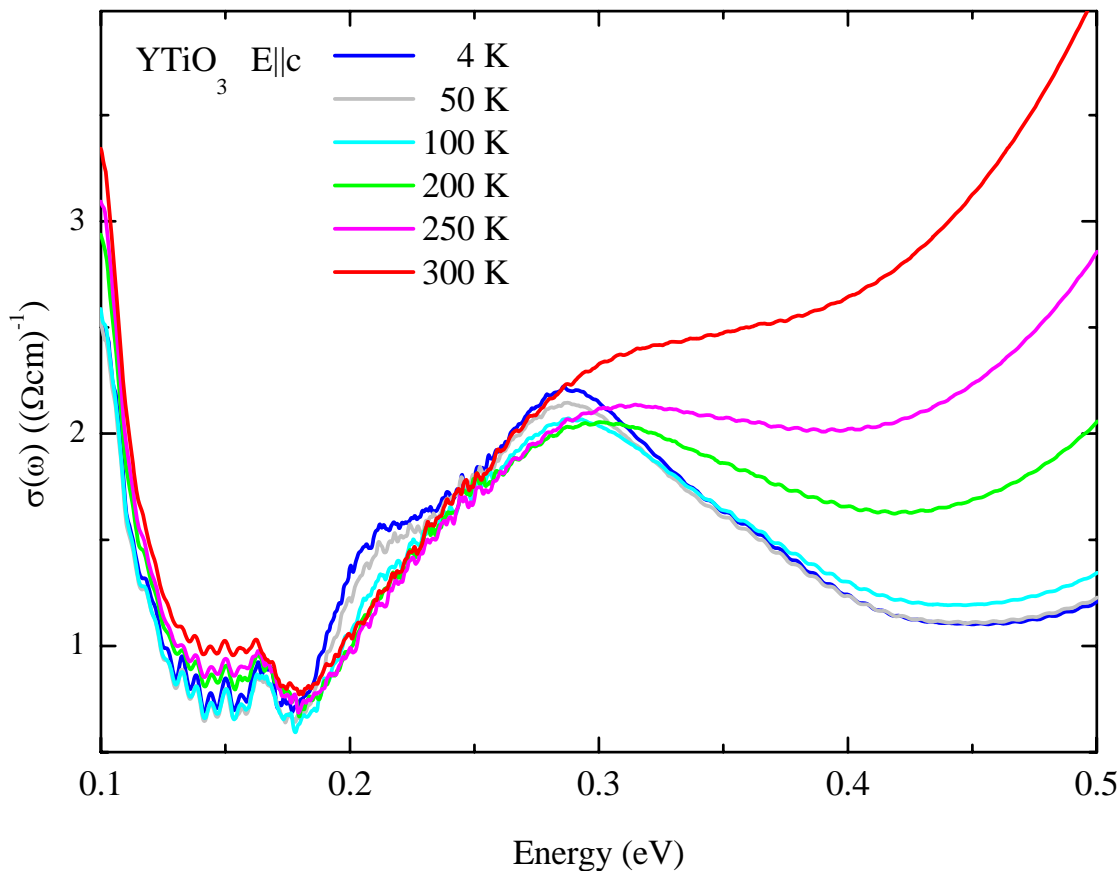
Figure 4.14: The temperature dependence of the orbital excitations observed in the optical conductivity for E∥ c is shown. Remarkable is the vanishing of the shoulder at 0.2 eV for temperatures above 100 K.

which the energy of an additional symmetry-breaking phonon has to be added. This is in good agreement with the strong absorption observed at around 0.3 eV.

So far this fits perfectly, but then the question about the origin of the shoulder arises. Obviously this can not be explained by a polarization dependence of the phonon since the energy difference of 0.08 eV is larger than the whole single phonon range. However, due to the cubic symmetry required for the orbital-liquid state the only polarization dependence arises from the phonon anisotropy. Therefore the polarization dependence of the second peak is not explained in an orbital-liquid scenario. We therefore regard the polarization dependence as strong evidence for the crystal-field scenario in $YTiO_3$. The existence of a second peak can in principle be attributed to the orbiton dispersion calculated within the orbital-liquid model (see Fig. 2.26). A two-orbiton absorption in $\sigma(\omega)$ requires $k_{total} = k_1 + k_2 \approx 0$, but the momentum k_1 of an orbiton may vary throughout the entire Brioullin zone.

This result shows also $LaTiO_3$ in a new light. It has been proposed that in $YTiO_3$ the major part of the orbital occupation is fluctuating and only a smaller part exhibits order [46].

The idea of orbital fluctuations in this compound is based on the experimental observation of an isotropic spin-wave dispersion by neutron scattering [155]. This would also explain why a transition to an orbitally ordered phase is missing not only in LaTiO$_3$ but also in YTiO$_3$. The lack of such a transition has been regarded [38] as evidence for the orbital-liquid scenario where no (or only partial) orbital order is expected. However, the similarity of YTiO$_3$ and LaTiO$_3$ now leads to the conclusion that the absence of a transition to an orbitally ordered phase is not due to the formation of an orbital-liquid state. Alternatively the mismatch of ionic radii may lead to a distortion present already at high temperatures. This distortion lifts the degeneracy of the t_{2g} orbitals so that no transition temperature is observed at which an additional Jahn-Teller distortion sets in. This result on YTiO$_3$ therefore strongly challenges also the orbital-liquid scenario in LaTiO$_3$.

4.4 Size of the electronic gap in RTiO$_3$

The electronic gap of ≈ 0.6 eV observed in YTiO$_3$ is of reasonable magnitude. Substituting larger ions on the rear-earth site can be regarded as a decrease of chemical pressure. The gap is expected to decrease with increasing ionic radius of the rare-earth ions, since the larger Ti-O-Ti bond angle gives rise to an increased band width. This relation of the gap and the ionic radius is observed for SmTiO$_3$ where the gap is lower than in YTiO$_3$ (see Fig. 4.6). However, LaTiO$_3$ does not seem to fit in this picture. In comparison, La has the largest ionic radius but the steep increase sets in only at ≈ 0.8 eV, which is even larger than in YTiO$_3$. This is also in contrast to predictions of the Hubbard gap of LaTiO$_3$ and YTiO$_3$ to be 0.3 eV and 1 eV, respectively [71] (these results have been obtained using the LDA + DMFT approach). Moreover in an orbital-liquid scenario as well as in a crystal-field picture a small Hubbard gap is required. For the former a small gap is necessary to enhance the superexchange coupling. In the latter a small gap leads to strong charge fluctuations that explain the reduction of the ordered magnetic moment.

The puzzling experimental observation in the optical data of LaTiO$_3$ can be reconciled with theoretical predictions by assuming that the electronic gap is indeed much smaller than 0.8 eV. However, the excitation into the lowest band may be dipole forbidden by additional selection rules (e.g. spin, momentum, the character of the occupied orbitals in the relaxed state, etc.). Such a mechanism would explain that the actual gap is not observed in the optical conductivity. This idea of a small but optically forbidden excitation gap is corroborated by the observation of an absorption tail that extends down to about 0.2 eV. We compare this absorption tail of four samples with different T_N in Figs. 4.7 and 4.15. A decrease of the Néel temperature is considered here as an increase of the amount of defects in the crystal. These defects are predominantly due to deviations of the oxygen content from 3.0. An absorption tail which increases strongly with the impurity concentration is naturally explained by the idea of a small but optically forbidden excitation gap. Since in the local environment of the defects the strict selection rule is broken, the transition into the lowest band becomes weakly allowed.

In [72] the optical conductivity of several compounds of the series La$_x$Y$_{1-x}$TiO$_3$ has been
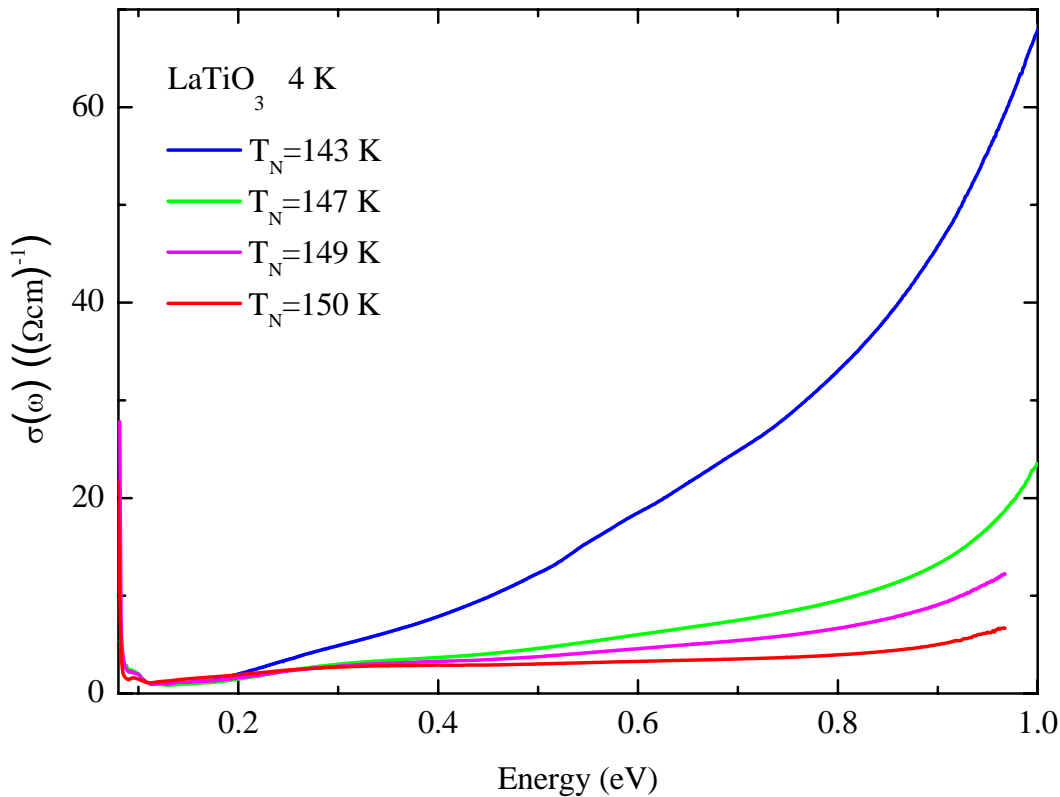
Figure 4.15: The optical conductivity of samples of LaTiO$_3$ with different Néel temperatures is compared. Below 1 eV a strong increase of $\sigma(\omega)$ is observed with decreasing T_N. Both $\sigma(\omega)$ and T_N depend on the oxygen stoichiometry, as determined by thermo-gravimetry measurements [54].

presented (see Fig. 4.16). These results have been obtained by a Kramers-Kronig analysis of reflectivity data. The data of the pure compounds ($x = 0$ and $x = 1$) can be compared with our results. For YTiO$_3$ the values in the gap are much higher than what we found from the transmittance. This discrepancy may be attributed to the Kramers-Kronig analysis (see discussion of the results on LaMnO$_3$ in section 3.3). In the case of LaTiO$_3$ the discrepancy is far too large to be explained in the same way. Since the background in the optical conductivity is strongly increasing with oxygen doping (see Fig. 4.15), a deviation from the stoichiometric value of 3.0 could be responsible for the obtained values of $\sigma(\omega)$. Remarkably, the onset of $\sigma(\omega)$ in LaTiO$_3$ is observed at about 0.2 eV in Fig. 4.16, in agreement with our data.

Summary

In summary we state that the orbital excitation energy and the observed distortions [57] can be described satisfactorily within a local crystal-field scenario, in which the t_{2g} splitting
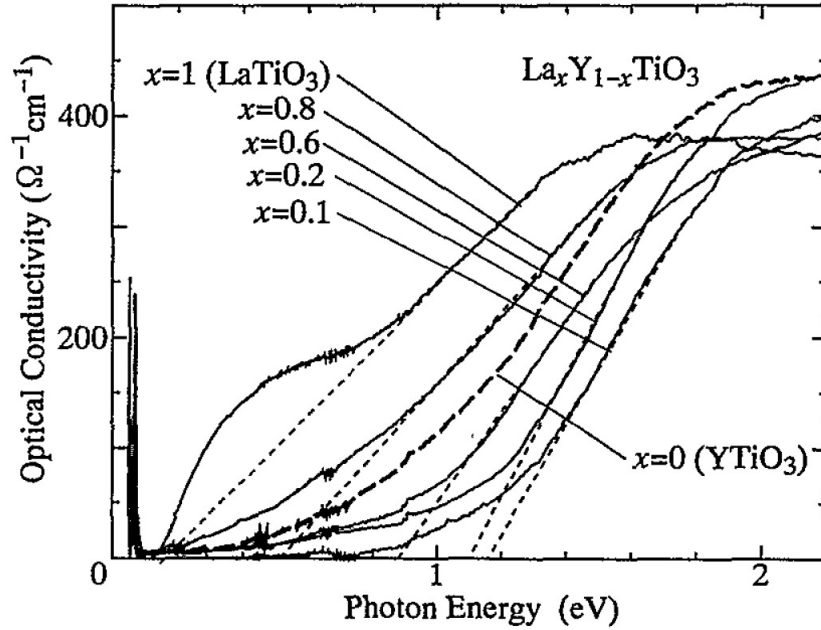
Figure 4.16: The optical conductivity of samples of $La_xY_{1-x}TiO_3$ at 300 K for several values of x [72]. These data were obtained by a Kramers-Kronig analysis of the reflectance.

is dominated by the coupling to the lattice. On the basis of our optical conductivity data, we did not find any clear evidence for strong orbital fluctuations. Also the isotropic spin-wave dispersion of $LaTiO_3$ observed in inelastic neutron scattering [49] can be explained within a crystal-field scenario [157, **?**]. The small ordered moment may result from the combination of quantum fluctuations within the spin channel, spin-orbit coupling and the small Hubbard gap. The latter gives rise to enhanced fluctuations both in the charge and in the orbital channel and thus may contribute significantly to the reduction of the ordered moment [158].[6] The observation of a polarization dependence in $YTiO_3$ strongly challenges the interpretation of predominant orbital fluctuations in this compound.

---

[6]At the same time, this is the central idea behind the orbital liquid scenario: the small gap gives rise to strong orbital fluctuations which in turn reduce the spin order [34].

Chapter 5

Zero-field incommensurate spin-Peierls phase with interchain frustration in TiOX

Low-dimensional quantum spin systems have generated a great deal of interest since the discovery of high-T_c superconductivity in the cuprates. These systems have in common two-dimensional $S = 1/2$ layers. The proposal that the mechanism behind high-temperature superconductivity in these systems may be related to exotic properties of low-dimensional quantum spin systems has been a major driving force behind the advance of quantum magnetism. Although a lot of effort has been spent, many interesting questions still remain in such systems. Naturally, the initial emphasis was placed on understanding materials involving Cu^{2+} ions with the $3d^9$ configuration [123, 124]. However, more recently $S = 1/2$ systems containing ions of the early transition-metal oxides with a $3d^1$ configuration like V^{4+} and Ti^{3+} have attracted considerable interest. For the doped metallic states of these Mott insulating systems, superconductivity has been predicted [145]. The main difference of the $3d^1$ systems and the $3d^9$ systems is that the orbital degeneracy is within the t_{2g} orbitals instead of the e_g degeneracy in the cuprates (in cubic symmetry). In contrast to the e_g systems with an almost completely quenched orbital moment, in the early transition-metal ions the orbital angular momentum is partially preserved by a *pseudo* angular momentum $\tilde{L} = 1$. In lower symmetry the orbital degeneracy is removed further, but for a sufficiently small splitting within the t_{2g} subshell some orbital angular momentum is still present. As an example for such an interesting system we consider NaV_2O_5 [125, 126] where due to the mixed valency of V^{4+} and V^{5+} also a charge degree of freedom is present. This system undergoes an orbital-ordering and charge-ordering transition at 34 K, where a large energy gap of $E_g = 98$ K opens [126, 127, 128, 129]. The ratio of $2E_g/k_BT = 6$ is much larger than the BCS value of 3.5 expected for conventional spin-Peierls transitions with lattice dimerization. Intensive theoretical and experimental effort has been spent to understand this exotic phase. Also in the absence of charge degrees of freedom fascinating physics may arise, as for instance the concept of orbital-liquid states that has been discussed in the previous chapter.
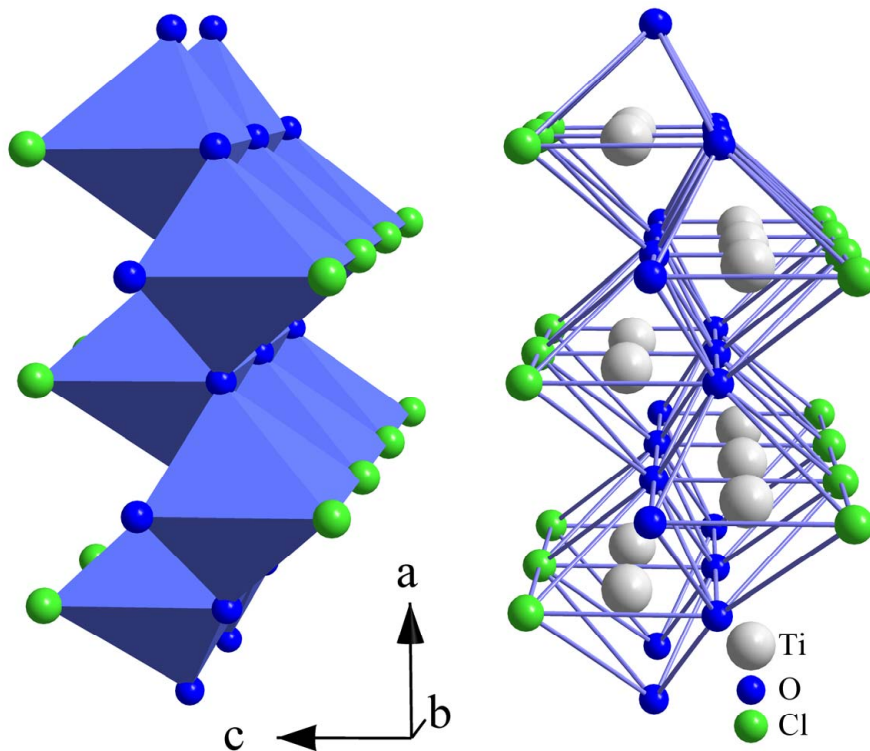
Figure 5.1: View along the b (y) axis on the crystal structure of TiOCl. TiOBr is isostructural with slightly different lattice constants due to the larger ionic radius of bromine compared to chlorine. In the bilayer on the left the arrangement of the strongly distorted $[TiO_4Cl_2]$ octahedra is depicted, whereas on the right the open faces of the octahedra give a view on the buckled Ti-O layers. As a local reference frame we use $x \parallel a$, $y \parallel b$, and $z \parallel c$. For convenience, we use this coordinate system not only in the high-temperature phase, but for the whole temperature range.

5.1 The case of TiOX

Another material that fits well in this class of $3d^1$ $S = 1/2$ systems with peculiar properties is TiOX (X=Cl, Br). From a structural point of view it is a two-dimensional system. At room temperature it is present in the space group $Pmmn$ (No.59). As seen from the crystal structure shown in Fig. 5.1 it is build up from buckled Ti-O bilayers which are well separated from each other by Cl ions. The bilayers are stacked along the c direction. The local environment of the Ti ions is an octahedron $[TiO_4Cl_2]$ where two adjacent corners are occupied by Cl ions. Throughout this chapter we will use the crystallographic axes a, b, c as the local reference frame x, y, z. Note that with this choice xy and $3x^2 - r^2$ are e_g orbitals and zx, yz, $y^2 - z^2$ are t_{2g} orbitals.

It has been suggested by Beynon and Wilson in [121] that TiOCl is a realization of
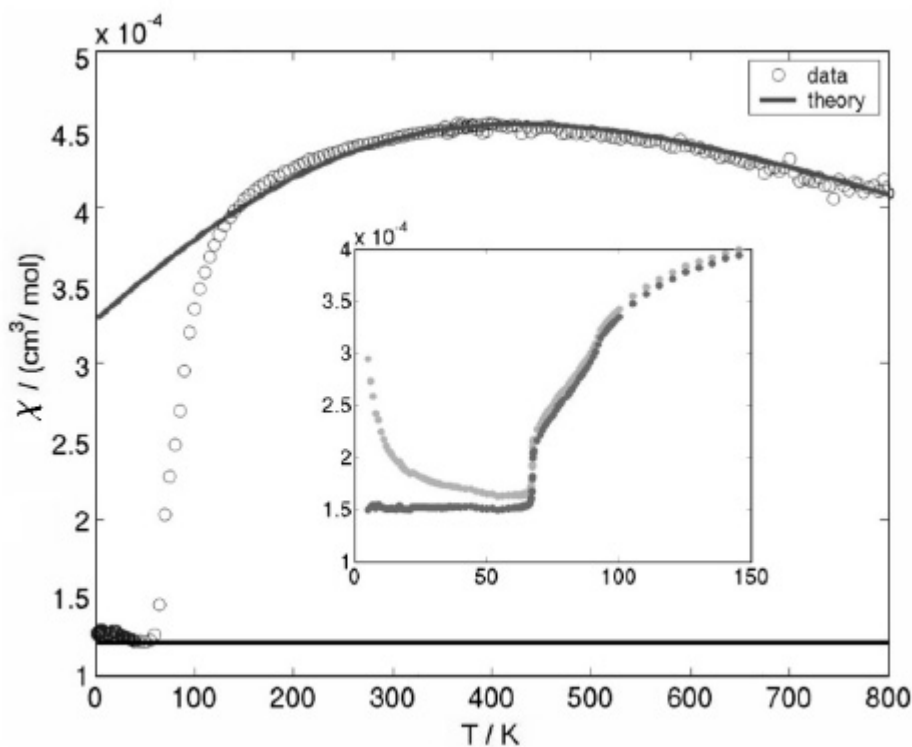
Figure 5.2: The magnetic susceptibility of TiOCl with Curie subtraction [50]. The solid curve is the result of a fit assuming a $S = \frac{1}{2}$ Heisenberg chain. The fit yields a coupling parameter $J = 660$ K. The inset shows the low-temperature range magnified. The data with substraction of a Curie tail (dark grey) and without (light grey) are plotted.

a resonating valence-bond state. This suggestion has been based on the two-dimensional structure that built an analogy to the high-T_c cuprates and on an unusual temperature dependence of the magnetic susceptibility. The latter does neither show a Curie-Weiss type behavior nor does it exhibit standard antiferromagnetic order, giving rise to the expectation that an unconventional state is present in this compound.

However, recently TiOCl has been investigated by Seidel *et al.* [50]. Renewed measurements of the magnetic susceptibility led to the results shown in Fig. 5.2, different from the former ones [121]. For temperatures above 130 K the susceptibility can be fitted to a Bonner-Fisher curve [205] of a $S = 1/2$ chain with a magnetic coupling constant J of 660 K. Below 130 K the data starts to deviate from the fit, and at 67 K the magnetic susceptibility drops suddenly to zero.

Additionally the results of LDA+U band-structure calculations [50] are shown in Fig. 5.3. In LDA (without U) six bands around the Fermi level are identified as t_{2g} bands which are well separated from the e_g bands. As seen from Fig. 5.3, two nearly degenerate, one-dimensional bands split off from the rest of the t_{2g} bands in LDA+U. From this gap the
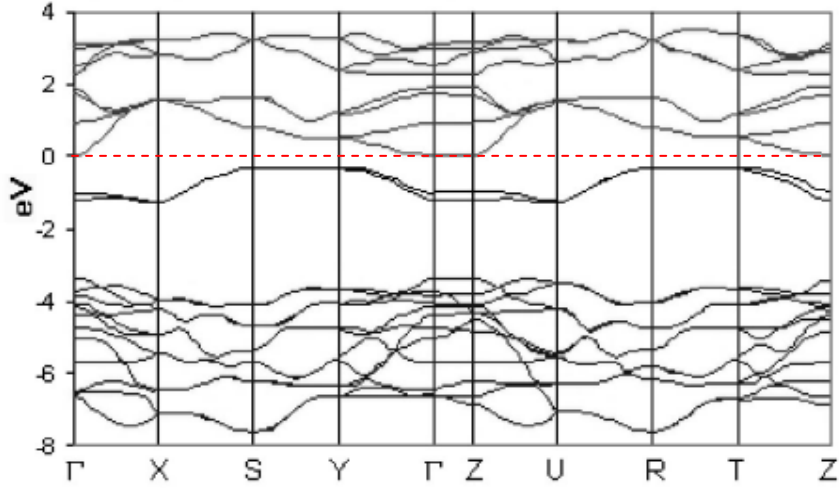
Figure 5.3: The results of a LDA+U calculation for TiOCl [50]. The two bands lying directly below the Fermi energy (indicated by the dashed red line) are t_{2g} bands. They are separated from the other d bands that are lying above the Fermi level.

insulating behavior of TiOCl results (note that there are two atoms per unit cell). These two bands are derived from the $d_{y^2-z^2}$ orbitals (d_{xy} in the coordinate system used in [50]) corresponding to linear chains shown in the left panel of Fig. 5.4. The exchange constant in an effective Heisenberg model has been estimated via $J = 4t^2/U = 714$ K (the bandwidth of 0.9 eV has been identified with $4t$, where t is the nearest-neighbor hopping in a one-dimensional tight-binding model, $U = 3.3$ eV), in agreement with the value derived from the fit of the
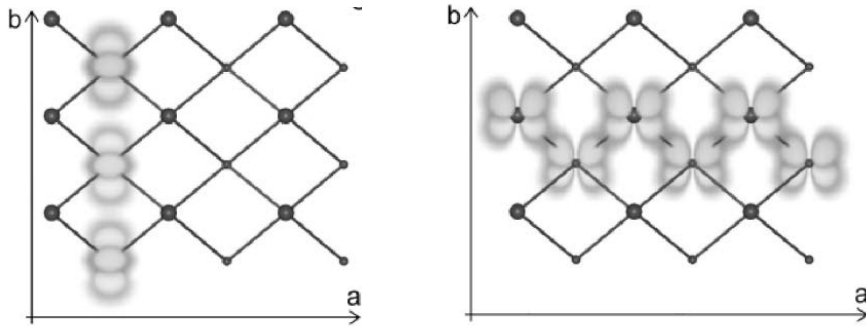
Figure 5.4: The direction of the occupied states calculated by LDA+U for TiOCl [50]. Two possible directions of the chains: On the left side the occupied $d_{y^2-z^2}$ band (d_{xy} in the coordinate system used in [50]) leads to the formation of spin chains in the crystallographic b direction. On the right a zigzag chain along the a direction results from the occupation of the $(d_{xy} + d_{xz})/\sqrt{2}$ orbital. Also the $(d_{xy} - d_{xz})/\sqrt{2}$ orbital could form a chain. Thus orbital ordering is needed to break this symmetry. However, interchain coupling effects and LDA+U favor the scenario of linear chains along the b direction.
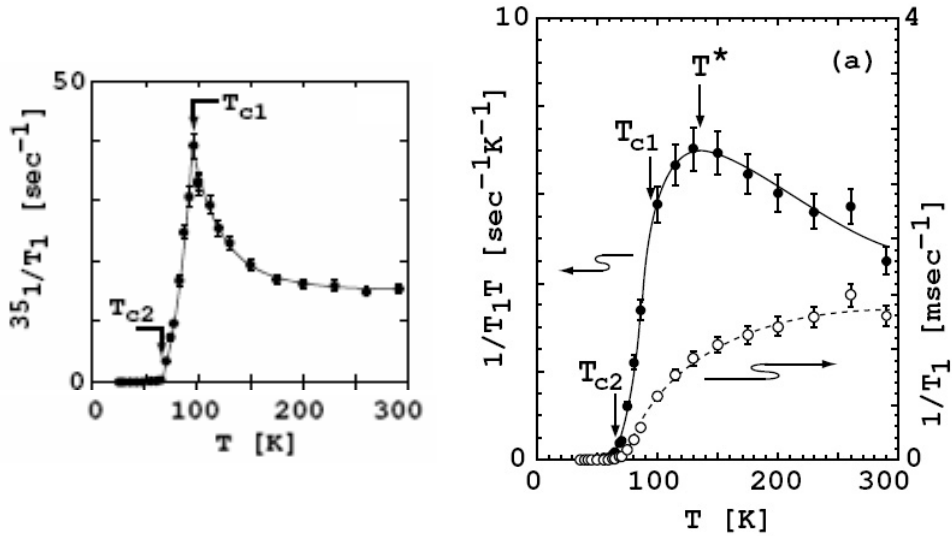
Figure 5.5: NMR data for the Cl ions (left) and Ti ions (right). The reciprocal relaxation time $1/T_1$ is displayed by the open circles. Since this property is proportional to $T \times \sum_{\mathbf{q}} \chi_2(\mathbf{q}, \omega_n)$ it is useful to consider $1/(T_1 T)$ (given by the closed circles) in order to get insight in the magnetic structure. Note that here the labeling of the transition temperatures is $T_{c1} = 94$ K and $T_{c2} = 67$ K. This plot is taken from [122].

magnetic susceptibility. Thus the band structure suggests the existence of one-dimensional spin-1/2 chains in TiOCl, where the spins are localized in Ti d_{yz} orbitals. Hence the system turned out to be actually one-dimensional instead of the two-dimensionality suggested from the structure.

From this one-dimensional electronic structure the vanishing of the magnetic susceptibility at low temperatures is assigned to the opening of a spin gap, which corresponds to a dimerization within the spin chain. Such a nonmagnetic spin-Peierls ground state at low temperatures has been confirmed in many experiments and calculations that followed [51, 113, 122, 130, 131, 132, 133, 134, 135, 137, 141, 142, 143, 145, 146, 147]. In particular temperature-dependent x-ray scattering revealed a doubling of the unit cell in b direction at low temperature (the direction of the chains) [135]. Note that besides $CuGeO_3$ TiOCl is hence the second example of an inorganic spin-Peierls system.

Additionally there is a well pronounced kink in the magnetic susceptibility at about 94 K, indicating another transition. However, a second phase transition is not expected in a conventional spin-Peierls scenario.

NMR data of TiOCl [122] provides a lot of further information on the transition at $T_{c1} = 67$ K and in particular about the striking feature at $T_{c2} = 94$ K, that actually turns out to be a second phase transition. Due to relaxation-time measurements the feature at T_{c2} has been interpreted as the actual emerging of a gap in the spin-excitation spectrum accompanied by a static distortion of the lattice. Consider the nuclear spin-lattice relaxation rate of Ti (see Fig. 5.5) [122]. The closed circles display the property $1/(T_1 T)$ which is
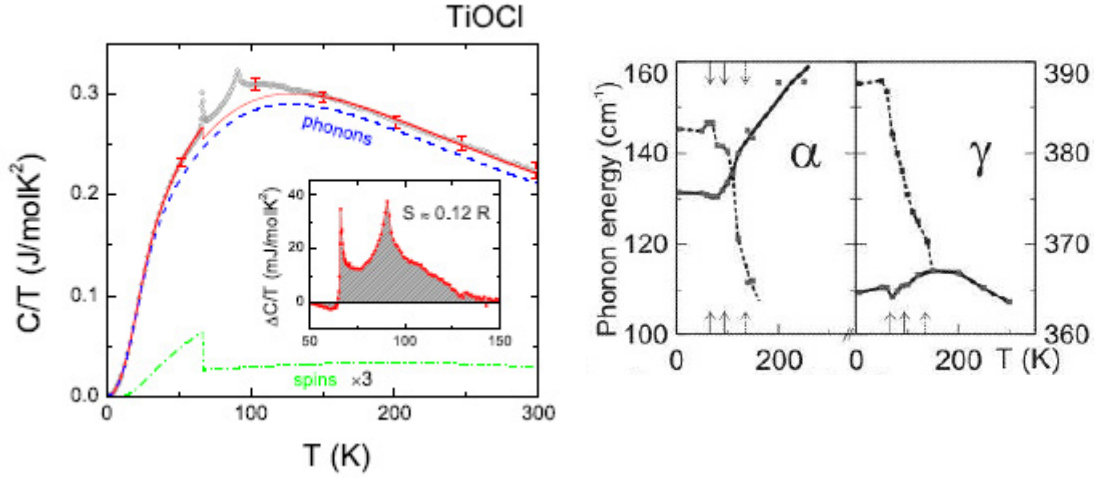
Figure 5.6: On the left the specific heat is shown [134]. In the inset the difference between the data and a fit considering spin and phonon contributions is depicted. On the right the temperature dependence of phonon energies of two strong Raman modes is displayed. The dashed curves belong to phonon modes that are emerging around T^*. This plot has been taken from [130].

proportional to the low-frequency magnetic fluctuations. These fluctuations are enhanced by the growth of short-range correlations with decreasing temperature in absence of a gap in the spin excitation spectrum. The suppression of spin fluctuations starts already at $T^* \approx 135$ K, discussed as a pseudo-gap phase [122]. At $T_{c2} \approx 94$ K the drop of $1/(T_1T)$ is accelerated, suggesting a second-order phase transition at T_{c2}. The opening of the spin gap already at 94 K is also corroborated by the analysis of specific heat measurements [134] (see Fig. 5.6).

Moreover, considering $1/T_1$ of ^{35}Cl it is found that the curve starts to deviate from a constant value even far above T^*, somewhere below 200 K. This has been interpreted in the way that the pseudo-gap phase is driven by a drastic softening of the lattice [122]. This is observed in Raman data as unusual softening of phonons that sets in already at temperatures much higher than T^*. These results are depicted in the right panel of Fig. 5.6 [130].

The lineshape of the NMR signal at the resonance reflects the thermal motion of the ion in the electrical potential surrounding its equilibrium position. This electrical potential is given by the lattice so that a change in the line shape indicates a structural change of the lattice. The lineshapes of the central resonance of ^{47}Ti / ^{49}Ti and ^{35}Cl are shown in Fig. 5.7 [122]. At temperatures above T_{c2} only a single NMR line is observed for both the Cl and the Ti signal, indicating that all Ti sites as well as all Cl sites are equivalent. Below T_{c2} the lineshape of the Ti signal and the Cl signal exhibit a broad continuum. This implies the presence of numerous inequivalent Ti and Cl sites in the crystal suggesting an incommensurate structure. The involvement of the lattice is corroborated by Raman measurements of the phonon spectrum [130]. The temperature dependence of the phonon energies shows a feature at T_{c2} [130] as seen from Fig 5.6.
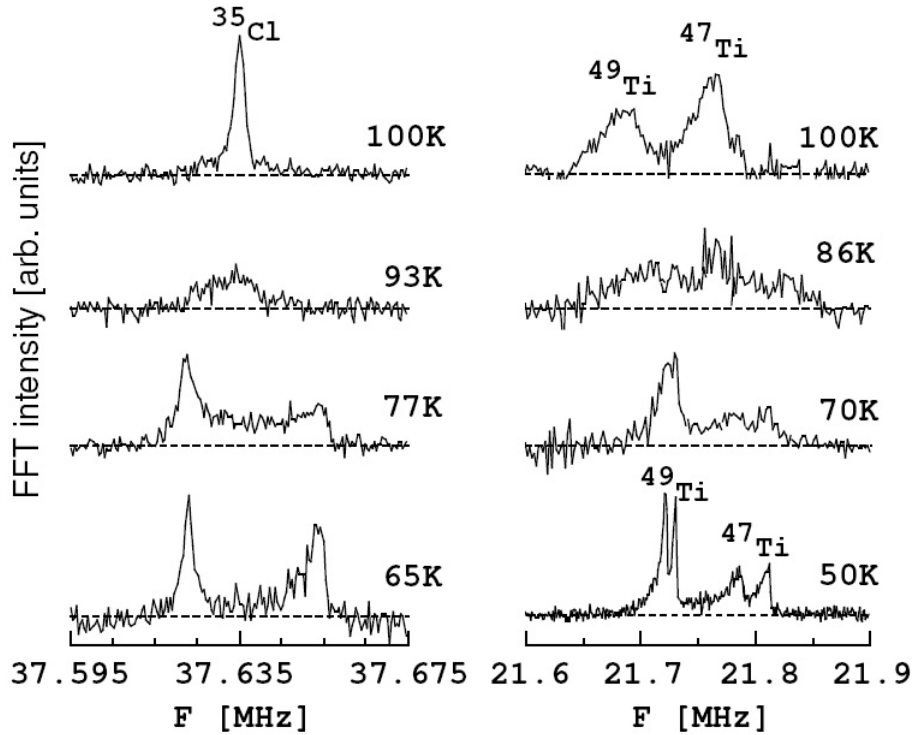
Figure 5.7: The lineshape of the NMR signal of Cl (left) and Ti (right) for different temperatures. For both Cl and Ti the lineshape broadens below T_{c2} and the peaks are split up below T_{c1}. This plot is taken from [122].

At T_{c1} the lineshape exhibits again sharp peaks but the former (above T_{c2}) single lines are now split into two close-lying peaks. This is unexpected for a dimerized chain since all sites are equal. The existence of two inequivalent sites indicates that interchain coupling plays a role in TiOCl. The peaks are already emerging above 67 K in the vicinity of T_{c1} as a kind of precursor of the transition. This transition into a nonmagnetic (fully dimerized) ground state turns out to be of first order due to a hysteresis that has been observed in the specific heat [134].

Summarizing these results we can state that TiOCl undergoes two phase transitions. One of first order at $T_{c1} = 67$ K and another one of second order at $T_{c2} = 94$ K. Additionally at $T^* \approx 135$ K the onset of an instability of the lattice is observed. The different phases are interpreted as follows:

- Coming from room temperature, the lattice begins to soften somewhere below 200 K. At about $T^* \approx 135$ K a suppression of the spin fluctuations emerges, which indicates a pseudo-gap phase [122].

- At $T_{c2} = 94$ K a second-order structural transition into an incommensurate phase takes place. It is characterized by accelerated decrease of the magnetization.

111
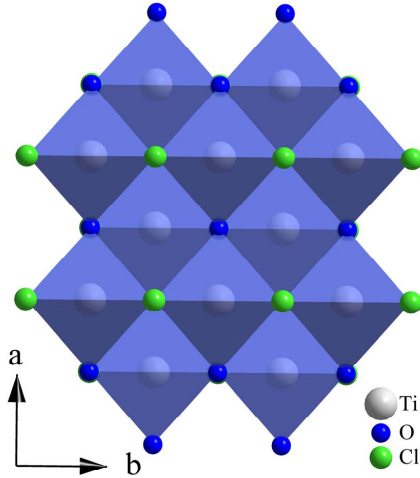
Figure 5.8: View along the c direction onto the ab plane. Note the alternating positions of the Ti sites within the two Ti-O layers of one bilayer. See also Fig. 5.29.

- Finally at $T_{c1} = 67$ K a first-order transition to a nonmagnetic ground state takes place. Here the system appears to be in a conventional spin-Peierls state with a doubling of the room-temperature unit cell in chain direction (crystallographic b direction).

The question that is still open at this point is why the system is not entering the low-temperature spin-Peierls phase already at $T_{c2} = 94$ K when the spin gap opens. What is the actual driving force for interesting physics observed in TiOCl? It has been speculated [50, 113, 122, 130, 131, 132, 133, 134] that this unconventional behavior is caused by strong orbital fluctuations, assuming a near degeneracy of the t_{2g} subshell or at least two nearly degenerate orbital states. This assumption has been the starting point for our investigation of this system. Our aim has been to determine the orbital excitations.

5.2 Crystal structure of TiOX

Before discussing our results in the next section, we will take a closer look at the crystal structure of TiOCl. TiOBr is isostructural to TiOCl. The structure of TiOCl consists of bilayers that are build up from edge sharing [TiO$_4$Cl$_2$] octahedra. In Fig 5.8 the view is along the c axis onto an ab plane, i.e. onto the bilayers. This viewpoint is obtained by rotating the layer in Fig. 5.1 by 90° around the vertical (x) axis. The Ti sites of the two layers that make up one bilayer are shifted with respect to each other by half of the Ti-Ti distance in both the a and the b direction.

Remarkable is also that the [TiO$_4$Cl$_2$] octahedra are strongly distorted (see Fig. 5.9). In particular, they are strongly compressed along the a (x) axis. At room temperature, the Ti-O bond lengths differ considerably, as seen from table 5.1.

The space group is $Pmmn$ at 300 K and $P2_1/m$ at 4 K [135]. The low-temperature structure results from the dimerization along the chains. In the low-symmetry phase the ions
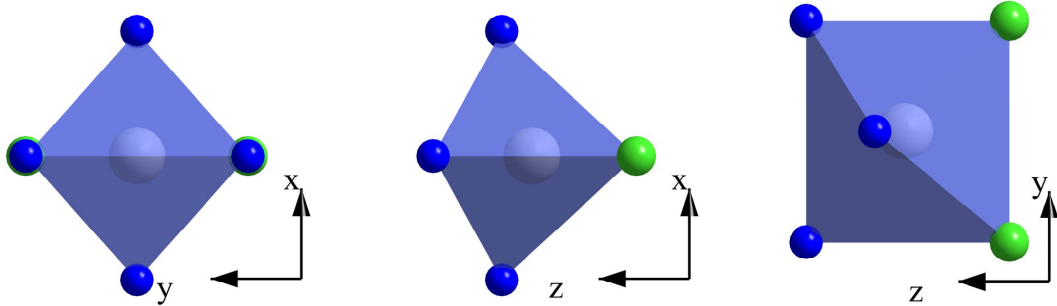
Figure 5.9: View along the three crystallographic axes on the local octahedral environment of the Ti ions. Ti (gray) is placed in the center of the $[O_4(blue)Cl_2(green)]$ octahedron. Remarkable is the strong distortion that destroys the inversion symmetry at the Ti site. The local symmetry at the Ti site is given by two mirror planes, namely the yz and the zx plane. These two symmetry elements give a strong restriction on the orbital contribution with odd character.

are shifted only within the bc plane (with respect to the $Pmmn$ structure), minimizing the strain that is introduced by the dimerization. Important is also that there is no inversion symmetry on the Ti site (see Fig. 5.9). Thus orbital excitations are directly infrared active, i.e., they contribute to $\sigma(\omega)$ without the additional excitation of a phonon, in contrast to $RTiO_3$ and $LaMnO_3$ (see also section 2.3.2). From the symmetry at the Ti site it is also possible to deduce the polarization dependence of the directly allowed dipole excitations by considering p-d dipole matrix elements.

5.3   Orbital excitations vs. orbital fluctuations

The crucial question in the system TiOX is what kind of mechanism prevents the system to undergo a simple second-order transition into a dimerized phase already at the opening of a spin gap at T_{c2}. This mechanism should also be capable of producing an incommensurate structure in the chain direction and also perpendicular to it [122, 136]. It has been speculated [50, 113, 122, 130, 131, 132, 133, 134] that this unconventional behavior is caused by strong

Table 5.1: Some characteristic bond lengths are given from [138] for X=Cl and [142] for X=Br. Both data sets are obtained at room temperature.

bond	direction	TiOCl	TiOBr
Ti-O	x direction	1.962	
	yz plane	2.191	
Ti-X	yz plane	2.398	
Ti-Ti	y (chain) direction	3.361	3.4853
Ti-Ti	interchain direction	3.177	3.1787

113

orbital fluctuations of the single $3d$ electron on the Ti site, assuming a near degeneracy of the t_{2g} subshell or at least two nearly degenerate orbital states. Such a near degeneracy should lie in the range of thermal fluctuations ($\ll$100 meV $\hat{=}$ 1140 K). It would contribute to the optical conductivity at low frequencies. Our aim has therefore been the observation of the orbital excitations in this system.

The samples we measured in optical spectroscopy were prepared by a gas transport reaction [206]. The crystals were grown by L. Jongen[1]. The purity of the crystals was checked by x-ray powder diffraction. The typical dimensions of single crystalline samples are a few mm^2 in the ab plane and less than 30 μm in c direction. The magnetic susceptibility of these TiOCl samples has been measured in a Faraday balance in a temperature range from 4 K - 550 K, and in case of the TiOBr samples in a SQUID magnetometer from 4 K - 300 K in an applied magnetic field of 1 Tesla[2]. In order to increase the signal several crystals were aligned so that the total quantity had been $\approx$ 10 mg [113, 143]. Additionally, the specific heat C_p has been determined on pressed pellets from crashed single crystals. The measurements were performed in different calorimeters using the continuous heating method for TiOCl ($\approx$ 29 mg) in a temperature range from 40 K to 300 K and the relaxation-time method for TiOBr ($\approx$ 3 mg) for temperatures from 2 K to 300 K. The linear thermal expansion $\alpha = \partial \ln L / \partial T$ has been measured along the c axis ($L \parallel c$) using a capacitance dilatometer. To increase the effect, seven single crystals have been stacked on top of each other. The results are compared in Fig. 5.10. For the magnetic susceptibility the results are in agreement with the data shown in [50]. The thermal expansion exhibits the strongest features at both transition temperatures. The data clearly show that TiOBr exhibits the same physics as TiOCl, only with somewhat reduced energy scales ($J_{Br} \approx$ 375 K, T_{c1} = 48 K, T_{c2} = 28 K). Thus the appearance of a second transition is an intrinsic feature of this system.

In order to determine the orbital excitations we performed transmittance measurements of single-crystalline samples of TiOCl as well as of TiOBr. The result on TiOCl is depicted in Fig. 5.11 for two polarization directions, $E \parallel a$ and $E \parallel b$. Unfortunately, measurements with $E \parallel c$ could not be performed since the available samples are very thin in the stacking direction. Our data are in agreement with unpolarized measurements reported for energies above 1.3 eV [139]. Above about 2 eV, the sample is opaque due to excitations across the electronic gap. The transmittance is strongly suppressed at 0.6-0.7 eV for $E \parallel a$ and 1.5-1.6 eV for $E \parallel b$. The absorption feature at 0.65 eV appears as a weak peak also for $E \parallel b$, and the feature at 1.5 eV gives rise to a weak shoulder for $E \parallel a$. The corresponding data of TiOBr are shown in Fig. 5.13. Since the sample measured here has been thicker than the one of TiOCl, the transmittance drops to zero at the strong absorption features. Therefore the transmittance T itself and not $(-\ln T)$ is plotted. The similarity to TiOCl is obvious. In both polarization directions, $E \parallel a$ and $E \parallel b$, peaks are observed at slightly lower energies than in TiOCl, 0.62 eV ($E \parallel a$) and 1.4 eV ($E \parallel b$). Also the electronic gap is about 0.1 eV lower in energy compared to TiOCl. Due to the larger sample thickness, the shoulder at 1.4 eV for $E \parallel a$ is more pronounced in the transmittance of TiOBr than in the data for TiOCl.

---

[1]L. Jongen, A. Möller, G, Meyer, Institut f. Anorganische Chemie, University of Cologne.

[2]The data of the magnetic susceptibility, the thermal expansion, and the specific heat have been measured by J. Baier and M. Kriener at the II. Physical Institute, University of Cologne.
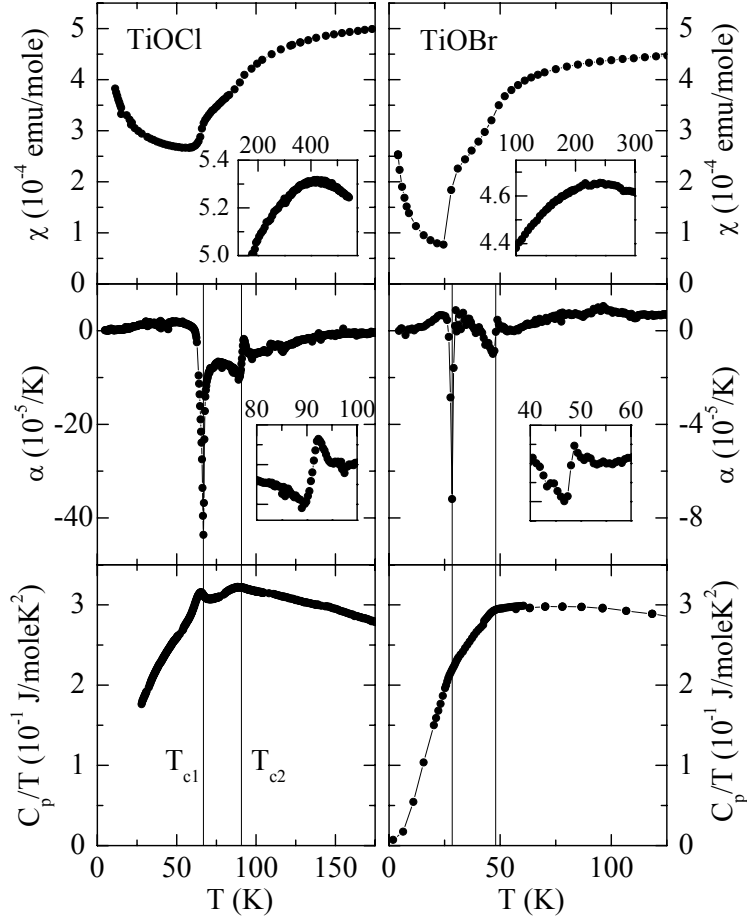
Figure 5.10: The macroscopic properties of TiOCl (left column) and TiOBr (right column). These are from the top the magnetic susceptibility, the thermal expansion, and the specific heat. The vertical lines indicate the two transition temperatures T_{c1} and T_{c2}. The inset in the upper panel shows the high-temperature range of the magnetic susceptibility in each case. In the middle panel the inset magnifies the range around T_{c2}. The plot is taken from [143].

Moreover it is remarkable that a strong background rises immediately after the phonon range at 0.2 eV, especially for $E \parallel b$. From our measurements it is not clear whether this is an intrinsic feature of the compound or due to scattering at defects.

An interpretation of the strong absorption features in terms of phonons or magnetic excitations can be excluded at such high energies. The excitation energies and in particular the polarization dependence are in good agreement with the results for the orbital excitations obtained in a cluster calculation (see table 5.2). We conclude therefore that these features can unambiguously be attributed to orbital excitations.

The dependence of the peak positions on temperature is very small. The peak at 1.5
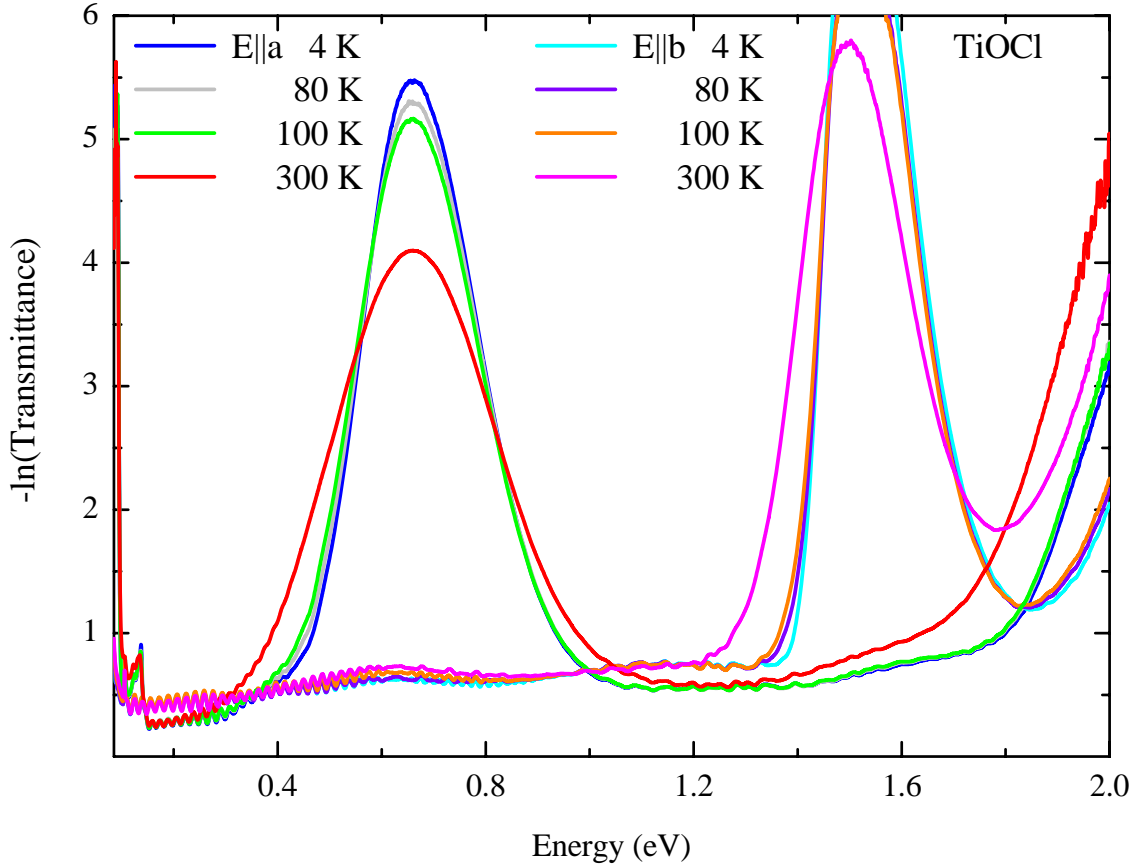
Figure 5.11: The negative logarithm of the transmittance of TiOCl is shown. Below $\approx 0.1\,\text{eV}$ phonon absorption sets in, multi-phonon peaks are observed up to about $0.15\,\text{eV}$, orbital excitations at about $0.65\,\text{eV}$ ($E \parallel a$) and $1.5\,\text{eV}$ ($E \parallel b$), and the band gap $\Delta \approx 2\,\text{eV}$. The periodic Fabry-Perot fringes in the highly transparent range indicate multiple reflections within the sample.

eV shifts between 300 K and 4 K about 40 meV towards higher frequencies. Additionally a broadening of the peaks for increasing temperature is observed. Such a behavior is expected for peaks which are broadened due to the Franck-Condon effect. At the transition temperatures T_{c1} and T_{c2} no sizable changes occur. This clearly rules out a significant change of the orbital occupation as a function of temperature. A more detailed discussion of the temperature dependence is given below.

The absorption at about $1.5\,\text{eV}$ shows an asymmetric profile with a steep drop of the transmittance on the low-energy side, in agreement with the expectations for phonon sidebands in case of small changes of the relaxed bond length (see Fig. 2.28). A precise determination of the line shape requires measurements of a thinner sample, in which the transmittance is not suppressed to zero in the vicinity of the center frequency (see TiOCl Fig. 5.11).
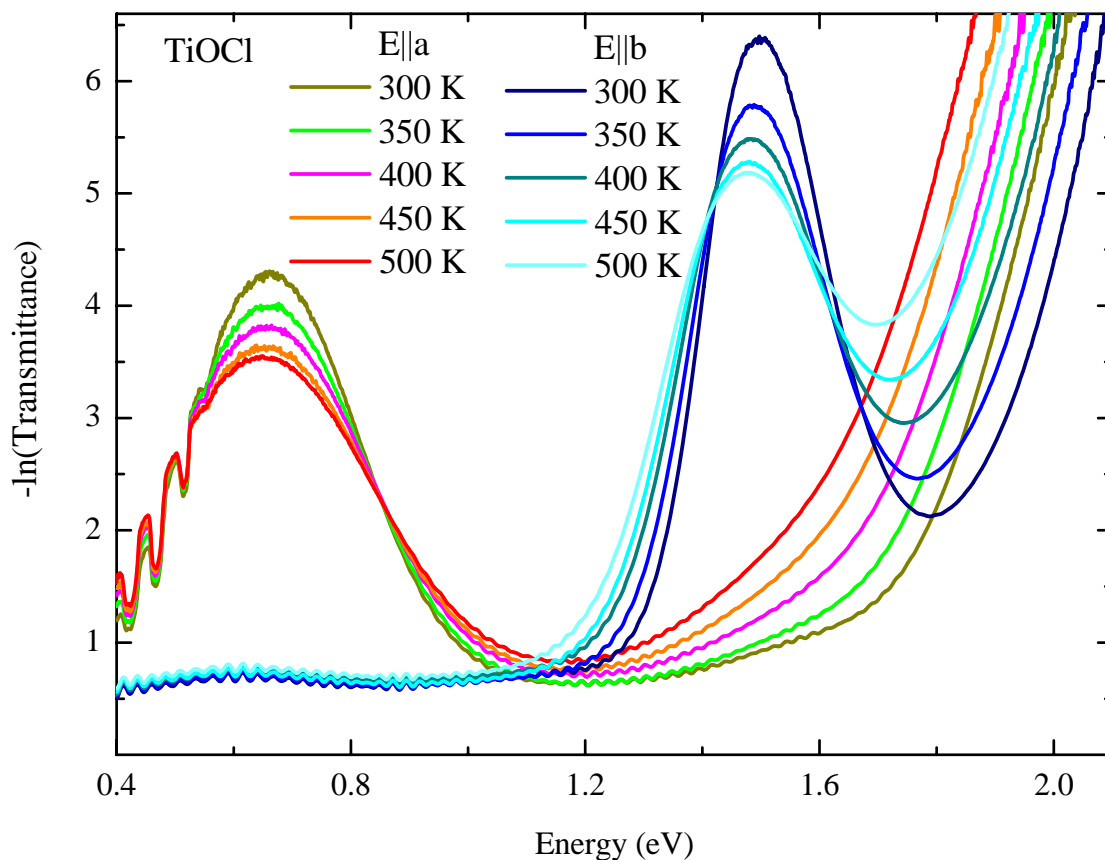
Figure 5.12: The negative logarithm of the transmittance of TiOCl for temperatures above room temperature is shown. The dips that occur below 0.6 eV are an artefact from the polarizer. The sample used here was slightly thicker compared to the one used for the measurements depicted in Fig. 5.11.

The two phase transitions of TiOX are observed in the phononic absorption spectrum (see section 5.4). Therefore we have clear evidence that these transitions are structural transitions. We have also demonstrated that the orbital excitations do not change significantly at the transition temperatures. However, at the transition temperatures the orbital excitations should be influenced somehow. In Fig. 5.14 we plot the negative logarithm of the transmittance of TiOCl for $E \parallel a$ at 471 meV over the temperature. This energy is on the low-energy side of the orbital excitation centered at 650 meV. Unfortunately the peak position could not be determined with satisfying accuracy, therefore this energy at the side has been chosen. The absolute value of the transmittance at 471 meV will reflect a shift of the center frequency, but it also may change due to broadening of the absorption band. We find an exponential increase with temperature above 100 K. This increase is due to the broadening of the absorption peak that transfers spectral weight from the center of the peak to its sides. Towards

117
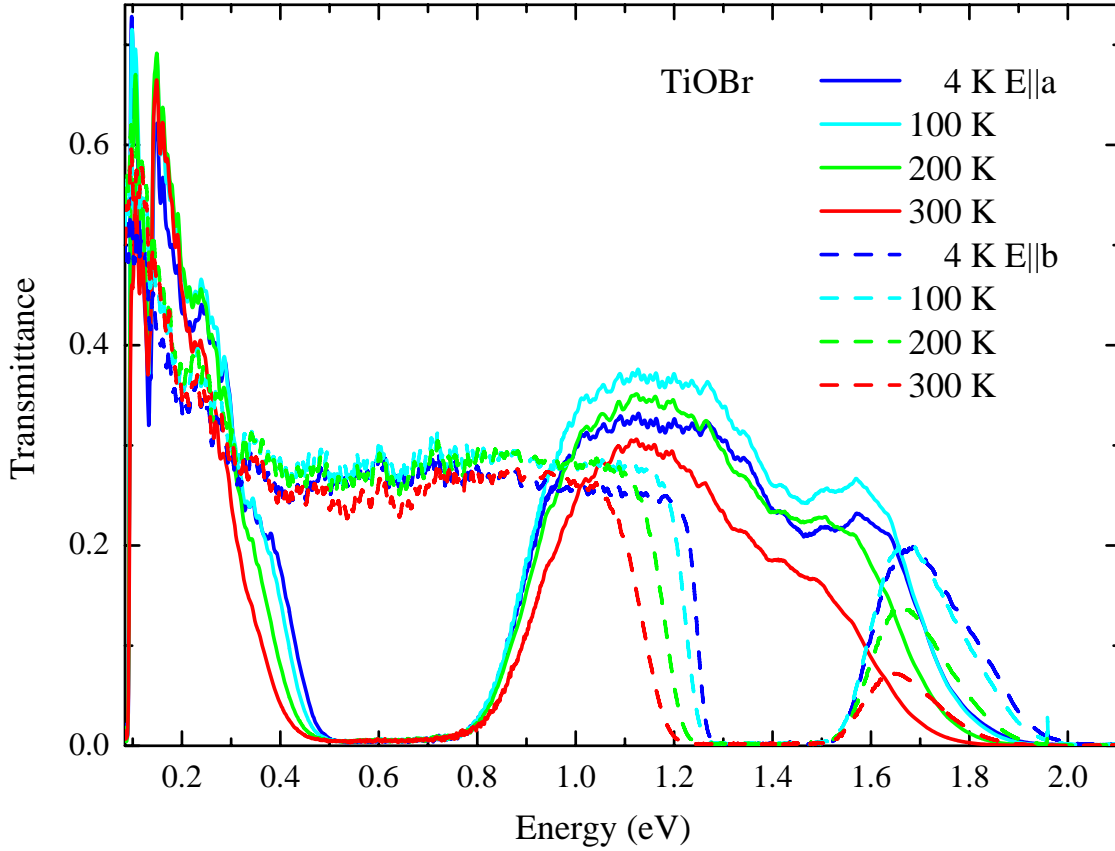
Figure 5.13: The transmittance of TiOBr is shown. Below $\approx 0.1\,\mathrm{eV}$ phonon absorption sets in, multi-phonon peaks are observed up to about $0.15\,\mathrm{eV}$, orbital excitations at about $0.6\,\mathrm{eV}$ ($E \parallel a$) and $1.4\,\mathrm{eV}$ ($E \parallel b$), and the band gap $\Delta \approx 2\,\mathrm{eV}$. The periodic Fabry-Perot fringes in the highly transparent range indicate multiple reflections within the sample.

low temperatures the slope of this increase decreases and it becomes very small in the limit $T \to 0$. In between these two ranges we observe a sharp step at T_{c1} and a decrease of the slope, which is in opposition to the trend that the slope increases with temperature. In order to check that this behavior is not merely observed by accident, we compare the temperature dependence of the negative logarithm of the transmittance at 471 meV with that at 446 meV in the inset of Fig. 5.14.

The negative logarithm of the transmittance of TiOCl for temperatures up to 500 K is shown in Fig. 5.12. The measurements before and after heating the sample were on top of each other within the small error bar of time stability of the spectrometer. This indicates that the sample has not been modified during the heating procedure. We observe a broadening of the two absorption peaks and a narrowing of the gap as the temperature increases. The orbital occupation clearly does not change up to 500 K. The dips observed below 0.6 eV for

118
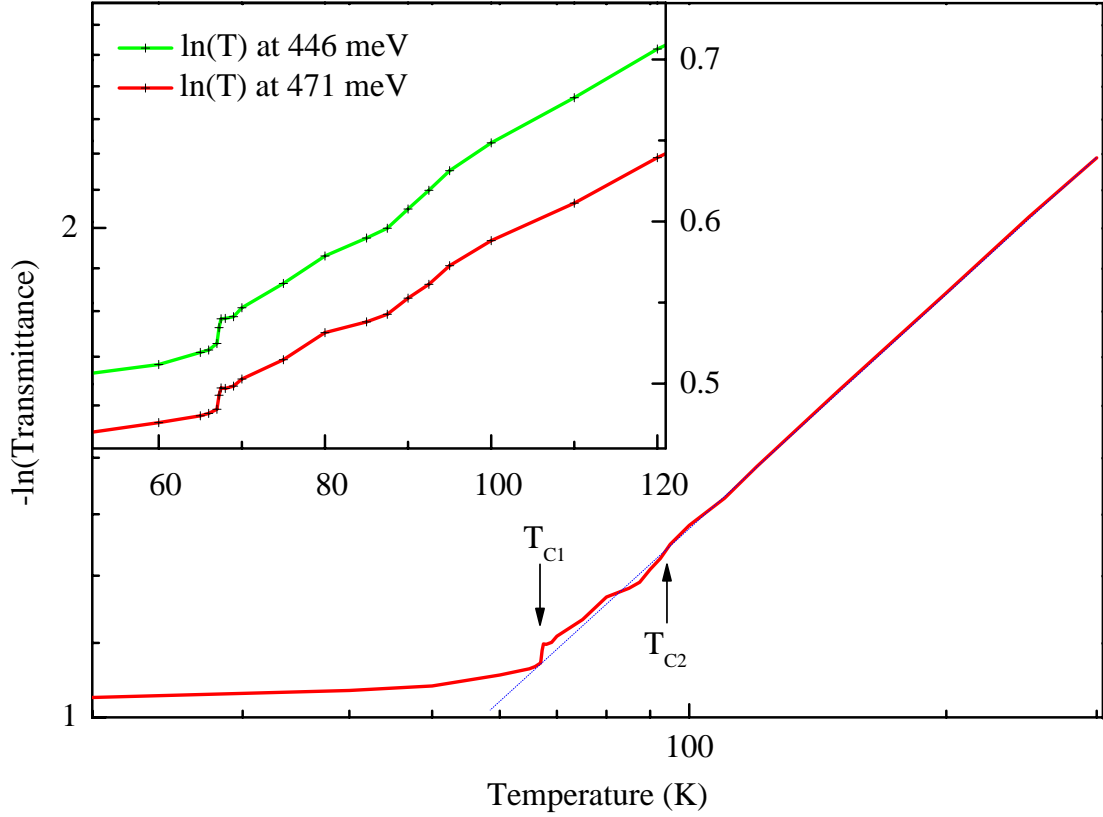
Figure 5.14: The temperature dependence of the negative logarithm of the transmittance at 471 meV is shown. The inset compares this data in the temperature region around the intermediate phase with the data obtained at a second energy (446 meV).

$E \parallel a$ are artificially produced by absorptions of the polarizer (Glan-Thomson prism), as seen from comparison with the data in Fig. 5.11.

A weak and broad feature is observed, especially in the data of TiOCl shown in Fig. 5.15, at about 0.62 eV for $E \parallel b$, i.e. in the polarization perpendicular to the one for which the strong absorption is found. This feature may possibly be attributed to a small misalignment of the polarizer. However, this is unlikely since this weak peak appears in different measurements using different samples and polarizers. Another origin of this absorption could be the phonon-activated mechanism, but the temperature dependence is hard to understand by this mechanism since one would expect that the peak is becoming sharper by lowering the temperature. The most plausible explanation is a very small admixture of xy character to the ground state (see below), e.g. by spin-orbit coupling or due to the dispersion (i.e. away from the Γ point).

In the cluster calculation for TiOCl, we have to take into account the hybridization between the Ti ions and both, O as well as Cl ions. In comparison to for instance LaTiO$_3$ or LaMnO$_3$, we thus have two additional parameters, namely the charge-transfer energy
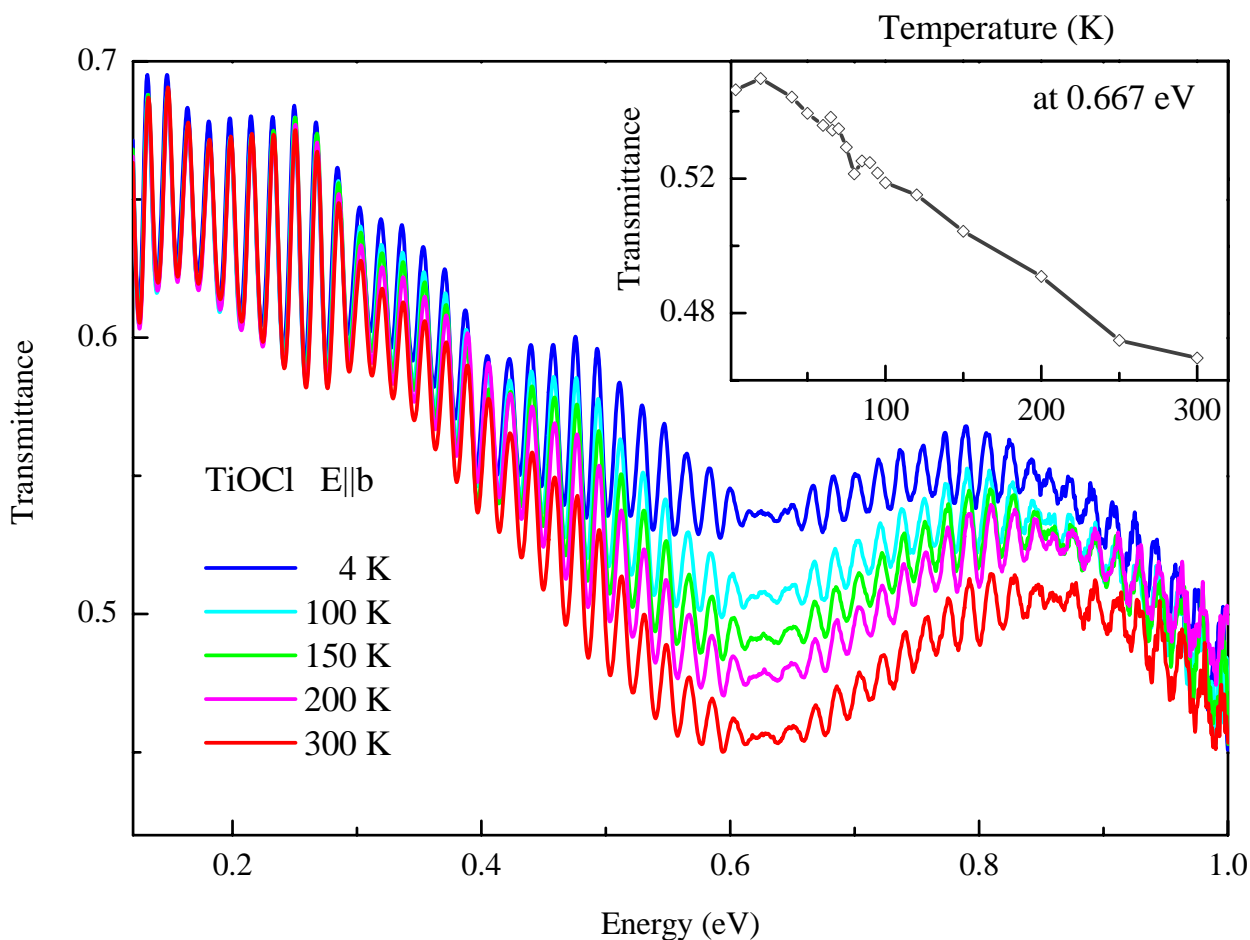
Figure 5.15: The transmittance of TiOCl for $E \parallel b$ is displayed in the mid-infrared region for some temperatures. A weak absorption is observed as broad dip in the transmittance which is loosing weight with decreasing temperature. The temperature dependence of the transmittance at one energy at the center of this dip is shown in the inset. The Fabry-Perot fringes indicate multiple scattering within the sample.

Δ_{Cl} between Ti and Cl, and the Ti-Cl hybridization t_{Cl}. A comparison of the results of a cluster calculation with the results of a point-charge model is given in table 5.2. The ground-state orbital obtained in both models is the $y^2 - z^2$ orbital. Note that due to the choice of the axes in the yz plane this orbital has t_{2g} character. It turns out that an accurate description of hybridization effects is essential in order to reproduce the splitting between the t_{2g} and e_g subshells. Due to the strong compression of the octahedra along x, the electrostatic contribution of the point-charge model predicts that the lowest excited state has d_{yz} character, i.e., belongs to the e_g subshell.[3] At the same time, the polarization selection rules given in

---

[3] The ligands are located approximately along the diagonals of the yz plane, hence d_{yz} denotes a state from

table 5.2 predict for 300 K that this transition to the d_{yz} level (with a small admixture of y character) can be observed for $E \parallel b$. Experimentally, the corresponding absorption feature for $E \parallel b$ is found at about 1.5 eV, i.e., more than 1 eV higher than predicted by the point-charge model. However, the energy of this transition can be described correctly by taking into account the hybridization between Ti and its ligands, which typically adds more than 1 eV to the splitting between t_{2g} and e_g subshells (see the discussion of the molecular-orbital theory in section 2.1.1).

The parameters U_{dd}=4 eV, Δ_O=5 eV, and Δ_{Cl}=3 eV are estimated following the LDA+U results of reference [133]. The orbital excitation energies depend only weakly on U_{dd}. In order to model the relative strength of the Ti-O and the Ti-Cl hybridization, we have to consider the larger ionic radius of Cl compared to O ($r_{Cl} - r_O \approx 0.4$ Å) as well as the larger polarizability. For the former we assume that the hybridization is the same for the two ligands if the bond length equals $r_{Ti} + r_X$ (X=O, Cl). Additionally, the larger polarizability of Cl compared to O is modelled by a factor t^* by which the Ti-Cl hybridization is further enhanced. Good agreement between the calculated energies and the experimental results at both temperatures, 4 K and 300 K, is obtained for $t^* \approx 1.3$ (see table 5.2).[4]

The point-charge model does allow to estimate the polarization dependence and the strength of the orbital excitations can be predicted (see equation 2.1). In principle the polarization dependence can be seen from the symmetry of the structure by utilizing p-d matrix elements (see Appendix D). The strength is obtained by adding $4p$ states to the possible states considered in the point-charge calculation. These $4p$ states are assumed to be some eV away from the $3d$ states. However, there will be a small $4p$ contribution to the ground state giving rise to a finite $3d$ to $4p$ dipole transition probability. In particular, this leads to strict polarization selection rules in the room-temperature structure (see table 5.2).

The energy of the lowest excited state (xy orbital) is crucial in order to determine whether orbital fluctuations are the correct explanation for the interesting physics observed in TiOCl. In the room-temperature structure, the transition to the first excited state is not directly infrared active, but it becomes directly infrared active in the distorted low-temperature structure below T_{c1}. According to our cluster calculation, the lowest excited state is expected at about 0.2-0.25 eV. However, our infrared data do not show a distinct absorption feature in this range (see Fig. 5.11). A rough estimate of the spectral weight is obtained from the point-charge model, which predicts that the dipole matrix element at 4 K is about one order of magnitude smaller than for the transition to the xz orbital. Due to a factor of $1/\omega$, this means that the spectral weight of the excitations to the xy and to the xz orbital should be comparable in $\sigma(\omega)$. One possible explanation for the lack of a corresponding feature in our infrared data is that the first and the second excited states are nearly degenerate, as indicated by band-structure results [50, 133].

The scenario of strong orbital fluctuations assumes a near degeneracy of the states y^2–z^2 and xy. However, a sizeable admixture of the state with xy character to the ground state

---

the e_g subshell.

[4]Enhancing t_{Cl} by t^* is necessary in order to push the d_{yz} level (from the e_g subshell) up to 1.5 eV. With increasing t^*, the energy of the d_{yz} orbital increases strongly, whereas the energies of d_{xy} and d_{xz} (from the t_{2g} subshell) decrease. For t^*=1 we find the following excitation energies: 0.32, 0.79, 1.32, and 2.21 eV at 4 K for the site labeled Ti_a in table 5.2.

would have drastic consequences for the selection rules. A transition from xy to $xz + x$ $(yz + y)$ will give rise to absorption for $E \parallel b$ ($E \parallel a$), i.e. just the opposite of the selection rules derived for the transitions from the y^2-z^2 state. This may explain the weak features at about $0.65\,\mathrm{eV}$ for $E \parallel b$ and $1.5\,\mathrm{eV}$ for $E \parallel a$, but at the same time the weakness of these features compared to the strong absorption in the perpendicular direction puts a severe limit to the admixture of xy character to the ground state. Moreover, the g factor observed in ESR spectroscopy is close to 2 [113], which indicates that the orbital moment is quenched by a significant splitting ($\geq 0.2\,\mathrm{eV}$) within the t_{2g} subshell. A sizeable splitting of the t_{2g} subshell is in agreement with recent LDA+U and LDA+DMFT results [145, 146, 147]. However, the degree of orbital polarization still needs to be clarified. In reference [145], the lowest orbital (y^2-z^2 in our notation) is populated by only 70%, indicating the possible importance of inter-orbital fluctuations, whereas a population with 0.98 electrons was reported in reference [146].

Both our cluster calculation and in particular the observed polarization dependence show

Table 5.2: Crystal-field splitting of $3d^1$ Ti^{3+} in TiOCl and polarization dependence for infrared absorption at $300\,\mathrm{K}$ and $4\,\mathrm{K}$. Comparison of experimental data (see Fig. 5.11) and theoretical results obtained using the point-charge model and a cluster calculation based on the molecular-orbital theory (see section 2.1.1 and appendix F). The cluster calculation uses U_{dd}=4 eV, Δ_{O}=5 eV, Δ_{Cl}=3 eV, and an enhancement of the Ti-Cl hybridization by t^*=1.3 (see text). The calculations are based on the $300\,\mathrm{K}$ structure reported in reference [138] and on the $4\,\mathrm{K}$ data of reference [135]. At $4\,\mathrm{K}$, there are two inequivalent Ti sites. For convenience, we use $x \parallel a$, $y \parallel b$, and $z \parallel c$ at both temperatures. All energies are given in eV. At $300\,\mathrm{K}$, the given polarization selection rules are strict. Due to the lower symmetry at $4\,\mathrm{K}$, only "effective" selection rules survive in the sense that the dipole matrix elements for the "main" transitions indicated at $4\,\mathrm{K}$ are about three orders of magnitude (or more) larger than those not given in the table.

theory:	character	y^2-z^2	xy	xz	yz	$3x^2-r^2$
	admixture (300 K)	z	$-$	x	y	z
	main admixture (4 K)	y, z	x	x	y, z	y, z
	point charge (300 K)	0	0.39	0.68	0.34	1.28
	cluster (300 K)	0	0.25	**0.69**	**1.24**	2.11
	cluster (4 K, Ti$_a$)	0	0.26	**0.73**	**1.53**	2.20
	cluster (4 K, Ti$_b$)	0	0.25	**0.77**	**1.47**	2.18
	polarization (300 K)		-	$E \parallel a$	$E \parallel b$	$E \parallel c$
	main polarization (4 K)		$E \parallel a$	$E \parallel a$	$E \parallel b, c$	$E \parallel b, c$
exp.:	energy		-	**0.65**	**1.5**	-
	polarization		-	$E \parallel a$	$E \parallel b$	-

that there is no significant admixture of the xy orbital to the ground state. Thus orbital fluctuations are clearly suppressed. In order to understand the interesting physics of TiOCl it is therefore sufficient to consider the interplay of lattice and spin degrees of freedom. We suggest that the occurrence of two phase transitions results from the frustration of interchain interactions in this peculiar bilayer structure (see section 5.5)[143].

The remarkable splitting of 0.65 eV of the t_{2g} subshell is caused by the strong distortions of the [TiO_4Cl_2] octahedra and by the different charges on O and Cl sites within an octahedron. This large splitting clearly shows that t_{2g} systems are not necessarily good model compounds for the study of orbital effects based on (near) orbital degeneracy within the ground state.

5.4 Far-infrared data of TiOX

We will now consider the far-infrared data of TiOX. We measured both reflectance and transmittance since both compounds are transparent over a wide range due to the small number of phonons. The number of phonons is determined by the number of ions in the unit cell. In the case of TiOX this is twice the stoichiometric formula ($2 \times 3 = 6$ ions) at 300 K (space group $Pmmn$) [138]. This gives ($3 \times 6 - 3$) 15 optical phonons. Not all of these phonons are dipole active. It turns out that only six modes are actually dipole active, as seen from the group theoretical analysis for the space group $Pmmn$.

$$\Gamma_{vibr} = \underbrace{3A_g}_{\text{Raman}} + \underbrace{2B_{1u}}_{\text{IR}} + \underbrace{3B_{2g}}_{\text{Raman}} + \underbrace{2B_{2u}}_{\text{IR}} + \underbrace{3B_{3g}}_{\text{Raman}} + \underbrace{2B_{3u}}_{\text{IR}}$$

The infrared-active modes are the odd modes (u from the german "ungerade"). They are labelled by the representation of the point group according to which the phonon is transforming (here D_{2h} [5]). The infrared-active phonons correspond to the representations B_{1u}, B_{2u}, and B_{3u}. For room temperature, group theory thus predicts two infrared-active phonons in each of the three polarization directions, $E \parallel a$, $E \parallel b$, and $E \parallel c$. The symmetry considerations hold for both compounds (Cl and Br) since they have the same symmetry.

5.4.1 Far-infrared reflectance

First we will consider the reflectivity data at 300 K. The results of the reflectance for both compounds (X=Br,Cl) are compared in Fig. 5.16 and Fig. 5.17. The identical space group and the similarity of the structure leads to very similar reflectivity spectra of the two crystals. For polarization parallel to the a axis, two dominant phonons are observed (Fig. 5.16). There is one sharp phonon at low energies (at 9.3/13.0 meV for Br/Cl, respectively). For TiOBr this phonon is at the lower end of the frequency range of this measurement. Reflectivity data at lower frequency require the use of larger samples. However, this mode is clearly observed in

---

[5]The group $D_{2h}(mmm)$ consists of the following symmetry elements: twofold axes along x, y, and z, three mirror planes at the coordinate planes yz, zx, and xy, inversion, and identity. Since there occur only one-dimensional representations there ought to be eight of them (the number of representations is determined by the order of the group). These are labeled A, B_1, B_2, B_3, each with an index u or g that accounts for their behavior under inversion.
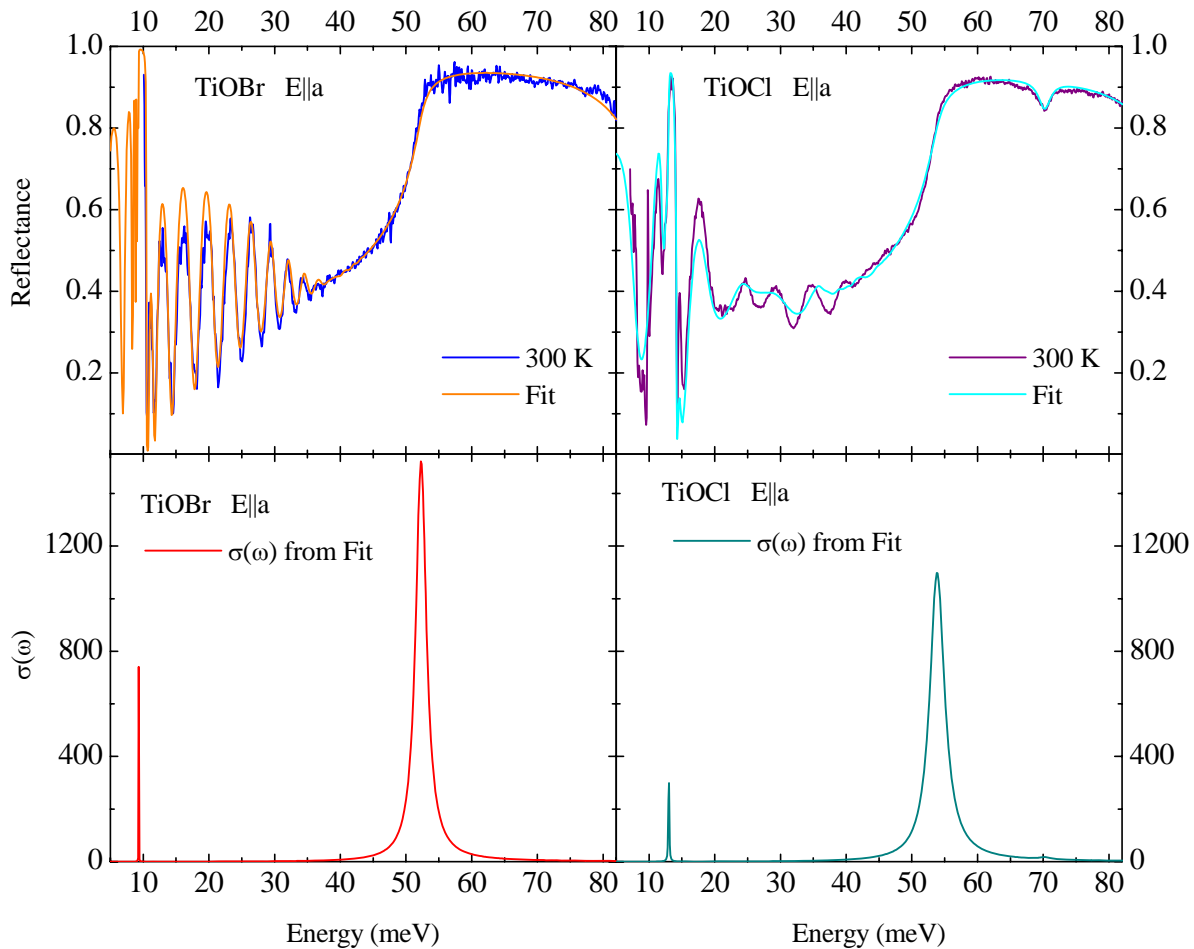
Figure 5.16: The reflectance of TiOBr and TiOCl at 300 K together with a fit for polarization $E \parallel a$ is shown. The data of TiOBr show strong interference fringes in the transparent region due to backside reflections in the thin sample. These fringes are partially suppressed by surface defects especially of the backside, and they are modulated by slightly non-parallel surfaces.

our transmittance data (see below). A second, much stronger phonon is observed at 52.2/53.5 meV for Br/Cl, respectively. The region of high reflectivity reaches beyond 80 meV, the range that had been observed in the far-infrared measurement. For light polarized parallel to the b axis, also two phonons are observed. A strong phonon at 34.2/36.4 meV for Br/Cl, and a weaker one at 24.1/25.0 meV. The spectra of both compounds exhibit interference fringes in the range of weak absorption. In TiOBr these fringes are much stronger and more regular, caused by the sample geometry of two nearly parallel surfaces. In TiOCl these fringes are not that regular corresponding to a bit more irregular surfaces. The weaker phonon at 25.0 meV is lying within the fringes, which makes it difficult to observe it directly. However its
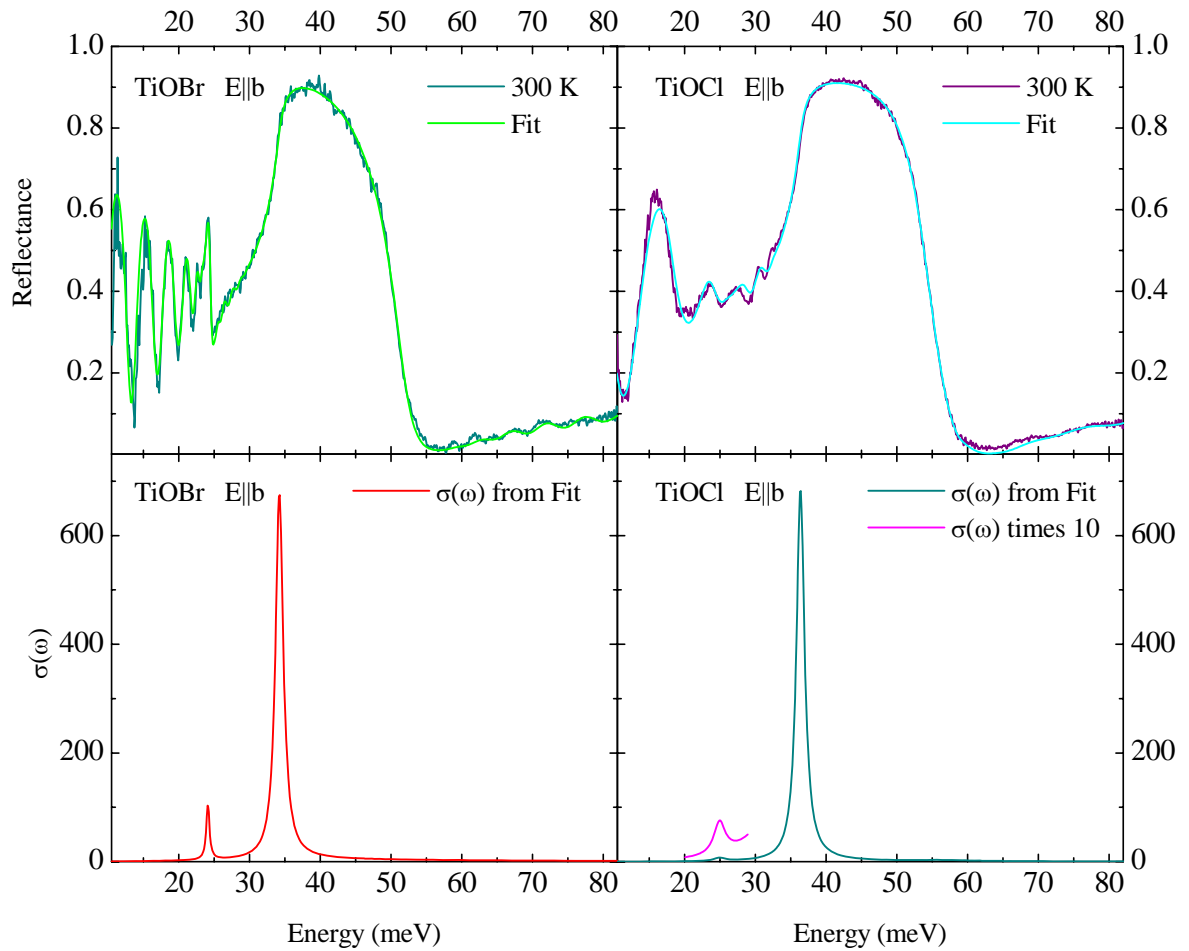
Figure 5.17: The reflectance of TiOBr and TiOCl at 300 K together with a fit for polarization $E \parallel b$ is shown. The data of TiOBr show strong interference fringes in the transparent region due to backside reflections in the thin sample. These fringes are partially suppressed by surface defects especially of the backside, and they are modulated by slightly non-parallel surfaces.

presence can be extracted by a fit unambiguously. It is also observed in the transmittance data in Fig. 5.22.

Additionally a fit[6] to the data based on a Drude-Lorentz model is plotted. The parameters of the fitting curves are given in Table 5.3. In the high-temperature structure at 300 K one expects two IR-active phonon modes in each of the three polarizations ($E \parallel a$, b, c). As already mentioned, the polarization $E \parallel c$ is not accessible due to the sample geometry. The

---

[6]For the fitting procedure we made use of the program RefFIT of Alexey Kuzmenko. This program is freely available on his homepage at the University of Geneva.
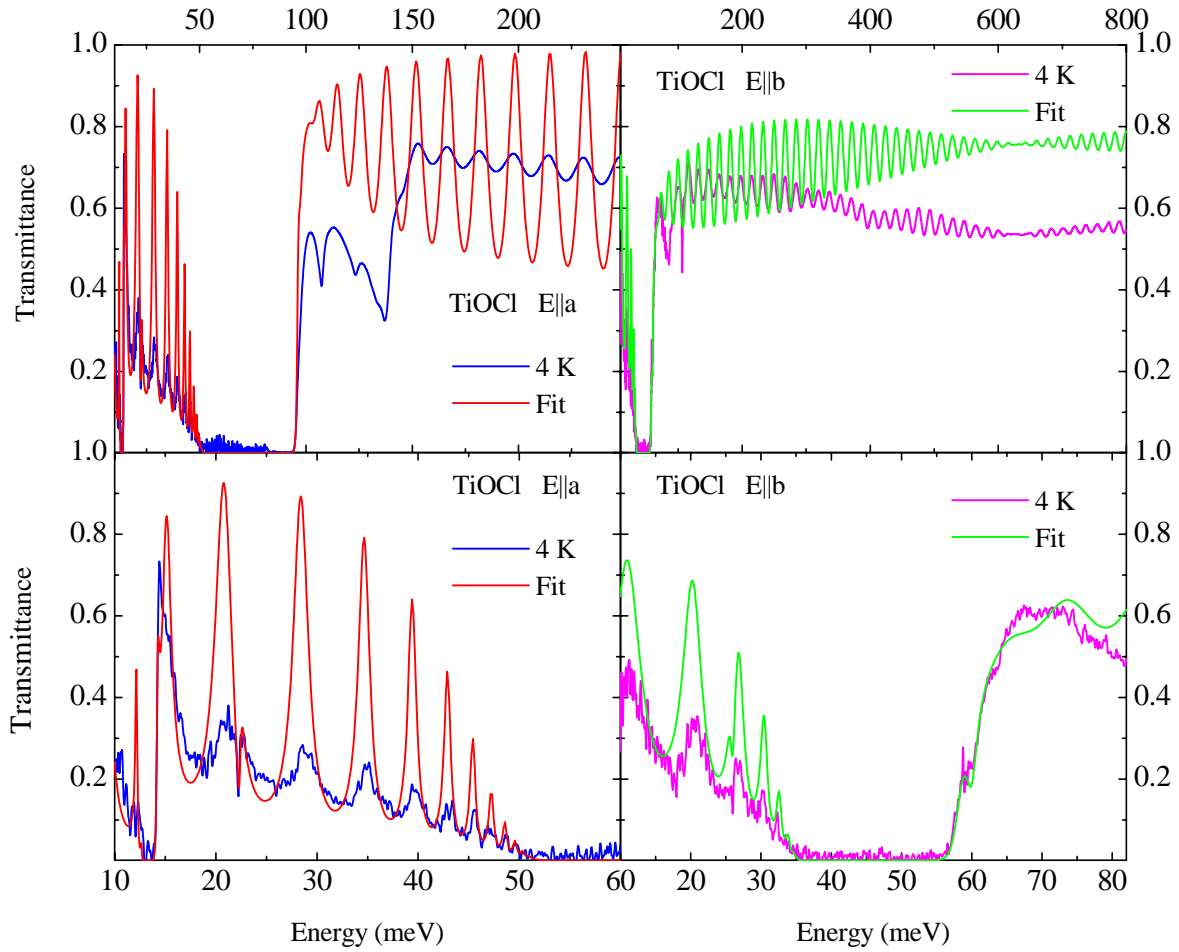
Figure 5.18: The transmittance at 4 K of TiOCl from the far- to the mid-infrared region is displayed in the upper two panels for the two polarization directions. The far-infrared region is magnified in the bottom panels.

energies of the phonon modes have been calculated in a shell model in [132]. We compare these theoretical results with the energies (given in wave numbers, cm^{-1}) obtained from the fits of our data in the following Table.

| | **TiOBr** | | | | **TiOCl** | | | |
	$\mathbf{E} \parallel a$		$\mathbf{E} \parallel b$		$\mathbf{E} \parallel a$		$\mathbf{E} \parallel b$	
experiment	75.03	421.69	194.49	276.02	104.81	434.40	201.78	294.13
theory [132]	69	410	148	311	91	431	198	333

The overall agreement between experiment and theory is rather satisfactory. The largest discrepancy (≈ 25 %) is observed in TiOBr for $E \parallel b$. In three of the four cases (Br/Cl, a/b) an additional mode has been included into the model in order to reduce the deviation
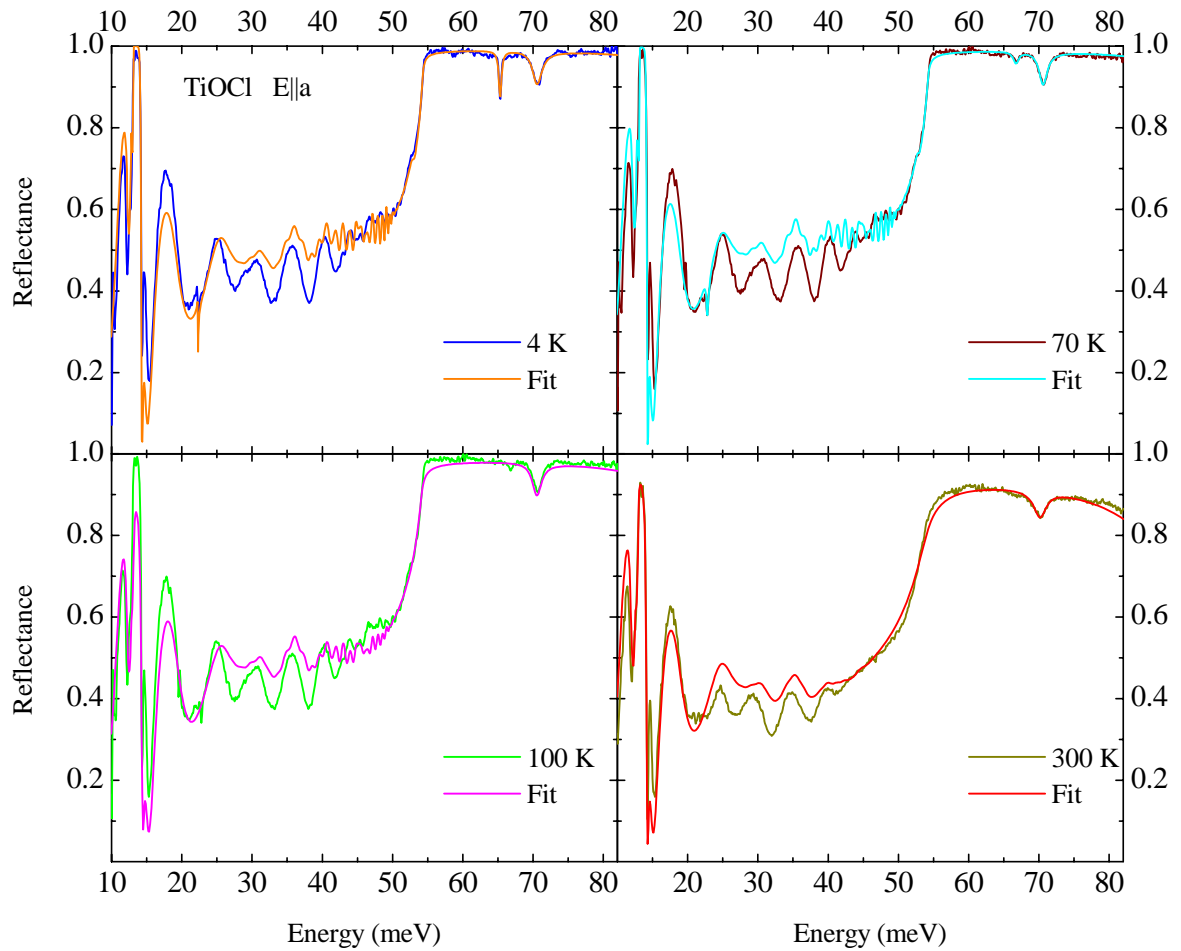
Figure 5.19: The reflectance at four different temperatures of TiOCl in the far-infrared region for $E \parallel a$ is shown. For the reference measurement, in-situ gold evaporation has been used.

from the measured data. These additional modes are only very weak as seen from the optical conductivity. They may be assigned to multi-phonon contributions[7]. The very broad modes lying at the shoulder of a strong mode are typical and also observed in other oxides [140].

The temperature dependence of the phonon excitations in the far-infrared range is of particular interest since any structural change of a crystal at a phase transition will result in a change of its phonon absorption. The reflectance of TiOCl at four different temperatures is given in Fig. 5.19 and in Fig. 5.20 for $E \parallel a$ and $E \parallel b$, respectively. These temperatures are chosen as they are in the different phases. Only 100 K and 300 K belong structurally to the

---

[7]The multi-phonon excitations are not restricted to $k \approx 0$ for the contributing phonons but may involve phonons from the entire Brioullin zone. Since only the total momentum has to be zero, the single phonon momenta have to vanish in the sum but each on its own may differ from zero momentum. Via the dispersion of the phonon modes, the energy of the multi phonon is not necessarily twice the energy of a $k = 0$ mode.

Table 5.3: Parameters of the fit to the reflectance of TiOCl and TiOBr at 300 K. The variation of the thickness d is assumed to be of the shape of a wedge with the relative change in thickness $\frac{\delta d}{d}$.The proportion is given here in percent of the absolute thickness. The contribution of oscillators far above the considered frequency range is taken into account by a constant contribution ε_∞ to the dielectrical function. The phonon modes are fitted with oscillators determined by the eigenfrequency ω_0, the plasma frequency ω_p, and the damping γ.

TiOCl				TiOBr			
E∥a				**E∥a**			
ε_∞	4.103			ε_∞	4.5437		
d	16.9 μm			d	39.2 μm		
$\frac{\delta d}{d}$	20.6 %			$\frac{\delta d}{d}$	5.217 %		
	ω_0	ω_p	γ		ω_0	ω_p	γ
1. oscillator	104.81	163.97	0.7060	1. oscillator	75.03	142.80	0.0887
2. oscillator	434.40	1211.8	22.27	2. oscillator	421.69	1213.09	16.11
3. oscillator	566.77	87.99	17.05				
E∥b				**E∥b**			
ε_∞	4.069			ε_∞	4.7386		
d	16.8 μm			d	38.5 μm		
$\frac{\delta d}{d}$	20.9 %			$\frac{\delta d}{d}$	5.530 %		
	ω_0	ω_p	γ		ω_0	ω_p	γ
1. oscillator	201.78	91.33	26.40	1. oscillator	194.49	163.91	4.434
2. oscillator	294.13	695.13	11.165	2. oscillator	276.02	656.72	10.67
3. oscillator	457.99	111.56	92.88	3. oscillator	308.83	273.60	372.35
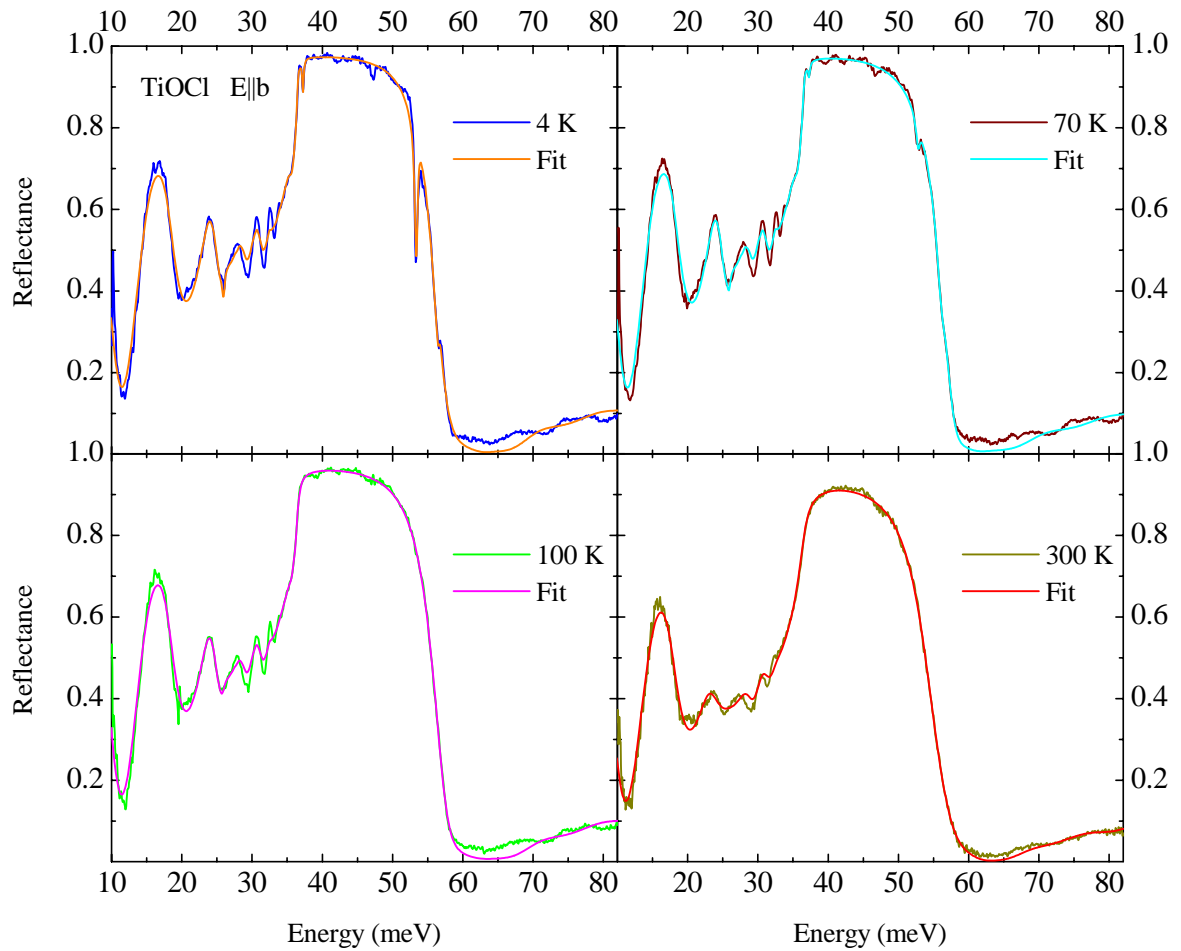
Figure 5.20: The reflectance at four different temperatures of TiOCl in the far-infrared region for $E \parallel b$ is shown.

same phase, but 100 K is in the proposed pseudogap phase. So changes at the two transition temperatures T_{c1} and T_{c2} and also in the pseudogap phase may be observed in the phonon spectrum.

The main phonon modes in both polarizations do not change significantly with temperature, except a conventional broadening due to an increase of damping. However, for both polarizations (a, b) a closer look at the ascent of the reflectance towards the strongest mode (at 53, 36 meV) reveals that in the 4 K and 70 K data a shoulder emerges which is foreshadowed already at 100 K, as seen from Fig. 5.24. By comparison with a fit to the 4 K data it is shown that such a shoulder arises from the splitting of the single mode at 300 K. This splitting occurs since the dimerization along b leads to new modes along all other crystallographic directions. In addition to the splitting of the dominant phonon mode, weak
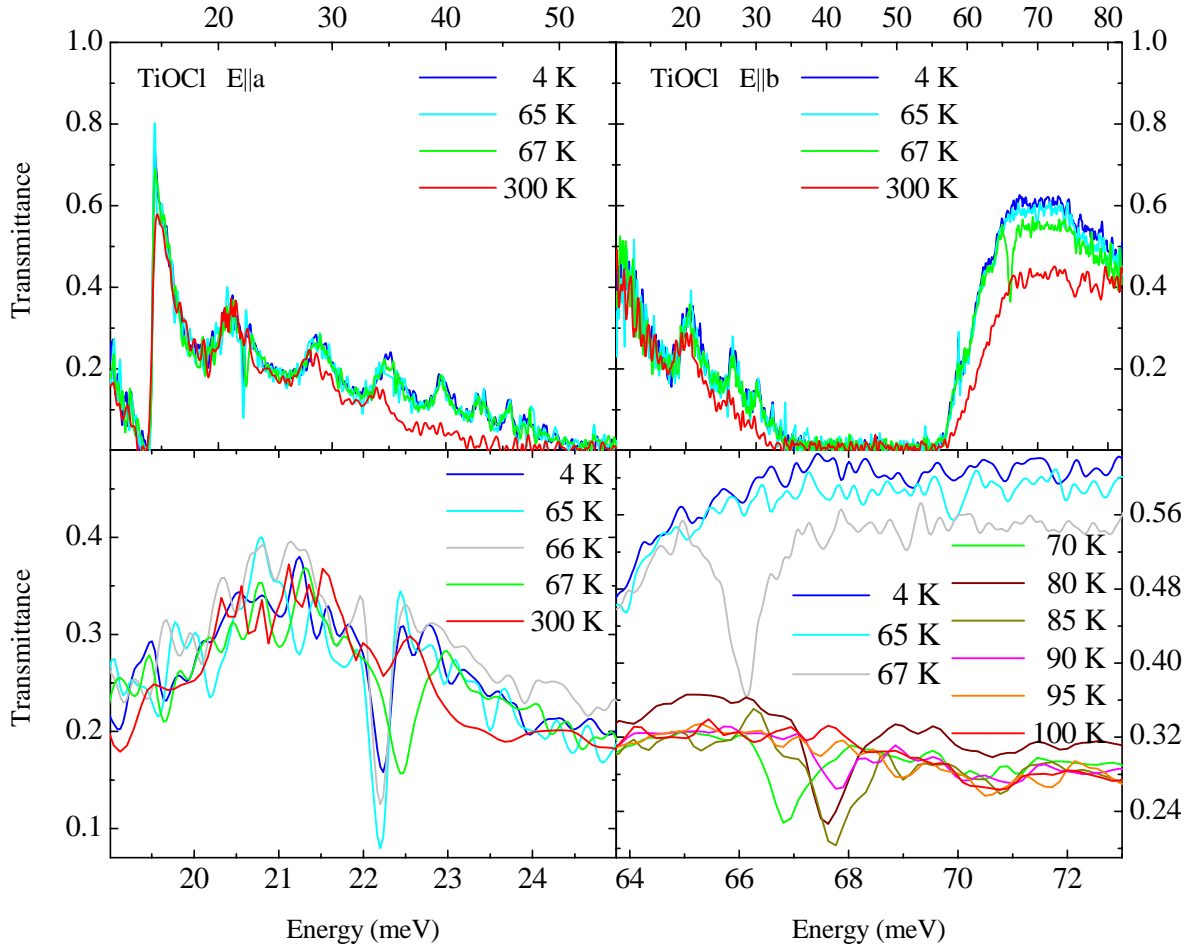
Figure 5.21: The transmittance of TiOCl at different temperatures is shown in the far-infrared region for $E \parallel a$ and $E \parallel b$ in the top. The bottom panels are magnifying two phonon modes at 22 meV for $E \parallel a$ and 66 meV for $E \parallel b$, respectively. For the latter data at additional temperatures of a different (thicker) sample are plotted. This measurement has been performed without polarizing the light. However, since the a direction is opaque due to strong phonon absorption the sample itself acts like a polarizer.

absorptions emerge at T_{c1} and also at T_{c2} for both polarizations. For E $\parallel a$ a phonon mode at 22.7 meV occurs as a weak dip at 70 K which is softened to 22.2 meV and getting stronger at 4 K. For E $\parallel b$ four absorptions are observed at 4 K at the energies 19.6, 37.2, 47.2, and 53.3 meV. The strongest of this four at 53.3 meV is discussed in detail later. These modes are preceded more weakly at 70 K. We summarize the values of parameters and oscillators in table 5.4.1. Especially at T_{c1} additional phonons are expected to occur in the low-temperature spin-Peierls phase, wherein the unit cell is doubled and the symmetry is lowered. However, already below T_{c2} additional weak phonon absorptions emerge (see Fig. 5.19, Fig. 5.20, and
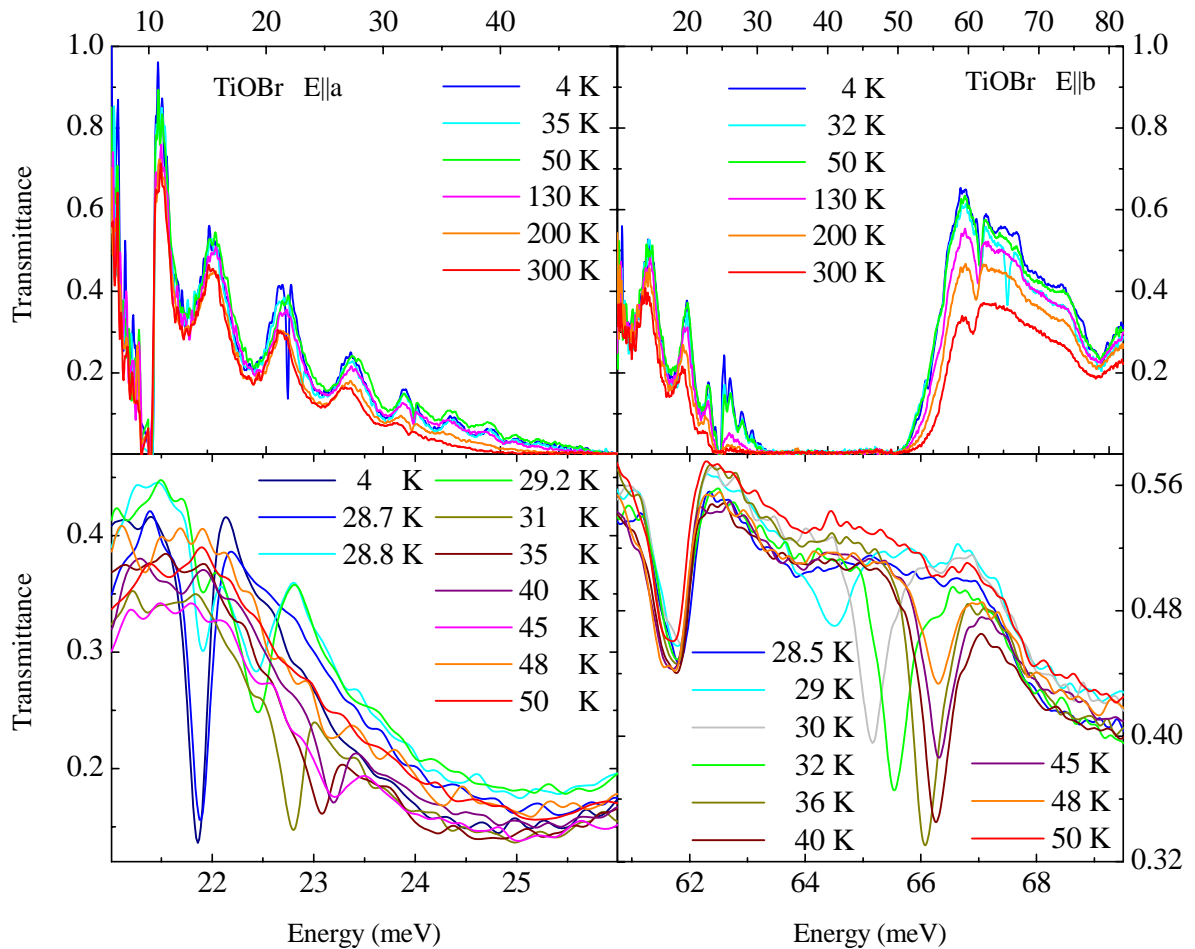
Figure 5.22: The transmittance of TiOBr at several temperatures is shown in the far-infrared region for $E \parallel a$ and $E \parallel b$ in the top panels. The bottom panels are magnifying two phonon modes at 22 meV for $E \parallel a$ and 66 meV for $E \parallel b$, respectively. The temperatures shown here are focused on the intermediate phase.

Fig. 5.23), indicating that the lattice is involved in this transition, too. These results are in agreement with a transition to an incommensurate phase due to the opening of a spin gap at T_{c2} followed by at first-order lock-in transition at T_{c1} which is discussed below (see section 5.5).

We analyze now the temperature dependence of the most apparent phonon mode at 53 meV for E $\parallel$ b that occurs only in the low-temperature phase. Its temperature dependence observed in the reflectance is depicted in Fig. 5.23. Remarkable is that already at temperatures above T_{c1} a precursor is observed at 70 K and possibly even at 85 K (the latter is a bit ambiguous due to superposition by noise). Moreover, the increase of the reflectance observed
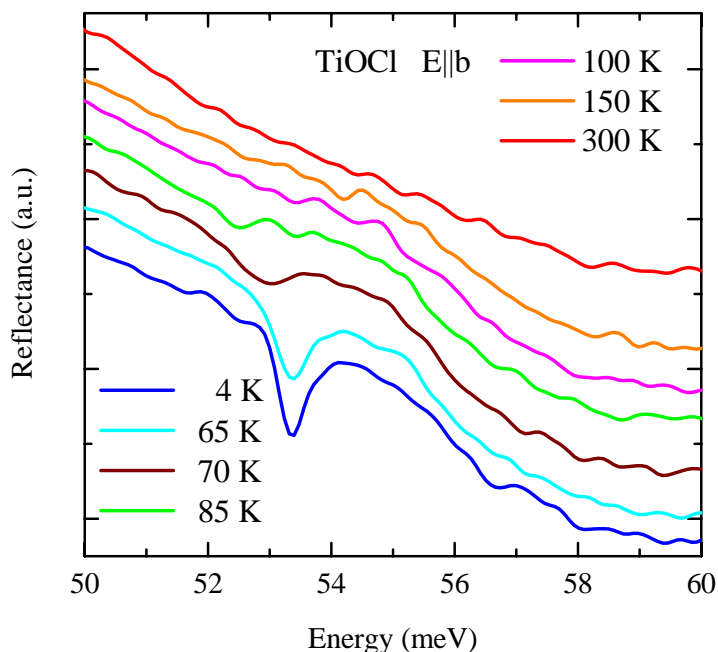
Figure 5.23: Magnified view on the strongly temperature dependent phonon mode observed in the reflectance of TiOCl. The curves of different temperature are shifted along the vertical axis for clarity.

as a broad bump around 55 meV is already present at 150 K (compared with the 300 K data). Above T_{c2} the system "feels" the spin-gapped state which becomes nearly degenerate with the high-temperature ground state. Also above T_{c1} in the vicinity of the first-order transition to the commensurate phase, the weak dip at 53 meV indicates that the system moves towards that transition. The appearance of this feature indicates that the periodicity of the incommensurate structure increases strongly. The phonon mode that occurs stronger and sharper in the low-temperature phase becomes already weakly allowed in the incommensurate phase for increasing periodicity of the incommensurability, i.e. the local environment becomes similar to the low-temperature phase. The deviation of the perfectly ordered commensurate state may lead to a lower energy of this mode above T_{c1} compared to the corresponding mode below T_{c1}. This softening emerges since the dimerized structure is yet not that rigid as it is in the low-temperature phase.

5.4.2 Far-infrared transmittance

To measure the transmittance provides a complementary method to reflectance measurements for the observation of weak absorptions. On the one hand, in an energy region of high values of the reflectivity only a tiny absorption within the crystal leads to a considerable lowering of the reflectivity, whereas the crystal turns out to be opaque in this region which prevents

Table 5.4: Parameters of the fits to the far-infrared data of TiOCl. Note that the energies are given in cm^{-1}.

TiOCl							
E∥a	**300 K**			**100 K**			
ε_∞	4.103			ε_∞	4.107		
d	16.9 μm			d	16.3 μm		
$\frac{\delta d}{d}$	20.6 %			$\frac{\delta d}{d}$	20.65 %		
	ω_0	ω_p	γ		ω_0	ω_p	γ
1. oscillator	104.81	163.97	0.933	1. oscillator	106.41	162.09	1.79
2. oscillator	434.40	1211.8	22.27	2. oscillator	436.22	1211.8	5.36
3. oscillator	566.77	87.99	17.05	3. oscillator	569.36	80.21	12.65
70 K				**4 K**			
ε_∞	3.728			ε_∞	3.742		
d	16.8 μm			d	17.0 μm		
$\frac{\delta d}{d}$	20.24 %			$\frac{\delta d}{d}$	20.24 %		
	ω_0	ω_p	γ		ω_0	ω_p	γ
1. oscillator	106.10	157.09	0.032	1. oscillator	106.12	149.97	0.041
2. oscillator	183.63	19.17	2.525	2. oscillator	179.87	13.73	0.21
3. oscillator	426.10	284.04	4.787	3. oscillator	426.61	302.70	5.78
4. oscillator	437.24	1201.3	3.407	4. oscillator	437.64	1135.3	2.62
5. oscillator	538.30	48.90	7.395	5. oscillator	527.11	73.47	3.67
6. oscillator	569.81	80.21	11.14	6. oscillator	569.65	79.95	12.80
E∥b	**300 K**			**100 K**			
ε_∞	4.069			ε_∞	4.642		
d	16.8 μm			d	15.1 μm		
$\frac{\delta d}{d}$	20.9 %			$\frac{\delta d}{d}$	19.98 %		
	ω_0	ω_p	γ		ω_0	ω_p	γ
1. oscillator	201.78	91.33	26.40	1. oscillator	206.34	62.77	7.17
2. oscillator	294.13	695.13	11.165	2. oscillator	285.18	334.29	12.66
3. oscillator	457.99	111.56	92.88	3. oscillator	294.66	693.92	4.63
				4. oscillator	487.42	133.77	121.0
70 K				**4 K**			
ε_∞	4.730			ε_∞	4.632		
d	15.0 μm			d	15.1 μm		
$\frac{\delta d}{d}$	19.61 %			$\frac{\delta d}{d}$	19.93 %		
	ω_0	ω_p	γ		ω_0	ω_p	γ
1. oscillator	207.17	68.22	5.28	1. oscillator	207.49	68.93	4.02
2. oscillator	284.76	344.29	11.06	2. oscillator	285.17	378.62	10.85
3. oscillator	294.35	676.58	3.00	3. oscillator	294.22	638.46	2.24
4. oscillator	301.04	140.35	2.46	4. oscillator	300.88	188.49	1.90
5. oscillator	426.22	16.08	5.35	5. oscillator	431.16	29.24	3.44
6. oscillator	454.46	16.14	9.04	6. oscillator	456.07	13.42	4.49
7. oscillator	502.93	156.27	187.53	7. oscillator	477.83	119.02	90.13
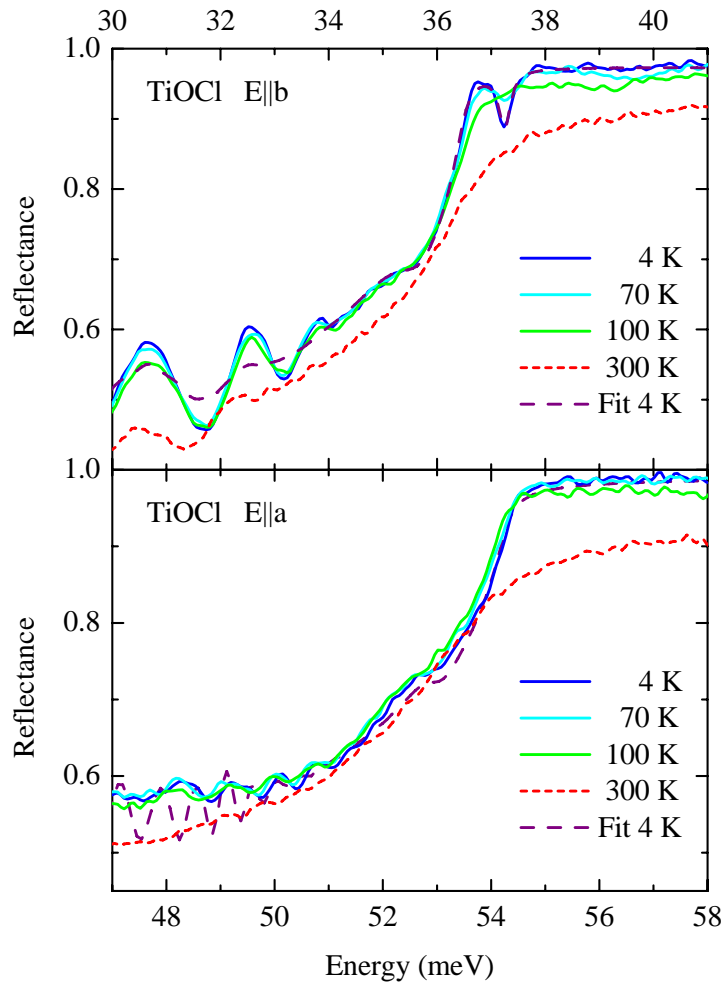
Figure 5.24: The reflectance of TiOCl at several temperatures is shown in the region of the ascent towards the strong phonon mode. The 4 K data is compared to a fit assuming two phonon modes close to each other in order to reproduce the shoulder at 35 (top) and 53 meV (bottom).

to measure transmittance data. On the other hand in energy regions that exhibit high values of the transmittance, weak absorptions are superposed by noise in the reflectance, but the lowering of the transmittance can be clearly observed. For the reflectance an example is shown in Fig. 5.19. The mode in TiOCl at 70 meV for $E \parallel a$ is rather weak, but clearly observed in the reflectance, whereas the transmittance vanishes in that energy range. A mode seen only in the transmittance is for example the mode at 66 meV for $E \parallel b$ in Fig. 5.21. This mode, that exists only in the intermediate phase, is clearly observed in the transmittance, but not detectable in the reflectance (see Fig. 5.20). Thus to regard the transmittance of a crystal will certainly provide additional information.
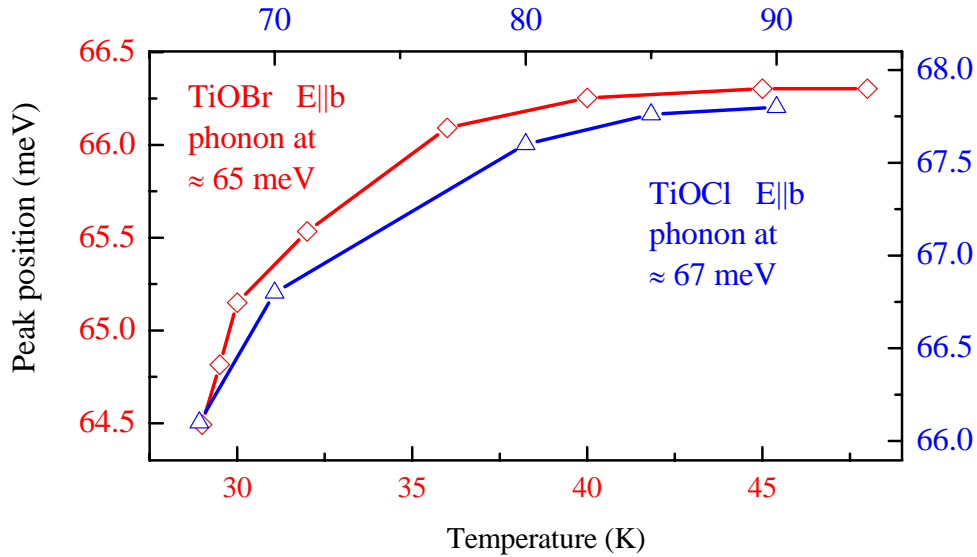
Figure 5.25: The frequency of the phonon mode at $\approx$66 meV observed in the polarization along the b axis in both compounds TiOBr/Cl is plotted against temperature. Since this mode is absent above T_{c2} and below T_{c1}, the relevant temperature range is that of the intermediate phase. The left and bottom axis scaling belongs to the data of TiOBr (red), and the right and top axis scaling belongs to the data of TiOCl (blue).

The far-infrared transmittance of TiOCl and TiOBr for both polarizations (a and b) is displayed in the top panels of Fig. 5.21 and of Fig. 5.22, respectively. For polarization along a the temperature dependence of the phonon mode at about 22 meV is considered more closely in the bottom left panel. In the range of the strong modes that have been observed in the reflectance, the transmittance is vanishing. For E $\parallel$ a this is the case for energies above $\approx$ 50 meV up to the highest measured frequencies 80 meV in both compounds. Hence the data are shown only below 50 meV. For E $\parallel$ b this region lies between $\approx$30 meV and $\approx$50 meV. As the temperature decreases the phonon modes get sharper and hence the region of opaqueness shrinks. Towards low energies the transmittance is dominated by interference fringes, as seen from a fit for TiOCl in the bottom panel of Fig. 5.18.

Besides the two strong modes which are expected in the $Pmmn$ structure, a new mode emerges for E $\parallel$ a in the low-temperature phase. This mode is observed nearly at the same energy ($\approx$ 22 meV) in both compounds, which indicates that it involves almost exclusively Ti and O ions. Also the temperature dependence is similar: for both compounds the mode softens with decreasing temperature (see Fig. 5.21 and Fig. 5.22). The more detailed temperature resolution of the data of TiOBr provides further inside in the evolution of this mode. It starts to rise below T_{c2}, and its spectral weight increases as it shifts to lower energies for decreasing temperature. Towards lower temperatures this shift gets accelerated, and in the vicinity of T_{c1} spectral weight is transferred to the low-temperature position which is not reached continuously. It is not clear from the data if the transfer starts already above T_{c1}
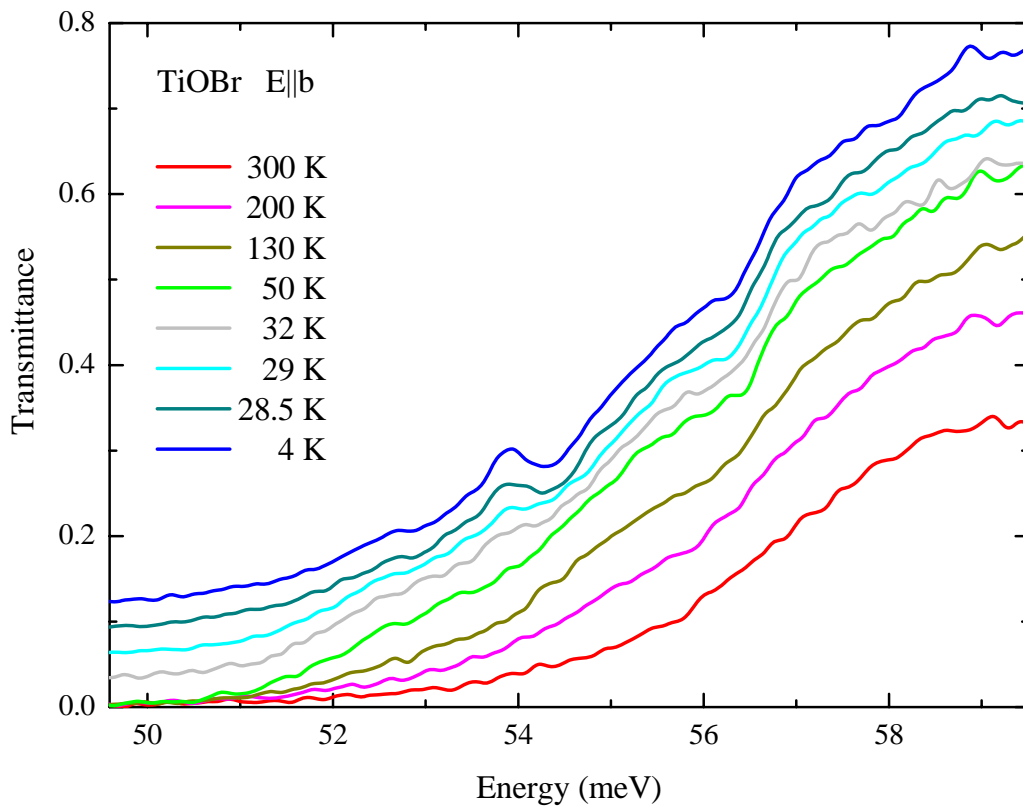
Figure 5.26: The temperature dependence of the transmittance in the ascent for energies above the strong phonon absorption is magnified. The curves for temperatures below 50 K are shifted by offset of 0.03 with respect to each other for clarity.

or if the occurrence at higher temperature is due to temperature inhomogeneity (< 1 K) within the sample, i.e. some parts are already in the low-temperature phase whereas other parts are not. However, the transition at T_{c1} is found to be of first order in thermodynamical properties which makes a jump more likely.

For E $\parallel b$ also new modes appear below T_{c2} in both compounds, as seen from Fig. 5.21 and Fig. 5.22. The most obvious mode is magnified in the bottom right panels of these figures. Its temperature dependence is similar to the one observed for E $\parallel a$, but it vanishes below T_{c1} instead of jumping to a new position. The acceleration of the softening towards T_{c1} is depicted in Fig. 5.25. Also this mode appears at roughly the same energy in both compounds, which gives again evidence for a mode that predominantly involves Ti and O ions. This temperature behavior is due to a lowering of the symmetry in the incommensurate phase which lifts the strict dipole selection rule for this phonon.

Other additional modes that occur in the low-temperature phase and have a precursor in the intermediate phase are shown in Fig. 5.26. Also weak and broad features are observed

above T_{c2}. One mode is observed at 56 meV, another one at 54 meV, and there may be a rather weak feature at 52.8 meV which is not separable unambiguously from the underlying noise.

In Fig. 5.18 we show results for the transmittance of TiOCl at 4 K in the far- and mid-infrared region. The transmittance drops to zero in the range of strong phonon absorption, outside this range the samples are sufficiently transparent. We compare the data of each polarization with a fit to the curve. This fit is based on a Drude-Lorentz model and has been performed using RefFit (see footnote above). It includes only the assumption of a Lorentzian line shape and the adjustment of experimental parameters like the thickness and the thickness spread of the sample. We find good agreement between the fit and the experimental data over the entire range. Exceptions to this good agreement are the multi-phonon range, the suppression of interference fringes, and for $E \parallel b$ in the mid-infrared range. The deviation in the range of the multi phonons has a rather simple origin. Since multi-phonon absorptions are difficult to describe theoretically, they have not been included in the model used in the fitting procedure. The reason why we show the data of E $\parallel a$ only up to 250 meV is that for higher energies the strong orbital absorption in this polarization sets in (see Fig. 5.11). This absorption is not included in the model and leads hence to a strong deviation of the experimental results from the fitted curve. The strong suppression of the interference fringes in the experimental result compared to the fit is due to the fact that the surfaces in the model are assumed to be absolutely even planes. This is however not the case for real crystals where always surface defects occur. Remarkable is also the deviation of the fit for E $\parallel b$ in the region above 300 meV. This discrepancy is attributed to an absorption that shows a significant temperature dependence as discussed above (Fig. 5.15). Probably, this has to be attributed to an orbital excitation to the xy level which is dipole forbidden as a direct excitation but becomes weakly allowed for a phonon-assisted transition.

Summarizing the results of this section it can be stated that at both transition temperatures structural changes are observed. In conclusion these results are in agreement with an incommensurate structure in the intermediate phase and a doubling of the unit cell in the low-temperature phase, as reported from x-ray structure analysis [136].

5.4.3   Interference fringes vs. additional phonon modes

Far-infrared data of TiOX have been reported by Caimi *et al.* in [131, 132]. They claim that additional phonon modes are present at room temperature which are not expected from a symmetry analysis (see above). In the following we will discuss these results in comparison to our data. Lets first consider briefly the procedure of acquiring infrared data in general. For obtaining optical properties of the sample, one has to measure the sample and additionally a reference in order to eliminate the contribution of the experimental setup (source, beam splitter, detector, etc.) to the spectrum. For transmittance measurements the reference spectrum is obtained by a second measurement where simply the sample has been removed from the sample aperture. For reflectance measurements this is obviously not practical and one is therefore returning to measuring a gold mirror ($R \approx 1$ for infrared light) at the position of the sample. This method of obtaining a reference is working well for large samples with a planar, polished surface. However, in the case of TiOX the samples are not rigid crystals
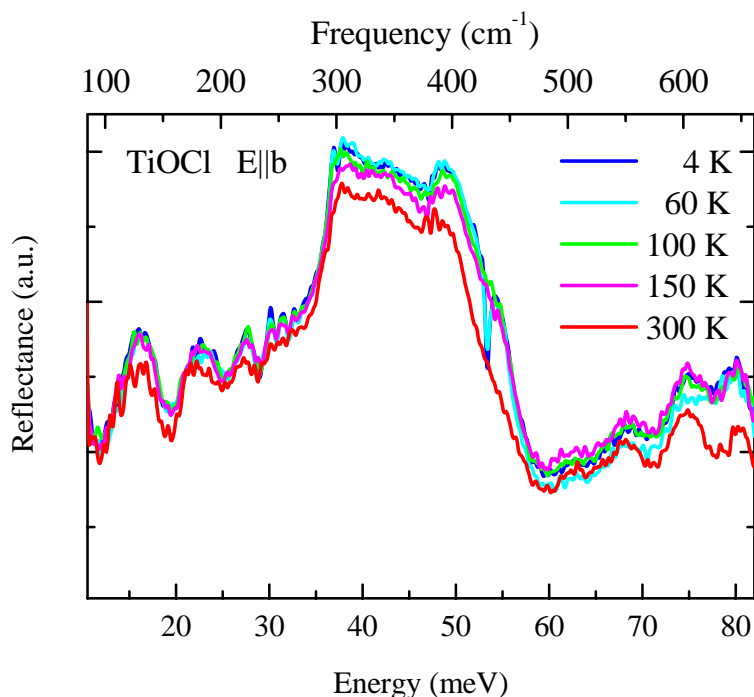
Figure 5.27: The result of a temperature-dependent reflectance measurement of TiOCl is shown. The data have been acquired using a gold mirror as reference.

but flexible and it is hence impossible to prepare them within the standard procedure. One can only take a crystal as it has been grown and fix it on the sample holder. By doing so one achieves only a more or less planar surface. However, the result is far from the flatness of a surface prepared by grinding and polishing. It is clear that one will not get reliable results by using a planar mirror as reference for such a sample. The method of choice in such a case is to coat the sample's surface in situ with gold after measuring and create by this a golden surface exactly equal to the sample surface measured before. The reflectance data discussed above have been obtained using in-situ gold evaporation. For comparison, the result of a measurement with a planar Au mirror as reference is shown in Fig. 5.4.3.

Another problem occurring in the reflectance measurements of TiOX is the small thickness of the available samples. In the transparent range, thin samples show strong interference fringes not only in transmittance but also in reflectance measurements. (One therefore usually uses thick samples with an uneven backside in order to suppress fringes.) The interference fringes are strongly modulated for samples of varying thickness. We have proofed by fitting the reflectance at 300 K of both compounds in the far-infrared region (covering the phononic excitations) that no additional phonon contributions are present (see Figs. 5.16 and 5.17). This is corroborated by the analysis of the transmittance data at 300 K where also a reasonable fit is obtained without additional phonon modes.

In Fig. 5.4.3 we plot the polariton dispersion obtained from the extrema of the interference
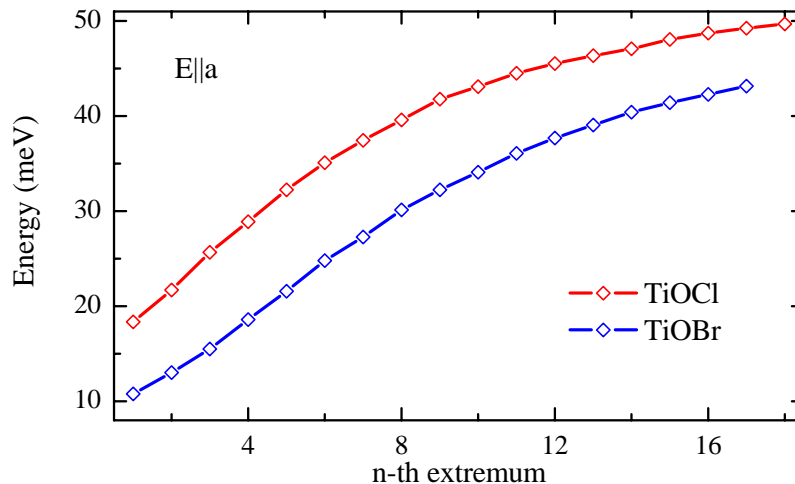
Figure 5.28: The energy of the minima and maxima of the 4 K transmittance data are plotted over the order in energy in which they occur. The resulting curves correspond to the polariton dispersion.

fringes observed in the reflectance for both compounds (see for instance [140]). The regularity is not expected for phonon energies. From this result it is evident that the additional phonons reported in [131, 132] actually have to be interpreted as interference fringes, although the authors of [131, 132] exclude this origin.

5.5 Incommensurate spin-Peierls phase

The question "what is the driving force for the formation of an incommensurate phase at the actual emerging of the spin gap" is still open. As it has been shown in the beginning of this chapter, orbital fluctuations as origin can be ruled out. Now we will discuss the bilayer geometry as the origin of this unusual behavior. The particular geometry of one bilayer is sketched in Fig. 5.29.

The remarkable feature of this structure is that the Ti sites of one layer are in the middle of the Ti-plaquettes of the second layer (indicated by the dashed boxes in Fig. 5.30). This opens in principle the way to the possible formation of several different dimerization patterns. Consider first only a single $S=1/2$ chain. In one chain we will distinguish neighboring Ti-Ti bonds, denoting one bond even and the adjacent bond odd. So the dimers may reside either on the even or on the odd bonds. A single layer can be regarded as an array of parallel chains. The dimerization in such an array of nearest-neighbor chains may be in-phase (dimers on the same odd/even bonds; Fig. 5.30 a) or out-of-phase with respect to each other (dimers alternating on odd and even bonds; Fig. 5.30 b). In the out-of-phase case, all Ti sites are equivalent (Fig. 5.30b), facing one dimer on the surrounding plaquette. However, there are two inequivalent Ti sites in the in-phase case, facing either two or zero dimers, as indicated by

139
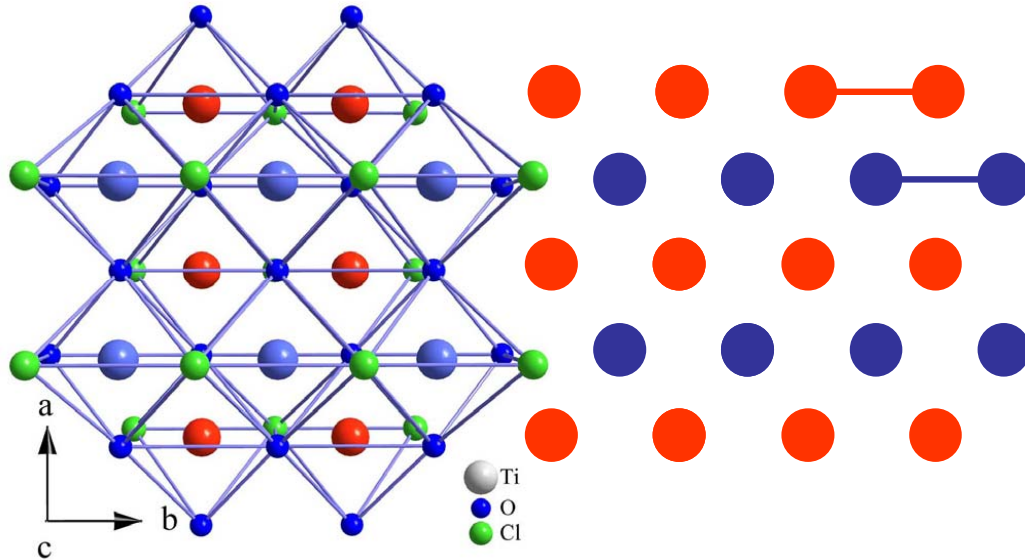
Figure 5.29: View along the crystallographic c axis of the real structure of TiOCl on the left. On the right only the Ti ions are depicted for clarity. The Ti ions of two distinct layers are distinguished by color. A connection of two Ti ions symbolizes the formation of a dimer as shown in the upper right. We will use this schematic picture in the following discussion.

the yellow and the green dashed boxes in Fig. 5.30a). The observation of two distinct Ti sites in NMR [122] at low temperatures thus clearly indicates that an in-phase pattern is realized. This is corroborated by structural data [135], which show that two Ti ions forming a dimer display displacements with different signs perpendicular to the layers, and by an analysis of the phonons in Raman data of TiOBr [148].

For a single bilayer there exist four degenerate in-phase patterns, with dimers on the even/even, even/odd, odd/even or odd/odd bonds of the red/blue layers (see Fig. 5.30a). In principle, this allows for several phase transitions between different superstructures, e.g., from an undimerized high-temperature phase to a dimerized phase where all bilayers realize the even/even pattern and finally to a low-temperature phase in which the dimerization alternates between even/even and odd/odd on adjacent bilayers. However, in this scenario both the NMR signal of two inequivalent Ti sites and the commensurate superstructure satellites are expected to appear at the high-temperature phase transition at T_{c2}, in contrast to the experimental observation.

The second scenario we will discuss focuses on the experimental observation of two inequivalent Ti sites at low temperatures [122, 135]. In principle, this inequivalence may serve as a second order parameter, i.e., the system may undergo both a spontaneous spin-Peierls transition and, at a different temperature, a spontaneous transition to a state with Ti site inequivalence. In the present bilayer structure these two order parameters are coupled, but a Landau expansion [143, 144] shows that there still may be two distinct phase transitions.
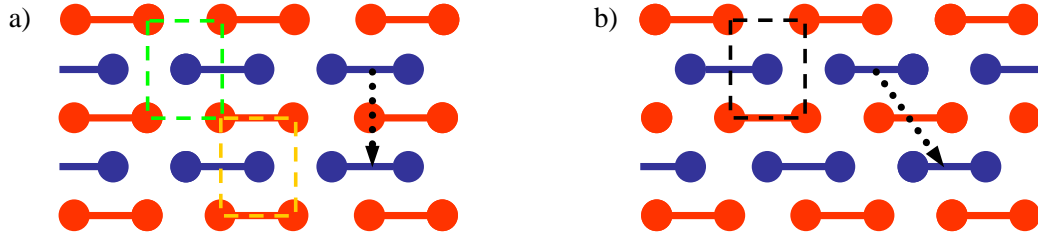
Figure 5.30: Schematic view onto one bilayer (ab plane). On the left the in-phase dimerization pattern is shown. All dimers of one layer (blue/red) reside on the same bonds (even/odd) indicated by the dotted arrow. The two inequivalent sites created in this dimerization pattern are indicated by the dashed boxes. The Ti ion at the center of the green box is facing no dimers in the red layer, whereas the ion at the center of the yellow box is surrounded by two dimers of the red layer. On the right the out-of-phase dimerization pattern is depicted. The dimers of one layer (blue/red) reside on alternate bonds as shown by the arrow. For such a dimerization pattern all Ti sites are equal. They face one dimer of the ajacent layer.

Roughly, this scenario predicts the onset of dimerization with some admixture of site inequivalence at T_{c2}, and the development of full site inequivalence below T_{c1} (or vice versa). In fact, indications of two inequivalent Ti sites are observed in NMR already above T_{c1} [122]. In this scenario, commensurate superstructure satellites are predicted to appear at the high-temperature phase transition at T_{c2}, in disagreement with the experimental data on both TiOCl and TiOBr [136, 142].

In the intermediate phase, superstructure satellites have been reported which are incommensurate both in b and a direction [136, 137]. Incommensurate order was also proposed to explain the very broad NMR signal in the intermediate phase. In compounds with commensurate band filling, incommensurability may arise from the frustration of competing interactions
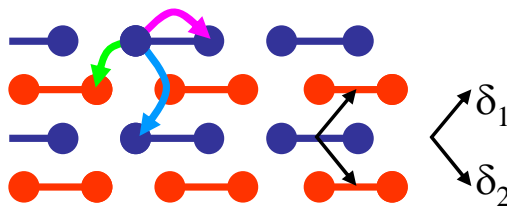
Figure 5.31: The definition of δ_1 and δ_2 is shown on the right. The arrows are indicating the couplings. Magenta for the intra-chain coupling, green for the inter-chain coupling to the second layer (red), and light blue for the inter-chain coupling within one layer. The former two are taken into account in the expansion of the free energy (Eq. 5.1). The latter coupling arises from displacements perpendicular to the chain direction (see text).

which favor different ordering wave vectors. We propose that the incommensurate wave vector arises from the frustration inherent to the bilayer structure. The Landau expansion for the free energy as a function of the displacement ϕ_i^y of the Ti ion i parallel to the chains reads to quadratic order [143, 144]

$$
\begin{aligned}
\Delta F &= \frac{a_0}{2}\sum_i (\phi_i^y)^2 + \frac{a_1}{2}\sum_i \phi_i^y \phi_{i+\delta_1+\delta_2}^y \\
&\quad + \frac{b}{2}\sum_i \phi_i^y (\phi_{i+\delta_1}^y + \phi_{i-\delta_2}^y) \\
&= \frac{1}{2}\sum_{(k,h)} |\phi_{(k,h)}^y|^2 (a_0 + a_1\cos(k) + 2b\cos(\frac{k}{2})\cos(\frac{h}{2}))
\end{aligned}
\tag{5.1}
$$

where k and h denote the momenta parallel and perpendicular to the chains, respectively. Here, the a_1 term describes the tendency towards a spin-Peierls distortion ($a_1 > 0$). For $b=0$, the system undergoes spontaneous dimerization with $k = \pi$ if $a_0 - a_1 < 0$. However, for $b \neq 0$ the free energy is minimized for $h = 0$ and $k = 2\arccos(-b/2a_1) \approx \pi + b/a_1$, i.e., the system becomes incommensurate for any finite value of b. This is due to the fact that the coupling between the layers described by the b term vanishes for $k = \pi$. The system has to become incommensurate in order to gain energy from the interlayer coupling.

In order to explain the additionally observed incommensurability perpendicular to the chains we have to consider a coupling of ϕ_i^y to the displacements ϕ_j^x and ϕ_i^z in a and in c direction, where i and j are neighbors on adjacent chains. The formation of a dimer on sites i and $i+\delta_1+\delta_2$ and the corresponding ϕ_i^y and $\phi_{i+\delta_1+\delta_2}^y$ push away the Ti ion on site $i+\delta_1$, i.e., they couple to $\phi_{i+\delta_1}^{x,z}$. This gives rise to an effective intralayer coupling between the chains, i.e., between site i and $i+\delta_1-\delta_2$. The coupling via ϕ^z leads to a term approximately proportional to $-\cos(h/2)$, favoring the in-phase pattern (Fig. 5.30 a). In contrast, the coupling via ϕ^x produces a term approximately proportional to $\sin(h/2)$, favoring the out-of-phase pattern. In total this yields an incommensurate value of h. This scenario implies two consequences which can be tested experimentally. First, it predicts finite values of ϕ_i^x in the intermediate phase. Second, the incommensurability $\Delta k = b/a_1$ is predicted to decrease with decreasing temperature, because the tendency a_1 towards a spin-Peierls distortion grows with decreasing temperature. Considering in addition $\Delta F_{quartic} = \sum_i (\phi_i^4)^4$, a first-order lock-in transition to commensurate order is expected for small enough Δk at low-temperatures, as observed.

In conclusion, we have shown that TiOCl and TiOBr do not display canonical spin-Peierls behavior. The peculiar properties of TiOX cannot be attributed to orbital fluctuations due to the large crystal-field splitting of the $3d$ levels. The bilayer structure offers a clear explanation for the appearance of two distinct phase transitions. The incommensurate phase at intermediate temperatures arises due to the frustration of interchain interactions. These compounds offer the possibility to study a spin-Peierls transition in a predominantly two-dimensional, frustrated lattice.

Chapter 6

Summary

Here we will collect the main results of this thesis and give an outlook to further investigations.

The nature of orbital excitations in LaMnO$_3$

The e_g system LaMnO$_3$ with the electronic configuration $t_{2g}^3\ e_g^1$ has been predicted to exhibit collective orbital excitations (termed orbitons) from an orbitally ordered ground state [45]. These excitations are expected to have a significant dispersion. Saitoh *et al.* claimed the first experimental observation of orbitons in Raman data of LaMnO$_3$ [44]. The claim is based on a comparison with theory and on the assumption that the observed peaks around 150 meV are too high in energy to originate from two-phonon scattering. We have determined the phonon spectrum from reflectance measurements and observed the highest phonon mode at about 80 meV. Moreover the peaks around 150 meV are observed in the optical conductivity at nearly the same energies, although orbital excitations in $\sigma(\omega)$ require an additional phonon to be excited in order to break the dipole selection rule. Thus orbital excitations should be shifted in $\sigma(\omega)$ by the phonon energy which typically amounts to 50-80 meV. Hence we conclude that these peaks have to be attributed to two-phonon excitations. Additionally weak features are observed around 230 meV and around 300 meV in both Raman and IR data. These features are interpreted as three and four phonon excitations corroborating the nature of the peaks around 150 meV. We found no further low-energy absorptions. However a shoulder at the rise of the first electronic excitation has been observed. By comparison with the results of a cluster calculation it is attributed to a local crystal-field excitation. From this we conclude that the coupling to the lattice is the dominant mechanism that lifts the degeneracy of the e_g orbitals in LaMnO$_3$.

Orbital excitations and ground state properties in the titanates

For the t_{2g} system LaTiO$_3$ a novel ground state has been proposed by Khaliullin and Maekawa in order to reconcile the seemingly contradicting observations of a small spin-wave gap and a strongly reduced magnetic moment [34]. The Hamiltonian they considered accounts for the orbital and spin system (interactions with the lattice are not taken into account). The

ground state they obtain is dominated by orbital fluctuations and has been termed orbital liquid. On the other hand a sizeable distortion of the octahedral environment of the Ti site has been found [57]. By this distortion an intra t_{2g} splitting of about 0.25 eV has been predicted. In this scenario, the electrons occupy the lowest orbital at each site, giving rise to orbital order. The controversially discussed question in this system is whether in the ground state orbital order or orbital fluctuations are present [34, 35, 49, 62, 60, 71, 57]. The former corresponds to dominating coupling to the lattice, whereas the latter arises in the presence of dominating superexchange interactions. We have determined the optical conductivity of $RTiO_3$ (R=La, Sm, Y) in order to observe the low-energy excitations. We have found a broad peak at about 0.3 eV in all three compounds. The peak energies as well as the lineshape are in good agreement with a crystal-field scenario. For such a large intra t_{2g} splitting a significant role of fluctuations can be ruled out. However, a back door has been opened up for the orbital-liquid picture by assuming that the large observed energy actually corresponds to a $t$wo-orbiton process [38]. The fact that only one peak with a not very characteristic lineshape is observed makes it impossible to draw a final conclusion for the ground state of $LaTiO_3$. The observation of a polarization dependence in $LaTiO_3$ has been complicated by the twinning of crystals. Furthermore both scenarios predict only a small polarization dependence in this compound. In $YTiO_3$ orbital order has been observed experimentally [149, 150, 151]. But the proportion that orders is still under discussion since neutron scattering revealed an isotropic spin-wave dispersion [155]. In this compound a significant polarization dependence as well as two clearly separated peaks have been found. This observation is in agreement with the crystal-field scenario which predicts for $YTiO_3$ the largest difference between the intra t_{2g} excitations. In an orbital-liquid scenario the pure orbital excitation is predicted to be isotropic since in this scenario cubic symmetry remains unbroken [35]. In the light of our results on $YTiO_3$ the dominant role of orbital order in this compound becomes apparent. This definitely favors the description of $YTiO_3$ within the crystal-field scenario.

Unconventional spin-Peierls transition in TiOX (X = Cl, Br)

Structurally TiOX is a bilayer system. The magnetic susceptibility in contrast is well described in terms of a $S = \frac{1}{2}$ Heisenberg chain which shows that the magnetism is one-dimensional [50]. The susceptibility vanishes below a temperature T_{c1} which is attributed to a spin-Peierls transition. A second feature is observed at $T_{c2} > T_{c1}$ which is unexpected in a canonical spin-Peierls scenario. This second transition has been discussed in connection with orbital fluctuations [113, 122, 131, 132, 130, 141]. We have measured the transmittance of single crystals and observed in each polarization ($E \parallel a$ and $E \parallel b$) a strong absorption at 0.65 and 1.5 eV for X=Cl, 0.62 and 1.4 eV for X=Br, respectively. Comparison with the results of a cluster calculation for TiOCl gives good agreement between experiment and theory. The lowest intra t_{2g} excitation is not directly dipole allowed due to symmetry. The cluster calculation predicts it at 0.25 eV. Such a large splitting of the t_{2g} orbital suppresses orbital fluctuations. This result is corroborated by ESR data which give a g-factor of ≈ 2 [113]. We have shown that the bilayer geometry is responsible for the unconventional second phase transition [143]. The interchain coupling between chains of one layer and chains of the

adjacent layer is frustrated in the spin-Peierls order pattern realized at low temperatures. This leads to a second-order transition to an incommensurate phase below T_{c2} which is the actual spin-Peierls transition temperature. At T_{c1} the fully dimerized spin-Peierls phase locks in by a first-order transition. Experimental evidence for this scenario is found in the phonon spectra. In the range of phonon excitations we have measured the transmittance and the reflectance. In both properties changes are observed at T_{c1} and T_{c2}, which indicates that the lattice is involved in both transitions. Moreover, in the intermediate phase phonon modes are observed which are absent in the low- and the high-temperature phase and which show a significant shift with temperature. This indicates that the symmetry is lowered, as expected for the incommensurate phase.

Outlook

In the e_g system $LaMnO_3$ the Jahn-Teller coupling is found to be the driving force towards orbital order. Therefore orbital excitations are local crystal-field excitations. For $LaTiO_3$ an orbital-liquid ground state is not ruled out but the experimental results are well explained in a conventional crystal-field scenario, which suggests that coupling to the lattice has to be considered in order to describe the system properly.

At this point one might pose the question: Are there new systems worth looking at in terms of dispersive orbital excitations? Considering transition-metal oxides which exhibit an orbital degeneracy and are Jahn-Teller active one finds two limiting cases. On one side there are Jahn-Teller distorted compounds indicating that the coupling to the lattice lifts the distortion. On the other side there are compounds which exhibit no distortion at all. However these compounds turn out to be metallic which indicates that the formation of bands provides the largest energy gain. These limiting cases will not be suitable for the search for orbitons but one has to find systems placed somewhere in between.

One peculiar compound in this context is CoO in which from a structural point of view a degeneracy persists down to lowest temperatures. However, spin-orbit coupling is strong in this system and may do the job of lifting the degeneracy. Anyway it will be interesting to look at the orbital excitations in this compound, too.

The vanadates are an interesting candidate since the degeneracy lies within the t_{2g} orbitals and they show a small crystal-field splitting in a cluster calculation (especially for the large rare-earth ions). Also different to the titanates, the vanadates exhibit an orbital order transition. The transition temperatures of orbital ordering are comparable or even equal ($LaVO_3$) to the magnetic ordering temperature. This suggests that the spin and orbital interactions originate from the same mechanism, namely superexchange. A puzzling polarization dependence of low-energy excitations has been observed in YVO_3 recently [97]. This raises hope that unconventional orbital excitations may be observed in this compound.

It might be worth looking also at compounds different from the perovskites. One class one might mention in this context are the spinels. However, in this complex field one is never secure from surprises and there certainly are new and interesting phenomena still waiting to be revealed. So further work has to be done here.

Bibliography

[1] S.Sugano, Y. Tanabe and H. Kamimura *Multiplets of Transition-Metal Ions in Crystals* Academic Press, New York and London (1970)

[2] J.G. Bednorz and K.A. Müller, *Z. Phys.* **64**, 189 (1986)

[3] Y. Tokura, A. Urushibara, Y. Moritomo, T. Arima, A. Asamitsu, G. Kido, and N. Furukawa, *J. Phys. Soc. Jpn.* **63**, 3931 (1994)

[4] J. van den Brink, *New J. Phys.* **6** 201 (2004)

[5] F. W. Hehl and Y. N. Obukhov *Foundations of Classical Electrodynamics: Charge, Flux, and Metric* Birkhauser, Boston, MA (2003)

[6] S. Miyasaka, S. Onoda, Y. Okimoto, J. Fujioka, M. Iwama, N. Nagaosa, and Y. Tokura, *Phys. Rev. Lett.* , **94** 076405 (2005)

[7] S. Sugai and K. Hirota, *Phys. Rev.* B **73** 020409 (R) (2006)

[8] D. I. Khomskii and T.Mizokawa, *Phys. Rev. Lett.* **94** (2005) 156402

[9] SP. G. Radaelli *Nature* **416** 155 (2002)

[10] M. Schmidt, W. Ratcliff II, P.G. Radaelli, K. Refson, N.M. Harrison, and S.W. Cheong, *Phys. Rev. Lett.* **92** 056402 (2002)

[11] Y. Kitaoka, T. Kobayashi, A. Ko-da, H. Wakabayashi, Y. Niino, H. Yamakage, S. Taguchi, K. Amaya, K. Yamaura, M. Takano, A. Hirano and R. Kanno, *J. Phys. Soc. Jpn.* **67** 3703 (1998)

[12] L. Craco, M. S. Laad, and E. Müller-Hartmann, *Phys. Rev. Lett.* **90** 237203 (2003)

[13] M. Imada, A. Fujimori, and Y.Tokura, *Rev. Mod. Phys.* **70** 1039 (1998)

[14] Y. Tokura and N. Nagaosa, *Science* **288** 462 (2000)

[15] A. Auerbach *Interacting Electrons and Quantum Magnetism*, Springer, New York (1994)

[16] A. O. Gogolin, A. A. Nersesyan, and A. M. Tsvelik *Bosonization and Strongly Correlated Systems*, Cambridge University Press, Cambridge (1998)

[17] P. C. Hohenberg, *Phys. Rev.* **158** 383 (1967)

[18] N. D. Mermin and H. Wagner, *Phys. Rev. Lett.* **22** 1133 (1966)

[19] T. Barnes, E. Dagotto, J. Riera, and E. S. Swanson, *Phys. Rev.* B **47** 3196 (1993)

[20] F. D. M. Haldane, *Phys. Rev. Lett.* **50** 1153 (1983)

[21] L. D. Faddeev and L. A. Takhtajan, *Phys. Lett.* **85A** 375 (1981)

[22] N. Andrei and J. H. Lowenstein, *Phys. Rev. Lett.* **43** 1698 (1979)

[23] M. Karbach, G. Müller, A. H. Bougourzi, A. Fledderjohann, and K.-H. Mütter, *Phys. Rev.* B **55** 12510 (1997)

[24] M. Arai, M. Fujita, M. Motokawa, J. Akimitsu, and S. M. Bennington, *Phys. Rev. Lett.* **77** 3649 (1996)

[25] K. P. Schmidt and G. S. Uhrig, *Phys. Rev. Lett.* **90** 227204 (2003)

[26] O. P. Sushkov and V. N. Kotov, *Phys. Rev. Lett.* **81** 1941 (1998)

[27] M. Windt, M. Grüninger, T. Nunner, C. Knetter, K. P. Schmidt, G. S. Uhrig, T. Kopp, A. Freimuth, U. Ammerahl, B. Büchner, A. and Revcolevschi, *Phys. Rev. Lett.* **87** 127002 (2001)

[28] E. Dagotto, J. Riera, and D. Scalapino, *Phys. Rev.* B **45** 5744 (1992)

[29] E. Dagotto, *Rep. Prog. Phys.* **62** 1525 (1999)

[30] M. Uehara, T. Nagata, J. Akimitsu, H. Takahashi, N. Môri, and K. Kinoshita, *J. Phys. Soc. Jpn.* **65** 2764 (1996)

[31] S. Ishihara, M. Yamanaka, and N. Nagaosa, *Phys. Rev.* B **56** 686 (1997)

[32] L. F. Feiner, A. M. Oles and, J. Zaanen, *Phys. Rev. Lett.* **78** 2799 (1997)

[33] T. Wagner, *private communication*

[34] G. Khaliullin and S. Maekawa, *Phys. Rev. Lett.* **85** 3950 (2000)

[35] G. Khaliullin *Phys. Rev.* B **64** 212405 (2001)

[36] D. Khomskii and J. van den Brink *Phys. Rev. Lett.* **85** 3229 (2000)

[37] G. Khaliullin, P. Horsch and A. M. Oleś, *Phys. Rev. Lett.* **86** 3879 (2001)

[38] G. Khaliullin, *Prog. Theor. Phys. Suppl.* **160**, 155 (2005)

[39] D. I. Khomskii, *Physica Scripta* **72** CC8-14 (2005) (Comments Cond. Mat. Phys.)

[40] R. Rückamp, E. Benckiser, M. W. Haverkort, H. Roth, T. Lorenz, A. Freimuth, L. Jongen, A. Möller, G. Meyer, P. Reutler, B. Büchner, A. Revcolevschi, S-W. Cheong, C. Sekar, G. Krabbes and M. Grüninger, *New J. Phys.* **7** 144 (2005)

[41] J. Sirker and G. Khaliullin, *Phys. Rev.* B **67** 100408(R) (2003)

[42] G. Khaliullin, *Phys. Rev.* B **64** 212405 (2003)

[43] P. Horsch, G. Khaliullin, and A. M. Oleś, *Phys. Rev. Lett.* **91** 257203 (2003)

[44] E. Saitoh, S. Okamoto, K. T. Takahashi, K. Tobe, K. Yamamoto, T. Kimura, S. Ishihara, S. Maekawa, and Y. Tokura, *Nature* **410** 180 2001

[45] S. Ishihara, J. Inoue, and S. Maekawa, *Phys. Rev.* B **55** 8280 (1997)

[46] G. Khaliullin and S. Okamoto, *Phys. Rev. Lett.* **89** 167201 (2002)

[47] G. Khaliullin and S. Okamoto, *Phys. Rev.* B **68** 205109 (2003)

[48] S. Ishihara, *Phys. Rev.* B **69** 075118 (2004)

[49] B. Keimer, D. Casa, A. Ivanov, J. W. Lynn, M. von Zimmermann, J. P. Hill, D. Gibbs, Y. Taguchi, and Y. Tokura *Phys. Rev. Lett.* **85** 3946 (2000)

[50] A. Seidel, C. A. Marianetti, F. C. Chou, G. Ceder, and P. A. Lee *Phys. Rev.* B **67** 020405(R) (2003)

[51] A. Seidel and P. A. Lee *Phys. Rev.* B **69** 094419 (2004)

[52] C. Ulrich, G. Khaliullin, J. Sirker, M. Reehuis, M. Ohl, S. Miyasaka, Y. Tokura, and B. Keimer 2003 *Phys. Rev. Lett.* **91** 257202

[53] A. Gößling, Ph.D. Thesis, to be published

[54] H. Roth , Ph.D. Thesis, to be published

[55] M. Windt, Ph.D. Thesis, University of Cologne (2003)

[56] E. Benckiser, Diploma thesis (2004)

[57] M. Cwik, T. Lorenz, J. Baier, R. Müller, G. André, F. Bourée, F. Lichtenberg, A. Freimuth, R. Schmitz, E. Müller-Hartmann, and M. Braden *Phys. Rev.* B **68** 060401(R) (2003)

[58] G. I. Meijer, W. Henggeler, J. Brown, O.-S. Becker, J. G. Bednorz and C. Rossel, and P. Wachter, *Phys. Rev.* B **59** 11832 (1999)

[59] L. Craco, M. S. Laad, S. Leoni, and E. Müller-Hartmann, *Phys. Rev.* B **70** 195116 (2004)

[60] M. W. Haverkort, Z. Hu, A. Tanaka, G. Ghiringhelli, H. Roth, M. Cwik, T. Lorenz, C. Schüßler-Langeheine, S. V. Streltsov, A. S. Mylnikova, V. I. Anisimov, C. de Nadai, N. B. Brookes, H. H. Hsieh, H.-J. Lin, C. T. Chen, T. Mizokawa, Y. Taguchi, Y. Tokura, D. I. Khomskii, and L. H. Tjeng, *Phys. Rev. Lett.* **94** 056401 (2005)

[61] M. Mochizuki and M. Imada, *J. Phys. Soc. Jpn.* **70** 2872 (2001)

[62] M. Mochizuki and M. Imada *Phys. Rev. Lett.* **91** 167203 (2003)

[63] M. Mochizuki and M. Imada, *J. Phys. Soc. Jpn.* **73** 1833 (2004)

[64] M. Mochizuki and M. Imada, *New J. Phys.* **6** 154 (2004)

[65] V. Fritsch, J. Hemberger, M. V. Eremin, H.-A. Krug von Nidda, F. Lichtenberg, R. Wehn, and A. Loidl, *Phys. Rev.* B **65** 212405 (2002)

[66] J. Hemberger, H.-A. Krug von Nidda, V. Fritsch, J. Deisenhofer, S. Lobina, T. Rudolf, P. Lunkenheimer, F. Lichtenberg, A. Loidl, D. Bruns, and B. Büchner, *Phys. Rev. Lett.* **91** 066403 (2003)

[67] T. Kiyama and M. Itoh, *Phys. Rev. Lett.* **91** 167202 (2003)

[68] A. B. Harris, T. Yildirim, A. Aharony, O. Entin-Wohlmann, and I. Y. Korenblit, *Phys. Rev. Lett.* **91** 087206 (2003)

[69] A. B. Harris, T. Yildirim, A. Aharony, O. Entin-Wohlman, and I. Ya. Korenblit, *Phys. Rev.* B **69** 035107 (2004)

[70] K. Kikoin, O. Entin-Wohlmann, V. Fleurov, and A. Aharony, *Phys. Rev.* B **67** 214418 (2003)

[71] E. Pavarini, S. Biermann, A. Poteryaev, A. I. Liechtenstein, A. Georges, and O. K. Andersen, *Phys. Rev. Lett.* **92** 176403 (2004)

[72] Y. Okimoto, T. Katsufuji, Y. Okada, T. Arima, and Y. Tokura, *Phys. Rev.* B **51** 9581 (1995)

[73] I. V. Solovyev, *Phys. Rev.* B **69** 134403 (2004)

[74] Z. Fang and N. Nagaosa, *Phys. Rev. Lett.* **93** 176404 (2004)

[75] M. Grüninger, R. Rückamp, M. Windt, and A. Freimuth, *Nature* **418** 39 (2002)

[76] R. Krüger, B. Schulz, S. Naler, R. Rauer, D. Budelmann, J. Bäckström, K. H. Kim, S.-W. Cheong, V. Perebeinos, and M. Rübhausen, *Phys. Rev. Lett.* **92** 097203 (2004)

[77] L. Martín-Carrón and A. de Andrés, *Phys. Rev. Lett.* **92** 175501 (2004)

[78] C. F. Ballhausen, *Introduction to Ligand Field Theory* McGraw-Hill, New York (1962)

[79] K. A. Kikoin and V. N. Fleurov, *Transition Metal Impurities in Semiconductors. Electronic Structure and Physical Properties* World Scientific, Singapore (1994)

[80] E. D. Nelson, J. Y. Wong, and A. L. Schawlow, *Phys. Rev.* **156** 298 (1967)

[81] A. L. Schawlow, D. L. Wood, and A. M. Clogston, *Phys. Rev. Lett.* **3** 271 (1959)

[82] D. D. Sell, R. L. Greene, and R. M. White, *Phys. Rev.* **158** 489 (1967)

[83] M. Z. Hasan, E. D. Isaacs, Z.-X. Shen, L. L. Miller, K. Tsutsui, T. Tohyama, and S. Maekawa, *Science* **288** 1811 (2000)

[84] G. Khaliullin and R. Kilian, *Phys. Rev.* B **61** 3494 (2000)

[85] J. van den Brink, W. Stekelenburg, D. I. Khomskii, G. A. Sawatzky, and K. I. Kugel, *Phys. Rev.* B **58** 10276-10282 (1998)

[86] K. I. Kugel and D. I. Khomskii, *Sov. Phys. Usp.* **25** 231 (1982)

[87] J. B. Goodenough, *Magnetism and chemical bond*, Intersience, New York (1963)

[88] B. N. Figgis and M. A. Hitchman, *Ligand Field Theory and its Applications* Wiley (1999)

[89] M. Grüninger, M. Windt, E. Benckiser, T. S. Nunner, K. P. Schmidt, G. S. Uhrig, and T. Kopp, *Adv. Solid State Phys.* **43** 95 (2003)

[90] J. P. Falck, J. D. Perkins, A. Levy, M. A. Kastner, J. M. Graybeal, and R. J. Birgeneau, *Phys. Rev.* B **49** 6246 (1994)

[91] A. B. Schumacher, J. S. Dodge, M. A. Carnahan, R. A. Kaindl, D. S. Chemla, and L. L. Miller, *Phys. Rev. Lett.* **87** 127006 (2001)

[92] B. Fromme, M. Möller, T. Anschütz, C. Bethke, and E. Kisker, *Phys. Rev. Lett.* **77** 1548 (1996)

[93] J. Ferguson, H. J. Guggenheim, and Y. Tanabe, *J. Phys. Soc. Jpn.* **21** 692 (1966)

[94] O. Cador, C. Mathonière, and O. Kahn, *Inorg. Chem.* **39** 3799-3804 (2000)

[95] M. Guillaume, W. Henggeler, A. Furrer, R. S. Eccleston, and V. Trounov, *Phys. Rev. Lett.* **74** 3423 (1995)

[96] Y. Tanaka, A. Q. R. Baron, Y.-J. Kim, K. J. Thomas, J. P. Hill, Z. Honda, F. Iga, S. Tsutsui, D. Ishikawa, and C. S. Nelson, *New J. Phys.* **6** 161 (2004)

[97] E. Benckiser, Thesis *to be published*

[98] G. Khaliullin, *private communication*

[99] J. Lorenzana and G. A. Sawatzky, *Phys. Rev. Lett.* **74** 1867 (1995)

[100] J. Lorenzana and G. A. Sawatzky, *Phys. Rev.* B **52** 9576 (1995)

[101] H. Suzuura, H. Yasuhara, A. Furusaki, N. Nagaosa, and Y. Tokura, *Phys. Rev. Lett.* **76** 2579 (1996)

[102] J. Lorenzana and R. Eder, *Phys. Rev.* B **55** 3358(R) (1997)

[103] J. D. Perkins, J. M. Graybeal, M. A. Kastner, R. J. Birgeneau, J. P. Falck, and M. Greven, *Phys. Rev. Lett.* **71** 1621 (1993)

[104] J. D. Perkins, R. J. Birgeneau, J. M. Graybeal, M. A. Kastner, and D. S. Kleinberg, *Phys. Rev.* B **58** 9390 (1998)

[105] J. D. Perkins, D. S. Kleinberg, M. A. Kastner, R. J. Birgeneau, Y. Endoh, K. Yamada, and S. Hosoya, *Phys. Rev.* B **52** 9863(R) (1995)

[106] J. van den Brink, *Phys. Rev. Lett.* **87** 217202 (2001)

[107] R. D. Cowan, *The theory of atomic structure and spectra* University of California press, Berkely (1981)

[108] H. A. Jahn and E. Teller, *Proc. R. Soc. London* A **161**, 220 (1937)

[109] W. A. Harrison, *Electronic Structure and the Properties of Solids* W.H.Freeman and Company, San Francisco (1980)

[110] J. C. Slater and G. F. Koster, *Phys. Rev.* **94** 1498 (1954)

[111] T. Saitoh, A. E. Bocquet, T. Mizokawa, and A. Fujimori *Phys. Rev.* B **52** 5419 (1995)

[112] A. Tanaka and T. Jo *J. Phys. Soc. Jpn.* **63** 2788 (1994)

[113] V. Kataev, J. Baier, A. Möller, L. Jongen, G. Meyer, and A. Freimuth, *Phys. Rev.* B **68** 140405 (2003)

[114] F. Lichtenberg, D. Widmer, J. G. Bednorz, T. Williams, and A. Reller, *Z. Phys.* B **82** 211 (1991)

[115] J. Geck, P. Wochner, S. Kiele, R. Klingeler, A. Revcolevschi, M. von Zimmermann, and B. Büchner, *New J. Phys.* **6** 152 (2004)

[116] V. Massarotti, D. Capsoni, M. Bini, A. Altomare, and A. G. G. Moliterni, *Zeitschrift für Kristallographie* **214** 205 (1999)

[117] P. E. Sulewski and S.-W. Cheong, *Phys. Rev.* B **50** 551 (1994)

[118] C. Sekar, K. Ruck, G. Krabbes, A. Teresiak, and T. Watanabe, *Physica* C **378** 678 (2002)

[119] J. J. de Boer, D. Bright, and J. N. Helle, *Acta Crystallographica* B **28** 3436 (1972)

[120] M. Grüninger, M. Windt, T. Nunner, C. Knetter, K. P. Schmidt, G. S. Uhrig, T. Kopp, A. Freimuth, U. Ammerahl, B. Büchner, and A. Revcolevschi, *J. Phys. Chem. Solids* **63** 2167-2173 (2002)

[121] R. J. Beynon and J. A. Wilson, *J. Phys.: Condens. Matter* **5** 1983 (1993)

[122] T. Imai and F. C. Chou, 2003 *Preprint* cond-mat/0301425

[123] M. Hase, I. Terasaki, and K. Uchinokura, *Phys. Rev. Lett.* **70**, 3651 (1993).

[124] M. Azuma, Z. Hiroi, M. Takano, K. Ishida, and Y. Kitaoka, *Phys. Rev. Lett.* **73**, 3463 (1994).

[125] M. Isobe and Y. Ueda, *J. Phys. Soc. Jpn.* **65**, 1178 (1996)

[126] T. Ohama, M. Isobe, H. Yasuoka, and Y. Ueda, *J. Phys. Soc. Jpn.* **66**, 545 (1997).

[127] Y. Fagot-Revurat, M. Mehring, and R. K. Kremer, *Phys. Rev. Lett.* **84**, 4176 (2000)

[128] T. Ohama, H. Yasuoka, M. Isobe, and Y. Ueda, *Phys. Rev.* B **59**, 3299 (1999)

[129] T. Yoshihama, M. Nishi, K. Nakajima, K. Kakurai, Y. Fujii, M. Isobe, C. Kagami, and Y. Ueda, *J. Phys. Soc. Jpn.* **67**, 744 (1998).

[130] P. Lemmens, K.-Y. Choi, G. Caimi, L. Degiorgi, N. N. Kovaleva, A. Seidel, and F. C. Chou, *Phys. Rev.* B **70** 134429 (2004)

[131] G. Caimi, L. Degiorgi, N. N. Kovaleva, P. Lemmens, and F. C. Chou, *Phys. Rev.* B **69** 125108 (2004)

[132] G. Caimi, L. Degiorgi, P. Lemmens, and F. C. Chou, *J. Phys. Cond. Mat.* **16** 5583 (2004)

[133] T. Saha-Dasgupta, R. Valenti, H. Rosner, and C. Gros, *Europhys. Lett.* **67** 63 (2004)

[134] J. Hemberger, M. Hoinkis, M. Klemm, M. Sing, R. Claessen, S. Horn, and A. Loidl, *Phys. Rev.* B **72** 012420 (2005)

[135] M. Shaz, S. van Smaalen, L. Palatinus, M. Hoinkis, M. Klemm, S. Horn, and R. Claessen, *Phys. Rev.* B **71** 100405 (R) (2005)

[136] S. van Smaalen, L. Palatinus, and A Schönleber, *Phys. Rev.* B **72** 020105 (2005)

[137] E. Abel, K. Matan, F. C. Chou, and Y. S. Lee, *Bull. Amer. Phys. Soc.* **49** 317 (2004) *(APS March Meeting Montreal 2004, Session D25.014)*

[138] E. M. Snigireva, S. I. Troyanov, and V. B. Rybakov, *Zhurnal Neorganicheskoi Khimii* **35** 1945 (1990) (ICSD code 39314)

[139] C. H. Maule, J. N. Tothill, P. Strange, and J. A. Wilson *J. Phys. C: Solid State Phys.* **21** 2153-2179 (1988)

153

[140] M. Grüninger, Ph.D. Thesis, University of Groningen, 1999

[141] P. Lemmens, K.-Y. Choi, R. Valenti, T. Saha-Dasgupta, E. Abel, Y. S. Lee, and F. C. Chou, *Preprint* cond-mat/0501577 (2005)

[142] T. Sasaki, M. Mizumaki, K. Kato, Y. Watabe, Y. Nishihata, M. Takata, and J. Akimitsu *Preprint* cond-mat/0501691 (2005)

[143] R. Rückamp, J. Baier, M. Kriener, M. W. Haverkort, T. Lorenz, G. S. Uhrig, L. Jongen, A. Möller, G. Meyer, and M. Grüninger, *Phys. Rev. Lett.* **95** 097203 (2005)

[144] G. Uhrig, *private communication*

[145] L. Craco, M. Laad, and E. Müller-Hartmann, *Preprint* cond-mat/0410472 (2004)

[146] T. Saha-Dasgupta, A. Lichtenstein, and R. Valenti, *Phys. Rev.* B **71** 153108 (2005)

[147] L. Pisani, T. Maitra, and R. Valenti, *Phys. Rev.* B **73** (2006)

[148] P. van Loosdrecht, *private communciation*

[149] H. Nakao, Y. Wakabayashi, T. Kiyama, Y. Murakami, M. v. Zimmermann, J. P. Hill, D. Gibbs, S. Ishihara, Y. Taguchi, and Y. Tokura, *Phys. Rev.* B **66**, 184419 (2002)

[150] M. Itoh, M. Tsuchiya, H. Tanaka, and K. Motoya, *Jour. Phys. Soc. Jpn.* **68**, 2783 (1999)

[151] H. Ichikawa, J. Akimitsu, M. Nishi, and K. Kakurai, *Physica* B **281&282**, 482 (2000)

[152] D. Barba, S. Jandl, V. Nekvasil, M. Maryško, M Diviš, A. A. Martin, C. T. Lin, M. Cardona, and T. Wolf, *Phys. Rev.* B **63** 054528 (2001)

[153] C. Ulrich, A. Gössling, M. Grüninger, M. Guennou, H. Roth, M. Cwik, T. Lorenz, G. Khaliullin, and B. Keimer, *Preprint* cond-mat/0503106 (2005)

[154] D. A. MacLean, H.-N. Ng, and J. E. Greedan, *J. Sol. State Chem.* **30** 35 (1979)

[155] C. Ulrich, G. Khaliullin, S. Okamoto, M. Reehuis, A. Ivanov, H. He, Y. Taguchi, Y. Tokura, and B. Keimer, *Phys. Rev. Lett.* **89** 167202 (2002)

[156] V. G. Zubkov, I. F. Berger, A. M. Artamonova, and G. V. Bazuyev, *Kristallografiya* **29** 494-497 (1984)

[157] R. Schmitz, O. Entin-Wohlman, A. Aharony, A. Brooks Harris, and E. Müller-Hartmann, *Phys. Rev.* B **71** 144412 (2005)

[158] K. Held, M. Ulmke, N. Blümer, and D. Vollhardt, *Phys. Rev.* B **56** 14469 (1997)

[159] S. Ishihara, Y. Murakami, T. Inami, K. Ishii, J. Mizuki, K. Hirota, S. Maekawa, and Y. Endoh, *New J. Phys.* **7** 119 (2005)

[160] J. van den Brink, G. Khaliullin, and D. I. Khomskii, *Preprint* cond-mat/0206053 (2002)

[161] Y. Murakami, J. P. Hill, D. Gibbs, M. Blume, I. Koyama, M. Tanaka, H. Kawata, T. Arima, Y. Tokura, K. Hirota, and Y. Endoh, *Phys. Rev. Lett.* **81** 582 (1998)

[162] J. Rodriguez-Carvajal, M. Hennion, F. Moussa, A. H. Moudden, L. Pinsard, and A. Revcolevschi, *Phys. Rev.* B **57** 3189(R) (1998)

[163] F. Moussa, M. Hennion, J. Rodriguez-Carvajal, A. H. Moudden, L. Pinsard, and A. Revcolevschi, *Phys. Rev.* B **54** 15149 (1996)

[164] T. Chatterji, F. Fauth, B. Ouladdiaf, P Mandal, and B. Ghosh, *Phys. Rev.* B **68** 052406 (2003)

[165] K. Hirakawa and Y.Kurogi, *Prog. Theor. Phys. (Suppl.)* **46** 147 (1970)

[166] B. Lake, D. A. Tennant, and S. E. Nagler, *Phys. Rev. Lett.* **85** 832 (2000)

[167] W. Reichardt and M. Braden, *Physica* b **263-264** 416 (1999)

[168] K. Y. Choi, P. Lemmens, G. Güntherodt, Y. G. Pashkevich, V. P. Gnezdilov, P. Reutler, L. Pinsard-Gaudart, B. Büchner, and A. Revcolevschi, *Phys. Rev. B* **72** 024301 (2005)

[169] E. Saitoh, S. Okamoto, K. Tobe, K. Yamamoto, T. Kimura, S. Ishihara, S. Maekawa, and Y. Tokura, *Nature* **418** 40 (2002)

[170] A. Paolone, P. Roy, A. Pimenov, A. Loidl, O. K. Mel'nikov, and A. Y. Shapiro, *Phys. Rev.* B **61** 11255 (2000)

[171] V. Perebeinos and P. B. Allen, *Phys. Rev.* B **64** 085118 (2001)

[172] W. Reichardt and M. Braden, *private communictaion*

[173] M. Grüninger, D. van der Marel, A. Damascelli, A. Zibold, H. P. Geserich, A. Erb, M. Kläser, T. Wolf, T. Nunner, and T. Kopp, *Physica* C **317-318** 286-291 (1999)

[174] S. L. Chaplot, W. Reichardt, L. Pintschovius, and N. Pyka, *Phys. Rev.* B **52** 7230 (1995)

[175] K. Tobe, T. Kimura, Y. Okimoto, and Y. Tokura, *Phys. Rev.* B **64** 184421 (2001)

[176] N. N. Kovaleva, A. V. Boris, C. Bernhard, A. Kulakov, A. Pimenov, A. M. Balbashov, G. Khaliullin, and B. Keimer, *Phys. Rev. Lett.* **93** 147204 (2004)

[177] J. H. Jung, K. H. Kim, D. J. Eom, T. W. Noh, E. J. Choi, J. Yu, Y. S. Kwon, and Y. Chung, *Phys. Rev. B* **55**, 15 489 (1997)

[178] P. B. Allen and V. Perebeinos, *Phys. Rev. Lett.* **83** 4828 (1999)

[179] A. J. Millis, *Phys. Rev.* B **53** 8434 (1996)

[180] W. E. Pickett and D. J. Singh, *Phys. Rev.* B **53** 1146 (1996)

[181] I. Solovyev, N. Hamada, and K. Terakura, *Phys. Rev.* B **53** 7158 (1996)

[182] I. S. Elfimov, V. I. Anisimov, and G. A. Sawatzky, *Phys. Rev. Lett.* **82** 4264 (1999)

[183] K. H. Ahn and A. J. Millis, *Phys. Rev.* B **61** 13545 (2000)

[184] J. Bala and A. M. Oles, *Phys. Rev.* B **62** 6085(R) (2000)

[185] J. Darriet and L. P. Regnault, *Solid State Comm.* **86** 409 (1993)

[186] G. Xu, G. Aeppli, M. E. Bisher, C. Broholm, J. F. DiTusa, C. D. Frost, T. Ito, K. Oka, R. L. Paul, H. Takagi, and M. M. J. Treacy, *Science* **289** 419 (2000)

[187] T. Nunner and T. Kopp, *private communication*

[188] J. B. Grant and A. K. McMahan, *Phys. Rev.* B **46** 8440 (1992)

[189] R. L. Martin and P. J. Hay, *J. Chem. Phys.* **98** 8680 (1993)

[190] H. Eskes, L. H. Tjeng, and G. A. Sawatzky *Phys. Rev.* B **41** 288 (1990)

[191] C. de Graaf, Ph.D. Thesis, University of Groningen (1998)

[192] H. P. Geserich, G. Scheiber, J. Geerk, H. C. Li, G. Linker, W. Assmus, and W. Weber, *Europhys. Lett.* **6** 277 (1988)

[193] P. Kuiper, J.-H. Guo, C. Såthe, L.-C. Duda, J. Nordgren, J. J. M. Pothuizen, F. M. F. de Groot, and G. A. Sawatzky, *Phys. Rev. Lett.* **80** 5204 (1998)

[194] C. L. Teske and H. K. Müller-Buschbaum, *Zeitschrift für Anorganische und Allgemeine Chemie* **370** 134 (1969)

[195] T. K. Kim, H. Rosner, S.-L. Drechsler, Z. Hu, C. Sekar, G. Krabbes, J. Málek, M. Knupfer, J. Fink, and H. Eschrig, *Phys. Rev.* B **67** 024516 (2003)

[196] Y. Yamashita and K. Ueda, *Phys. Rev. Lett.* **85** 4960 (2000)

[197] V. N. Kotov, M. E. Zhitomirsky, and O. P. Sushkov, *Phys. Rev.* B **63** 064412 (2001)

[198] P. Lemmens, K.-Y. Choi, E. E. Kaul, C. Geibel, K. Becker, W. Brenig, R. Valenti, C. Gros, M Johnsson, P. Millet, and F. Mila, *Phys. Rev. Lett.* **87** 227201 (2001)

[199] W. Brenig, *Phys. Rev.* B **67** 064402 (2003)

[200] J. M. P. Carmelo, N. M. R. Peres, and P. D. Sacramento, *Phys. Rev. Lett.* **84** 4673 (2000)

[201] E. Jeckelmann, F. Gebhard, and F. H. L. Essler, *Phys. Rev. Lett.* **85** 3910 (2000)

[202] F. H. L. Essler, F. Gebhard, and E. Jeckelmann, *Phys. Rev.* B **64** 125119 (2001)

[203] T. Saitoh, A. E. Bocquet, T. Mizokawa, and A. Fujimori, *Phys. Rev.* B **52**, 7934 (1995)

[204] P.W. Anderson, Science **235**, 1196 (1987)

[205] J. Bonner and M.Fisher *Phys. Rev.* **135**, A640 (1964)

[206] H. Schäfer, F. Wartenpfuhl, and E. Weise, *Z. Anorg. Allg. Chemie* **295** 268 (1958)

[207] F. Wooten *Optical Properties of Solids* Academic Press, New York (1972)

[208] E. P. Wigner *Group theory and its application to the quantum mechanics of atomic spectra* Academic Press, New York and London (1959)

Acknowledgement

An dieser Stelle möchte ich all denen danken, die das Entstehen dieser Arbeit begleitet haben:

Prof. Freimuth, der mir diese Arbeit ermöglich hat und Garant einer gute Arbeitsathmosphäre im gesamten Institut war.

Marco Windt, der mich mit viel Geduld in die experimentelle Arbeit eingeführt hat.

Der Optikgruppe Eva, Christina, Alex und Thomas für die tolle Zusammenarbeit, die Unterstützung bei Problemen und die vielen interessanten Diskussionen.

Jörg Baier und Kay Berggold für die stehte Hilfsbereitschaft und gute Zusammenarbeit.

Mauritz Haverkort für die Nutzung des Clusterprogramms und die Fehlersuche bei meinen Inputfiles.

Holger Roth für die vielen hervorragenden Einkristalle.

Matthias Cwik und Wolf Dieter Stein auch für Kristalle aber vor allem für deren Orientierung.

Ralf Müller für die fürsorgliche und vertrauensvolle Art nicht nur beim Nachschub an Laborchemikalien.

Inge Simons für die eine oder andere EDX Analyse.

Carmen Handels für Unterstützung in den kleinen Dingen und ihre herzliche und aufgeschlossene Art bei der Arbeit.

Halit Anapa für mache Diskussion speziell zu mathematisch Themen.

Prof. Khomskii für die stets offene Tür bei allen Fragen.

Prof. Mostovoi für die stets offene und geduldige Art auf Fragen mit hoher Kompetenz einzugehen.

Thomas Lorenz für geduldige Auskünfte und Erklärungen rund um Thermodynamik.

Götz Uhrig für viele Erleuterungen speziell zu allgemeineren Fragen.

Vladek Kataev für die Einführung in die ESR.
 Angela Möller für interessante Diskussionen viele Kristalle und gute Zusammenarbeit.

Prof. Markus Grüninger für die engagierte und kompetente Betreuung bei der seine Begeisterung für Physik motiviren bis ansteckend wirkte.

Vielen Dank!

Appendix A

Wigner-Eckhart theorem

Here we will derive the Wigner-Eckhart theorem as straight as possible without involving more mathematical framework as actually needed. The concept behind the deduction is to show that each step follows in a natural way by asking simple questions. Although there exists a large variety of literature on this subject we have not found a similar treatment there. However, for additional reading some texts may be recommended.

We start with the definition of the symmetry group and find representations naturally as transformations properties of eigenspaces. Simple questions about representations lead us to the definition of irreducible representations. Invariant physical properties are recognized as matrices that commutes with all representations. With some basic properties of homomorphisms we are then able to deduce the Wigner-Eckhart theorem. In the following the product of two physical objects (wave function or operator), i.e. of their representations, is shown to be the tensor product of the corresponding matrices. This yields the form of the theorem which is used in practice. Some examples illustrate the variety of applications. Since working with characters is convenient in practice they are also introduce. Followed by some further examples.

How does symmetry enter the quantum mechanical description of a physical system?

First we will sharpen the concept of symmetry. If a physical system is invariant under a certain transformation then we will call this transformation a symmetry transformation. For example three identical atoms on the corner of an equilateral triangle can be rotated by 120º or −120º without changing anything (Fig. A.1). We could also reflect the system on each of the three bisectors and it would look the same afterwards. There are three fundamental properties of symmetry transformations:

1. Applying consecutively two symmetry transformations (S, T), the system will remain unchanged since the first leaves the system as it has been before and the second does not change it, either. So we find that carrying out consecutively two symmetry transformations, the resulting transformation $ST = U$ is again a symmetry transformation.
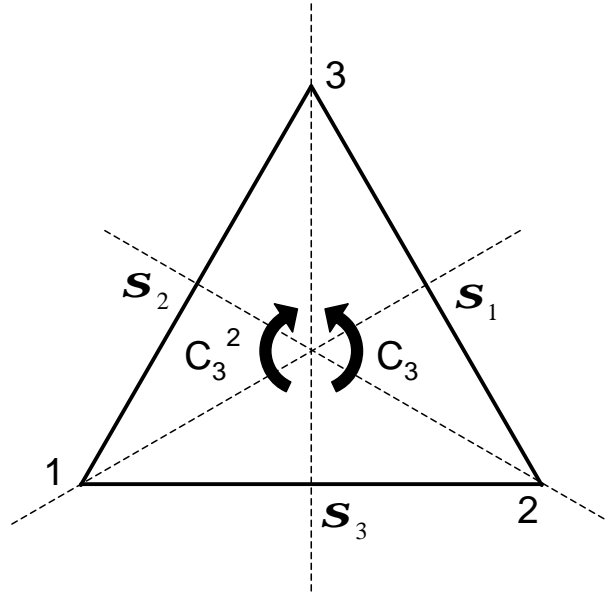
Figure A.1: The six symmetry elements of the equilateral triangle: Identity (id), counter clockwise rotation about 120° (C_3), clockwise rotation about 240° (C_3^2), mirror planes (σ_1, σ_2, σ_3).

2. Every transformation can be reversed (since one should not loose any points of space the transformation has to be bijective), and the reversed transformation of a symmetry transformation is also one.

3. Finally, mapping each point onto itself gives obviously a symmetry transformation (of every system), which moreover commutes with every other transformation (symmetry or not). It is called the neutral element or identity.

These three properties make the symmetry transformations to be a *group* in the mathematical sense. It is called the symmetry group. The number of symmetry transformations can be finite (compare Fig. A.1) as well as infinite (e.g. rotations). For convenience we will think first of finite groups in the following and consider infinite (continuous) groups later. But anyway everything known about a group can be applied to the symmetry group.

Now we come back to our main question proposed in the beginning. Consider an eigenfunction $|\psi\rangle$ of the system. $|\psi\rangle$ is a solution of the Schrödinger equation

$$H|\psi\rangle = \varepsilon|\psi\rangle \quad .$$

Applying a symmetry transformation T to the system, it will not change any of its physical properties. In particular the energy will stay the same. This implies that $THT^{-1} = H$ or equivalently $HT = TH$. Hence we find

$$
\begin{aligned}
THT^{-1}\,T|\psi\rangle &= T\,\varepsilon|\psi\rangle \\
HT|\psi\rangle &= \varepsilon\,T|\psi\rangle
\end{aligned}
$$
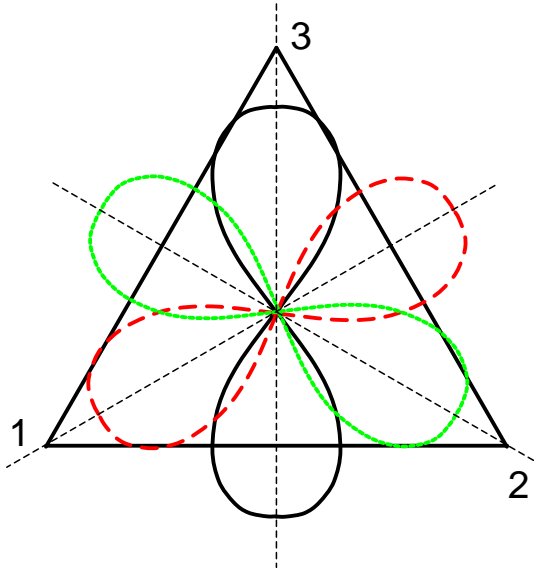
Figure A.2: the wave function solid black line transforms under C_3 into the red (dashed) one and under C_3^2 into the green (dotted) one. The mirror plane $\sigma_1(\sigma_2)$ leads to the green(red) wave function whereas σ_3 gives the original wave function.

Therefore $T|\psi\rangle$ is also an eigenfunction. Note that although the system remains unchanged, $T|\psi\rangle$ does not have to be equal to $|\psi\rangle$ in general. Consider Fig. A.2: the three wave functions are degenerate but well distinct. Applying every element of the symmetry group to $|\psi\rangle$ we get a set of degenerate eigenfunctions $T_1|\psi\rangle, T_2|\psi\rangle, ..., T_n|\psi\rangle$. This set includs also ψ itself since the identity is always among the transformations, $E|\psi\rangle = |\psi\rangle$. The so-caused degeneracy is only due to the symmetry of the system. It hence can only be removed by lowering the symmetry (reducing the symmetry group)[1]) and is therefore called **natural degeneracy**. Of course there might be by accident other eigenfunctions with the same eigenvalue ε, but this degeneracy can always be removed by varying only a parameter (e.g. the strength of the crystal field) and preserving the symmetry. Such a degeneracy is therefore called **accidental degeneracy**.

Representations

Now we focus on a naturally degenerate eigenspace $\mathcal{E}$ like the one spanned by $T_i|\psi\rangle$. Its dimension is $\leq n$ (n the number of elements in the symmetry group). The case $\dim(\mathcal{E}) = n$ means that the wave functions $T_i|\psi\rangle$ are all linear independent. Actually it is often the case that $\dim(\mathcal{E}) < n$, and then one has to choose linearly independent eigenfunctions as a

---

[1]This can not be done by leaving out only some arbitrary elements of the symmetry group. The group property would then be lost, which would be in contradiction to the above considerations about the group property of the symmetry elements. It therefore can only be reduced to a proper subgroup (a subset forming a group itself, it hence always contains the identity).

basis of $\mathcal{E}$. In the following we will always assume that this (if nessecary) has already been done. Under a transformation T_k the eigenspace $\mathcal{E}$ is mapped onto itself. Hence every wave

$$\mathcal{E} \longrightarrow \mathcal{E}$$
$$T_i \qquad T_k T_i = T_m$$
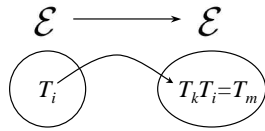
function will be in general sent onto a linear combination of the basis wave functions $T_i|\psi\rangle$ ($i = 1, ..., n$). For example T_k applied to the wave function $T_i|\psi\rangle$ will send it onto $T_k T_i|\psi\rangle$. If the product $T_k T_i$ equals T_m according to the group multiplication, then $T_k T_i|\psi\rangle$ will be equal to $T_m|\psi\rangle$. So the group multiplication of the symmetry group determines the result under consecutive transformations. Going now over from the eigenspace $\mathcal{E}$ to the coordinate vector space $\mathbb{R}^n$, the wave functions $|\psi_i = T_i|\psi\rangle$ correspond to vectors of the form $e_i = (0,..,1,..,0)^2$. For clarity the situation is shown in Fig. A.3 the symmetry Transformation T_i corresponds to a $n \times n$ matrix A_i mapping $\mathbb{R}^n$ (isomorphic to $\mathcal{E}$) onto itself. The matrix multiplication of two of the A_i has to obey also the group multiplication of the corresponding transformations.

$$T_k T_i = T_m \quad \Rightarrow \quad A_k \, A_i = A_m$$

Such a set of matrices A_i obeying the group multiplication is called **representation** of the (abstract) symmetry group. Note that two group elements may correspond to the same matrix. For example mapping all the elements of the group (all transformations) on the (1×1) matrix 1, we always get a representation since $1 \cdot 1 = 1$ fulfills every group multiplication. [3] The appearance of the matrices depends on the choice of the basis. Choosing one basis the matrices are determined and each basis function is transforming according to one row of the matrices. For instance for a five-dimensional eigenspace with the basis $\{|\psi_1\rangle, |\psi_2\rangle, |\psi_3\rangle, |\psi_4\rangle, |\psi_5\rangle\}$, the third function $|\psi_3\rangle$ transforms according to the third row of

---

[2]To be general one should consider here complex spaces. It will actually turn out that this is relevant in some aspects but we do not need this aspect here. However, here we want to use objects that are as familiar as possible.

[3]This is the so called trivial representation.

$$|\psi\rangle \xmapsto{\quad T_i \quad} T_i|\psi\rangle$$
$$\mathcal{E} \longrightarrow \mathcal{E}$$
$$\downarrow \qquad\qquad \downarrow$$
$$\mathbb{R}^n \longrightarrow \mathbb{R}^n$$
$$v \longmapsto A_i v$$
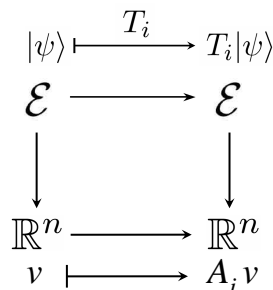
Figure A.3: The commutative diagram illustrates the relation of transformations and the corresponding matrices.

the matrix (a_{ij}).

$$(0,\ 0,\ 1,\ 0,\ 0) \begin{pmatrix} a_{11} & a_{12} & a_{13} & a_{14} & a_{15} \\ a_{21} & a_{22} & a_{23} & a_{24} & a_{25} \\ \mathbf{a_{31}} & \mathbf{a_{32}} & \mathbf{a_{33}} & \mathbf{a_{34}} & \mathbf{a_{35}} \\ a_{41} & a_{42} & a_{43} & a_{44} & a_{45} \\ a_{51} & a_{52} & a_{53} & a_{54} & a_{55} \end{pmatrix} = (\mathbf{a_{31}}, \mathbf{a_{32}}, \mathbf{a_{33}}, \mathbf{a_{34}}, \mathbf{a_{35}})$$

How many representations do exist?

Infinitely many! Two representations A_i and B_i can always be combined to give another set of matrices that act on the direct sum of the original vector spaces $V_a \oplus V_b$ and form another representation. By this we can easily produce arbitrarily large matrices that are block diagonal. By choosing a different basis in $V_a \oplus V_b$ one will destroy the from of the block diagonal character, i.e., the origin of this new representation is not obvious anymore.

$$\text{Example of a matrix that is block diagonal}: \quad \begin{pmatrix} \square & 0 \\ 0 & \square \end{pmatrix}$$

But what happens upon going in the opposite direction and trying to find invariant subspaces of a given representation? This means that we have to find a basis of the vector space for which *all* matrices of the representation will be block diagonal. Obviously we can not follow this procedure up to infinity, but we will end up with representations that do not contain invariant subspaces anymore. These representations are called **irreducible representations**, all the others are called reducible.

Now we ask: How many irreducible representations do exist?

The answer is: Not many! A finite number depending on the group. [4] This gives a strong restriction on possible naturally degenerate eigenspaces since they have to transform according to an irreducible representation. This is because reducible representations would include at least two accidentally degenerate eigenspaces.

Let us consider again the symmetry group of the triangle. What are its irreducible representations? First there must be the trivial representation, where all elements correspond to 1 (since it is one-dimensional it has to be irreducible, there are no subspaces possible). Then the transformations in the x-y plane represented by 2×2 matrices form another irreducible two-dimensional representation. That this is an irreducible one is clear due to the fact that the rotations (e.g. C_3) have no diagonal form with real eigenvectors and hence can not be made a block diagonal matrix by any transformation and has no invariant subspaces. There is only one other irreducible representation. To deduce it we will have to say a bit more about groups, so the reader interested purely in results may skip this part and continue with the next paragraph.

---

[4]Note that we have restricted ourselves to finite groups, for infinite groups things are different.

Invariant subgroups and classes

A subgroup is the same for groups as a subspace is for a vector space: a subset which is closed about multiplication and so forms a group of its own. If G is a group and $H(\subset G)$ is a subgroup, then for every pair of elements $a, b \, \epsilon \, H$ the product ab is still in H ($ab \, \epsilon \, H$). We also consider now the mapping xgx^{-1} where g is one fixed element and x runs over the group (it is called the inner homomorphism). Before turning to its properties we will first recall that the set xg (g fixed, x variable), called left translation, covers the whole group[5]. This is in general not the case for xgx^{-1}. If there is an element x so that $xax^{-1} = b$, then a and b are called equivalent. This is actually an equivalence relation[6] and hence the group splits up in disjunct subsets of pairwise equivalent elements which are called classes. An invariant subgroup ($H \subset G$) is a subgroup consisting only of whole classes. It has the property that for every element $a \, \epsilon \, H$ and any element $x \, \epsilon \, G$ the element $b = xax^{-1}$ is still in H.[7] With an invariant subgroup we can construct a new group. One element x of G multiplied by every element of H gives a set $K \subseteq G$. This set has the property that every $y \, \epsilon \, K$ multiplied again by every element of H will be in K. The elements of our new group are then these disjunct equivalence classes K_l of G according to the invariant subgroup H. The multiplication is the multiplication of G for one arbitrarily chosen element of each K_l. More practically: take one element of K_l (no matter which one) and multiply it according to the multiplication of G with one element of K_m (it also does not matter which one). If the result lies in the equivalence class K_n, then $K_m \cdot K_l = K_n$ is the multiplication in the new group. The new group is called the factor group and is denoted by G/H. Its order is $order(G)/order(H) \, \epsilon \, \mathbb{N}$. By this one finds that the order of an invariant subgroup must be a divisor of the order of the group. What does this mean for representations of the group? Every representation of the factor group provides a representation of the whole group by identifying each element $x \epsilon K_l$ with the matrix belonging to its equivalence class K_l.

In case of the symmetry group of the equilateral triangle we find one invariant subgroup consisting of $\{id, C_3, C_3^2\}$. The corresponding group contains only two elements which are $\{id, C_3, C_3^2\}, \{\sigma_1, \sigma_2, \sigma_3\}$. Since there exists (up to isomorphism) only one group with two elements and with two (1dim) representations, i.e., one besides the trivial one we have now found the third representation of the symmetry group of the triangle. The elements $\{id, C_3, C_3^2\}$ are identified with 1 an the rest $\{\sigma_1, \sigma_2, \sigma_3\}$ are identified with -1. Since one can proof that the dimension of the representations (dimension of the representation = dimension of the corresponding vector space) squared and summed up equal the order of the group, we are sure to have found all irreducible representations ($1^2 + 1^2 + 2^2 = 6$).

---

[5]This is clear if we find that every left translation is injective because their are n (order of the group) elements x mapped on a set (the group) with n elements xg. So injectivity implies surjectivity. Consider two elements $x_1 \, \epsilon \, G$ and $x_2 \, \epsilon \, G$ with the same image $x_1g = x_2g = y$, $y \, \epsilon \, G$. Multiplying this equation with g^{-1} from the right gives $x_1 = x_2$. So there can not be different elements with the same image xg and with this the left translation and analog the right translation are injective.

[6]For an equivalence relation the following holds:
1) Every element is equivalent with itself: $eae^{-1} = a$
2) The relation is symmetric: $xax^{-1} = b$ then $a = x^{-1}bx$
3) The relation is transitive: $xax^{-1} = b$ and $yby^{-1} = c$ then $y(xax^{-1})y^{-1} = (yx)a(x^{-1})y^{-1}) = c$

[7]This is obvious since a and b are in the same class and the hole class belongs to H as assumed.

So in conclusion we have the following representations:

	A_1	A_2	T_1
id	1	1	$\begin{pmatrix} 1 & \\ & 1 \end{pmatrix}$
C_3	1	1	$\begin{pmatrix} \frac{1}{2} & \frac{\sqrt{3}}{2} \\ -\frac{\sqrt{3}}{2} & \frac{1}{2} \end{pmatrix}$
C_3^2	1	1	$\begin{pmatrix} \frac{1}{2} & -\frac{\sqrt{3}}{2} \\ \frac{\sqrt{3}}{2} & \frac{1}{2} \end{pmatrix}$
σ_3	1	-1	$\begin{pmatrix} -1 & \\ & 1 \end{pmatrix}$
σ_2	1	-1	$\begin{pmatrix} \frac{1}{2} & \frac{\sqrt{3}}{2} \\ -\frac{\sqrt{3}}{2} & \frac{1}{2} \end{pmatrix}$
σ_1	1	-1	$\begin{pmatrix} \frac{1}{2} & -\frac{\sqrt{3}}{2} \\ \frac{\sqrt{3}}{2} & \frac{1}{2} \end{pmatrix}$

Let us look at another example highly relevant in this theses: In octahedral (cubic) symmetry, the symmetry group O has only five irreducible representations of dimensions 3 (two times), 2 and 1 (two times). So for instance the fivefold degenerate 3d orbitals have to split up in at least two eigenspaces which are well known as e_g and t_{2g}.[8] We will discuss this group later on (see Appendix B). Here we want to emphasize that only by general considerations of the symmetry group we are able to predict a splitting of the fivefold degenerate d wave functions. The question which of the irreducible representations occur can not be answered this way. To determine them one has to apply some transformations to the eigenstates and look at the resulting linear combinations. This gives the corresponding matrices. It would be a lot of work to find the irreducible representation by considering the products of these matrices.[9]

Since the eigenfunctions of one eigenspace transform into linear combinations of each other, their form will in general not be invariant under symmetry transformations as in real space vectors change their coordinates under an orthogonal transformation. [10] With this we might ask: What is then an invariant property of the physical system? Let's look at real space again. The angle of two vectors, i.e. the scalar product is an invariant property.

---

[8]Even the labeling of these eigenspaces is adopted from the irreducible representations according to which they transform.

[9]A simplification of this procedure is given by the use of characters which is discussed later on.

[10]As a geometrical object they are of course invariant but their appearance depend on the choice of the coordinate system.

Corresponding to this we find the scalar product $\langle\psi|\phi\rangle$ to be an invariant property. Obviously the overlap of two arbitrary wave functions should stay the same under a symmetry transformation, as it does even under the more general group of unitary transformations.

The crucial point

Consider the scalar products $\langle\psi_i|\phi_j\rangle$ of two sets of eigenfunctions $\{\langle\psi_1|,\ldots,\langle\psi_n|\}$ and $\{|\phi_1\rangle,\ldots,|\phi_m\rangle\}$, each building a basis of their eigenspaces (E_ψ, E_ϕ). The matrix $(m_{ij}) = \langle\psi_i|\phi_j\rangle$ corresponds to a map of E_ψ onto E_ϕ. Applying the same symmetry transformation T_k to both eigenspaces, the matrix $M = (m_{ij})$ has to have the same form since the scalar product is not changed by T_k. As the overlap of two wave functions is a physical property it can not depend on the choice of the coordinate system (it is therefore invariant even under the wider class of unitary transformations). From a mathematical point of view one would say that the diagram in Fig. A.4 commutes. This simply means one should get the same result first applying M and then T_k or vice versa.

Moreover we find that M is a vector-space homomorphism (E_ψ, E_ϕ) since it is a linear map.[11] The set of the elements that are mapped onto neutral element $e = (0,0,...,0)$ is called the kernel of M $(M^{-1}\vec{0})$. The kernel of a homomorphism is always an invariant subspace. On the right side of the diagram A.4 the T_k is mapping the neutral element onto itself for all transformations T_k. On the left side kern(M) is an invariant subspace of E_ψ that has to be mapped onto itself by T_k. Otherwise it would not be sent to the identity by applying M afterwards. In general every map has two trivial invariant subspaces, namely the whole space V and $e = (0,0,...,0)$.

Up to this point we have collected all necessary parts. For getting the theorem we desire we just have to look at the diagram again. Remember that we are considering an irreducible representation, i.e., one without invariant subspaces different from the trivial ones (the transformations are mixing the whole space). But the kernel has to be an invariant subspace. Hence, there are two possibilities for the kernel. It has to be one of the two trivial invariant subspaces i.e. it can only be the whole space or e. If not, kern(M) would be also an invariant subspace of T_k. Since the diagram in Fig. A.4 commutes it is $MT = TM$. So whatever the transformation T will be it will map e' on e' on the right hand side therefore the invariant subspace has to be mapped onto itself. Hence it would be an invariant subspace of T_k but this would be in opposition to our assumption that T_k is irreducible.

Consequences:

1. If the whole space is mapped on e, M has to be identical to (0). This is especially the case if E_ψ and E_ϕ are of different dimensions. In this case the kernel of M is non zero (or maybe M^{-1} depending on which of the eigenspaces is of larger dimensions). For equal dimension this argument does not hold. Consider now a transformation for which the corresponding matrices of the two representations give different results (at least there must

---

[11]Homomorphy requires that $M(|\psi\rangle + |\phi\rangle) = M(|\psi\rangle) + M(|\phi\rangle)$ and $M(\alpha|\psi\rangle) = \alpha M(|\psi\rangle)$, which certainly is fulfilled here.
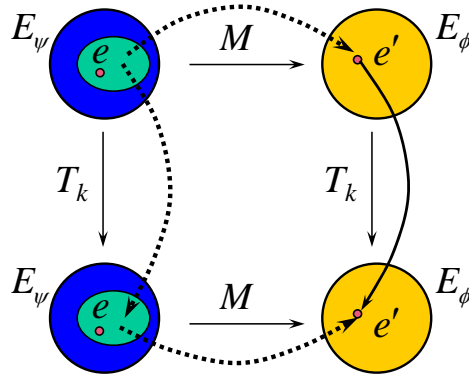
Figure A.4: Let's assume that the kernel of M is not e or the whole space but a certain subspace represented by the green ellipse. On the right side e' is mapped onto itself under (the homomorphism) T_k. Since in the bottom M is the same map as above, the kernel will again be the subspace of the green ellipse. In order to make the diagram commute as we required, the green ellipse would be mapped onto itself. This consideration holds for every transformation T_k. Hence the kernel of M (the green ellipse) would be an invariant subspace for all T_k, in contradiction to the assumption of an irreducible representation.

be one that gives different results, otherwise the two representations would be the same). But with two different matrices A_k the diagram does not commute anymore for a nonzero matrix M. Since it has to commute from the physical background M has to be identical to (0).

2. If E_ψ is mapped onto E_ϕ they have the same dimension and moreover they transform according to the same representation, hence M is a nonzero matrix. We can assume then that we get at least one (perhaps even complex) eigenvalue $M|\psi\rangle = \lambda|\psi\rangle$. It follows that $(M - \lambda\mathrm{id})|\psi\rangle = 0$. But this matrix is as well as M commuting with the transformations T_k since diagonal matrices are always commuting.[12] So $|\psi\rangle \neq 0$ is obviously in the kernel of $(M - \lambda Id)$. Hence the whole map must be equal to (0) (remember consequence (1)). But then the image of an arbitrary element under $(M - \lambda Id)$ equals 0. We can conclude that all the basisvectors are eigenvectors of M with the same eigenvalue λ. M has the form

$$\lambda M = \begin{pmatrix} 1 & 0 & \cdots & 0 \\ 0 & 1 & & \vdots \\ \vdots & & \ddots & 0 \\ 0 & \cdots & 0 & 1 \end{pmatrix}$$

.

Summarizing in short we get:

---

[12]In a more formal language one could say that they build the center of the group of all regular (invertible) $(n \times n)$ matrices $(\mathrm{GL}(R/C))$. Which means a bit more, namely that the diagonal matrices are the only elements of $\mathrm{GL}(R/C)$ which commute with all others. They form a subgroup of $\mathrm{GL}(R/C)$

The basis vectors of two eigenspaces transforming under different representations are orthogonal ($\langle\psi|\phi\rangle = 0$).

The basis vectors of two eigenspaces transforming under the same representation are also orthogonal if they transform under different rows. But transforming according to the same row they are multiples of each other($\langle\psi| = \lambda\langle\phi|$). The factor λ does not depend on the row, but it is equal for all corresponding pairs of basis functions.

Matrix elements and selection rules

This states the theorem, but the full benefit is not derived considering $\langle\psi|\phi\rangle$ but matrix elements like $\langle\psi|A|\phi\rangle$. Now we have to combine three objects transforming according to three in general different representations. Yes, operators are transforming as well as wave functions according to irreducible representations. By keeping things simple we have omitted this point in the beginning by choosing the scalar operator H. Scalar operators commute with all transformations (they transform according to the trivial representation), which gets us round the trouble we are dealing with here. In general we find that operators A_i transform as $TA_iT^{-1} = \sum a_{ij}A_i$ where the coefficients a_{ij} belong to the jth row of matrices of an irreducible representation. Consider $\langle\psi|(A|\phi\rangle)$. Knowing the transformation properties of $(A|\phi\rangle)$ we could proceed as in the case above. If $\langle\psi|$ and $(A|\phi\rangle)$ would transform under different irreducible representations we could conclude that $\langle\psi|A|\phi\rangle = 0$ and so on.

But how (according to which representation) does the term $(A_i|\phi_k\rangle)$ transform? Let us assume that A_i transforms according to R_A and ϕ_k according to R_ϕ which have the corresponding matrices D_A and D_ϕ. Let's assume further that R_A and R_ϕ are of dimension m, n, respectively (A_i, $i = 1, ..., m$); ($|\phi_k\rangle$, $k = 1, ..., n$). So we get $m \cdot n$ product states which can be enumerated by $A_1|\phi_1\rangle$, ... , $A_1|\phi_n\rangle$, $A_2|\phi_1\rangle$, ... , $A_2|\phi_n\rangle$, ... , ... , $A_m|\phi_1\rangle$,..., $A_m|\phi_n\rangle$. For the sake of simplicity let $m = n = 2$. To approach the task to apply a symmetry transformation to a product state $TA_iT^{-1}T|\phi\rangle$ we consider first A_i and $|\phi_k\rangle$ alone:

$$TAT^{-1} = \begin{pmatrix} A_{11}^T & A_{12}^T \\ A_{21}^T & A_{22}^T \end{pmatrix} \cdot \begin{pmatrix} A_1 \\ A_2 \end{pmatrix}$$

$$T|\phi\rangle = \begin{pmatrix} \Phi_{11}^T & \Phi_{12}^T \\ \Phi_{21}^T & \Phi_{22}^T \end{pmatrix} \cdot \begin{pmatrix} |\phi_1\rangle \\ |\phi_2\rangle \end{pmatrix}$$

Here the matrix (A_{ij}^T) is the matrix of the representation under which the operator A transforms under the transformation T. Analog, ϕ is transforming according to Φ_{ij}^T under T. Combined together each of the resulting $|\phi\rangle$'s has to be multiplied with each of the resulting A's. This gives formally the **tensor product** of the two matrices.[13] So the product space

---

[13]The tensor product of two matrices is well explained with a simple example.

$$A \times B = \begin{pmatrix} a_{11} & a_{12} \\ a_{21} & a_{22} \end{pmatrix} \times \begin{pmatrix} b_{11} & b_{12} \\ b_{21} & b_{22} \end{pmatrix} = \left(\begin{array}{cc|cc} a_{11}b_{11} & a_{11}b_{12} & a_{12}b_{11} & a_{12}b_{12} \\ a_{11}b_{21} & a_{11}b_{22} & a_{12}b_{21} & a_{12}b_{22} \\ \hline a_{21}b_{11} & a_{21}b_{12} & a_{22}b_{11} & a_{22}b_{12} \\ a_{21}b_{21} & a_{21}b_{22} & a_{22}b_{21} & a_{22}b_{22} \end{array} \right)$$

is transforming according to the $m \cdot n \times m \cdot n$ matrix (in the example it is given by a 4×4 matrix) that is given by the tensor product of A_{ij}^T and Φ_{ij}^T. However the tensor product is in general not irreducible but it can be reduced in irreducible components. Every single irreducible component has to be considered if one wants to apply the theorem from above.

Summarizing this we get:

Matrix elements like $\langle \psi | A | \phi \rangle$ are vanishing if the irreducible representation according to which $\langle \psi |$ transforms is not among the irreducible representations of the reduction of the tensor product representation of $A|\phi\rangle$.

The Wigner-Eckhart theorem is the origin of all kinds of selection rules in quantum mechanics.

Some examples:

1) As mentioned in chapter 2 *d-d* excitations are forbidden by the parity selection rule. However, we will now consider this rule in the light of the above theorem. The symmetry group of the inversion symmetry is rather simple. It consists only of two elements, namely the identity e and the inversion i. The group multiplication table is given by

$\cdot$	e	i
e	e	i
i	i	e

So if a system is symmetric under inversion, its eigenfunctions have to transform under a representation of this group. There are only two elements in this group. Hence one expects only two one-dimensional representations ($1^2 + 1^2 = 2$ the order of the group). These two representations are the trivial one (all elements corresponds to (1)) and the so called alternating representation[14] given by

$\cdot$	1	-1
1	1	-1
-1	-1	1

Eigenfunctions transforming under the trivial representation are called *even* and the ones transforming under the alternating representation are called *odd*. However, if the physical system under investigation obeys additional symmetry transformations, there may be eigenspaces of dim > 1. But all eigenfunctions of one eigenspace have to transform according to either the trivial or the alternating representation. Back to the *d-d* transitions, we find

---

[14]The group of $\{e,i\}$ is isomorphic to any other group of order two since there is only one possible group multiplication table obeying the axioms required for a group. So it is especially isomorphic to the permutation group of two elements S_2 that consists of the elements $\{1,2\}$ and $\{2,1\}$. Each of these two elements is building a class. Since there are two representations there have to be two classes in the group. For any permutation group S_n the representations are corresponding to classes in a unique way (this identification is not achieved for arbitrary groups). From this the name "alternating representation" is derived since this representation corresponds to the element that is alternating the two entries 1 and 2.

that the d orbitals (denoted here $|d\rangle$) are transforming according to the even representation, i.e., they are mapped onto themselves under inversion. On the other hand, the dipole operator P is transforming according to the alternating representation. So according to which representation does the product $P|d\rangle$ transform? This is given by the reduction of the tensor product. The tensor product, however, is reduced to the product of real numbers for one-dimensional representations. Thus by $-1 \cdot 1 = -1$ we find that $P|d\rangle$ transforms according to the alternating representation. Then we are able to conclude by the Wigner-Eckhart theorem that $\langle d| P|d\rangle$ has to vanish, since $\langle d|$ and $P|d\rangle$ are transforming according to different representations.

2) It is a well known statement that in cubic symmetry the e_g states are non magnetic - the orbital angular momentum is quenched. This statement will be elucidated in the following. The value of the magnetic moment M of a state $|\psi\rangle$ is given by $M|\psi\rangle = m|\psi\rangle$. In order to get m one is projecting with $\langle\psi|$:

$$\langle\psi|M|\psi\rangle = m$$

The state $|\psi\rangle$ transforms according to the E representation as required for an e_g state. The magnetic moment is transforming according to T_1 since it is a vector operator. Therefore, the product $M|\psi\rangle$ is transforming according to the tensor product $T_1 \times E$. The crucial point we have to show now is that the product $T_1 \times E$ is not containing the representation E when it is reduced to irreducible representations. The reduction can easily be achieved by analyzing the characters of the tensor product. However, the easiest way to do this is to look up the result in a table. There one finds that

$$T_1 \times e_g = T_1 \oplus T_2$$

This proofs the proposition. Note that *all* matrix elements between an operator transforming according to T_1 and an e_g state are vanishing. In particular, all vector operators do not contribute to the e_g states.

Characters

Any set of linear maps (given by a set of matrices for a choice of the basis) forming a representation of a group is only defined up to a similarity transformation of the underlying vector space. One is free to choose a coordinate system and for a new basis the matrices look in general completely different, but they describe the same linear map of the vectorspace.[15] If all these sets of matrices are describing essentially the same thing, then one may ask whether they have something in common that distinguishes them from other representations which belong to a different set of linear maps?

The answer is: Yes! And it is the well know trace of matrices which is the relevant property [208].

---

[15]The vectors as elements of the vector space are objects independent of the coordinate assigned to them and therefore a map between vector spaces is well defined beyond any choice of coordinate system.

The trace of a matrix of one representation is called its character. So for each representation each symmetry element is represented only by one number (namely the trace of the matrix belonging to it for an arbitrary choice of basis). For the common groups (especially the crystallographic point groups) these numbers, the characters, are tabled.

What is the benefit of working with characters?

The property making characters very useful in practice is that they obey orthogonality relations, just as matrix elements do. For one representation we can regard the characters of the matrices as an element of R^n, with n being the order (number of elements in the group) of the group under consideration. For each representation we will find one vector. These vectors build an orthogonal basis $\mathcal{B}$ of R^n. If one wishes to decompose a reducible representation into its irreducible constituents one can form a vector of the traces of matrices. This vector is then also an element of the R^n and there will be a unique decomposition into the basis $\mathcal{B}$ with only integer coefficients. These coefficients tells then how many times the corresponding irreducible representation occurs in the considered reducible representation.

Rotational symmetry

If their is no direction in space distinguished from the others then one has full rotational symmetry, i.e. any rotation applied to the system is a symmetry transformation. So the symmetry group is the group of rotational transformations in $\mathbb{R}^3$: SO(3). There is a big difference to the groups considered previously: SO(3) contains infinitely many elements since there are as many axes of rotation as points on a hemisphere, and for each axis the angle of rotation is any real number out of the interval $[0, 2\pi[$. Therefore we expect infinitely many irreducible representations. But before considering them we look at the quantum-mechanical implication first. The operator connected with the rotational symmetry is that of angular momentum. This is seen in the classical case from the Noether theorem, and by applying the correspondence principle one obtains the operator L. Since everything we ever may know about a quantum-mechanical system is its wave function, the value of the angular momentum L and its z-component L_z have to be inherent properties of the wave function. Let's consider eigenfunctions of L^2 and L_z like for instance the spherical harmonics Y_{lm}. The quantum number m of L_z gives the transformation of the wave function by rotation around the z axis. For a given wave function, m is the number of times the wave function comes onto itself by a rotation about 2π, or in other words the wave function is mapped onto itself by a rotation of $2\pi/m$. However, it will transform into a linear combination of other eigenfunctions of L^2 by a rotation around an arbitrary axis. The eigenvalue l of L ($l(l+1)$ of L^2) is then given by the maximal value of m that may occur in this linear combination. In other words, L gives the representation of SO(3) and L_z gives the row under which the eigenfunction transforms. For rotations around the z-axis it is possible to choose a basis the matrices become diagonal.
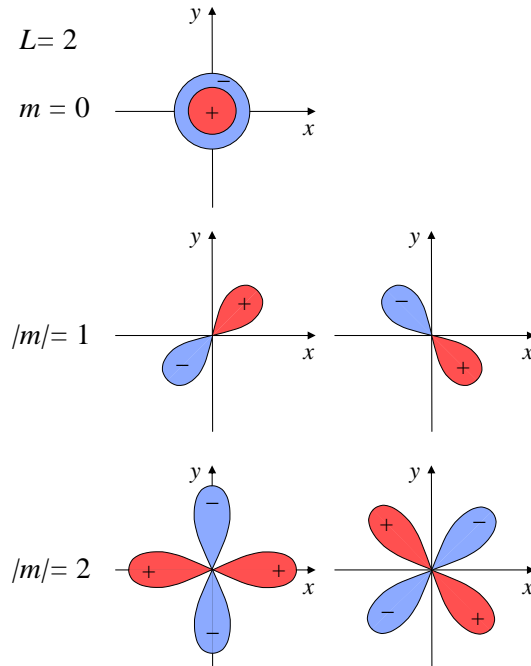
Figure A.5: The projection of the five eigenfunctions of the angular momentum $L = 2$ (i.e. the spherical harmonics $Y_{2\,m}$) onto the xy plane is shown. It is easy to see that the wave functions are symmetric for a rotation around the z axis about an angle $\phi = 2\pi/m$. Which sign of m is according to which of the two wave functions is only a question of the choice of phase. It is interchanged by applying a factor of $e^{i\pi}(= -1)$.

For the case of $L = 2$ this is

$$
\begin{pmatrix}
e^{i2\alpha} & 0 & 0 & 0 & 0 \\
0 & e^{i1\alpha} & 0 & 0 & 0 \\
0 & 0 & e^{i0\alpha} & 0 & 0 \\
0 & 0 & 0 & e^{i(-1)\alpha} & 0 \\
0 & 0 & 0 & 0 & e^{i(-2)\alpha}
\end{pmatrix}
$$

in the basis of the spherical harmonics $\{Y_{2\,2}, Y_{2\,1}, Y_{2\,0}, Y_{2\,-1}, Y_{2\,-2}\}$. These properties are easily seen from the shape of the orbitals in the xy plane as obtained by a projection along the z axis (see Fig. A.5).

The procedure for adding two angular momenta L_1 and L_2 the result is well known from textbooks. The possible values of the resulting angular momentum are $L_1 + L_2, \ldots, |L_1 - L_2|$. In terms of representations this result follows from the reduction of the tensor product of the representations of L_1 and L_2 into its irreducible components. This can be done with ease. Note that here every irreducible representation occurs in the product at most once. In general a product may contain a palticular irreducible representation several times.

The origin of the Landé or g factor

The so-called g factor gives the magnetic moment according to the angular momentum of a system. It is by no means mysterious on the background of the Wigner-Eckhart theorem. The angular momentum and the magnetic moment transform both like a vector, i.e. they transform according to the same irreducible representation. We know from the Wigner-Eckhart theorem that they have common eigenspaces and eigenfunctions. The eigenvalues of these eigenfunctions are proportional to each other. The proportionality factor (above we termed it λ) is independent from the row of the irreducible representation according to which the eigenfunction transforms. The g factor is exactly this proportionality factor for the case of angular momentum and magnetic moment. It is given by

$$g = 1 + \frac{J(J+1) - L(L+1) + S(S+1)}{2J(J+1)}$$

and therefor only dependent on J, L, S, i.e. on the irreducible representation and independent of J_z, L_z or S_z i.e. the row of the irreducible representation. The formula given above is derived by projecting one magnetic eigenstate onto its angular momentum counterpart. The angular momentum eigenstates are choosen as reference since the angular momentum is the generator of the rotation.

Appendix B

The octahedral group O

The symmetry group of a regular octahedron and of a cube is the same[1]. It consists of 24 elements which are depicted in Fig. B.1. All symmetry transformations map the set of the three coordinate axes onto itself with either the same or the opposite direction. So every element corresponds to one of the symmetric group S_3 (the group of the permutations of three elements) which has the order six. (This is a crucial point for gaining more insight in the structure of the octahedral group and its representations.) The additional choice that can be made concerns the orientation of the axes which can be left the same or be reversed. So two possibilities for each of the three axes. The number of combinations equals $2 \cdot 2 \cdot 2 = 8$ in total. From a pure combinatorial point of view this is correct but then the inversion of all three axes would give the inversion of the whole space. However, the group O is a subgroup of SO(3) and therefore the inversion is not included in the pure rotational group (for the group O_h the inversion is included and one ends up with $6 \cdot 8 = 48$ elements). By this restriction one looses a factor of 2. We find always pairs of rotations, and these rotations combine with the inversion, the latter elements are giving the second half (24 elements) of O_h. For the pure rotation we hence get $6 \cdot 4 = 24$ elements.

What are the irreducible representations of the octahedral group ?

First we can map all elements on the 1×1 matrix (1). This is certainly an irreducible representation since $1 \cdot 1 = 1$ fulfills the multiplication of every group. It is denoted by A_1 or Γ_1 (for a general group it is called the trivial representation). The matrices which correspond to the rotation of the point (x, y, z) in the three-dimensional space of course also provide a representation. It is irreducible since there is obviously no invariant subspace for *all* elements (the axis of rotation is always an invariant subspace but certainly the elements do not have the same axis of rotation). This representation is denoted T_1 or Γ_4. In order to find the remaining irreducible representations we have to remember the relation to the symmetric group S_3. It is isomorphic (i.e. they have the same multiplication table and hence the same

---

[1]They are two of the five platonic solenoids. They are called adjoined since they are inscribed in each other by connecting the middle of neighboring faces. The other pair of adjoined platonic solenoids are the dodecahedron and the ikosahedron, the last remaining platonic solenoids the tetrahedron is adjoined to itself.
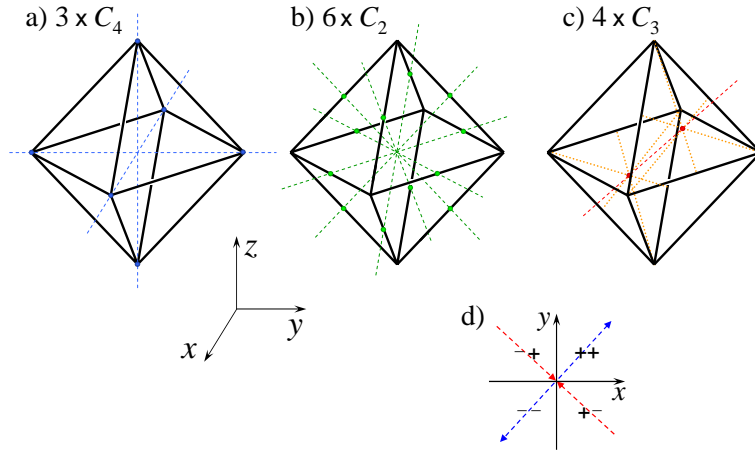
Figure B.1: The octahedral group O consists of 3 fourfold axes along the three coordinate axes (x, y, z) (9 elements) shown in a), 6 twofold axes along the two diagonals of the three coordinate planes (xy, zx, yz) (6 elements) shown in b), 4 threefold axes along the four space diagonals (8 elements) (for clarity only one of them) shown in c), and the identity $(9 + 6 + 8 + 1 = 24)$. The labeling of the elements is as follows. A rotation by $\pi/2$ about one of the fourfold axes is denoted C_4. An additional index (x, y, z) is specifying which of the coordinate axis is the axis of rotation. $C_4 \times C_4 = C_4^2$ is hence a rotation by π and C_4^3 by $3\pi/2$. For example a rotation about the y axis by $3\pi/2$ is denoted C_{4y}^3. A rotation about the twofold axes is denoted C_2 with an additional index specifying the coordinate plane (xy, zx, yz). We distinguish between the two diagonals within one plane by the order of the indices specifying the plane. Cyclic order (xy, zx, yz) is assigned to the diagonal for which the product of the two coordinates is positive (i.e. lying in the first and third quadrant of the coordinate plane), anti-cyclic order (yx, xz, zy) for the second diagonal in this plane. C_3 (C_3^2) are the rotations by $2\pi/3$ $(4\pi/3)$ about the threefold axes along the space diagonals. They are labeled with an additional index $(++, +-, -+, --)$ giving the sign of the two coordinates $(x$ and $y)$ when projecting the upper part (for positive values of z) into the xy plane. The signs are given by the signs of (x,y) as sketched in d). All rotations are assumed to be in a mathematically positive sense. The orientation of the axes of rotation is chosen for the fourfold axes along the coordinate axes, for the twofold axes it does not matter anyway, and for the threefold axes the orientation is indicated by the arrows in d) (the (111) axis is orientated according to the product xyz).

representations) to the symmetry group of the equilateral triangle (see Fig. A.1).

One irreducible representation of S_3 besides the trivial one consists of the two-dimensional matrices of the symmetry operations of the triangle. Therefore, it is also one irreducible representation of the octahedral group. This representation is called E or Γ_3.[2] The fact that

---

[2]There exists an invariant subgroup H of the octahedral group that gives rise to a factor group O/H which is isomorphic to S_3. Since this isomorphism is due to the permutation of the coordinate axes this invariant subgroup has to be containing all elements that does not change the order of the coordinate axes. This subgroup hence contains the 180° rotations about the three coordinate axes which just changes the direction

the elements of S_3 can be distinguished in cyclic and anti-cyclic[3] gives the starting point for finding another irreducible representation. Cyclic permutations are $\{123, 321, 231\}$, they correspond to an even number of transpositions.[4] Anti-cyclic permutations $\{213, 321, 132\}$ correspond to an odd number of transpositions. Since even×even and odd×odd equals even whereas even×odd and odd×even equals odd we can substitute even by $+1$ and odd by -1. So we get another one-dimensional (and hence irreducible) representation of S_3 and therefore also of O by assigning every cyclic permutation to $(+1)$ and every anti-cyclic permutation (-1). As a representation of O it is called A_2 or Γ_2. A possibility to check weather one has got all irreducible representation is that there must be as many as the number of classes in the group.[5] Since O consists of five classes we are still missing one. Because of the equivalence between the sum over the squared dimensions of all irreducible representations and the order of the group one can state the dimension of the missing representation. $1^2 + 1^2 + 2^2 + 3^2 + x^2 = 24 \curvearrowright x = 3$ is the dimension of the last irreducible representation of O. This last representation is not a completely new one but it is the (tensor) product of A_2 with T_1. By multiplying half of the matrices of T_1 with (-1) their sign is reversed, whereas the other half remains unchanged. This is a substantially different representation from T_1 since it cannot be obtained from T_1 only by changing the choice of the basis vectors. This representation is called T_1 or Γ_5. Now we have found all 5 irreducible representations which are A_1, A_2, E, T_1, and T_2.

For every irreducible representation there exists a set of generating polynomials. These are functions of the coordinates x, y, z building the basis of a linear space. This space of generating polynomials transforms like the corresponding irreducible representation under a transformation applied to x, y, z in the real three-dimensional space. The number of functions in the set is obviously determined by the dimension of the representation. For the group O the most simple polynomials that generate the five representations are by:

A_1	A_2	E	T_1	T_2
1	xyz	$\{\ x^2 - y^2;\ 2z^2 - x^2 - y^2\ \}$	$\{\ x;\ y;\ z\ \}$	$\{\ yz;\ zx;\ xy\ \}$

In the following table we list for all 24 elements the matrices of the five irreducible representations (elements that are zero are omitted for clarity) and additionally the permutation of coordinate axes. A minus sign denotes that the new axis is inverted. The choice of the coordinate system is the one of Fig. B.1. Usually only the characters are given.

---

of two of the three axes and additionally the identity. So all together this subgroup has four elements and hence (by the Lagrande formula) the corresponding factor group contains $24/4 = 6$ elements in agreement with the order of S_3.

[3]Cyclic permutation correspond to rotations whereas anti-cyclic permutations are mirror planes of the equilateral triangle.

[4]A transposition is a permutation that permutes only two elements. Every permutation can be decomposed into a minimal number of transpositions.

[5]That there are at most as many irreducible representations as classes follows from the orthogonality of the characters. There can not be more orthogonal vectors than dimensions of the vector space, which equals the number of classes.

	A_1	A_2	E	T_1	T_2	$x\quad y\quad z$
id	1	1	$\begin{pmatrix} 1 & \\ & 1 \end{pmatrix}$	$\begin{pmatrix} 1 & & \\ & 1 & \\ & & 1 \end{pmatrix}$	$\begin{pmatrix} 1 & & \\ & 1 & \\ & & 1 \end{pmatrix}$	$x\quad y\quad z$
C_{4x}^2	1	1	$\begin{pmatrix} 1 & \\ & 1 \end{pmatrix}$	$\begin{pmatrix} 1 & & \\ & -1 & \\ & & -1 \end{pmatrix}$	$\begin{pmatrix} 1 & & \\ & -1 & \\ & & -1 \end{pmatrix}$	$x\ -y\ -z$
C_{4y}^2	1	1	$\begin{pmatrix} 1 & \\ & 1 \end{pmatrix}$	$\begin{pmatrix} -1 & & \\ & 1 & \\ & & -1 \end{pmatrix}$	$\begin{pmatrix} -1 & & \\ & 1 & \\ & & -1 \end{pmatrix}$	$-x\quad y\ -z$
C_{4z}^2	1	1	$\begin{pmatrix} 1 & \\ & 1 \end{pmatrix}$	$\begin{pmatrix} -1 & & \\ & -1 & \\ & & 1 \end{pmatrix}$	$\begin{pmatrix} -1 & & \\ & -1 & \\ & & 1 \end{pmatrix}$	$-x\ -y\quad z$
C_{3++}	1	1	$\begin{pmatrix} -\frac{1}{2} & -\frac{\sqrt{3}}{2} \\ \frac{\sqrt{3}}{2} & -\frac{1}{2} \end{pmatrix}$	$\begin{pmatrix} & & 1 \\ 1 & & \\ & 1 & \end{pmatrix}$	$\begin{pmatrix} & & 1 \\ 1 & & \\ & 1 & \end{pmatrix}$	$z\quad x\quad y$
C_{3--}	1	1	$\begin{pmatrix} -\frac{1}{2} & -\frac{\sqrt{3}}{2} \\ \frac{\sqrt{3}}{2} & -\frac{1}{2} \end{pmatrix}$	$\begin{pmatrix} & & -1 \\ 1 & & \\ & -1 & \end{pmatrix}$	$\begin{pmatrix} & & -1 \\ 1 & & \\ & -1 & \end{pmatrix}$	$-z\quad x\ -y$
C_{3+-}	1	1	$\begin{pmatrix} -\frac{1}{2} & -\frac{\sqrt{3}}{2} \\ \frac{\sqrt{3}}{2} & -\frac{1}{2} \end{pmatrix}$	$\begin{pmatrix} & & 1 \\ -1 & & \\ & -1 & \end{pmatrix}$	$\begin{pmatrix} & & 1 \\ -1 & & \\ & -1 & \end{pmatrix}$	$z\quad x\quad y$
C_{3-+}	1	1	$\begin{pmatrix} -\frac{1}{2} & -\frac{\sqrt{3}}{2} \\ \frac{\sqrt{3}}{2} & -\frac{1}{2} \end{pmatrix}$	$\begin{pmatrix} & & -1 \\ -1 & & \\ & 1 & \end{pmatrix}$	$\begin{pmatrix} & & -1 \\ -1 & & \\ & 1 & \end{pmatrix}$	$z\quad x\quad y$

	A_1	A_2	E	T_1	T_2	$x\quad y\quad z$
C_{3++}^2	1	1	$\begin{pmatrix} -\frac{1}{2} & \frac{\sqrt{3}}{2} \\ -\frac{\sqrt{3}}{2} & -\frac{1}{2} \end{pmatrix}$	$\begin{pmatrix} & 1 & \\ & & 1 \\ 1 & & \end{pmatrix}$	$\begin{pmatrix} & 1 & \\ & & 1 \\ 1 & & \end{pmatrix}$	$y\quad z\quad x$
C_{3--}^2	1	1	$\begin{pmatrix} -\frac{1}{2} & \frac{\sqrt{3}}{2} \\ -\frac{\sqrt{3}}{2} & -\frac{1}{2} \end{pmatrix}$	$\begin{pmatrix} & 1 & \\ & & -1 \\ -1 & & \end{pmatrix}$	$\begin{pmatrix} & 1 & \\ & & -1 \\ -1 & & \end{pmatrix}$	$y\ -z\ -x$
C_{3+-}^2	1	1	$\begin{pmatrix} -\frac{1}{2} & \frac{\sqrt{3}}{2} \\ -\frac{\sqrt{3}}{2} & -\frac{1}{2} \end{pmatrix}$	$\begin{pmatrix} & 1 & \\ & & 1 \\ 1 & & \end{pmatrix}$	$\begin{pmatrix} & 1 & \\ & & 1 \\ 1 & & \end{pmatrix}$	$-y\quad z\ -x$
C_{3-+}^2	1	1	$\begin{pmatrix} -\frac{1}{2} & \frac{\sqrt{3}}{2} \\ -\frac{\sqrt{3}}{2} & -\frac{1}{2} \end{pmatrix}$	$\begin{pmatrix} & -1 & \\ & & -1 \\ 1 & & \end{pmatrix}$	$\begin{pmatrix} & -1 & \\ & & -1 \\ 1 & & \end{pmatrix}$	$-y\ -z\quad x$
C_{4x}	1	-1	$\begin{pmatrix} \frac{1}{2} & \frac{\sqrt{3}}{2} \\ -\frac{\sqrt{3}}{2} & -\frac{1}{2} \end{pmatrix}$	$\begin{pmatrix} 1 & & \\ & & -1 \\ & 1 & \end{pmatrix}$	$\begin{pmatrix} -1 & & \\ & & 1 \\ & -1 & \end{pmatrix}$	$x\ -z\quad y$
C_{4x}^3	1	-1	$\begin{pmatrix} \frac{1}{2} & \frac{\sqrt{3}}{2} \\ -\frac{\sqrt{3}}{2} & -\frac{1}{2} \end{pmatrix}$	$\begin{pmatrix} 1 & & \\ & 1 & \\ & & -1 \end{pmatrix}$	$\begin{pmatrix} -1 & & \\ & & -1 \\ & 1 & \end{pmatrix}$	$x\quad z\ -y$
C_{2yz}	1	-1	$\begin{pmatrix} \frac{1}{2} & \frac{\sqrt{3}}{2} \\ -\frac{\sqrt{3}}{2} & -\frac{1}{2} \end{pmatrix}$	$\begin{pmatrix} -1 & & \\ & & 1 \\ & 1 & \end{pmatrix}$	$\begin{pmatrix} 1 & & \\ & & -1 \\ & -1 & \end{pmatrix}$	$-x\quad z\quad y$
C_{2zy}	1	-1	$\begin{pmatrix} \frac{1}{2} & \frac{\sqrt{3}}{2} \\ -\frac{\sqrt{3}}{2} & -\frac{1}{2} \end{pmatrix}$	$\begin{pmatrix} -1 & & \\ & & -1 \\ & -1 & \end{pmatrix}$	$\begin{pmatrix} 1 & & \\ & & 1 \\ & 1 & \end{pmatrix}$	$-x\ -z\ -y$

	A_1	A_2	E	T_1	T_2	$x\ \ y\ \ z$
C_{4y}	1	-1	$\begin{pmatrix} \frac{1}{2} & -\frac{\sqrt{3}}{2} \\ \frac{\sqrt{3}}{2} & -\frac{1}{2} \end{pmatrix}$	$\begin{pmatrix} & & 1 \\ & 1 & \\ -1 & & \end{pmatrix}$	$\begin{pmatrix} & & -1 \\ & -1 & \\ 1 & & \end{pmatrix}$	$z\ \ y\ -x$
C_{4y}^3	1	-1	$\begin{pmatrix} \frac{1}{2} & -\frac{\sqrt{3}}{2} \\ \frac{\sqrt{3}}{2} & -\frac{1}{2} \end{pmatrix}$	$\begin{pmatrix} & & -1 \\ & 1 & \\ 1 & & \end{pmatrix}$	$\begin{pmatrix} & & 1 \\ & -1 & \\ -1 & & \end{pmatrix}$	$-z\ \ y\ \ x$
C_{2zx}	1	-1	$\begin{pmatrix} \frac{1}{2} & -\frac{\sqrt{3}}{2} \\ \frac{\sqrt{3}}{2} & -\frac{1}{2} \end{pmatrix}$	$\begin{pmatrix} & & 1 \\ & -1 & \\ 1 & & \end{pmatrix}$	$\begin{pmatrix} & & -1 \\ & 1 & \\ -1 & & \end{pmatrix}$	$z\ -y\ \ x$
C_{2xz}	1	-1	$\begin{pmatrix} \frac{1}{2} & -\frac{\sqrt{3}}{2} \\ \frac{\sqrt{3}}{2} & -\frac{1}{2} \end{pmatrix}$	$\begin{pmatrix} & & -1 \\ & -1 & \\ -1 & & \end{pmatrix}$	$\begin{pmatrix} & & 1 \\ & 1 & \\ 1 & & \end{pmatrix}$	$-z\ -y\ -x$
C_{4z}	1	-1	$\begin{pmatrix} -1 & \\ & 1 \end{pmatrix}$	$\begin{pmatrix} & -1 & \\ 1 & & \\ & & 1 \end{pmatrix}$	$\begin{pmatrix} & 1 & \\ -1 & & \\ & & -1 \end{pmatrix}$	$-y\ \ x\ \ z$
C_{4z}^3	1	-1	$\begin{pmatrix} -1 & \\ & 1 \end{pmatrix}$	$\begin{pmatrix} & 1 & \\ -1 & & \\ & & 1 \end{pmatrix}$	$\begin{pmatrix} & -1 & \\ 1 & & \\ & & -1 \end{pmatrix}$	$y\ -x\ \ z$
C_{2xy}	1	-1	$\begin{pmatrix} -1 & \\ & 1 \end{pmatrix}$	$\begin{pmatrix} & 1 & \\ 1 & & \\ & & -1 \end{pmatrix}$	$\begin{pmatrix} & -1 & \\ -1 & & \\ & & 1 \end{pmatrix}$	$y\ \ x\ -z$
C_{2yx}	1	-1	$\begin{pmatrix} -1 & \\ & 1 \end{pmatrix}$	$\begin{pmatrix} & -1 & \\ -1 & & \\ & & -1 \end{pmatrix}$	$\begin{pmatrix} & 1 & \\ 1 & & \\ & & 1 \end{pmatrix}$	$-y\ -x\ -z$

Appendix C

Transformation of standing d waves under rotation

For considering the linear combination of real d orbitals one sometimes wishes to change the orthogonal basis of the three-dimensional real space into a particular rotated basis. This problem occurs for instance in the calculation of the eigenstates of a cluster using the crystallographic axes of an orthorhombic system. For an octahedron that is tilted with respect to the crystallographic axes the local coordinate system of the octahedral axes is rotated with respect to the crystallographic axes. Since the orbital occupancy is easy to understand only in the local coordinates (for instance distinguish between e_g and t_{2g} orbitals), one wishes to rotate the linear combination of the considered d orbitals. However, this task is not as easy as for p orbitals which transform like the coordinate system itself, i.e. by the 3×3 rotation matrix. Since there are five d orbitals the transformation matrix has to be a 5×5 matrix. The components of these matrix depend only on the rotation, i.e. on the nine components of the corresponding rotation matrix. It can be derived by considering the transformation properties of the well known quadratic polynomials which display the symmetry of the d orbitals. Note that one has to be careful with the normalization of these polynomials. The normalized basis is:

$$
\begin{aligned}
u &= \tfrac{1}{\sqrt{3}} & |3z^2 - r^2\rangle \\
v &= \tfrac{1}{2} & |x^2 - y^2\rangle \\
a &= & |yz\rangle \\
b &= & |zx\rangle \\
c &= & |xy\rangle
\end{aligned}
$$

Consider a rotation that is given by a matrix R,

$$
R = \begin{pmatrix} r_{11} & r_{12} & r_{13} \\ r_{21} & r_{22} & r_{23} \\ r_{31} & r_{32} & r_{33} \end{pmatrix}
$$

To obtain the transformation matrix for the five d orbitals, one first rotate the basis x, y, z of real space.

$$\begin{pmatrix} r_{11} & r_{12} & r_{13} \\ r_{21} & r_{22} & r_{23} \\ r_{31} & r_{32} & r_{33} \end{pmatrix} \cdot \begin{pmatrix} x \\ y \\ z \end{pmatrix} = \begin{pmatrix} x' \\ y' \\ z' \end{pmatrix}$$

The new coordinates x', y', z' are hence linear functions of x, y, z. Building again the quadratic polynomials (u', v', a', b', c') in x', y', z' and replacing the new coordinates x', y', z' by their dependence on x, y, z,

we get quadratic polynomials in x, y, z. Now we have to develop these new quadratic polynomials in x, y, z in a linear combination of the old polynomials (u, v, a, b, c). The rotated orbitals are hence obtained by a linear combination given in the basis (u, v, a, b, c) that is given by the 5×5 matrix T depending only on the components of R. Doing this one obtains the

$$
\begin{array}{ccc}
\mathbb{R}^3 & \xrightarrow{\ \ R\ \ } & \mathbb{R}^3 \\
(x, y, z) & & (x', y', z') \\
\pi \downarrow & & \downarrow \pi \\
\mathbb{R}^5 & \xrightarrow{\ \ T\ \ } & \mathbb{R}^5 \\
(u, v, a, b, c) & & (u', v', a', b', c')
\end{array}
$$

Figure C.1: The diagram explains the situation where the matrix T is obtained by using the equation $T \circ \pi = \pi \circ R$. Where π is the map from three space onto the five-dimensional space of quadratic polynomials. It is defined just be building the quadratic polynomials u, v, a, b, c at each point (x, y, z).

following matrix T depending on the components of R:

$$
T = \begin{pmatrix}
r_{33}^2 - \frac{1}{2}(r_{13}^2 + r_{23}^2) & \frac{1}{\sqrt{3}}\left(\frac{1}{2}(-r_{11}^2 + r_{12}^2 - r_{21}^2 + r_{22}^2) + r_{31}^2 - r_{32}^2\right) \\
\frac{1}{2}\sqrt{3}(r_{13}^2 - r_{23}^2) & \frac{1}{2}(r_{11}^2 - r_{12}^2 - r_{21}^2 + r_{22}^2) \\
\sqrt{3}r_{23}r_{33} & r_{21}r_{31} - r_{22}r_{32} \\
\sqrt{3}r_{13}r_{33} & r_{11}r_{31} - r_{12}r_{32} \\
\sqrt{3}r_{13}r_{23} & r_{11}r_{21} - r_{12}r_{22}
\end{pmatrix}
$$

$$
\begin{array}{ccc}
\frac{1}{\sqrt{3}}(-r_{12}r_{13} - r_{22}r_{23} + 2r_{32}r_{33}) & \frac{1}{\sqrt{3}}(-r_{11}r_{13} - r_{21}r_{23} + 2r_{31}r_{33}) & \frac{1}{\sqrt{3}}(-r_{11}r_{12} - r_{21}r_{22} + 2r_{31}r_{32}) \\
r_{12}r_{13} - r_{22}r_{23} & r_{11}r_{13} - r_{21}r_{23} & r_{11}r_{12} - r_{21}r_{22} \\
r_{23}r_{32} + r_{22}r_{33} & r_{23}r_{31} + r_{21}r_{33} & r_{22}r_{31} + r_{21}r_{32} \\
r_{13}r_{32} + r_{12}r_{33} & r_{13}r_{31} + r_{11}r_{33} & r_{12}r_{31} + r_{11}r_{32} \\
r_{22}r_{13} + r_{12}r_{23} & r_{21}r_{13} + r_{11}r_{23} & r_{21}r_{12} + r_{11}r_{22}
\end{array}
\Bigg)
$$

Appendix D

p-d matrix elements

The matrix element for dipole transitions from an initial state $|\psi_i\rangle$ to a final state $|\psi_f\rangle$ is in general given by

$$\langle \psi_f | p | \psi_i \rangle$$

where $|\psi_i\rangle$ and $|\psi_f\rangle$ are normalized wave functions and p is the dipole operator. The latter is a vector operator and hence proportional to a spatial vector r. Since matrix elements are linear in their arguments we may rewrite the former matrix element by

$$\sum_{j=1}^{3} p_j \langle \psi_f | e_j | \psi_i \rangle$$

with the basis vectors e_j and $p = (p_1, p_2, p_3)$ given in cartesian coordinates. We consider here the special case where the final and initial states are among the non-rotating p and d orbitals on the same ion. These orbitals have been used already in appendix C. Their definition in terms of spherical harmonics is listed below. As shown in an example in appendix A, p-p and d-d dipole matrix elements vanish due to symmetry reasons. So we have only to consider matrix elements that contain one p and one d state. Note that they are symmetric under permutation of final and initial state [1] ($\langle \psi_f | p | \psi_i \rangle = \langle \psi_i | p | \psi_f \rangle$). So in order to include the most general case we have to calculate the p-d matrix elements for the three p orbitals $\times$ the five d orbitals, and this for the dipole moment parallel to each of the coordinate axes $x_1(x)$, $x_2(y)$, and $x_3(z)$. The resulting matrix elements are listed below were obtained by calculation of integrals of the form

$$\int \int \int \psi_d^* \, x_i \, \psi_p \, dx_1 \, dx_2 \, dx_3 \ .$$

Spherical coordinates are used in order to separate the radial part of the wave functions from their angular dependence. Since the integration of the radial part gives a constant factor for all matrix elements, we consider only the angular contribution. The p and d wave functions are given by a linear combination of the spherical harmonics ($|l, m_l\rangle$):

---

[1] This follows from the fundamental property of physical operators to be hermitian (or vice versa if one likes).

$$
\begin{aligned}
|x\rangle &= \sqrt{\tfrac{3}{4\pi}}\tfrac{x}{r} &&= \sqrt{\tfrac{3}{4\pi}}\cos(\phi)\sin(\theta) &&= -\tfrac{1}{\sqrt{2}}|1,1\rangle + \tfrac{1}{\sqrt{2}}|1,-1\rangle \\
|y\rangle &= \sqrt{\tfrac{3}{4\pi}}\tfrac{y}{r} &&= \sqrt{\tfrac{3}{4\pi}}\sin(\phi)\sin(\theta) &&= \tfrac{i}{\sqrt{2}}|1,1\rangle + \tfrac{i}{\sqrt{2}}|1,-1\rangle \\
|z\rangle &= \sqrt{\tfrac{3}{4\pi}}\tfrac{z}{r} &&= \sqrt{\tfrac{3}{4\pi}}\cos(\theta) &&= |1,0\rangle
\end{aligned}
$$

$$
\begin{aligned}
|3z^2 - r^2\rangle &= \tfrac{1}{4}\sqrt{\tfrac{5}{\pi}}\tfrac{3z^2-r^2}{r^2} &&= \tfrac{1}{4}\sqrt{\tfrac{5}{\pi}}(3\cos^2(\theta)-1) &&= |2,0\rangle \\
|x^2 - y^2\rangle &= \tfrac{1}{4}\sqrt{\tfrac{15}{\pi}}\tfrac{x^2-y^2}{r^2} &&= \tfrac{1}{4}\sqrt{\tfrac{15}{\pi}}(\cos^2(\phi)-\sin^2(\phi))\sin^2(\theta) &&= \tfrac{1}{\sqrt{2}}|2,2\rangle + \tfrac{1}{\sqrt{2}}|2,-2\rangle \\
|yz\rangle &= \tfrac{1}{2}\sqrt{\tfrac{15}{\pi}}\tfrac{yz}{r^2} &&= \tfrac{1}{2}\sqrt{\tfrac{15}{\pi}}\sin(\phi)\sin(\theta)\cos(\theta) &&= \tfrac{i}{\sqrt{2}}|2,1\rangle + \tfrac{i}{\sqrt{2}}|2,-1\rangle \\
|zx\rangle &= \tfrac{1}{2}\sqrt{\tfrac{15}{\pi}}\tfrac{zx}{r^2} &&= \tfrac{1}{2}\sqrt{\tfrac{15}{\pi}}\cos(\phi)\sin(\theta)\cos(\theta) &&= -\tfrac{1}{\sqrt{2}}|2,1\rangle + \tfrac{1}{\sqrt{2}}|2,-1\rangle \\
|xy\rangle &= \tfrac{1}{2}\sqrt{\tfrac{15}{\pi}}\tfrac{xy}{r^2} &&= \tfrac{1}{2}\sqrt{\tfrac{15}{\pi}}\cos(\phi)\sin(\phi)\sin^2(\theta) &&= -\tfrac{i}{\sqrt{2}}|2,2\rangle + \tfrac{i}{\sqrt{2}}|2,-2\rangle
\end{aligned}
$$

$p \parallel x$	$|3z^2-r^2\rangle$	$|x^2-y^2\rangle$	$|yz\rangle$	$|zx\rangle$	$|xy\rangle$
$|x\rangle$	$-\frac{1}{\sqrt{15}}$	$\frac{1}{\sqrt{5}}$	0	0	0
$|y\rangle$	0	0	0	0	$\frac{1}{\sqrt{5}}$
$|z\rangle$	0	0	0	$\frac{1}{\sqrt{5}}$	0

$p \parallel y$	$|3z^2-r^2\rangle$	$|x^2-y^2\rangle$	$|yz\rangle$	$|zx\rangle$	$|xy\rangle$
$|x\rangle$	0	0	0	0	$\frac{1}{\sqrt{5}}$
$|y\rangle$	$-\frac{1}{\sqrt{15}}$	$-\frac{1}{\sqrt{5}}$	0	0	0
$|z\rangle$	0	0	$\frac{1}{\sqrt{5}}$	0	0

$p \parallel z$	$|3z^2-r^2\rangle$	$|x^2-y^2\rangle$	$|yz\rangle$	$|zx\rangle$	$|xy\rangle$
$|x\rangle$	0	0	0	$\frac{1}{\sqrt{5}}$	0
$|y\rangle$	0	0	$\frac{1}{\sqrt{5}}$	0	0
$|z\rangle$	$\frac{2}{\sqrt{15}}$	0	0	0	0

Appendix E

Kramers-Kronig relations

The Kramers-Kronig relations, derived independently by Kramers and Kronig in 1926, connect the real and the imaginary part of a linear response function. These relations are based on causality, i.e. that there is no response or "answer" before there is a stimulus or "question". Before we formally deduce the integral formula we sketch a phenomenological view of the proposition. We show with only qualitative means that there has to be a certain relation between the real and imaginary part, or in our example between the amplitude and the phase of a response function.

The need of a relation between the two properties becomes obvious regarding the complex reflectance $\hat{r}(\omega) = R(\omega)e^{i\theta(\omega)}$, where $R(\omega)$ is the amplitude of the reflected light and $\theta(\omega)$ the phase shift on reflection. These properties are of particular importance for the use in practice since the reflectance is determined rather easily in experiment. If both properties are known we are able to derive other optical properties of the medium. However, the direct experimental determination of $\theta(\omega)$ requires more sophisticated experimental technics such as ellipsometry. With the use of the Kramers-Kronig relations it is sufficient to determine $R(\omega)$ only.

Consider now a wave packet in the vacuum hitting the surface of a medium as depicted in Fig. E.1 1). Assume that in the medium only one frequency is absorbed (see Fig. E.1 2) (this is clearly a simplification to the real case where all frequencies suffer a more or less strong decay in the medium). The resulting signal contains the absorbed frequency with negative sign for $t < 0$ since after the absorption it is missing everywhere the wave packet has been zero before. This is the case for all times and throughout the whole space, i.e. it exists for times before the wave packet has hit the surface (Fig. E.1 3)). This however violates the principle of causality, since the response is present before there has been any stimulus. The only way to restore causality is that the phases of the other cosine terms are shifted in order to cancel the missing contribution for negative times (Fig. E.1 4)).

For the formal deduction one has to use complex functions, so we will briefly give some basic information on this. Functions from the complex plane onto itself would be identical to functions $\mathbb{R}^2 \rightarrow \mathbb{R}^2$ and would therefore be not very interesting by themselves. But since there are restrictions for the complex functions $C^2 \rightarrow C^2$, they differ from the former substantially. These restrictions follow from the requirement that the derivative should be written in the form $f'(z_0) = \Delta(z_0)$, where $f(z) = f(z_0) + (z - z_0)\Delta(z)$ in the neighborhood of z_0 (analog to
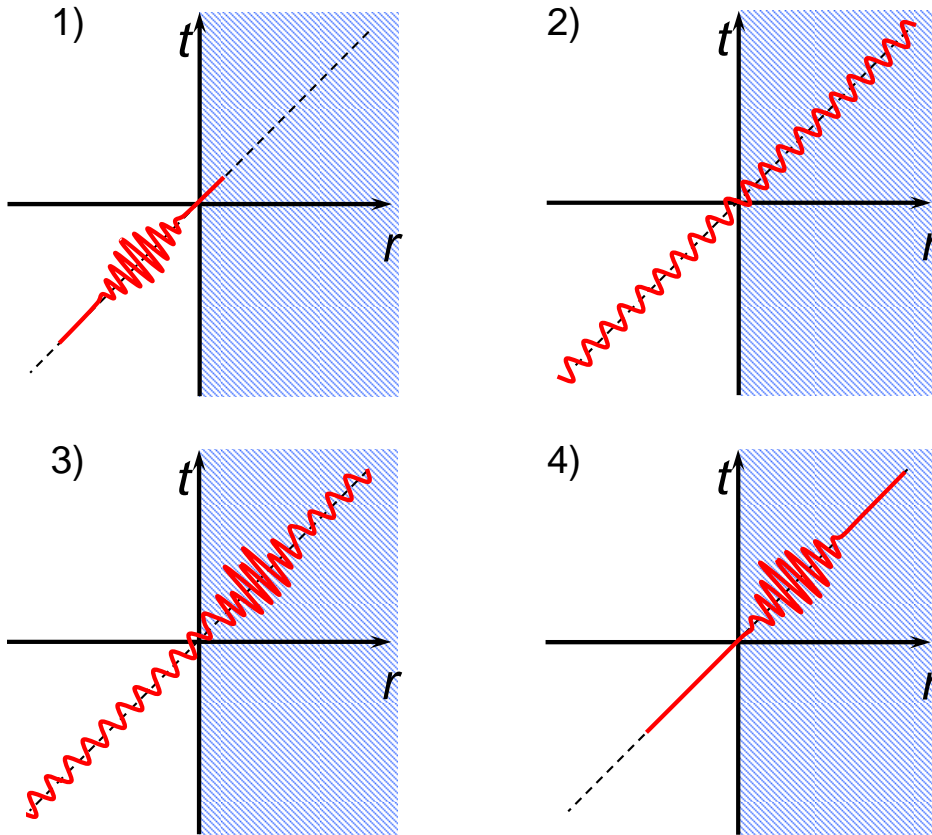
Figure E.1: The space-time diagrams to emphasize the fact that the signal without phase shift is going back not only in space but also in time (see 3)). For clarity only one dimension is shown. Note that the amplitude of the wave is not as drawn in the $r-t$ plane but extended in a second dimension.

real case $\mathbb{R} \to \mathbb{R}$). There exists a complex linear coherency of the image and the preimage. Note that in contrast to the real case, this is not a general property of any arbitrary complex function, but a restriction of the general case. For a function $f(x+iy) = g(x+iy)+ih(x+iy)$ (g,h real functions) this implies:

$$\frac{\partial g}{\partial x} = \frac{\partial h}{\partial y} \text{ (i)} \qquad \text{and} \qquad \frac{\partial g}{\partial y} = -\frac{\partial h}{\partial x} \text{ (ii)}$$

These equations are called Cauchy-Riemann differential equations. A complex function satisfying them is termed holomorphic.

How can the Cauchy-Riemann differential equations be interpreted? One may think of functions from $\mathbb{R}^2$ onto $\mathbb{R}^2$ as of vector fields in the plane. Each point of the plane ($\epsilon \mathbb{R}^2$) gets one vector ($\epsilon \mathbb{R}^2$) attached. So the Cauchy-Riemann differential equations can be understood as restrictions on these vector fields. The vector fields satisfying the Cauchy-

Riemann equations actually turn out to be curlefree (corresponding to (i)) and solenoidal (of zero divergence corresponding to (ii)). Hence the corresponding vector field is conservative. So on a simple connected region (which contains no poles[1]) a path integral of $f(z)$ over a closed path γ is always zero.

$$\oint_\gamma f(z)\, dz = 0$$

In the case of a pole at z_0 within the closed path the integral gives the constant value $2\pi i$:

$$\oint_\gamma \frac{f(z)}{z - z_0}\, dz = 2\pi i\, f(z_0)$$

In terms of vector fields this means that a pole gives a well of the strength $2\pi i$. This is seen as generalization from the case of the function $f(z) \equiv 1$, $z_0 = 0$ and the path γ to be a unit circle $e^{i\phi}$, $\phi \, \epsilon \, [0, 2\pi]$.

$$\int_\gamma \frac{1}{z}\, dz \overset{z \to e^{i\phi}}{=} \int_0^{2\pi} \frac{1}{e^{i\phi}} \underbrace{ie^{i\phi}}_{= \frac{dz}{d\phi}}\, d\phi = i|_0^{2\pi} = 2\pi i$$

Now let's turn to the Kramers-Kronig relations, which relates the real and imaginary part of a complex response function. A response function in general is describing how a physical system (e.g. a crystal) reacts to an external stimulus. We consider here linear response which means that the response of the system is proportional to the strength of the stimulus. A stimulus is given by its dependence on time and space, $f(t', r')$. As stimulus we will have a sinusoidal oscillating electromagnetic wave in mind. A response function $G(t', t, r', r)$ gives the connection between the stimulus $f(t', r')$ and the response $a(t, r)$,

$$a(t, r) = \int_{-\infty}^{\infty} \int_{-\infty}^{\infty} G(t', t, r', r) f(t', r') dt' dr'$$

This is valid in general for the linear regime. For the case of light interacting with matter we are able to make some additional assumptions:

- The response is only local, i.e. a stimulus at r' does only contribute to a response at r'. So the dependence on r is given by $\delta(r - r')$. This seems to be a bit crude since there are a lot mechanisms that relate a stimulus at r' with a response somewhere else at $r \neq r'$ (e.g. phonons, magnons). But after all we have restricted ourselves to the linear regime where the deviation from the ground state of the system is negligible.

- The other assumption is that only the difference in time $t - t'$ between the stimulus and the response is relevant. This is obvious since the system is regarded in a stationary ground state which is independent of time. (Homogeneity of time is of course necessary here, too.)

---

[1]Towards a pole the absolute value of the function diverges so that the function is not defined at the pole. For instance $1/z$ has a pole in z=0.

With this the response $a(t,r)$ looks like:

$$a(t,r) = \int_{-\infty}^{\infty} \int_{-\infty}^{\infty} G(t-t',r',r)f(t',r')\delta(r'-r)dt'dr'$$

The integration over the whole space of the delta function gives just the value at r'. Therefore G and f spatially depend only on r', and for clarity the spatial argument will be suppressed in the following. Including this the response reduces to

$$a(t) = \int_{-\infty}^{\infty} G(t-t')f(t')dt' \ .$$

The answer $a(t)$ is related by the response function $G(t-t')$ to any stimulus $f(t')$ at any time t'. Such an integral of the product of two functions appears more simple when one moves over to the Fourier-transformed functions[2]

$$a(\omega) = \int_{-\infty}^{\infty} a(t)e^{i\omega t}dt$$

$$G(\omega) = \int_{-\infty}^{\infty} G(t-t')e^{i\omega(t-t')}dt$$

$$f(\omega) = \int_{-\infty}^{\infty} f(t')e^{i\omega t'}dt'$$

Inserting this we get[3]

$$a(\omega) = G(\omega) \cdot f(\omega)$$

In the following we will allow ω to be a complex number $\hat{\omega} = \omega_1 + i\omega_2$. This is not an elegant mathematical trick but necessary in order to include dissipation. The response function G becomes

$$G(\hat{\omega}) = \int_{-\infty}^{\infty} G(t-t')e^{i\omega_1(t-t')}e^{-\omega_2(t-t')}dt$$

Analyzing the integrand we find that $e^{i\omega_1(t-t')}$ is bounded for all frequencies ω_1 whereas the term $e^{-\omega_2(t-t')}$ is bounded only if $\omega_2(t-t') \geq 0$. This result is depicted in Fig. E.2.

---

[2]The form $a(t) = \int_{-\infty}^{\infty} G(t-t')f(t')dt'$ in real space is just the definition of the convolution integral of G with f.

[3]Formally this is seen from

$$\begin{aligned} a(\omega) &= \int_{-\infty}^{\infty} e^{(i\omega t)} \underbrace{\left[\int_{-\infty}^{\infty} G(t-t')f(t')dt'\right]}_{=a(t)} dt \\ &= \int_{-\infty}^{\infty} f(t') \left[\int_{-\infty}^{\infty} G(t-t')e^{i\omega t}dt\right] dt' \\ &= \int_{-\infty}^{\infty} f(t')e^{i\omega t'} \left[\int_{-\infty}^{\infty} G(t-t')e^{i\omega(t-t')}dt\right] dt' \end{aligned}$$

More instructive is that the Fourier transforms of both functions (G, f) are given in general by an infinite sum of cosine functions $f(t) = \sum a_i \cos(\omega_i)$. The product of two functions is hence containing a sum of products of cosine terms $a_i \cos(\omega_i t) \cdot b_j \cos(\omega_j t)$. Integrating these products from $-\infty$ to ∞ only the products of cosine terms with the same frequency survive due to their orthogonality. So one has to consider the products of the corresponding amplitudes of cosine terms with the same frequency, i.e. $G(\omega)f(\omega)$.
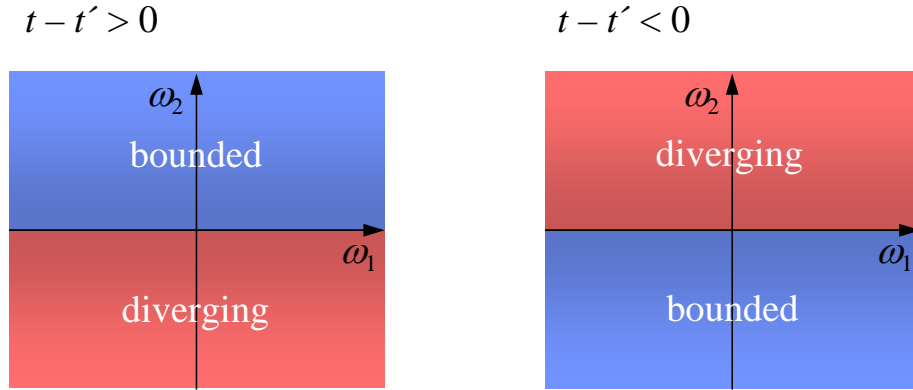
Figure E.2: The behavior of the complex function $G(\hat{\omega})$ is shown in the complex $\hat{\omega}$ plane. It depends on the sign of $t - t'$. Due to causality one only has to consider the left side, where $G(\hat{\omega})$ is defined only in the upper half-plane.

The principle of causality states that there will be no answer before the stimulus. The response function has to be identical to zero $G(t - t') \equiv 0$ for $t - t' < 0$ before a stimulus f occurs at $t = t'$. Hence the integral $\int_{-\infty}^{\infty} G(t-t')e^{i\omega_1(t-t')}e^{-\omega_2(t-t')}dt$ only has to be evaluated for $t - t' > 0$. Then $G(\hat{\omega})$ can be defined only in the upper half-plane. This simply means that due to absorption processes there has to be damping ($\omega_2 \geq 0$) instead of an increase of the amplitude. In order to get the Kramers-Kronig relations one considers the integral

$$\oint_\gamma \frac{G(\omega)}{\omega - \omega_0} \, d\omega$$

The closed integration path γ is shown in Fig. E.3. It can be decomposed into three parts: first the large circle γ_1, second the small circle γ_2, and third the part on the ω_1 axis γ_3 ($\gamma = \gamma_1 + \gamma_2 + \gamma_3$). Remember the fact that the integral of a holomorphic function vanishes over a closed path surrounding an area which contains no poles. Hence the integral over the closed path γ becomes

$$\int_{\gamma_1} \frac{G(\omega)}{\omega - \omega_0} \, d\omega + \int_{\gamma_2} \frac{G(\omega)}{\omega - \omega_0} \, d\omega + \int_{\gamma_3} \frac{G(\omega)}{\omega - \omega_0} \, d\omega = 0$$

We will consider now the limiting case where the radius of the small circle r_2 is decreasing to zero and the radius of the large circle r_1 becomes infinite. An infinite radius of the large circle $|\hat{\omega}| \to \infty$ corresponds to an infinitely large frequency ω_1 or to an infinite damping ω_2, or both. In any case there should be no response of the system ($G(\hat{\omega}) = 0$ for $|\hat{\omega}| \to \infty$). It can be assumed that $G(\omega)$ is decreasing faster than $1/\omega$ so that its decrease overcompensates the linear increase of the integration path. Therefore the integral over γ_1 is vanishing.[4] The integrals of the remaining two contributions are hence equal with opposite sign:

$$\int_{\gamma_2} \frac{G(\omega)}{\omega - \omega_0} \, d\omega = - \int_{\gamma_3} \frac{G(\omega)}{\omega - \omega_0} \, d\omega$$

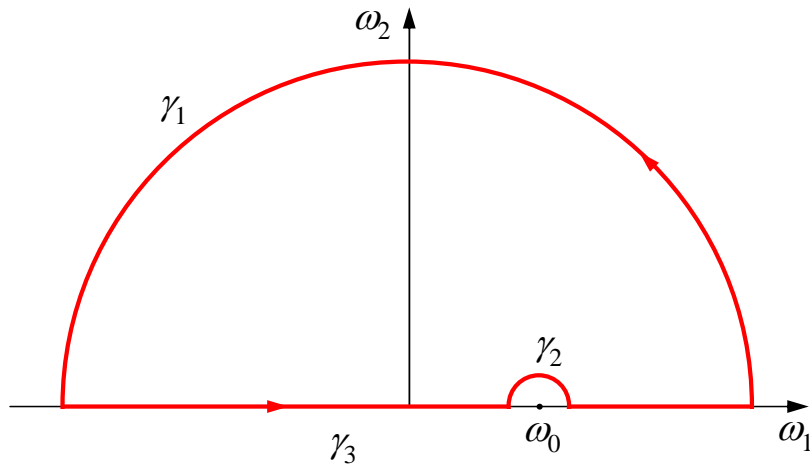[4]Note that the zero of the denominator is not lying on γ anyway.

Figure E.3:

Consider the two parts separately:

$$\int_{\gamma_2} \frac{G(\omega)}{\omega - \omega_0} = \lim_{\varepsilon \to 0} \int_{\pi}^{0} \frac{G(\varepsilon e^{i\phi} + \omega_0)}{\varepsilon e^{i\phi}} \, d\phi = -i\pi G(\omega_0)$$

This equation needs some additional explanation. The integral over a closed path around ω_0 equals $2\pi i G(\omega_0)$ as stated above. For sufficiently small neighborhood of ω_0 the value of $G(\omega)$ will approach $G(\omega_0)$ and so we may consider for a sufficiently small radius ε of the circle around ω_0, $G(\omega) = G(\omega_0) = $ constant. Then the integral over the semi-circle of r_2 is half of the value of a full circle ($\frac{1}{2} \, 2i\pi G(\omega_0)$). Note that the minus sign on the right hand side results from the mathematically negative sense of rotation of γ_2.

$$\int_{\gamma_3} \frac{G(\omega)}{\omega - \omega_0} = \lim_{\varepsilon \to 0} \left[\int_{-\infty}^{\omega_0 - \varepsilon} \frac{G(\omega)}{\omega - \omega_0} d\omega + \int_{\omega_0 + \varepsilon}^{\infty} \frac{G(\omega)}{\omega - \omega_0} d\omega \right] =: \mathcal{P} \int_{-\infty}^{\infty} \frac{G(\omega)}{\omega - \omega_0} d\omega$$

Such an integral is termed *principle value* and denoted be $\mathcal{P}$. With this the above equation reads

$$-i\pi G(\omega_0) = -\mathcal{P} \int_{-\infty}^{\infty} \frac{G(\omega)}{\omega - \omega_0} d\omega$$

$$G(\omega_0) = \frac{1}{i\pi} \mathcal{P} \int_{-\infty}^{\infty} \frac{G(\omega)}{\omega - \omega_0} d\omega$$

The last equation is the general form of the Kramers-Kronig relation. Separating the real and the imaginary part we find

$$\Re G(\omega_0) = \frac{1}{\pi} \mathcal{P} \int_{-\infty}^{\infty} \frac{\Im G(\omega)}{\omega - \omega_0} d\omega$$

$$\Im G(\omega_0) = -\frac{1}{\pi} \mathcal{P} \int_{-\infty}^{\infty} \frac{\Re G(\omega)}{\omega - \omega_0} d\omega$$

192

From this we finally see that the real and imaginary part of a response function are not independent.

For obtaining the real and imaginary part of optical properties only from reflectance data the above formula is not practical since it does not contain the measured quantity. An integral equation which is relevant for the practical use is derived for example in [207].

Appendix F

Cluster calculation and the point-charge model

Configuration-interaction cluster calculations have been performed for many years in order to assign the correct symmetry and orbital occupancy to d-d excitations (see, e.g., chapter 10 of reference [78]). A typical cluster consists of the transition-metal ion and the surrounding anions, e.g., $[\mathrm{TiO_6}]^{9-}$. More distant ions are taken into account as point charges only. The following parameters are being used: (i) the Slater integrals, (ii) the local crystal field, and (iii) the tight-binding parameters.

ad (i) The Slater integrals describe the full local electron-electron interactions which give rise to the main multiplet structure. They have been obtained from Hartree-Fock calculations for a bare ion [107]. Then, these values have been reduced to 80% in order to account for the neglect of the $4s$ shell.

ad (ii) The crystal field or Madelung potential represents the electrostatic potential of all ions within the crystal, which is assumed to be infinite. The ions are considered to be point charges. The crystal field controls the on-site energies and gives rise to the energy splitting between the orbitals. We have calculated the crystal field using an Ewald summation, i.e., the summation is partly performed in real space, partly in momentum space, and thus pertains to the infinite crystal.[1] The orbital splitting depends on the local derivatives of the Madelung potential. Therefore we expanded the Madelung potential in terms of spherical harmonics, which allows to calculate the ionic crystal-field splitting if the expectation values of $< r^k >$ are known [1], where r is the electron coordinate with respect to the transition-metal site and k is the order of the expansion. These expectation values have been obtained from Hartree-Fock calculations [107].

ad (iii) The tight-binding parameters account for hopping processes between the ligands and the transition-metal ion [109, 110]. For many materials they are well known from fits to LDA band-structure calculations. Some general rules have been derived for the dependence of the parameters $pd\sigma$ and $pd\pi$ on the distance between two ions [109]. Finally, the values for the on-site Coulomb repulsion on the transition-metal site (U_{dd}) and on the ligands (U_{pp}) as well as the charge-transfer energy Δ have been taken as reported from core-level and photo-

---

[1]This is necessary in order to achieve convergency of the $1/r$ potential.

emission spectroscopy [111]. The cluster calculations have been performed using the code XTLS8 by A. Tanaka [112].

Kurzzusammenfassung

Im Rahmen dieser Arbeit haben wir verschiedene Übergangsmetalloxide untersucht. Dazu wurde die optische Leitfähigkeit aus Daten der Transmission und der Reflexion bestimmt. Als experimentelle Methode der Wahl hierzu diente die Fourier Spektroskopie. Die untersuchten Systeme werden im Folgenden separat diskutiert.

Für das e_g System LaMnO$_3$ wurde die Exsistenz neuartiger orbitaler Anregungen vor hergesagt. Diese Anregungen, die als Orbitonen bezeichnet werden, unterscheiden sich von gewöhnlichen Kristallfeldanregungen durch eine aus geprägte Dispersion. Saitoh *et al.* hat die erste Beobachtung dieser Anregungen in Raman Daten berichtet. Seine Behauptung stützt sich auf den Vergleich von drei beobachteten Peaks mit theoretischen Vorhersagen hinsichtlich der Übereinstimmung in der Energie, der Polarisations- und der Temperaturabhängigkeit. Aufgrund der Energie der Anregungen (ca. 150 meV) wurden Multiphononen als mögliche Ursache ausgeschlossen. Unsere Reflexionsdaten der zeigen jedoch, dass die höchste Phononanregung bei 80 meV liegt. Darüber hinaus beobachten wir in der optischen Leitfähigkeit Peaks bei fast denselben Energien wie in den Raman Daten. Die direkte Beobachtung von orbitale *d-d* Anregungen ist jedoch in der IR Spektroskopie aus Symmetriegründen verboten und sind nur bei der simultanen Anregung eines Phonons erlaubt. Somit müssten die Anregungen aber um die Energie des Phonons, typischerweise 50-80 meV, höher liegen als in den Raman Daten. Daraus schließen wir, dass es sich nicht um Orbitonen sondern um Zweiphononprozesse handelt. Unterhalb der Energielücke könnten wir keine weiteren Anregungen gefunden. Allerdings haben wir am Fuß des Anstiegs der optischen Leitfähigkeit zur elektronischen Anregung eine Schulter beobachtet. Im Vergleich mit den Ergebnissen einer Cluster-Rechnung weisen wir die Schulter einer lokalen Kristallfeldanregung zu. Die Kopplung an das Gitter erweist sich somit als der dominante Mechanismus zur Aufhebung der orbitalen Entartung.

Im System LaTiO$_3$ wurde ein neuartiger Grundzustand von Khaliullin und Maekawa vorgeschlagen, um die sich scheinbar widersprechenden Beobachtungen eines kleinen Anregungslücke im Spinwellenspektrum und eines kleinen geordneten magnetischen Moments zu erklären. Dieser Grundzustand wird geprägt von starken Quantenfluktuationen im orbitalen Sektor und deshalb als orbitale Flüssigkeit bezeichnet. Andererseits wird eine beträchtliche Verzerrung des umgebenden Sauerstoffoktaeders beobachtet, für die eine Kristallfeldaufspaltung der t_{2g} Orbitale von ungefähr 0.25 eV vorhergesagt wird und einen orbital geordneten Grundzustand nahe legt. Die Frage nach dem Grundzustand in diesem System wird kontrovers diskutiert. Wir haben die optische Leitfähigkeit von RTiO$_3$ (R=La, Sm, Y) aus Reflexions- und Transmissionsdaten bestimmt und beobachten bei 0.3 eV einen breiten Peak in der optischen Leitfähigkeit von LaTiO$_3$. Diese Anregung kann hinsichtlich der Energie und der Linienform gut durch die Kristallfeldaufspaltung erklärt werden, wobei die Größe der Aufspaltung orbitale Fluktuationen ausschließen würde. Andererseits wird für den Grundzustand einer orbitalen Flüssigkeit eine Zwei-Orbiton-Anregung vorhergesagt, die ebenfalls die Anregung erklären kann. Eine Polarisationsabhängigkeit wurde in beiden Szenarien als schwach vorhergesagt und im Experiment auch nicht eindeutig nachgewiesen. In YTiO$_3$ wurde orbitale Ordnung experimentell nachgewiesen, obwohl auch in diesem System die Rolle orbitaler Fluktuationen diskutiert wird. Die in der optischen Leitfähigkeit von YTiO$_3$ beobachteten Anregungen sind hinsichtlich ihrer Energie in guter Übereinstimmung mit dem Kristallfeld-

197

szenario. Sie weisen darüber hinaus eine starke Polarisationsabhängigkeit auf. Für eine orbitale Flüssigkeit bleibt jedoch die kubische Symmetrie erhalten, so dass hier die reine orbitale Anregung isotrop ist. Unsere Ergebnisse für $YTiO_3$ zeigen, dass orbitale Ordnung in diesem System eine wichtige Rolle spielt, was eindeutig für ein Kristallfeldszenario spricht.

In dem Doppelschichtsystem TiOX (X=Br, Cl) wird die magnetische Suszeptibilität bei hohen Temperaturen gut durch das Modell einer $S = \frac{1}{2}$ Heisenbergkette beschrieben. Unterhalb einer kritischen Temperatur T_{c1} verschwindet sie jedoch vollständig, was mit einem Spin-Peierls Übergang erklärt wird. Darüber hinaus wird ein Knick bei einer Temperatur $T_{c2} > T_{c1}$ beobachtet, jedoch wird ein zweiter Übergang in einem kanonischen Spin-Peierls Szenario nicht erwartet. Dieser weitere Übergang wird mit orbitalen Fluktuationen in Verbindung gebracht. Wir beobachten in den Transmissionsdaten gemessen an Einkristallen starke Absorptionen. Pro Polarisation ($E \parallel a$, $E \parallel b$) jeweils eine bei 0.65 eV bzw. 1.5 eV für TiOCl und bei 0.62 eV bzw. 1.4 eV für TiOBr. Diese Resultate sind hinsichtlich der Energie und der Polarisationsabhängigkeit in sehr guter Übereinstimmung mit den Ergebnissen einer Cluster-Rechnung. Der ersten angeregte Zustand, der Dipol verboten ist, weist in der Rechnung einen Abstand von 0.25 es zum Grundzustand auf. Die Größe der Aufspaltung wird auch durch einen g-Faktor von fast 2 bestätigt. Bei einer so großen Aufspaltung innerhalb der t_{2g} Orbitale können orbitale Fluktuationen ausgeschlossen werden. Wir haben gezeigt, dass die Geometrie der Doppelschicht für das ungewöhnliche Verhalten verantwortlich ist. Frustration der Zwischenkettenkopplung führt bei T_{c2}, die eigentliche Spin-Peierls-Übergangstemperatur, zu einem zeiter-Ordungs-Übergang in eine inkommensurable Phase. Bei T_{c1} rastet dann die vollständig dimerisierte Phase in einem erster Ordnungs Übergang ein. Experimentell beobachten wir bei beiden Übergangstemperaturen Änderungen im Phononenspektrum. Darüber hinaus beobachten wir einige Phononenmoden nur zwischen T_{c2} und T_{c1}, was auf eine niedrigere Symmetrie hinweist. Dies ist in Übereinstimmung mit der Existenz einer inkommensurablen Phase.

Abstract

In the framework of this thesis orbital excitations of different transition-metal oxides are investigated. We have obtained the optical conductivity from reflectance and transmittance measurements. This data were obtained by Fourier spectroscopy.

The nature of orbital excitations in $LaMnO_3$

The e_g system $LaMnO_3$ with the electronic configuration $t_{2g}^3 \, e_g^1$ has been predicted to exhibit collective orbital excitations (termed orbitons) from an orbitally ordered ground state [45]. These excitations are expected to have a significant dispersion. Saitoh *et al.* claimed the first experimental observation of orbitons in Raman data of $LaMnO_3$ [44]. The claim is based on a comparison with theory and on the assumption that the observed peaks around 150 meV are too high in energy to originate from two-phonon scattering. We have determined the phonon spectrum from reflectance measurements and observed the highest phonon mode at about 80 meV. Moreover the peaks around 150 meV are observed in the optical conductivity at nearly the same energies, although orbital excitations in $\sigma(\omega)$ require an additional phonon to be excited in order to break the dipole selection rule. Thus orbital excitations should be shifted in $\sigma(\omega)$ by the phonon energy which typically amounts to 50-80 meV. Hence we conclude that these peaks have to be attributed to two-phonon excitations. Additionally weak features are observed around 230 meV and around 300 meV in both Raman and IR data. These features are interpreted as three and four phonon excitations corroborating the nature of the peaks around 150 meV. We found no further low-energy absorptions. However a shoulder at the rise of the first electronic excitation has been observed. By comparison with the results of a cluster calculation it is attributed to a local crystal-field excitation. From this we conclude that the coupling to the lattice is the dominant mechanism that lifts the degeneracy of the e_g orbitals in $LaMnO_3$.

Orbital excitations and ground state properties in the titanates

For the t_{2g} system $LaTiO_3$ a novel ground state has been proposed by Khaliullin and Maekawa in order to reconcile the seemingly contradicting observations of a small spin-wave gap and a strongly reduced magnetic moment [34]. The Hamiltonian they considered accounts for the orbital and spin system (interactions with the lattice are not taken into account). The ground state they obtain is dominated by orbital fluctuations and has been termed orbital liquid. On the other hand a sizeable distortion of the octahedral environment of the Ti site has been found [57]. By this distortion an intra t_{2g} splitting of about 0.25 eV has been predicted. In this scenario, the electrons occupy the lowest orbital at each site, giving rise to orbital order. The controversially discussed question in this system is whether in the ground state orbital order or orbital fluctuations are present [34, 35, 49, 62, 60, 71, 57]. The former corresponds to dominating coupling to the lattice, whereas the latter arises in the presence of dominating superexchange interactions. We have determined the optical conductivity of $RTiO_3$ (R=La, Sm, Y) in order to observe the low-energy excitations. We have found a broad peak at about 0.3 eV in all three compounds. The peak energies as well as the lineshape are in

good agreement with a crystal-field scenario. For such a large intra t_{2g} splitting a significant role of fluctuations can be ruled out. However, a back door has been opened up for the orbital-liquid picture by assuming that the large observed energy actually corresponds to a *t*wo-orbiton process [38]. The fact that only one peak with a not very characteristic lineshape is observed makes it impossible to draw a final conclusion for the ground state of LaTiO$_3$. The observation of a polarization dependence in LaTiO$_3$ has been complicated by the twinning of crystals. Furthermore both scenarios predict only a small polarization dependence in this compound. In YTiO$_3$ orbital order has been observed experimentally [149, 150, 151]. But the proportion that orders is still under discussion since neutron scattering revealed an isotropic spin-wave dispersion [155]. In this compound a significant polarization dependence as well as two clearly separated peaks have been found. This observation is in agreement with the crystal-field scenario which predicts for YTiO$_3$ the largest difference between the intra t_{2g} excitations. In an orbital-liquid scenario the pure orbital excitation is predicted to be isotropic since in this scenario cubic symmetry remains unbroken [35]. In the light of our results on YTiO$_3$ the dominant role of orbital order in this compound becomes apparent. This definitely favors the description of YTiO$_3$ within the crystal-field scenario.

Unconventional spin-Peierls transition in TiOX (X = Cl, Br)

Structurally TiOX is a bilayer system. The magnetic susceptibility in contrast is well described in terms of a $S = \frac{1}{2}$ Heisenberg chain which shows that the magnetism is one-dimensional [50]. The susceptibility vanishes below a temperature T_{c1} which is attributed to a spin-Peierls transition. A second feature is observed at $T_{c2} > T_{c1}$ which is unexpected in a canonical spin-Peierls scenario. This second transition has been discussed in connection with orbital fluctuations [113, 122, 131, 132, 130, 141]. We have measured the transmittance of single crystals and observed in each polarization ($E \parallel a$ and $E \parallel b$) a strong absorption at 0.65 and 1.5 eV for X=Cl, 0.62 and 1.4 eV for X=Br, respectively. Comparison with the results of a cluster calculation for TiOCl gives good agreement between experiment and theory. The lowest intra t_{2g} excitation is not directly dipole allowed due to symmetry. The cluster calculation predicts it at 0.25 eV. Such a large splitting of the t_{2g} orbital suppresses orbital fluctuations. This result is corroborated by ESR data which give a g-factor of ≈ 2 [113]. We have shown that the bilayer geometry is responsible for the unconventional second phase transition [143]. The interchain coupling between chains of one layer and chains of the adjacent layer is frustrated in the spin-Peierls order pattern realized at low temperatures. This leads to a second-order transition to an incommensurate phase below T_{c2} which is the actual spin-Peierls transition temperature. At T_{c1} the fully dimerized spin-Peierls phase locks in by a first-order transition. Experimental evidence for this scenario is found in the phonon spectra. In the range of phonon excitations we have measured the transmittance and the reflectance. In both properties changes are observed at T_{c1} and T_{c2}, which indicates that the lattice is involved in both transitions. Moreover, in the intermediate phase phonon modes are observed which are absent in the low- and the high-temperature phase and which show a significant shift with temperature. This indicates that the symmetry is lowered, as expected for the incommensurate phase.

Offizielle Erklärung

Ich versichere, daß ich die von mir vorgelegte Dissertation selbstständig angefertigt, die benutzten Quellen und Hilfsmittel vollständig angegeben und die Stellen der Arbeit - einschließlich Tabellen, Karten und Abbildungen-, die anderen Werken im Wortlaut oder dem Sinn nach entnommen sind, kenntlich gemacht habe; dass diese Dissertation noch keiner anderen Fakultät oder Universität zur Prüfung vorgelegen hat; dass sie - abgesehen von unten angegeben Teilpublikationen - noch nicht veröffentlicht worden ist sowie, daß ich eine solche Veröffentlichung vor Abschluß des Promotionsverfahrens nicht vornehmen werde.

Die Bestimmungen dieser Promotionsordnung sind mir bekannt. Die von mir vorgelegte Dissertation ist von Prof. Dr. A. Freimuth betreut worden.

Köln, den 14. März 2006

Reinhard Rückamp

List of publications

1. Zero-Field Incommensurate Spin-Peierls Phase with Interchain Frustration in TiOCl 2000 *Phys. Rev. Lett.* **95** 097203 (2005)
   R. Rückamp, J. Baier, M. Kriener, M.W. Haverkort, T. Lorenz, G.S. Uhrig, L. Jongen, A. Möller, G. Meyer, and M. Grüninger

2. Optical study of orbital excitations in transition-metal oxides
   R. Rückamp, E. Benckiser, M.W. Haverkort, H. Roth, T. Lorenz, A. Freimuth, L. Jongen, A. Möller, G. Meyer, P. Reutler, B. Büchner, A. Revcolevschi, S-W. Cheong, C. Sekar, G. Krabbes and M. Grüninger, *New J. Phys.* **7** 144 (2005)

3. Experimental quest for orbital waves
   M. Grüninger, R. Rückamp, M. Windt, P. Reutler, C. Zobel, T. Lorenz, A. Freimuth, A. Revcolevschi, *nature* **418**, 39 (2002)